Feedback Linearized Controller Design and Switching Frequency Sensitivity Analysis of Distributed Generators

Author:
Mahmud, Md Rasel

Publication Date:
2021

DOI:
https://doi.org/10.26190/unsworks/2072

Feedback Linearized Controller Design and Switching Frequency Sensitivity Analysis of Distributed Generators

Md. Rasel Mahmud

A thesis submitted in fulfilment
of the requirements for the degree of
Doctor of Philosophy

School of Engineering and Information Technology
UNSW Canberra

September 10, 2021

Thesis/Dissertation Sheet

Surname/Family Name	:	**Mahmud**
Given Name/s	:	**Md. Rasel**
Abbreviation for degree as give in the University calendar	:	**PhD**
Faculty	:	**UNSW Canberra**
School	:	**SEIT**
Thesis Title	:	**Feedback Linearized Controller Design and Switching Frequency Sensitivity Analysis of Distributed Generators**

Abstract 350 words maximum: (PLEASE TYPE)

The conventional power system undergoes a massive change owing to the penetration of distributed generators into distribution networks and the standalone operation of microgrids. The characteristics of distributed generators largely depend on power electronic interfaces that are not matched with conventional synchronous machine-based generation systems. The changing behaviours of the distribution side of the electrical network continue to provide new challenges to power system design and operation engineers. To overcome such issues, the design of high-performance controllers plays a crucial role. In addition, investigation of the dynamic behaviours of the power electronic interfaces, including switching frequency is essential, which is the critical characteristic of the distributed generators.

The first contribution of this dissertation is the design of a robust nonlinear controller to enhance the transient stability of distributed generators. In this work, the feedback linearization technique is used to linearize the standalone solar photovoltaic including battery energy storage, grid-connected fuel cell, and grid-connected solar photovoltaic including battery energy storage systems. Robust H_∞ mixed-sensitivity loop-shaping controllers are designed to stabilize the linearized part of the nonlinear feedback linearized control laws. The proposed robust H_∞ controller for the feedback linearized control scheme provides several benefits over the existing feedback linearization that is stabilized by the conventional PI controller.

The second and unique contribution of this thesis is the developed single-input two-output feedback linearized control scheme based on the conventional single- input single-output feedback linearization approach. The third contribution of this dissertation is single-input two-output controller design for the islanded DC, AC, and hybrid DC/AC microgrids to enhance the voltage stability and minimize the circulating current among parallel-connected distributed generators.

The fourth and final contribution of this work is the developed multi-frequency averaging based dynamic phasor model of a standalone, grid-connected, and two-stage distributed photovoltaic generators. The developed dynamic phasor models are provided with switching frequency-dependent characteristics, showing the switching frequency effect on the distributed generators. This contribution provides the idea of a suitable switching frequency range for power electronic interfaces.

Copyright Statement

Authenticity Statement

Originality Statement

I hereby declare that this submission is my own work and to the best of my knowledge it contains no material previously published or written by another person, or substantial portions of material that have been accepted for the award of any other degree or diploma at UNSW or any other educational institute, except where due acknowledgment is made in the thesis. Any contribution made to the research by others, with whom I have worked at UNSW or elsewhere, is explicitly acknowledged in the thesis. I also declare that the intellectual content of this thesis is the product of my own work, except to the extent that assistance from others in the project's design and conception or in style, presentation and linguistic expression is acknowledged.

Signed: .....

Date: .....

INCLUSION OF PUBLICATIONS STATEMENT

UNSW is supportive of candidates publishing their research results during their candidature as detailed in the UNSW Thesis Examination Procedure.

Publications can be used in their thesis in lieu of a Chapter if:

- The candidate contributed greater than 50% of the content in the publication and is the "primary author", ie. the candidate was responsible primarily for the planning, execution and preparation of the work for publication
- The candidate has approval to include the publication in their thesis in lieu of a Chapter from their supervisor and Postgraduate Coordinator.
- The publication is not subject to any obligations or contractual agreements with a third party that would constrain its inclusion in the thesis

Please indicate whether this thesis contains published material or not:

☐ This thesis contains no publications, either published or submitted for publication
(if this box is checked, you may delete all the material on page 2)

☒ Some of the work described in this thesis has been published and it has been documented in the relevant Chapters with acknowledgement
(if this box is checked, you may delete all the material on page 2)

☐ This thesis has publications (either published or submitted for publication) incorporated into it in lieu of a chapter and the details are presented below

CANDIDATE'S DECLARATION

I declare that:

- I have complied with the UNSW Thesis Examination Procedure
- where I have used a publication in lieu of a Chapter, the listed publication(s) below meet(s) the requirements to be included in the thesis.

Candidate's Name	Signature	Date (dd/mm/yy)

Abstract

The conventional power system undergoes a massive change owing to the penetration of distributed generators into distribution networks and the standalone operation of microgrids. The characteristics of distributed generators largely depend on power electronic interfaces that are not matched with conventional synchronous machine-based generation systems. The changing behaviours of the distribution side of the electrical network continue to provide new challenges to power system design and operation engineers. To overcome such issues, the design of high-performance controllers plays a crucial role. In addition, investigation of the dynamic behaviours of the power electronic interfaces, including switching frequency is essential, which is the critical characteristic of the distributed generators.

The first contribution of this dissertation is the design of a robust nonlinear controller to enhance the transient stability of distributed generators. In this work, the feedback linearization technique is used to linearize the standalone solar photovoltaic including battery energy storage, grid-connected fuel cell, and grid-connected solar photovoltaic including battery energy storage systems. Robust H_∞ mixed-sensitivity loop-shaping controllers are designed to stabilize the linearized part of the nonlinear feedback linearized control laws. The proposed robust H_∞ controller for the feedback linearized control scheme provides several benefits over the existing feedback linearization that is stabilized by the conventional PI controller.

The second and unique contribution of this thesis is the developed single-input two-output feedback linearized control scheme based on the conventional single-input single-output feedback linearization approach. The third contribution of this dissertation is single-input two-output controller design for the islanded DC, AC, and hybrid DC/AC microgrids to enhance the voltage stability and minimize

the circulating current among parallel-connected distributed generators.

The fourth and final contribution of this work is the developed multi-frequency averaging based dynamic phasor model of a standalone, grid-connected, and two-stage distributed photovoltaic generators. The developed dynamic phasor models are provided with switching frequency-dependent characteristics, showing the switching frequency effect on the distributed generators. This contribution provides the idea of a suitable switching frequency range for power electronic interfaces.

Acknowledgments

This thesis would not have been possible without blessings, encouragement and support of several individuals around me, to only some of whom it is possible to give particular mention here.

First and foremost, I would like to express my sincere gratitude and appreciation to my supervisor, Associate Professor Hemanshu Roy Pota, for his continuous support, guidance, and insightful discussions about the research throughout my PhD candidature. His suggestions, both in academic and non-academic matters, have served as life lessons and helped me grow as a researcher and an individual. More importantly, he has always given me great freedom to pursue independent work by showing his faith in me and has always been a strong advocate for me in all the meetings where I have faced people from different backgrounds. He is not only my supervisor, but also a local guardian as I have received very fruitful support regarding mental and personal problems.

I would like to thank Mr. Sheik Mohammad Mohiuddin, from Stevens Institute of Technology, for helping with the simulations in the hardware in loop. He was always willing to help during his busy schedule. His help in developing simulation models is also unforgettable.

I sincerely acknowledge the School of Engineering & Information Technology, UNSW, Canberra for giving me the opportunity to carry out my doctoral research and for their financial support. It would have been impossible for me to start my study even if they had not given me a scholarship.

It is not possible to describe in words the role my friends have played in the unforgettable time I have spent in UNSW@ADFA and in Australia in general. They made the difficult times worthwhile and if some of them are not mentioned here, I can only attribute it to my aging memory. Thank you Forhad Bhai, Palash Bhai, Sumon Bhai, Alvi Bhai, Nazrul Bhai, and Kartik for the cherished times

we spent together in the campus, soccer and cricket sessions, barbecues, trips and places around town. Special thanks to the other members of Probasee Bengali Susheel Somaz - Asad Vai, Imran Vai, Kamrul Vai and Rahi - with whom I shared remarkable times, suddenly going to Sydney for Afghan food in the middle of the night, without whom life would be hard to imagine.

Above all, I would like to thank my family members, who stood by me through thick and thin. To my brother, I thank you for being my guiding light for life. To my sister-in-law, thank you for your care. To my little nephew and niece, you make my life brighter. To my wife you are awesome. I am forever indebted to my father and mother who have worked painstakingly to help me realize my dreams while caring little for their own comfort.

Dedicated to my brother Md Apel Mahmud

List of Publications

Journal Papers

[1] Mahmud, M. R. and Pota, H. Nonlinear controller design to enhance voltage restoration and current sharing accuracy of islanded dc microgrids. *IEEE System Journal*. Accepted.

[2] Mahmud, M. R. and Pota, H. Robust nonlinear controller design for dc-ac converter in grid connected fuel cell system. *IEEE Journal of Emerging and Selected Topics in Industrial Electronics*, 2021.

[3] Mahmud, M. R. and Pota, H. Robust partial feedback linearized controller design for standalone hybrid pv-bes system. *Electronics*, 10(7):772, 2021.

[4] Abdou, A.F. Mahmud, M. R. and Pota, H. Stability analysis of grid-connected photovoltaic systems with dynamic phasor model. *Electronics*, 8(7):747, 2019.

[5] Mahmud, M. R. and Pota, H. Nonlinear feedback linearized controller design for islanded ac microgrids. *IEEE Transactions on Power Systems*. Under Revision.

[6] Mahmud, M. R. and Pota, H. Transient stability analysis of partial feedback linearized islanded hybrid dc/ac microgrids. *IEEE Transactions on Smart Grid*. Submitted.

[7] Mahmud, M. R. and Pota, H. Multi-frequency averaging detail model of distributed photovoltaic generators. Under Preparation.

Conference Papers

[1] Mahmud, M. R. and Pota, H. Robustness analysis of h_∞ controller for feedback linearized model of grid connected inverter. In *2018 IEEE International Conference on Power Electronics, Drives and Energy Systems (PEDES)*, pages 1–6. IEEE, 2018.

[2] Hossain, M. A. Mahmud, M. R. and Pota, H. Nonlinear output feedback droop control for parallel inverters in standalone microgrids. In *2019 9th International Conference on Power and Energy Systems (ICPES)*, pages 1–6. IEEE, 2019.

[3] Hossain, M. A. Mahmud, M. R. and Pota, H. Robust nonlinear controller design for islanded photovoltaic system with battery energy storage. In *2020 IEEE International Conference on Power Electronics, Smart Grid and Renewable Energy (PESGRE2020)*, pages 1–6. IEEE, 2020.

[4] Mahmud, M. R. and Pota, H. Robust feedback linearizing controller design for dc microgrid connected dc-dc converter. In *2021 IEEE Texas Power and Energy Conference (TPEC)*, pages 1–6. IEEE, 2021.

[5] Md Rasel Mahmud and Hemanshu Pota. Nonlinear partial feedback linearized controller design for islanded ac microgrid connected distributed generations. In *2021 IEEE International Conference on Environment and Electrical Engineering and 2021 IEEE Industrial and Commercial Power Systems Europe (EEEIC/I&CPS Europe)*, pages 1–6. IEEE, 2021.

Contents

Abstract **i**

List of Publications **vii**

List of Figures **xv**

List of Tables **xix**

List of Abbreviations **xxi**

1 Introduction **1**
1.1 Background 2
1.1.1 Overview on distributed generators control 5
1.1.2 Overview on islanded microgrids control 6
1.1.3 Overview on switching frequency sensitivity of distributed PV generators 7
1.2 Research Motivations 8
1.3 Contributions of Thesis 9
1.4 Thesis Outline 11

2 Distributed Generators Modeling and Controller Design Methods **13**
2.1 Introduction 14
2.2 Mathematical Model of Distributed Generators 15
2.2.1 Dynamic model of standalone distributed PV-BES generator 16
2.2.2 Dynamic model of grid-connected distributed FC generator 20
2.2.3 Dynamic model of two-stage distributed PV-BES generator 22
2.3 Mathematical Model of Islanded Microgrids 24
2.3.1 Dynamic model of islanded DC microgrid 27
2.3.2 Dynamic model of islanded AC microgrid 29
2.3.3 Dynamic model of islanded hybrid DC/AC microgrid . . . 32
2.4 Mathematical Model of Distributed PV Generators 34
2.4.1 Dynamic model of standalone distributed PV generator . . 35
2.4.2 Dynamic model of grid-connected distributed PV generator 36

2.4.3 Dynamic model of two-stage distributed PV generator . . 37
2.5 Feedback Linearization of SISO Control Problem 38
2.6 Feedback Linearization of SITO Control Problem 42
2.7 Overview on Dynamic Phasor Modeling Technique 46
2.8 Chapter Summary 49

3 Robust Controller Design for Distributed Generators 51
3.1 Introduction 52
3.2 Feedback Linearization of Standalone Distributed PV-BES Generator 57
3.2.1 Determine relative degree 58
3.2.2 Nonlinear coordinate transformation 59
3.2.3 Zero internal dynamic stability 59
3.2.4 Feedback linearized control law 60
3.2.5 Transfer function of linearized system 61
3.3 Robust Controller Design for Linearized Standalone Distributed PV-BES generator 62
3.3.1 Uncertainty modeling 62
3.3.2 Noise decoupling capability of designed control scheme . . 65
3.3.3 Robust H_∞ mixed-sensitivity loop-shaping controller design 67
3.4 Feedback Linearization of Grid-Connected Distributed FC Generator 69
3.4.1 Determine relative degree 71
3.4.2 Nonlinear coordinate transformation 72
3.4.3 Zero internal dynamic stability 72
3.4.4 Feedback linearized control law 74
3.4.5 Transfer function of linearized system 75
3.5 Robust Controller Design for Linearized Grid- Connected Distributed FC Generator 76
3.5.1 Uncertainty modeling 76
3.5.2 Noise decoupling capability of designed control scheme . . 79
3.5.3 Robust H_∞ mixed-sensitivity loop-shaping controller design 81
3.6 Feedback Linearization of Two-Stage Distributed PV-BES Generator 83
3.6.1 Determine relative degree 85
3.6.2 Nonlinear coordinate transformation 86
3.6.3 Zero internal dynamic stability 87
3.6.4 Feedback linearized control law 88
3.6.5 Transfer function of linearized system 89
3.7 Robust Controller Design for Linearized Two-Stage Distributed PV-BES Generator 90
3.7.1 Uncertainty modeling 90
3.7.2 Noise decoupling capability of designed control scheme . . 90
3.7.3 Robust H_∞ mixed-sensitivity loop-shaping controller design 92
3.8 Performance Evaluation of Design Controllers 92

3.8.1 Stability analysis of distributed generators 92
3.8.2 Performance evaluation of standalone distributed PV-BES generator 96
3.8.3 Performance evaluation of grid-connected distributed FC generator 102
3.8.4 Performance evaluation of two-stage PV-BES generator . . 107
3.9 Chapter Summary 109

4 Nonlinear Controller Design for Islanded Microgrids 111
4.1 Introduction 112
4.2 Feedback Linearization of Islanded DC Microgrid 117
4.2.1 Lie derivative and relative degree 118
4.2.2 Nonlinear coordinate transformation 119
4.2.3 Stability of internal dynamics 120
4.2.4 Feedback linearized control law 121
4.3 Feedback Linearization of Islanded AC Microgrid 122
4.3.1 Lie derivative and relative degree 125
4.3.2 Nonlinear coordinate transformation 127
4.3.3 Stability of internal dynamics 128
4.3.4 Feedback linearized control law 129
4.4 Feedback Linearization Hybrid DC/AC Microgrid 129
4.4.1 Lie derivative and relative degree 133
4.4.2 Nonlinear coordinate transformation 134
4.4.3 Stability of internal dynamics 135
4.4.4 Feedback linearized control law 137
4.5 Linear Controller Design for Feedback Linearized Control Laws . . 137
4.6 Performance Evaluation of Designed Controllers 141
4.6.1 Stability analysis of islanded microgrids 141
4.6.2 Performance evaluation of islanded DC microgrid 143
4.6.3 Performance evaluation of islanded AC microgrid 155
4.6.4 Performance evaluation of hybrid DC/AC microgrid 163
4.7 Chapter Summary 170

5 Dynamic Phasor Modeling and Sensitivity Analysis 171
5.1 Introduction 172
5.2 Dynamic Phasor Modeling of Standalone Distributed PV Generator 175
5.2.1 Conventional state space model 176
5.2.2 Dynamic phasor model for index zero 177
5.2.3 Dynamic phasor model for index one 178
5.2.4 State space representation of dynamic phasor model 179
5.3 Dynamic Phasor Modeling of Grid-Connected Distributed PV Generator 181
5.3.1 Conventional state space model 182

5.3.2 Dynamic phasor model for index zero 182
5.3.3 Dynamic phasor model for index one 183
5.3.4 State space representation of dynamic phasor model 186
5.4 Dynamic Phasor Modeling of Two-Stage Distributed PV Generator 188
5.4.1 Conventional state space model 189
5.4.2 Dynamic phasor model for index zero 189
5.4.3 Dynamic phasor model for index one 191
5.4.4 State space representation of dynamic phasor model 194
5.5 Switching Frequency Sensitivity Analysis of MFA Model 197
5.5.1 Performance analysis of standalone distributed PV generator 197
5.5.2 Performance analysis of grid-connected distributed PV generator 199
5.5.3 Performance analysis of two-stage distributed PV generator 201
5.6 Chapter Summary 206

6 Conclusions and Directions for Further Research 207
6.1 Directions for Future Research 210
6.2 Outcome and Benefit of Research 211

References 213

A Supplementary Material for Chapter 3 227
A.1 Standalone Distributed PV-BES Generator 227
A.1.1 Calculation of the uncertainties 227
A.1.2 Parameters of design robust H_∞ controller 228
A.1.3 Parameters of existing conventional PI controller 228
A.1.4 Physical parameters of standalone distributed PV-BES generator 228
A.2 Grid-Connected Distributed FC Generator 229
A.2.1 Calculation of the uncertainties 229
A.2.2 Parameters of designed robust H_∞ controller 230
A.2.3 Parameters of existing conventional PI controller 230
A.2.4 Physical parameters of grid-connected distributed FC generator 231
A.3 Two-Stage Distributed PV-BES Generator 231

B Supplementary Material for Chapter 4 233
B.1 Islanded DC Microgrid 233
B.1.1 Physical parameters of islanded DC microgrid 233
B.1.2 Formulas for Table 4.4 233
B.2 Islanded AC Microgrid 234
B.2.1 Physical parameters of islanded AC microgrid 234
B.3 Islanded Hybrid DC/AC Microgrid 234

C Supplementary Material for Chapter 5 **235**
C.1 Standalone Distributed PV Generator 235
C.2 Grid-Connected Distributed PV Generator 235
C.3 Two-Stage Distributed PV Generator 236

List of Figures

2.1 Schematic diagram of DC-link capacitor connected distributed PV-BES generator. 17
2.2 Circuit diagram of DC-link capacitor connected distributed PV generator. 18
2.3 Circuit diagram of DC-link capacitor connected BES system. . . . 19
2.4 Circuit diagram of grid-connected distributed FC generator. . . . 20
2.5 Schematic diagram of two-stage distributed PV-BES generator. . 23
2.6 Flexible configuration of microgrid components. 24
2.7 Typical layout of hybrid DC/AC microgrid connected distributed generators. 26
2.8 Proposed layout of islanded hybrid DC/AC microgrid. 27
2.9 Circuit diagram of DC microgrid connected DC-DC boost converters. 28
2.10 Circuit diagram of AC microgrid connected DC-AC converters. . . 29
2.11 Circuit diagram of islanded hybrid DC/AC microgrid. 32
2.12 Circuit diagram of standalone distributed PV generator. 35
2.13 Circuit diagram of grid-connected distributed PV generator. . . . 36
2.14 Circuit diagram of two-stage PV generator. 37

3.1 Circuit diagram of DC-link capacitor connected generalized distributed generator. 57
3.2 Weight and sensitivity functions in sigma plot. 68
3.3 Circuit diagram of grid-connected distributed FC generator. . . . 69
3.4 Weight and sensitivity functions in sigma plot. 82
3.5 Circuit diagram of two-stage distributed PV-BES generator. . . . 84
3.6 Sensitivity functions responses with proposed H_∞ and existing PI controller for standalone distributed PV-BES generator. 93
3.7 Sensitivity functions responses with proposed H_∞ and existing PI controller for grid-connected distributed FC generator. 94
3.8 Implementation block diagram of proposed controller for standalone distributed PV-BES generator. 96
3.9 Bus voltage and different power responses under generation change (FBL_{H_∞}-solid line and FBL_{PI}-desh line). 98

3.10 Bus voltage and different power responses under load variation (FBL_{H_∞}-solid line and FBL_{PI}-desh line). 99
3.11 Bus voltage and different power responses under parameter variation (FBL_{H_∞}-solid line and FBL_{PI}-desh line). 100
3.12 Bus voltage and different power responses under measurement noise (FBL_{H_∞}-solid line and FBL_{PI}-desh line). 101
3.13 Implementation block diagram of the proposed controller for grid-connected distributed FC generator. 102
3.14 In dq frame output current and power under power factor change (FBL_{H_∞}-solid line and FBL_{PI}-desh line). 103
3.15 In dq frame output current and power under three-phase short-circuit fault (FBL_{H_∞}-solid line and FBL_{PI}-desh line). 103
3.16 In dq frame output current and power under parameter variation (FBL_{H_∞}-solid line and FBL_{PI}-desh line). 105
3.17 In dq frame output current and power under measurement noise (FBL_{H_∞}-solid line and FBL_{PI}-desh line). 106
3.18 DC-bus voltage under (a) generation change, (b) power factor change and (c) measurement noise (FBL_{H_∞}-solid line and FBL_{PI}-desh line). 107
3.19 AC output current under (a) generation change, (b) power factor change and (c) measurement noise (FBL_{H_∞}-solid line and FBL_{PI}-desh line). 109

4.1 Circuit diagram of DC microgrid connected DC-DC boost converter. 117
4.2 Circuit diagram of AC microgrid connected DC-AC converter. . . 123
4.3 Circuit diagram of islanded hybrid DC/AC microgrid. 130
4.4 Responses of functions $S(s)$ and $T(s)$ with different stability analysing tools. 143
4.5 Proposed control implementation diagram for parallel connected DC-DC converters in DC microgrid. 144
4.6 Output voltage under equal power generation. 146
4.7 Output current under equal power generation. 147
4.8 Output power under equal power generation. 147
4.9 Output voltage under unequal power generation with $P_1 = 2P_2$. . 148
4.10 Output current under unequal power generation with $P_1 = 2P_2$. . 149
4.11 Output power under unequal power generation with $P_1 = 2P_2$. . . 149
4.12 Output voltage under equal power generation with $R_{l1} = 5R_{l2}$. . . 150
4.13 Output current under equal power generation with $R_{l1} = 5R_{l2}$. . . 151
4.14 Output power under equal power generation with $R_{l1} = 5R_{l2}$. . . . 151
4.15 Output current, voltage and power deviation under equal generation. 153
4.16 Proposed control implementation block diagram for parallel-connected VSCs in islanded AC microgrids. 154
4.17 Generated modulating signals by proposed control scheme. 156

4.18 Signals based on PWM switching strategy. 157
4.19 Pulse width modulation in abc frame. 157
4.20 Control input in dq frame under demand power variation. 158
4.21 Output current of VSIs under demand power variation. 159
4.22 Output voltage of VSIs under demand power variation. 159
4.23 Total load of microgrid under demand power variation. 160
4.24 Control input in dq frame under terminal fault. 161
4.25 Output current of VSIs under terminal fault. 161
4.26 Output voltage of VSIs under terminal fault. 162
4.27 Total load of microgrid under terminal fault. 162
4.28 Frequency response of microgrid under different case studies. . . . 163
4.29 Output voltage of DC buses. 164
4.30 DC supply and demand power. 164
4.31 Input current and output active power of DC-AC VSCs. 165
4.32 Frequency of AC sub-microgrid. 165
4.33 DC-buses currents. 168
4.34 Input current and output active power of DC-AC VSCs. 168
4.35 Output currents of DC-AC VSCs. 169
4.36 Output voltages of DC-AC VSCs. 169

5.1 Circuit diagram of standalone distributed PV generator. 176
5.2 Circuit diagram of grid-connected distributed PV generator. . . . 182
5.3 Circuit diagram of two-stage PV generator. 188
5.4 Output voltage of the standalone distributed PV generator. 198
5.5 Output current of grid-connected distributed PV generator in d-axis. 201
5.6 Output current of grid-connected distributed PV generator in q-axis. 202
5.7 DC output voltage of two-stage distributed PV generator. 203
5.8 AC output current of two-stage distributed PV generator in d axis. 204
5.9 AC output current of two-stage distributed PV generator in q axis. 205

List of Tables

2.1 Different configuration of distributed generators. 25

3.1 Summary of controller design methods for distributed generators. 56
3.2 H_∞ norm value of weighting and sensitivity functions. 69
3.3 H_∞ norm value of weighting and sensitivity functions 83

4.1 Summary of controller design methods for islanded microgrids. . . 116
4.2 Amplitude of output current, voltage and power under three different case studies for proposed control scheme. 152
4.3 Amplitude of output current, voltage and power under equal generation for three different droop-control. 152
4.4 Deviation under equal power generation. 153

5.1 Summary of dynamic modeling methods for distributed PV generators. 175
5.2 Eigenvalues of the standalone distributed PV generator under different switching frequencies. 198
5.3 Eigenvalues of grid-connected distributed PV generator at different switching frequencies. 200
5.4 Eigenvalues of two-stage distributed PV generator at different switching frequencies. 203

List of Abbreviations

BES	Battery Energy Storage
CDC	Conventional Droop Control
CSDC	Current-Sharing Droop Control
DG	Distributed Generator
DP	Dynamic Phasor
FC	Fuel Cell
KCL	Kirchoff's Current Law
KVL	Kirchoff's Voltage Law
MFA	Multi-Frequency Averaging
MIMO	Multi-Input Multi-Output
PCS	Proposed Control Scheme
PEC	Power Electronic Converter
PEI	Power Electronic Interface
PSDC	Power-Sharing Droop Control
PV	Photovoltaic
PWM	Pulse-Width Modulation
RES	Renewable Energy Source
SISO	Single-Input Single-Output
SITO	Single-Input Two-Output
SSA	State-Space Averaging
VSC	Voltage Source Converter
VSI	Voltage Source Inverter

Chapter 1

Introduction

Abstract

Nowadays, significant changes have been seen in power system generation sectors due to environmental pollution, shortages of fossil fuel-dependent energy resources, and rising fossil fuel prices. In addition, renewable energy resource-based power generation systems are gaining popularity worldwide and are closely associated with changes in the surrounding environment. Such dependency poses an additional risk to the transient stability and steady-state operation of conventional power systems. Simultaneously, the establishment of various types of small power systems based on renewable energy resources is increasing, which makes it imperative to emphasize their operation.

There is a particular need for power electronic interfaces to convert usable electric power from renewable energy resources. It is important to be concerned about the effects of appropriate control schemes and their switching frequencies to properly operate such devices. This dissertation is based on a nonlinear controller design and a sensitivity analysis of the switching frequency for different distributed

generators.

1.1 Background

In the current era of globalization, electricity is considered one of the driving forces of the global economic and technological revolution [1]. Electricity brings the present society to the brink of relief and development, but its generation system also puts the environment at risk. A large amount of carbon dioxide is emitted from the power generation sector, which plays a significant role in environmental pollution [2]. Carbon dioxide emissions have received the attention of world leaders and environmentalists for decades, and as a result, they are shifted to alternative resources for power generation [3].

Renewable energy sources (RESs) are considered alternatives to conventional power generation systems [4, 5, 6], including solar photovoltaics, wind turbines, tides, and hydrogen. The electricity generated from such alternative resources is environmentally friendly, but it is affected in many ways by its surroundings [7]. As a result, their operations are different from traditional power systems, and these generation systems are new for power system engineers, so they have no set guidelines [8].

Distributed RESs are naturally or necessarily installed in a distributed manner; therefore, they are often considered distributed generators (DGs). Their differences can also be noticed in their structures because they consider each one's power supply and flexibility. Such a DG can be operated in grid-connected or isolated conditions, or even a group of standalone sources can form a small grid [9, 10]. Regardless of the structural form, it is challenging to ignore power electronic interfaces (PEIs) in such a generation system [11]. A reliable controller

design is essential for such an interface to obtain usable electric power from the DGs [12].

The use of advanced control technology in power systems has been increased over the last few decades [13], and the proliferation of DG is taken to a stronger position. On the other hand, interest in expanding expensive physical systems has diminished, and advanced control-based expansion has increased. With advancements in modern computers and power electronic technology, a new horizon of power system control has been opened [14, 15].

The linear controller design methods are an established and powerful control strategy. Linear control theory is an effective controller design procedure for conventional power systems [16, 17], but nonlinear dynamic behaviour must be considered linear. It can be regarded as a linear system when a small amount of output or load changes in the power system. The dynamic structure does not change significantly in such a situation; the controller can be provided with the expected performance [18, 19].

A power system consists of several units or components, where each component can perform according to the specific criteria. After much investigation, robust control methods have been considered for power systems, and over the past few years, such control systems have undergone significant improvements [20, 21, 22]. A control system can only be regarded as robust when the designed controller completes the action, despite the discrepancies between the actual and mathematical models.

The main goal of installing a controller in a power system is to complete the operation, as expected by a reasonable effort. The key to designing a reliable controller is to keep the system stable, with minimal effort, a short-term fire after a problem, and a significant setback to prevent an imbalance. If one of

the interconnected components has a problem, the others will not be harmed by it. However, when there is a significant problem in any part of the power system, it impacts the dynamic stability of the entire system. In this case, the power system's behaviour is not linear, so the designed linear controller fails to maintain a stable operation [23]. In addition, the power system itself has some nonlinear behaviour that linear models cannot accurately represent.

However, the generated power from RESs depends on atmospheric conditions [24, 25]. In addition, the PEI used in these studies is naturally nonlinear [26]. More errors arise when considering the change in the state of the atmosphere as linear. Moreover, the efficiency of the linear controller is limited to the linearized system. Therefore, more emphasis needs to be placed on the design and implementation of nonlinear controllers.

The nonlinear control design method is a suitable tool for maintaining the dynamic operation of the power system. Such control methods can play an influential role in maintaining transient stability and solving practical problems [27, 28]. The nonlinear controller design technique can provide a more accurate idea of the power system. Even obstacles to the practical application of such controls have been overcome with computers' unprecedented advancement. Improvements to modern instruments to accomplish more extensive operations have been made nonlinear control methods easier.

Most of the design nonlinear controllers require additional effort for information that cannot be physically measured to be operated in the power system [29]. Sometimes, there are some issues in implementing such controllers in practice, and if they do not provide accurate information, the efficiency of the power system is further reduced. Moreover, differential intrusions correspond to most nonlinear controller designs, adding extra noise to the system, resulting in unwanted

actions. Such limitations have paved the way for the design and installation of nonlinear controllers for the power systems.

At present, the power system is leaning toward RESs, where PEI is inextricably linked. Therefore, for the power system to function correctly, it is essential to investigate the different operation modes of the PEI with renewable energy and improve its efficiency. The following subsections briefly discuss the robust nonlinear controllers for DGs, their parallel operation in islanded microgrids, and the effect of switching frequency on the PEIs.

1.1.1 Overview on distributed generators control

Distributed generators can perform connected or disconnected modes to the utility grid [30, 31]. A standalone operation mode is more realistic for electric power customers who are challenging or more expensive to bring under the established electrical network. However, such a standalone power system requires a battery or any other energy storage device; otherwise, it is bound to face power shortages or wastage [32, 33, 34]. The DG does not require an energy storage device in the grid-connected mode, whereas the utility grid acts as a large energy storage [35]. This type of operation mode is beneficial for the DGs covered by the electrical network. Both operation modes are suitable for their respective conditions, and a hybrid system should offer both types of benefits [36].

Most modern electrical loads are DC, and standalone generators are also likely DC type, which is easy to control. On the other hand, because the utility grid is AC type, the DG's output must be AC in grid-connected operation mode, and the combined system has both DC and AC outputs. As expected, a proper control strategy is required to obtain the output of all the different structural systems [37, 38, 39, 40]. A controller can only be considered successful if it performs as

expected under large disturbances and modeling uncertainties.

Many advanced nonlinear control methods have been proposed for DGs to effectively deal with different problems. However, in some cases, little attention has been paid to modeling uncertainty. Even if modeling uncertainty is considered, the system is considered to be linear. Above all, the controller should be designed using a control method in which the system's nonlinearity and robustness predominate.

1.1.2 Overview on islanded microgrids control

There is a growing tendency for day-to-day DGs to work in parallel [41], which is known as microgrids [42]. If a microgrid is formed by DGs that do not fall within the established electrical network, there is no way for the microgrid to work except for the islanded operation mode. When electric power consumers are uncovered by the electrical network and meet their electricity demand from a single DG, some extra money is needed to install an energy storage system, which is difficult for many to arrange at one time. The cost of installing such an energy storage system can be reduced by connecting microgrids, where the common point of the microgrid acts as virtual electric power storage.

The use of RESs is rising worldwide, maintaining the microgrid operation significantly different from conventional power systems [43, 44, 45, 46, 47]. Because power systems include both AC and DC loads and most of the RESs generate DC power, this DC can be directly supplied to the DC loads without the cost of controlling the frequency and reactive power. Simultaneously, the AC loads can be supplied through the conversion from DC to AC power. As a result, DC, AC, and hybrid DC/AC microgrids have been developed, and the design and implementation of suitable controllers are essential for their proper functioning.

Controlling the microgrids that perform in an isolated mode is more complicated than that in the utility grid-connected mode. However, with the advancement of control system design methods, these complexities are reduced, and isolated microgrid functioning has become more comfortable. Modern nonlinear controllers play a significant role, but most controller designs are focused entirely on the output voltage at an early stage. The controller should be designed to emphasize the output voltage and current to properly operate the isolated microgrids.

1.1.3 Overview on switching frequency sensitivity of distributed PV generators

Distributed solar photovoltaic (PV) generators are becoming one of the most popular RESs because of their sunlight-based power generation and environmentally friendly behaviours [48, 49]. In the literature has two modes of operation, standalone and grid-connected; both play a significant role in their perspective [50]. The standalone operation mode of the distributed PV generator is an effective for rural area where the electrical network is not present; conversely, the energy storage is not required in a grid-connected system. Furthermore, there have been initiatives from both local and federal governments to integrate a grid-connected distributed PV generator, resulting in more rooftop PV generators in recent years. As a result, households produce more power and supply extra power to the utility grid. The grid integration of distributed PV generators relies heavily on PEIs, and hence, there are more harmonics owing to the presence of PEIs [51].

The ongoing interactions between PEIs and RESs introduce new barriers to

uncertain power generation related to stability and control issues [52]. For the stability analysis of a system, a preliminary assessment of its reliable operation, and small- and large-signal analyses are widely used [53, 54]. In addition, time-domain detailed switch simulation tools provide helpful insights into the out-turn small-signal behaviours of PEIs [55]. Such an analysis is unable to provide proper transient behaviour estimation of interfaces [56]. The characterization of PEIs to estimate instability situations requires extensive simulations, which are time-consuming.

The switching frequency sensitive multi-frequency averaging (MFA) based dynamic phasor approach is proposed as a straightforward mathematical representation technique of a dynamic system, which can address DC, fundamental, and other harmonic components of the state variables in the Fourier series form [57, 58]. It is also provided with a conventional state-space averaging (SSA) model when the involvement of fundamental and harmonic components is not considered. Moreover, this modeling technique can provide little flexibility to the harmonic component, which has no considerable impact on the variables.

1.2 Research Motivations

From the above discussion, it can be concluded that there are opportunities to further improve the following issues regarding the controller design and the effect of switching frequencies on the PEIs used in the DGs to enhance the stability of the generation systems.

- It is necessary to consider how the stability of the distributed generators is affected by changes in physical parameters such as R, L and C elements.
- Linear controllers are widely used to maintain the stability of distributed

generators. While such controls can solve minor problems, they are not sufficient to handle significant changes.

- The system's nonlinear behaviour needs to be incorporated into its mathematical model to establish maximum harmony with the practical system.
- The nonlinear control methods are quite effective in nonlinear distributed generators, which improves the transient stability.
- The physical condition of the control law depends on the control objectives, which can be determined by the measured data.
- The controller's measured information may contact the noise by their measuring instrument; therefore, the measured noise should be considered in the controller design procedure.
- Distributed generators are heavily involved with the power electronic interfaces and rely on switching frequencies; therefore, a modeling approach is needed to consider such dependencies.
- It is imperative to investigate the sensitivity of switching frequencies on the power electronic interfaces.

1.3 Contributions of Thesis

This thesis looks at a nonlinear controller design and dynamic phasor modeling of the DGs to improve flexibility and enhance transient stability. It also covered the limitations of existing controls and the effect of changing the parameters on them. The limitations of the nonlinear controls currently in use have been improved. The proposed controllers are designed to improve the transient stability of DGs

and islanded microgrids. Furthermore, the effect of switching frequency on the PEIs used in these systems is analysed with the help of switching frequency sensitive models, where different physical configurations of distributed PV generators are considered examples. The main contributions of this thesis are considered as follows.

- The control problems of the distributed generators and the islanded microgrids are classified as nonlinear control problems with their corresponding control outputs to control inputs mapping.
- The control problem of various distributed generators falls into the single-input single-output control problem for which robust nonlinear controllers are designed.
- The unique contribution of this thesis is the developed single-input two-output feedback linearized control scheme based on the conventional single- input single-output feedback linearization approach.
- The control problem of islanded DC, AC, and hybrid DC/AC microgrids consisting of distributed generators are included in the single-input two-output control problem for which nonlinear controllers are designed.
- Mathematical models based on switching frequencies are established for distributed PV generators with different configurations, and the effect of switching frequencies on the power electronic interfaces used in distributed PV generators are observed.

The designed robust nonlinear controllers' performance for DGs and the designed single-input two-output nonlinear controllers for islanded microgrids are verified on the electromagnetic transient platform using MATLAB/Simulink. The

effect of switching frequencies on the PEIs in distributed PV generators are tested on a simulator platform. The designed controllers' performance is observed for various problems and the switching frequency sensitivity of the PEIs for different switching frequencies.

1.4 Thesis Outline

The outline of the overall content of this dissertation is as follows:

Chapter 1 presents the background to this dissertation, as well as the motivations, contributions, and dissertation outline.

Chapter 2 provides the characteristic models of the different distributed generators used throughout this thesis. This chapter as well introduces an overview of the nonlinear feedback linearized controller design technique and dynamic phasor modeling approach.

Chapter 3 concentrates on the robust nonlinear controller design for different distributed generators. The feedback linearization technique is used to linearize nonlinear distributed generators, where a mixed-sensitivity based robust H_∞ loop-shaping controller is applied to regulate the output functions in the obtained control law.

Chapter 4 presents a nonlinear feedback linearized controller for newly defined single-input two-output control problems in islanded DC, AC, and hybrid DC/AC microgrids.

Chapter 5 presents the sensitivity analysis of the power electronic interfaces of different distributed PV generators. The sensitivity analysis is conducted based on the dynamic phasor modeling approach.

Chapter 6 provides concluding remarks and potential recommendations for

further development.

Chapter 2

Distributed Generators Modeling and Controller Design Methods

Abstract

This thesis contributes to the design of feedback linearized controllers for distributed generators and islanded microgrids. Sensitivity analysis of switching frequency for power electronic interfaces in different distributed photovoltaic generators also develop using a dynamic phasor modeling approach. The design of controllers requires a meaningful mathematical model that represents dynamic characteristics that are quite similar to those of a practical system in terms of maintaining stability under different operating conditions. Such a mathematical model is also required to develop a dynamic phasor model corresponding to switching frequency dependency analysis of power electronic interfaces for distributed generators. This chapter includes a mathematical model of distributed generators and their controller design methods.

2.1 Introduction

Power system stability is an aging issue, but it has been acknowledged as a big challenge publicly [59]. Improving stability is essential for the proper operation of power systems. The stability of conventional power systems is stable, but the integration of DGs into the utility grid enriches a new challenge [60]. On the other hand, small-scale power systems have been introduced based on DGs. Such a small-scale system can be operated in a grid-connected mode or standalone mode [61].

Such changes in the distributed network or newly established small-scale standalone systems can be adapted or stabilized through a proper control scheme. In the literature, different control methods [62, 63], such as linear, nonlinear, and robust are proposed, whose performance largely depends on an accurate mathematical model. The used PEIs in DGs are mathematically nonlinear. There are various approaches to control such systems, in which a linear control system is widely established. Nonlinear systems are primarily considered linear for designing linear controllers. These control methods are effective for small changes, but they cannot play an influential role in significant changes. Nonlinear control methods are more effective for controlling significant changes and can be made more efficient by including robust controllers with such a control scheme.

On the other hand, PEIs are used to provide usable power from DGs that are largely dependent on high switching frequencies. The effect of a high switching frequency on the system stability cannot be traced from conventional mathematical models [64]. A mathematical model that is formed using the dynamic phasor method can properly trace such issues.

Thus, the controller plays a crucial role in keeping the power system stable,

which is largely dependent on the accurate mathematical model and the switching frequency of the PEIs. Based on the above discussion, the key contributions of this study are as follows:

- Dynamic models of the different distributed generators, the islanded microgrids and distributed photovoltaic generators are developed (Sections 2.2, 2.3 and 2.4).
- Introduce single-input two-output feedback linearized controller design technique based on the conventional feedback linearization approach (Sections 2.5 and 2.6).
- A clear idea is provided on the dynamic phasor modeling procedure for high switching frequency-dependent power electronic interfaces (Sections 2.7).

2.2 Mathematical Model of Distributed Generators

Nowadays, many consumers of electric power can produce most of their needs from DGs. As a result, electricity reached all the people who were brought under the conventional electrical network was very costly, and in many cases, impossible. Among such DGs, solar photovoltaic (PV) must be placed on top of the list due to available sunlight. Power storage devices have been used with standalone generators to make them more stable and efficient. The battery is still considered to be the most widely used and convenient among the various energy storage devices. The combination of distributed PV generator and battery energy storage (BES) can act as a reliable power source [65, 66].

On the other hand, particular emphasis is currently placed on fuel cell (FC) generators as a source of environmental balance and a collaborative power source for distributed PV generators. Since these sources are not so much affected by their surroundings, they can be considered more valuable than distributed PV generators in exceptional cases. BES devices are not required to rely on the energy produced from the distributed FC generator. Grid-connected distributed FC generator can be considered to complete the operation from being connected to a conventional electrical network [67].

However, the surplus power will happen to the BES after it is fully charged for all distributed generators that are not connected to the utility grid. In addition, there may be a situation where there is no power, even after taking the total power from the battery. Such problems can be easily solved by connecting to the grid. However, there has been a mismatch between the selling price of surplus energy and the purchase price of the required energy, where the selling price of energy produced from DGs is usually smaller than the selling price of energy purchased from the grid. The combination of these two structures may be able to overcome such a problem. Therefore, it can be said that the combined grid-connected (two-stage distributed) PV-BES generator can overcome the above problem and provide the benefits of both [68, 69]. Three separate structures and mathematical models are presented below.

2.2.1 Dynamic model of standalone distributed PV-BES generator

A generalized characteristics model of a DC-DC voltage source converter (VSC) is developed for standalone distributed PV generators with a BES unit. A schematic

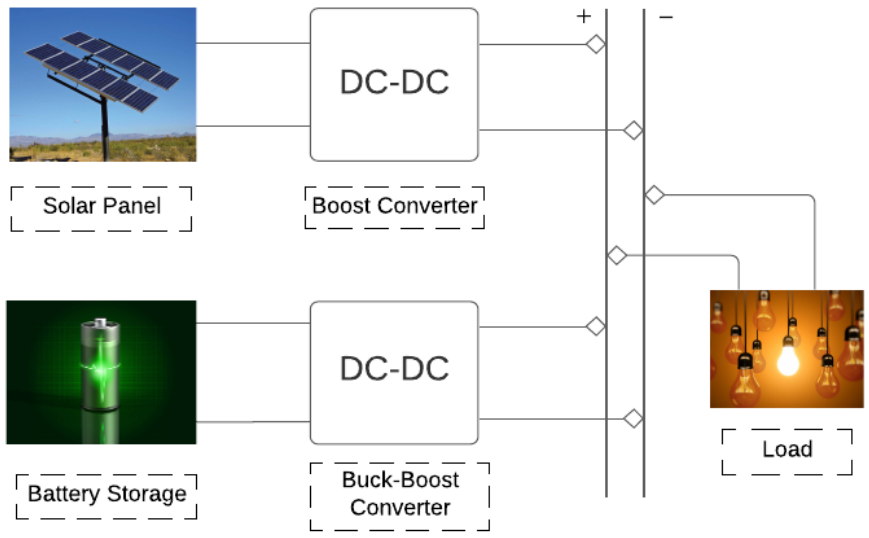

Figure 2.1: Schematic diagram of DC-link capacitor connected distributed PV-BES generator.

diagram of the considered hybrid type distributed generation system is shown in Figure 2.1, where solar PV generator and BES device are connected to a DC-link capacitor through a DC-DC boost and a bidirectional DC-DC buck-boost VSCs, respectively.

Dynamic model of PV system

Figure 2.2 presents that the distributed PV generator is connected to a DC-link capacitor by the DC-DC boost VSC. The output voltage is V_{sp} across the capacitor C_{sp}, i_{sp} is the output current and R_{sp} is the internal resistance. The input current through the inductor L_{dcp} and the output voltage across the DC-link capacitor C_{dc} are i_{Lp} and V_{dc}, respectively. The output current of the converter is i_{dcp}, which is injected into a common DC-link.

The characteristics model of the DC-link connected distributed PV generator

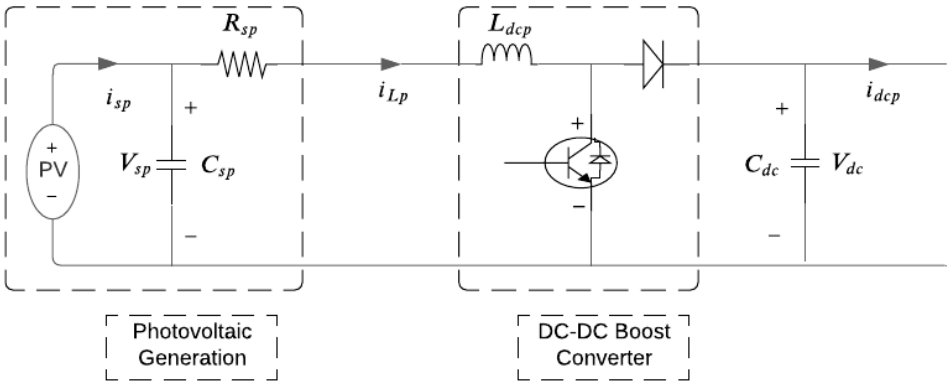

Figure 2.2: Circuit diagram of DC-link capacitor connected distributed PV generator.

is expressed, as shown in Figure 2.2:

$$\begin{aligned} \frac{dV_{sp}}{dt} &= \frac{1}{C_{sp}}\left(i_{sp} - i_{Lp}\right) \\ \frac{di_{Lp}}{dt} &= \frac{1}{L_{dcp}}\left(V_{sp} - R_{sp}i_{Lp} - m_p V_{dc}\right) \\ \frac{dV_{dc}}{dt} &= \frac{1}{C_{dc}}\left(m_p i_{Lp} - i_{dcp}\right) \end{aligned} \tag{2.1}$$

where the control objective is V_{dc} and the switching input is m_p of the DC-DC boost converter. For the more detailed dynamic model of the DC-DC VSC connected distributed PV generator can be found in [70].

Dynamic model of BES system

Figure 2.3 illustrates a circuit diagram of the BES system, which is coupled to the DC-link capacitor via the bidirectional DC-DC buck-boost VSC. The output voltage across C_{sb} is V_{sb} and the internal resistance is R_{s1}. The input current is i_{Lb} through filtering inductor L_{dcb} and the output voltage is V_{dc} across the DC-link capacitor C_{dc}. The bidirectional output current is i_{dcb}. The more detailed of reaming elements of the battery are V_g, R_{s2}, R_{sb} and C_{sb} can be found in [71].

The characteristics model of the common DC-link connected distributed PV

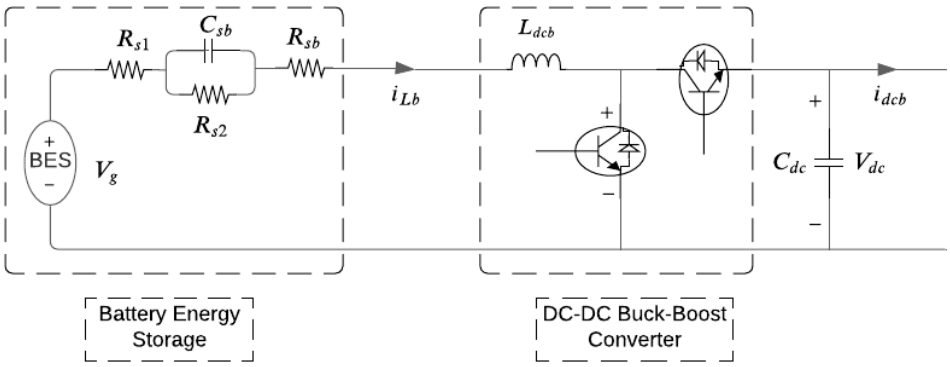

Figure 2.3: Circuit diagram of DC-link capacitor connected BES system.

generator-combined BES system is determined, as shown in Figure 2.3:

$$\begin{aligned} \frac{dV_{sb}}{dt} &= \frac{1}{C_{sb}}\left(i_{Lb} - \frac{V_{sb}}{R_{s2}}\right) \\ \frac{di_{Lb}}{dt} &= \frac{1}{L_{dcb}}\left[V_g - i_{Lb}\left(R_{s1} + R_{sb}\right) - V_{sb} - m_b V_{dc}\right] \\ \frac{dV_{dc}}{dt} &= \frac{1}{C_{dc}}\left(m_b i_{Lb} - i_{dcb}\right) \end{aligned} \tag{2.2}$$

where the control objective is V_{dc} and the switching input is m_b of the bidirectional DC-DC buck-boost VSC. The detailed mathematical model of the DC-DC VSC linked BES system can be found in [72].

Generalized dynamic model of PV-BES system

From both characteristics model of the DC-link capacitor connected distributed PV generator and the BES system are described by (2.1) and (2.2), where the first dynamic states do not have a significant impact on the stability properties [70]. Therefore, the remaining two dynamic states are presented with full system dynamics to control the output voltage. From the equations (2.1) and (2.2) can

be offered as a generalized characteristics model in the following form:

$$\begin{aligned} \frac{di_L}{dt} &= \frac{1}{L_{dc}}\left(V_s - mV_{dc}\right) \\ \frac{dV_{dc}}{dt} &= \frac{1}{C_{dc}}\left(mi_L - i_{dc}\right) \end{aligned} \tag{2.3}$$

where the subscript notation sp and sb are replaced by the subscript notation s, which represent the PV and BES systems, respectively. For distributed PV generator (sp), and the BES system (sb) with $V_s = V_{sp} - i_{sp}R_{sp}$ and $V_s = G_g - i_{Lb}(R_{s1} + R_{sb}) - V_{sb}$.

2.2.2 Dynamic model of grid-connected distributed FC generator

Figure 2.4 shows a grid-connected distributed FC generator that consists of a FC stack, a three-phases DC-AC VSC and an inductance filter. The three-phase terminal voltages V_{ta}, V_{tb} and V_{tc} can be written as follows:

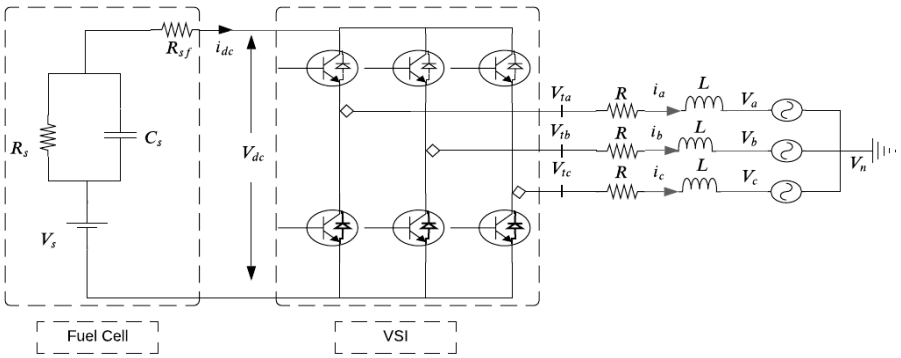

Figure 2.4: Circuit diagram of grid-connected distributed FC generator.

$$\begin{aligned} V_{ta} &= \frac{V_{dc}}{2} m_a(t) \\ V_{tb} &= \frac{V_{dc}}{2} m_b(t) \\ V_{tc} &= \frac{V_{dc}}{2} m_c(t) \end{aligned} \tag{2.4}$$

where $m_a(t)$, $m_b(t)$ and $m_c(t)$ are the modulating signals and V_{dc} is the DC-input voltage to the three-phase DC-AC VSC. The nonlinear dynamic model of the grid-connected distributed FC generator can be derived as follows [73]:

$$\begin{aligned} \frac{dV_c}{dt} &= \frac{V_{dc}}{R_s C_s} - \frac{V_s}{R_s C_s} + \left(\frac{1}{C_s} + \frac{R_{sf}}{R_s C_s} \right) i_{dc} \\ \frac{di_a}{dt} &= \frac{1}{L} \left(\frac{V_{dc}}{2} m_a - R i_a - V_a - V_n \right) \\ \frac{di_b}{dt} &= \frac{1}{L} \left(\frac{V_{dc}}{2} m_b - R i_b - V_b - V_n \right) \\ \frac{di_c}{dt} &= \frac{1}{L} \left(\frac{V_{dc}}{2} m_c - R i_c - V_c - V_n \right) \end{aligned} \tag{2.5}$$

In equation (2.5), the DC input voltage V_{dc} of the three-phase DC-AC VSC can be written as follows from Figure 2.4:

$$V_{dc} = V_s - V_c - R_{sf} i_{dc} \tag{2.6}$$

The details of the dynamic model are provided in [74]. The dynamic model (2.5), which can be transformed into a time-invariant model in the dq frame as follows [75]:

$$\begin{aligned} \frac{dV_c}{dt} &= \frac{V_{dc} - V_s}{R_s C_s} + \frac{4}{3} \left(\frac{1}{C_s} + \frac{R_{sf}}{R_s C_s} \right) i_d m_d + \frac{4}{3} \left(\frac{1}{C_s} + \frac{R_{sf}}{R_s C_s} \right) i_q m_q \\ \frac{di_d}{dt} &= \frac{1}{L} \left(\frac{V_{dc}}{2} m_d - R i_d - V_d \right) + \omega i_q \\ \frac{di_q}{dt} &= \frac{1}{L} \left(\frac{V_{dc}}{2} m_q - R i_q - V_q \right) - \omega i_d \end{aligned} \tag{2.7}$$

where ω is the angular frequency in dq frame. The powers delivered into the utility grid from the distributed FC generator can be derived as follows:

$$\begin{aligned} P &= \frac{3}{2} V_d i_d \\ Q &= -\frac{3}{2} V_d i_q \end{aligned} \tag{2.8}$$

where P and Q are the active and reactive powers injected into the utility grid from the distributed FC generator, respectively. From the above equation (2.8), the active power is directly proportional to the d-axis current, and reactive power is proportional to the q-axis current. Therefore, the output currents i_d and i_q are the control objectives of the grid-connected distributed FC generator to regulate the injected power into the grid.

2.2.3 Dynamic model of two-stage distributed PV-BES generator

This section develops a characteristic model of the two-stage distributed PV-BES generator. Figure 2.5 illustrates the considered system, where the PV array and BES are connected to the DC-link through the boost and buck-boost converters, respectively. A DC-AC VSC is used for transferring the AC power from the distributed PV-BES generator into the utility grid. The proposed two-stage distributed PV-BES generator configuration combines the previously discussed standalone distributed PV-BES and grid-connected distributed FC generators. Figure 2.5 can be obtained from Figure 2.4, where FC stack is replaced by standalone distributed PV-BES generator.

The characteristic model for the two-stage distributed PV-BES generator is

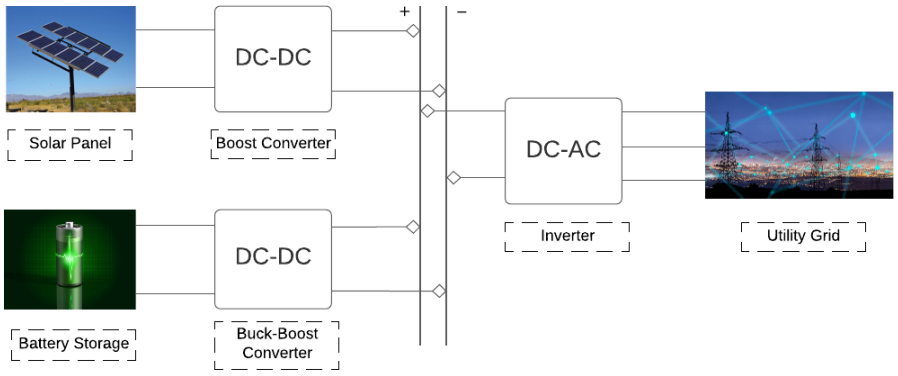

Figure 2.5: Schematic diagram of two-stage distributed PV-BES generator.

easily obtained from equations (2.3) and (2.7) as follows:

$$\begin{aligned}
\frac{di_L}{dt} &= \frac{1}{L_{dc}}\left(V_s - mV_{dc}\right) \\
\frac{dV_{dc}}{dt} &= \frac{1}{C_{dc}}\left(mi_L - i_{dc}\right) \\
\frac{di_d}{dt} &= \frac{1}{L}\left(\frac{V_{dc}}{2}m_d - Ri_d - V_d\right) + \omega i_q \\
\frac{di_q}{dt} &= \frac{1}{L}\left(\frac{V_{dc}}{2}m_q - Ri_q - V_q\right) - \omega i_d
\end{aligned} \tag{2.9}$$

The delivered active and reactive powers into the grid from the two-stage distributed PV-BES generator can be written as follows:

$$\begin{aligned}
P &= \frac{3}{2}V_d i_d \\
Q &= -\frac{3}{2}V_d i_q
\end{aligned} \tag{2.10}$$

The output DC voltage V_{dc} is the control objective of the DC-DC converters for both, which act as interfaces between the DC-link and PV-BES generator. From the above equations (2.10), the active and reactive powers are proportional to the d- and q-axis currents, respectively. Therefore, the output currents i_d and

i_q are the control variables of the DC-AC VSC to regulate the injected power into the grid.

This section introduces three different state-space characteristics models for the corresponding configurations of DGs. Thus, these dynamic models are the basis for designing a robust nonlinear single-input single-output feedback linearized controller of the standalone distributed PV-BES, grid-connected distributed FC, and two-stage distributed PV-BES generators. Section 2.5 introduces the conventional feedback linearization approach and the controller design and performance investigated in Chapter 3.

2.3 Mathematical Model of Islanded Microgrids

Renewable energy-dependent DGs are becoming a replacement for conventional power generation resources. This section addresses a structural evaluation of different electric power generation layouts from DGs in its continuity. Figure 2.6 shows a layout of the different stages to generated electric power from DGs such as solar PV panels and wind turbines. In addition, it is shown to be an associated energy storage system. Power electronic converters are vital for achieving usable electric power from DGs as DC-DC, DC-AC and AC-DC converters [76, 77].

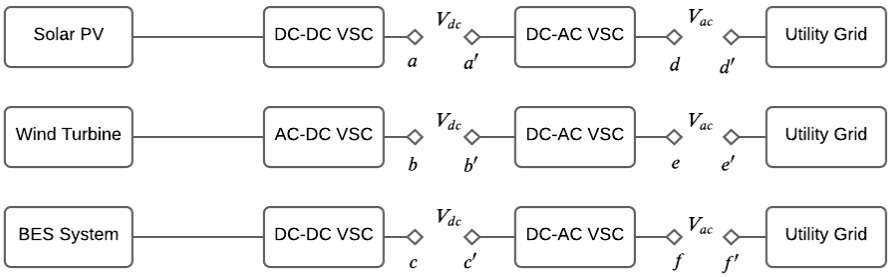

Figure 2.6: Flexible configuration of microgrid components.

Electrical energy can be categorized into two different types, DC and AC, as shown in Figure 2.6 terminal $a,\ b$ & c all provide DC electric power; on the other hand, these terminal are connected to terminal $a',\ b'$ & c', respectively. As a result, terminals $d,\ e$ & f provide AC electric power, where these terminals are individually connected to the utility grid by shorting with $d',\ e'$ & f', respectively ($d' = e' = f' = g'$). Table 2.1 shows that the electric power generated from DGs can be operated either in grid-connected or islanded modes. The interconnection concept among neighbouring DGs, which is a microgrid, is being accepted worldwide.

Table 2.1: Different configuration of distributed generators.

Generator type	**Standalone**		**Grid Connected**
Interface	*DC (1 stage)*	*AC (2 stage)*	*AC + grid*
PV	a	d (a & a' are shorted)	d & d' are shorted
Wind	b	e (b & b' are shorted)	e & e' are shorted
ESS	c	f (c & c' are shorted)	f & f' are shorted

The integration of DGs has been increasing worldwide. Owing to the integration of DGs, the operation of microgrids changes significantly compared to conventional power systems. Because power systems include both AC and DC loads and most of the renewable energy-based DG generate DC power, this DC power can be directly supplied to the DC loads without the cost of controlling the frequency and reactive power [78, 79]. At the same time, AC loads can be supplied through conversion from DC to AC power. The design and implementation of controllers play a crucial role in meeting the power requirements of hybrid DC/AC microgrids. The microgrid can be categorized into three different types based on their power or bus voltage: DC, AC and hybrid DC/AC microgrids.

Depending on whether the microgrids are connected to the utility grid, they are grouped into two separate categories: grid-connected or islanded operation

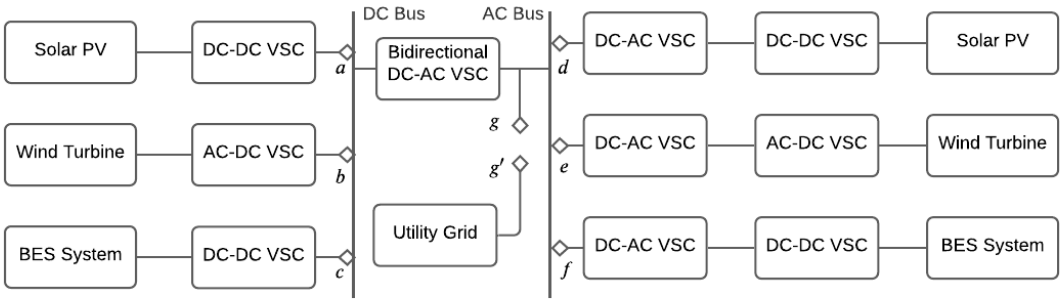

Figure 2.7: Typical layout of hybrid DC/AC microgrid connected distributed generators.

modes. The grid-connected operation mode is logical for microgrids covered by established electrical networks. However, if a microgrid is installed in a population not covered by a utility grid, it is more reasonable for them to be in an islanded operation mode. Thus, it is possible to benefit all these communities by establishing the islanded microgrid. For example, it is possible to buy and sell electricity and reduce the installation costs of energy storage systems.

Table 2.1 and Figure 2.6 shown the DC and AC terminals, where the DC terminal a, b & c are shorted to operate as a DC microgrid, and when d, e & f are shorted, then it performs as an AC microgrid. These configurations are operated in islanded mode; otherwise, to act in a grid-connected manner, the DC and AC microgrids can be connected to the utility grid via a DC-AC converter and direct, respectively. In addition, when the common buses of DC and AC microgrids are connected through one or more bidirectional DC-AC converters, the hybrid DC/AC microgrid in Figure 2.7. The conventional configuration of the hybrid DC/AC microgrid has more PEIs, which are responsible for higher harmonic currents and nonlinearities owing to their switching behaviour. A new configuration for the hybrid DC/AC microgrid, as shown in Figure 2.8 to overcome such limitations and make it as simple as possible.

Most of the generated electric power from the DGs is DC, except for the

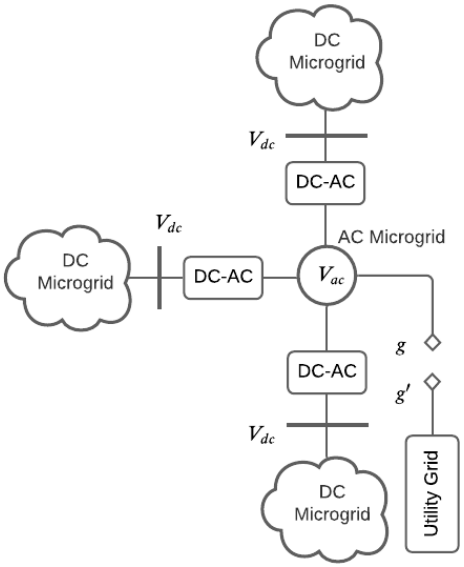

Figure 2.8: Proposed layout of islanded hybrid DC/AC microgrid.

wind turbine; however, the generated AC power from the wind turbine needs to be converted to DC power to maintain a constant frequency [80]. As a result, developing an AC microgrid from the DGs is not convenient compared to the DC microgrid. Subsequently, DC buses are connected through DC-AC VSCs. In Figure 2.8 different DC microgrids are connected to an AC bus through DC-AC converters. Therefore, the use of DC-AC converters is decreased, and correspondingly, the switching function from the whole system becomes less than the conventional configuration of the hybrid DC/AC microgrid. Three separate structures and mathematical models are presented below.

2.3.1 Dynamic model of islanded DC microgrid

A normalized structure of the islanded DC microgrid is displayed in Figure 2.9, where two different DGs are connected through DC-DC interfaces. These DGs are linked in parallel, and they have a common connecting point: DC-link/bus for DC microgrids. The DC-DC VSCs act as an interface between the DGs and

the connecting point of the DC microgrid, and they should work in coordination.

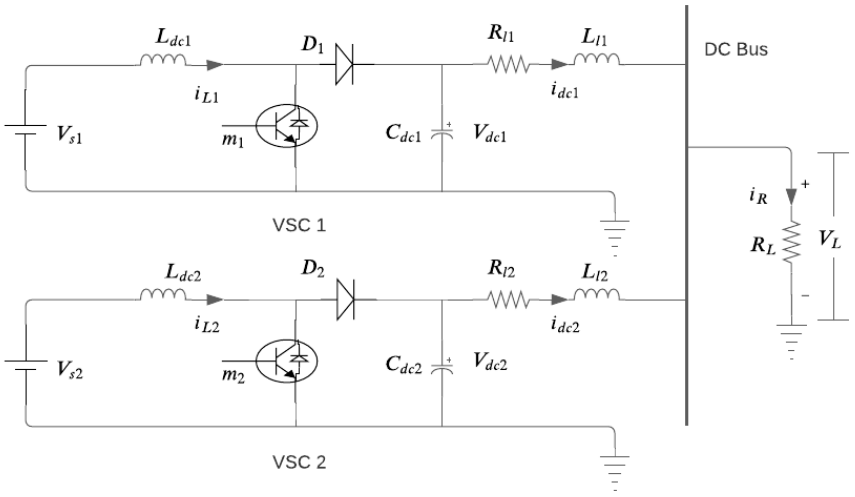

Figure 2.9: Circuit diagram of DC microgrid connected DC-DC boost converters.

Usually, the passive components of the short transmission line between the output terminal of the VSC and DC-bus are not considered. To develop a characteristic model of an islanded DC microgrid, the effect of the passive components has been considered. Figure 2.9 illustrates the schematic diagram of DGs in DC microgrid through DC-DC VSCs. The characteristic dynamic model of the DC microgrid-connected DC-DC boost VSC is developed in [81] from Figure 2.9. Transmission line losses and dynamics are also considered.

Applying Kirchhoff's current law (KCL) and Kirchhoff's voltage law (KVL), the following characteristic model of the DC-DC VSC from Figure 2.9 can be obtained as follows:

$$\begin{aligned} \frac{di_L}{dt} &= \frac{1}{L_{dc}}\left(V_s - mV_{dc}\right) \\ \frac{dV_{dc}}{dt} &= \frac{1}{C_{dc}}\left(mi_L - i_{dc}\right) \\ \frac{di_{dc}}{dt} &= \frac{1}{L_l}\left(V_{dc} - R_l i_{dc} - V_L\right) \end{aligned} \tag{2.11}$$

where i_L is the input current of the converter and V_s is the input voltage of the

converter. The passive energy storage elements of the converters are L_{dc} and C_{dc}, which are determined for the dynamic input current and output voltage V_{dc}, respectively. The transmission line resistance and inductance are R_l and L_l, respectively, where L_l adds additional dynamics of i_{dc} into the DC microgrid connected DC-DC VSCs. The bus voltage of the islanded DC microgrid is V_L.

2.3.2 Dynamic model of islanded AC microgrid

Figure 2.10 presents that a circuit diagram of an islanded AC microgrid, where two DGs are parallel connected through DC-AC VSCs. Applying KCL at the node where the DC-link is connected, obtained the dynamic equation as follows:

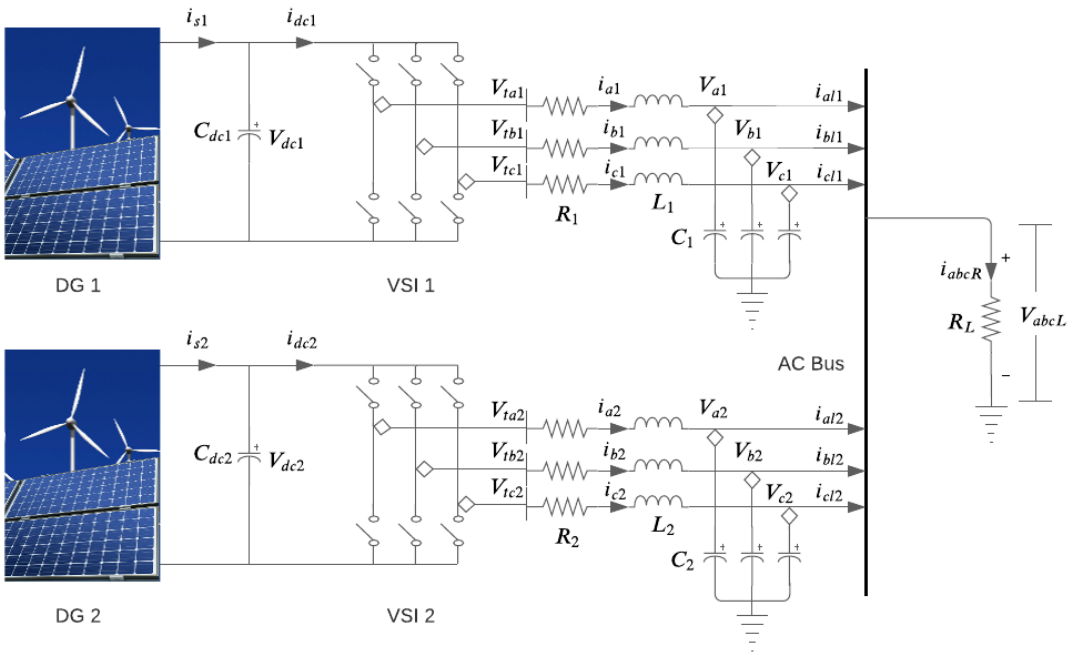

Figure 2.10: Circuit diagram of AC microgrid connected DC-AC converters.

$$\frac{dV_{dc}}{dt} = \frac{1}{C_{dc}}(i_s - i_{dc}) \tag{2.12}$$

where i_s is the source current and V_{dc} is the input voltage across the filtering DC-link capacitor C_{dc} of the DG. The input current of the VSCs is denoted as i_{dc}, which is expressed as follows:

$$i_{dc} = i_a m_a + i_b m_b + i_c m_c \tag{2.13}$$

which yields

$$\frac{dV_{dc}}{dt} = \frac{1}{C_{dc}}(i_s - i_a m_a - i_b m_b - i_c m_c). \tag{2.14}$$

Applying KVL at the branch where AC power is transmitted to a AC-bus from the DGs. The dynamics of the output currents of the DC-AC VSC are as follows:

$$\begin{aligned}
\frac{di_a}{dt} &= \frac{1}{L}\left(\frac{V_{dc}}{2}m_a - Ri_a - V_a\right) \\
\frac{di_b}{dt} &= \frac{1}{L}\left(\frac{V_{dc}}{2}m_b - Ri_b - V_b\right) \\
\frac{di_c}{dt} &= \frac{1}{L}\left(\frac{V_{dc}}{2}m_c - Ri_c - V_c\right)
\end{aligned} \tag{2.15}$$

where i_a, i_b and i_c are the three-phase output currents, and V_a, V_b and V_c are the three-phase output voltages.

Again, KCL is used at the point where the filtering capacitor C is linked and

the dynamics of the output voltage are obtained as follows:

$$\begin{aligned}\frac{dV_a}{dt} &= \frac{1}{C}\left(i_a - i_{al}\right)\\ \frac{dV_b}{dt} &= \frac{1}{C}\left(i_b - i_{bl}\right)\\ \frac{dV_c}{dt} &= \frac{1}{C}\left(i_c - i_{cl}\right)\end{aligned} \tag{2.16}$$

where i_{al}, i_{bl} and i_{cl} are the currents injected into the AC-bus in the islanded AC microgrid from the DGs corresponding to phases a, b and c.

Equations (2.14)-(2.16) represent the complete nonlinear time-variant dynamic model of the islanded AC microgrid. This dynamic model can convert into a nonlinear time-invariant model through the dq transformation. The nonlinear time-invariant characteristic model of the islanded AC microgrid can be obtained as follows:

$$\begin{aligned}\frac{dV_{dc}}{dt} &= \frac{1}{C_{dc}}\left(i_s - i_d m_d - i_q m_q\right)\\ \frac{di_d}{dt} &= \frac{1}{L}\left(\frac{V_{dc}}{2}m_d - Ri_d - V_d\right) + \omega i_q\\ \frac{di_q}{dt} &= \frac{1}{L}\left(\frac{V_{dc}}{2}m_q - Ri_q - V_q\right) - \omega i_d\\ \frac{dV_d}{dt} &= \frac{1}{C}(i_d - i_{dl}) + \omega V_q\\ \frac{dV_q}{dt} &= \frac{1}{C}\left(i_q - i_{ql}\right) - \omega V_d.\end{aligned} \tag{2.17}$$

The generated powers are supplied into the AC-bus with the following formulas:

$$\begin{aligned}P &= \frac{3}{2}(V_d i_d + V_q i_q)\\ Q &= \frac{3}{2}(V_q i_d - V_d i_q).\end{aligned} \tag{2.18}$$

From equation (2.18), the active power P and the reactive power Q are functions of the output currents and voltages i_d, i_q, V_d, and V_q.

2.3.3 Dynamic model of islanded hybrid DC/AC microgrid

This subsection illustrates the dynamic model of the proposed structure of the islanded hybrid DC/AC microgrid, which is essential for designing a primary level controller for the system. From the beginning of this section, a simple structure and a minimum number of VSCs dependent on a hybrid DC/AC microgrid are essential for regular operation without so much affords. Such a simple structure will be provided with an understanding through a mathematical model.

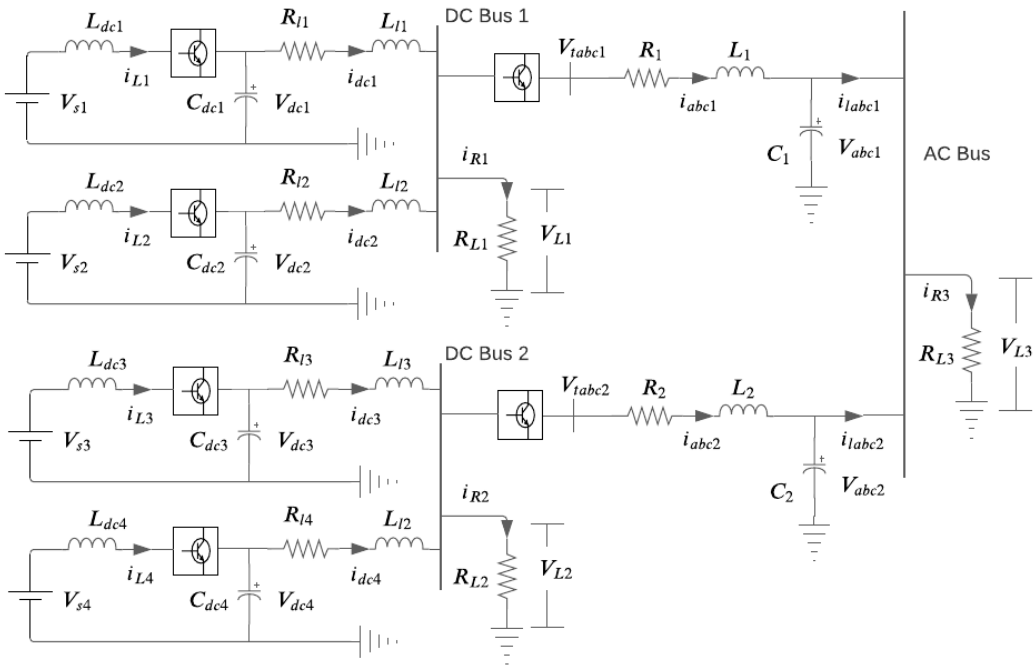

Figure 2.11: Circuit diagram of islanded hybrid DC/AC microgrid.

Figure 2.11 represents the hybrid DC/AC microgrid because of the brief discussion, where the islanded DC microgrids are parallel connected through DC-AC VSCs. The distributed energy resources are considered DC-DC boost VSC to reduce the complexity of the microgrids. Besides, it is considered to

maintain that the main characteristics of the system have no change; such type of consideration has been proposed in [70]. The proposed configuration of the hybrid DC/AC microgrid is presented in Figure 2.11, where a total of six PEIs is involved, and among them, four are DC-DC, and two are DC-AC VSCs. Moreover, Figure 2.11 has been shown the simplified circuit diagram of the hybrid DC/AC microgrid, which can be provided dynamic behaviours of the considered system.

The complete mathematical model of the hybrid DC/AC microgrid from (2.11) and (2.17) are expressed as follows:

$$\begin{aligned}
\frac{di_L}{dt} &= \frac{1}{L_{dc}}\left(V_s - mV_{dc}\right) \\
\frac{dV_{dc}}{dt} &= \frac{1}{C_{dc}}\left(mi_L - i_{dc}\right) \\
\frac{di_{dc}}{dt} &= \frac{1}{L_l}\left(V_{dc} - R_l i_{dc} - V_L\right) \\
\frac{di_d}{dt} &= \frac{1}{L}\left(\frac{V_L}{2}m_d - Ri_d - V_d\right) + \omega i_q \\
\frac{di_q}{dt} &= \frac{1}{L}\left(\frac{V_L}{2}m_q - Ri_q - V_q\right) - \omega i_d \\
\frac{dV_d}{dt} &= \frac{1}{C}\left(i_d - i_{dl}\right) + \omega V_q \\
\frac{dV_q}{dt} &= \frac{1}{C}\left(i_q - i_{ql}\right) - \omega V_d.
\end{aligned} \tag{2.19}$$

All notations of equation (2.19) are the same as the islanded DC and AC microgrids. In addition, the control objectives are six output variables, where two control objectives for DC-DC VSCs and the other four control objectives come from DC-AC VSCs.

This section introduces three different characteristics models for the corresponding configurations of islanded microgrids. Thus, these dynamic models are the basis for designing a nonlinear single-input two-output (SITO) feedback

linearized controller of the islanded DC, AC, and hybrid DC/AC microgrids. Section 2.6 describes the development of a SITO feedback linearized control scheme, and the controller design and performance for islanded microgrids are presented in Chapter 4.

2.4 Mathematical Model of Distributed PV Generators

The solar PV-based DGs have gained universal acceptance among various types of RESs. Owing to such a type of acceptance of distributed PV generators, differences in how they are used also visible, alleviating the structural differences. Electricity generation from solar energy sources has become a boon for a population that cannot be supplied with electricity by the established electrical network [82, 83]. However, because such systems are weather dependent, they sometimes run the risk of delivering a fixed DC voltage. Moreover, using a DC-DC VSC can minimize such risks, and DC power can be utilized.

Nowadays, generating electricity from solar energy is not limited to a small size, and now such systems have become significant in size. Such generation systems are now in big part as industry and commercial businesses, where three-phase AC electrical current and voltage are well established. As a result, this section establishes a characteristic model of the three different structures of electric power generation from the distributed PV generators.

2.4.1 Dynamic model of standalone distributed PV generator

Figure 2.12 is represented a circuit diagram of a standalone DC type distributed PV generator. The output DC voltage from a distributed PV generator is not constant, but a constant voltage is required to feeding loads. Consequently, the DC-DC VSC is essential between standalone distributed PV generator and DC loads. The characteristics model of such type of system can be obtained as follows:

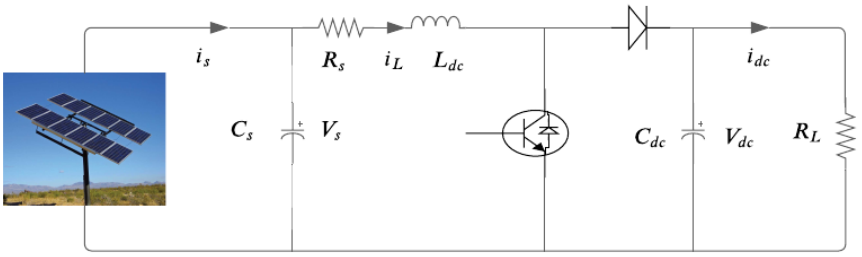

Figure 2.12: Circuit diagram of standalone distributed PV generator.

$$\begin{aligned} \frac{dV_s}{dt} &= \frac{1}{C_s}\left(i_s - i_L\right) \\ \frac{di_L}{dt} &= \frac{1}{L_{dc}}\left(V_s - R_s i_L - mV_{dc}\right) \\ \frac{dV_{dc}}{dt} &= \frac{1}{C_{dc}}\left(mi_L - \frac{V_{dc}}{R_L}\right) \end{aligned} \tag{2.20}$$

where V_s, i_L and V_{dc} are the elements of state vector of the dynamic system corresponding to the energy storage passive elements C_s, L_{dc} and C_{dc}, respectively. The output current is i_s of the solar PV panel, the input current of the VSC is i_L, the internal resistance is R_s, and the resistive load is R_L. The switching is m of the VSC.

2.4.2 Dynamic model of grid-connected distributed PV generator

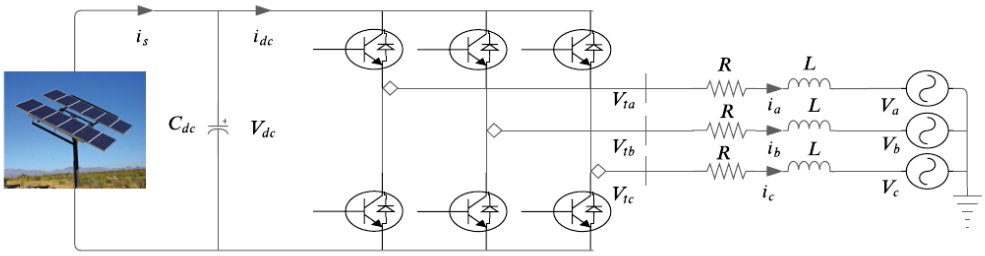

Figure 2.13: Circuit diagram of grid-connected distributed PV generator.

Figure 2.13 shows a circuit diagram, which can be considered as a grid-connected AC type distributed PV generator. To inject AC output power into the grid, a DC-AC VSC has been applied as an interface between distributed PV generator and grid or AC load. The dynamic model of such type of system can be obtained as follows:

$$\begin{aligned}
\frac{dV_{dc}}{dt} &= \frac{1}{C_{dc}}\left(i_s - i_d m_d - i_q m_q\right) \\
\frac{di_d}{dt} &= \frac{1}{L}\left(\frac{V_{dc}}{2}m_d - Ri_d - V_d\right) + \omega i_q \\
\frac{di_q}{dt} &= \frac{1}{L}\left(\frac{V_{dc}}{2}m_q - Ri_q - V_q\right) - \omega i_d
\end{aligned} \tag{2.21}$$

where V_{dq} and i_{dq} are the output voltage and current in the dq frame, respectively. Additionally, m_{dq} and ω represent the DC-AC VSC switching signals and the angular speed at the dq frame transformation, respectively.

2.4.3 Dynamic model of two-stage distributed PV generator

The standalone and grid-connected distributed PV generators individually have some limitations that a hybrid grid-connected (two-stage) distributed PV generator can overcome. A circuit diagram of the two-stage distributed PV generator is presented in Figure 2.14, which is a combination of the standalone and grid-connected distributed PV generators. The characteristic model of this configuration can be obtained as follows:

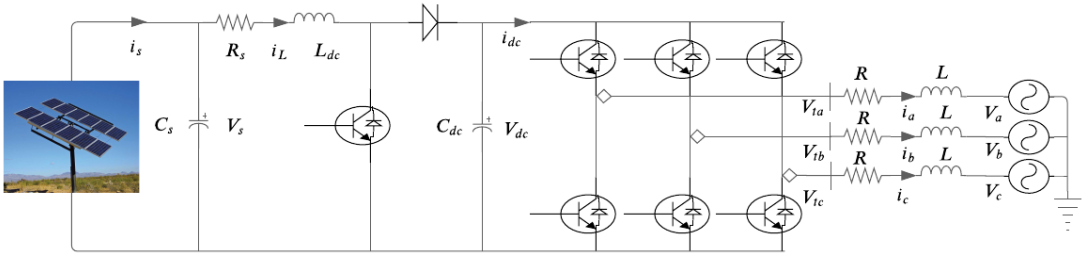

Figure 2.14: Circuit diagram of two-stage PV generator.

$$
\begin{aligned}
\frac{dV_s}{dt} &= \frac{1}{C_s}\left(i_s - i_L\right) \\
\frac{di_L}{dt} &= \frac{1}{L_{dc}}\left(V_s - mV_{dc}\right) \\
\frac{dV_{dc}}{dt} &= \frac{1}{C_{dc}}\left(mi_L - i_d m_d - i_q m_q\right) \\
\frac{di_d}{dt} &= \frac{1}{L}\left(\frac{V_{dc}}{2}m_d - Ri_d - V_d\right) + \omega i_q \\
\frac{di_q}{dt} &= \frac{1}{L}\left(\frac{V_{dc}}{2}m_q - Ri_q - V_q\right) - \omega i_d.
\end{aligned}
\tag{2.22}
$$

All notations of equation (2.22) are the same as those of the standalone and grid-connected distributed PV generators. The output voltage of the DC-DC VSC and the input voltage for the DC-AC VSC are the same as V_{dc}.

This section has developed three different state-space characteristics models for the corresponding configurations of distributed PV generators. The determined state-space characteristic models cannot capture the switching effect on the system. Thus, these dynamic models are the basis for developing such a characteristic model, providing an idea of switching frequency on PEIs. Section 2.7 introduces a switching-frequency-dependent modeling approach, and a detailed analysis is presented in Chapter 5.

2.5 Feedback Linearization of SISO Control Problem

Usually, linear controllers have been extensively used in various purposes, as well as power systems. Linear controller design approaches are commonly used for the linear system, which is found from a naturally nonlinear plant around a specification operating point. Therefore, such controller is often on the operating points of the system, and the performance may reduce drastically when the operation situation shifts and may be unstable the actual system. Feedback linearization is an efficient technique established in control theory among different nonlinear controller design approaches to linearize the nonlinear system.

This section presents a feedback linearized control technique for a single-input single-output (SISO) control problem [84]. The dynamic model of the nonlinear system is written as follows:

$$\begin{aligned} \dot{x} &= f(x) + g(x)u \\ y &= h(x) \end{aligned} \tag{2.23}$$

where x is the state vector $(n \times 1)$, $\dot{x}$ is the time derivative of the state vector $(n \times 1)$, u is the input vector $(p \times 1)$, $f(x)$ is the vector field $(n \times 1)$, $g(x)$ is the vector field $(n \times p)$, and $y = h(x)$ is the output vector $(q \times 1)$ and $p = q$. p can be equal to or greater than 1 $(q \geq 1)$, if either $q = 1$ or $(q > 1)$, the system is a single-input single-output or multi-input multi-output (MIMO) system, respectively.

A coordinate transformation for the system that can be expressed as follows:

$$z = \phi(x) \tag{2.24}$$

where x and z are the equal dimensional vectors and ϕ is the nonlinear function of the state vector x. There is an inverse transformation for the state vector x, that is,

$$x = \phi^{-1}(z). \tag{2.25}$$

Each component of the nonlinear function ϕ and ϕ^{-1} can be differentiated up to any n^{th}-order. In this step, the original x states are converted into z states by a nonlinear coordinate transformation by choosing.

$$z = h(x) = L_f^{1-1} h(x). \tag{2.26}$$

The dynamics of transform state is expressed as follows:

$$\dot{z} = \frac{\partial h(x)}{\partial (x)} \dot{x}. \tag{2.27}$$

Substituting equation (2.23) into (2.27) become as follows:

$$\dot{z} = \frac{\partial h(x)}{\partial(x)} f(x) + \frac{\partial h(x)}{\partial(x)} g(x)u. \tag{2.28}$$

The linearized r^{th} order dynamic state can be obtained as follows:

$$\dot{z}_r = L_f^r h(x) + L_g L_f^{r-1} h(x)u \tag{2.29}$$

where $L_f^r h(x)$ and $L_g L_f^{r-1} h(x)$ are the Lie derivatives corresponding to the vector fields $f(x)$ and $g(x)$, respectively. The partial derivation of the new scalar function $L_f^{r-1} h(x)$ is not equal to zero, corresponding to the vector field $f(x)$ and $g(x)$,

$$\begin{aligned} L_g L_f^{\eta} h(x) &= 0 \qquad \eta \leq r-2 \\ L_g L_f^{r-1} h(x) &= \frac{\partial L_f^{r-1} h(x)}{\partial x} g(x) \neq 0 \end{aligned} \tag{2.30}$$

where r is the relative degree of the feedback linearized system and $r \leq n$.

$$\text{Linearization is} \begin{cases} \text{exact}, & \text{if } r = n \\ \text{partial}, & \text{if } r < n. \end{cases}$$

The r^{th}-order differentiation of the coordinate transform state z is obtained as follows:

$$v = L_f^r h(x) + L_g L_f^{r-1} h(x)u. \tag{2.31}$$

Finally, feedback linearized control law is expressed as follows:

$$u = \frac{v - L_f^r h(x)}{L_g L_f^{r-1} h(x)} \tag{2.32}$$

where v is the linear control synthesis, which is generated by the linear control technique.

If the system is partially linearized, the coordinate transformation can be written as follows:

$$z = \begin{bmatrix} \beta \\ \gamma \end{bmatrix} \tag{2.33}$$

where $\beta = \begin{bmatrix} z_1 & z_2 & \dots & z_r \end{bmatrix}^T$ characterises the states, which can be transformed from the x state to the z state and γ is the rest $\rho = 1,\ ...,\ n - r$ states that cannot be transformed in a straightforward manner.

$$\gamma = z_{r+\rho} = \phi_{r+\rho}. \tag{2.34}$$

The partial feedback linearization scheme can stabilize the system if the following condition satisfies:

$$L_g \phi_{r+\rho} = 0. \tag{2.35}$$

These ρ states are crucial for analysing the characteristics of the inner dynamics of a nonlinear system that should be well behaved for the operation of a partial feedback linearized control scheme, and their dynamic equations are written as follows:

$$\dot{z}_{r+\rho} = L_f \phi_{r+\rho}(x) + L_g \phi_{r+\rho}(x) u = L_f \phi_{r+\rho}(x). \tag{2.36}$$

This section introduces feedback linearized control scheme for the SISO con-

trol problem. The introduced control technique is used in Chapter 3 to design a robust nonlinear controller for DGs previously discussed as standalone distributed PV-BES, grid-connected distributed FC and two-stage distributed PV-BES generators.

2.6 Feedback Linearization of SITO Control Problem

This section develops two definitions of a feedback linearized control technique for a single-input two-output (SITO) control problem. The dynamic model of a nonlinear system is expressed as follows:

$$\begin{aligned} \dot{x} &= f(x) + g(x)u \\ y &= h(x) \end{aligned} \tag{2.37}$$

where x is the vector of state variables $(n \times 1)$, $\dot{x}$ is the time derivative of the state vector $(n \times 1)$, u is the input or control vector $(p \times 1)$, $f(x)$ is the vector field $(n \times 1)$, $g(x)$ is the vector field $(n \times p)$, and $y = h(x)$ is the output vector $(q \times 1)$ and $q = 2p$. p is equal to or greater than 1 $(p \geq 1)$, if either $p = 1$ or $(p > 1)$, the system is a SISO or MIMO system, respectively.

A second-order nonlinear dynamic model can be considered as a single-input system, as follows:

$$\begin{aligned} \dot{x_1} &= a_1 x_1 m + a_2 x_2 \\ \dot{x_2} &= a_3 x_1 + a_4 x_2 \end{aligned} \tag{2.38}$$

$$f(x) = \begin{bmatrix} a_2 x_2 \\ a_3 x_1 + a_4 x_2 \end{bmatrix} \qquad g(x) = \begin{bmatrix} a_1 x_1 \\ 0 \end{bmatrix} \quad \& \quad u = m$$

where $x = [x_1\ x_2\ ]^T$ is a vector, and $f(x)$ and $g(x)$ 2-dimensional vector fields of x. The control objective and input of the nonlinear system are y and u, respectively.

If the control objective $y = x_1$, then it is a SISO control problem; therefore, the Lie derivative is as follows:

$$\begin{aligned} L_f y &= a_2 x_2 \\ L_g L_f^{1-1} y &= a_1 x_1 \end{aligned} \tag{2.39}$$

The relative degree is $r < 2$, corresponding to $y = x_1$; as a result, the considered system is partially linearized. The control law is obtained as follows:

$$m = \frac{v - a_2 x_2}{a_1 x_1} \tag{2.40}$$

In addition, if the control objective $y = x_2$, then it is also a SISO control problem; therefore, the Lie derivative is as follows:

$$\begin{aligned} L_f y &= a_3 x_1 + a_4 x_2 \\ L_g L_f^{1-1} y &= 0 \\ L_f^2 y &= a_3 f_1 + a_4 f_2 \\ L_g L_f^{2-1} y &= a_1 a_3 x_1 \end{aligned} \tag{2.41}$$

The relative degree is $r = 2$, corresponding to $y = x_2$; and as a result, the

system is exactly linearized. The control law is determined as follows:

$$m = \frac{v - (a_3 f_1 + a_4 f_2)}{a_1 a_3 x_1} \tag{2.42}$$

Relative degree for SITO control problem

When the control objective $y = [x_1 \ x_2]^T$ of this system, it is a SITO control problem, with relative degrees of 1 and 2 corresponding to x_1 and x_2, respectively. The relative degree of the SITO control problem is as follows:

$$r = \begin{cases} r_1 + r_2 & r > 2 \\ max(r_1, r_2) & r = 2 \end{cases} \tag{2.43}$$

where the relative degree r is the order of the feedback linearized system, which is bounded by order of the nonlinear dynamic model as follows:

$$r \leq n \tag{2.44}$$

where $n = 2$ and the relative degree should not be greater than the order of the original nonlinear dynamic model; thus, equation (2.43) leads to the following definition:

$$r = max(r_1, r_2) \tag{2.45}$$

Control law for SITO control problem

From equations (2.40) and (2.42), we use a common control as follows:

$$\begin{gathered} m = \frac{v - a_2 x_2}{a_1 x_1} = \frac{v - (a_3 f_1 + a_4 f_2)}{a_1 a_3 x_1} \\ m = m_1 = m_2 \end{gathered} \tag{2.46}$$

where $v = v_1$ and $v = v_2$, corresponding to the control objectives x_1 and x_2, respectively. The control law for the SITO control problem is written as follows from equation (2.46):

$$m = \frac{1}{2} m_1 + \frac{1}{2} m_2 \tag{2.47}$$

To achieve the priority of the final control law corresponding to the output objectives $y = [x_1 \ x_2]$ is as follows:

$$m = \frac{1}{2} \alpha_1 m_1 + \frac{1}{2} \alpha_2 m_2 \tag{2.48}$$

where $\alpha_1 + \alpha_2 = 2$ is the priority function, 2 is the number of output objectives and $\alpha_1 = 0.0,\ 0.1,\ \ldots,\ 1.0,\ 1.1,\ \ldots,\ 1.9,\ 2$.

The control law for SITO control problem is as follows:

$$m = \alpha_1 \frac{v_1 - a_2 x_2}{2 a_1 x_1} + \alpha_2 \frac{v_2 - (a_3 f_1 + a_4 f_2)}{2 a_1 a_3 x_1} \tag{2.49}$$

System (2.38) represents a dynamic model, which is a nonlinear system regarding the first equation of (2.38). The control law (2.49) can be applied if the linear dynamic equation of the nonlinear equation (2.38).

Substituting equation (2.49) into (2.38) can be simplified as follows:

$$\dot{x_1} = \frac{1}{2}v_1 + \frac{1}{2a_3}v_2 - \frac{1}{2}f_1 - \frac{a_4}{2a_3}f_2 \tag{2.50}$$

where $\alpha_1 = 1$, and a and f are the coefficients and linear functions of the state variables, respectively. Equation (2.50) is a linear dynamic equation. As a result, the proposed nonlinear SITO control problem can be linearized using a feedback linearized approach. This section develops feedback linearized control scheme for the SITO control problem based on the conventional feedback linearized approach. The developed control technique is used in Chapter 4 to design a nonlinear controller for islanded DC, AC and hybrid DC/AC microgrids.

2.7 Overview on Dynamic Phasor Modeling Technique

This section briefly introduces the multi-frequency averaging (MFA) based dynamic phasor modeling approach. The fundamental concept of the dynamic phasor approach is that the differential equations are written for the rate of change of the Fourier coefficients of almost, but not precisely, periodic sinusoidal waveforms [85]. These equations are linear but of higher dimension, compared to the differential equations for voltages and currents with a nonlinear switching element. Some essential definitions of the terms applied in the dynamic phasor

analysis for an almost periodic waveform $x(\tau)$ are given as follows:

$$\begin{aligned} x(\tau) &= \sum_{k=-\infty}^{+\infty} \overline{x}_k(t) e^{jk\omega\tau} \\ \overline{x}_k(t) &= \frac{1}{T}\int_{t-T}^{t} x(\tau) e^{-jk\omega\tau} d\tau \end{aligned} \tag{2.51}$$

where $\omega = 2\pi/T$ and $\overline{x}_k(t)$ are the complex Fourier coefficients, which are defined as phasors. From this definition, the critical equation for the k^{th} Fourier coefficient is given as:

$$\frac{d}{dt}\overline{x}_k(t) = \overline{\frac{dx_k}{dt}}(t) - jk\omega\overline{x}_k(t) \tag{2.52}$$

If the change in the k^{th} Fourier coefficient is neglected, then the previous equations of the known as phasor relationship, in practice, imaginary and real parts of dynamic phasor equations are divided, and a system of differential equations is formed.

Another key property of the dynamic phasor is the calculation of the product of two signals or variables. The index k average of the product of variables $x(t)$ and $y(t)$ can be computed as follows:

$$\overline{xy}_k = \sum_{m=-\infty}^{\infty} \overline{x}_{k-m}\overline{y}_m \tag{2.53}$$

where m is the sum of all integers. To avoid complexity, if the state variables $x(t)$ and $y(t)$, and their index-0 and index-1 carry almost all properties of a state, then the other higher index can be negligible. We obtain the following expressions of

(2.53) as follows:

$$\begin{aligned} \overline{xy}_0 &= \overline{x}_0\overline{y}_0 + \overline{x}_1\overline{y}_{-1} + \overline{x}_{-1}\overline{y}_1 \\ \overline{xy}_{-1} &= \overline{x}_{-1}\overline{y}_0 + \overline{x}_0\overline{y}_{-1} \\ \overline{xy}_1 &= \overline{x}_1\overline{y}_0 + \overline{x}_0\overline{y}_1 \end{aligned} \tag{2.54}$$

Furthermore, except index-0, all other higher indexes have two parts, positive and negative, where both are complex conjugates of each other, which are written as:

$$\begin{aligned} \overline{x}_1 &= \overline{x}^*_{-1} \\ \overline{x}_1 &= \overline{x}^R_1 + j\ \overline{x}^I_1 \\ \overline{x}_{-1} &= \overline{x}^R_1 - j\ \overline{x}^I_1 \end{aligned} \tag{2.55}$$

where the real and imaginary parts of the complex conjugates are defined as R and I, respectively. This mathematical representation is as follows:

$$\begin{aligned} \overline{xy}_0 &= \overline{x}_0\overline{y}_0 + 2(\overline{x}^R_1\overline{y}^R_1 + \overline{x}^I_1\overline{y}^I_1) \\ \overline{xy}^R_1 &= \overline{x}_0\overline{y}^R_1 + \overline{x}^R_1\overline{y}_0 \\ \overline{xy}^I_1 &= \overline{x}_0\overline{y}^I_1 + \overline{x}^I_1\overline{y}_0 \end{aligned} \tag{2.56}$$

The multi-frequency averaging based dynamic phasor approach has a great opportunity owing to the increasing application of PEIs in modern power systems, and it has some advantages over traditional modeling approaches.

- The dynamic phasor can provide a larger bandwidth than conventional quasi-stationary assumptions by selecting index k for the transient stability program.

- The variations of index X_k are smoother than instantaneous quantities x. This property of the dynamic phasor approach can compute the electromagnetic transients; in this regard, the simulation is faster than an electro-

magnetic transient program such as simulation and addresses problems at a different frequency.

- The dynamic phasor X_k becomes constant at the steady-state.

One drawback of the MFA-based dynamic phasor approach is that the system order is higher than the conventional state-space method. However, this is not a big issue because of the powerful software-based tools, which can reduce the order of the system without losing system properties such as MATLAB or National Instruments (NI).

This section introduces a switching-frequency-dependent dynamic phasor modeling approach for PEIs. The introduced modeling approach is applied in Chapter 5 to the switching frequency sensitivity analysis of VSCs in a different configuration of the distributed PV generators.

2.8 Chapter Summary

This chapter describes dynamic models of distributed generators and islanded microgrids with different configurations and considers reliable models for implementing industry-standard simulation tools. Nonlinear models of power systems are presented in this chapter, as the primary purpose of this dissertation is to design and implement robust nonlinear controllers for distributed generators. The nonlinear feedback linearized controller was designed for the single-input two-output control problem of islanded microgrids and developed a dynamic phasor model for distributed PV generators.

Chapter 3

Robust Controller Design for Distributed Generators

The work presented in this chapter has been published in the following articles:

- **Mahmud, M. R.**, and Pota, H.. " Robust partial feedback linearized controller design for standalone hybrid pv-bes system," *Electronics* , 2021 (https://doi.org/10.3390/electronics10070772).
- **Mahmud, M. R.**, and Pota, H.. " Robust nonlinear controller design for dc-ac converter in grid-connected fuel cell system," *IEEE Journal of Emerging and Selected Topics in Industrial Electronics*, 2021 (DOI: 10.1109/JESTIE.2021.3088394).
- **Mahmud, M. R.**, Hossain, M. A., and Pota, H.. " Robust nonlinear controller design for islanded photovoltaic system with battery energy storage," in *Proceedings of IEEE International Conference on Power Electronics, Smart Grid and Renewable Energy (PESGRE)*, Kerala, India, 2020.

- **Mahmud, M. R.**, and Pota, H.. " Robustness analysis of h_∞ controller for feedback linearized model of grid connected inverter," in *Proceedings of IEEE International Conference on Power Electronics, Drives and Energy Systems (PEDES)*, Chennai, India, 2018.

Abstract

This chapter presents a mixed-sensitivity based robust H_∞ *loop-shaping feedback linearized control technique to improve the transient stability of distributed generators. The proposed control approach is applied to standalone distributed photovoltaics with battery energy storage, grid-connected distributed fuel cells and two-stage distributed photovoltaics with battery energy storage systems. The design controllers for different distributed generators have provided independent operating points. Parametric uncertainty models are developed for the dynamic model, and the noise-separating merit of the proposed control approach is demonstrated. The performance of the designed controller is investigated under various scenarios and assessed with the conventional proportional-integral controller for feedback linearized control scheme.*

3.1 Introduction

The generation sector of the traditional power system undergoes a significant change, where DGs are receiving more attention than traditional fossil fuel-based generators [86]. For the last few decades, the power generation sector has been faced different types of experience, such as oil and coal crises, environmental worming, and financial barriers [87]. Owing to such difficulties, battery integrated standalone distributed PV generators are gaining worldwide acceptance as an

alternative to fossil fuels. The DGs can operate in either grid-connected or standalone modes [88], where the control objective selection is an essential task for obtaining better performance from generation systems [89].

The output voltage across the DC-link capacitor is the primary control variable of the standalone distributed PV with battery energy storage (PV-BES) generator to achieve stable operation [90]. In addition, the active and reactive powers are the main control issues for grid-connected distributed FC generators, where the output currents of the DC-AC VSC in the dq frame are proportional to the injected power into the utility grid. Therefore, the AC output currents are considered as the control objectives of grid-connected DGs [91]. The output voltage and currents are becoming control objectives for DC-DC and DC-AC VSCs, respectively. In a two-stage distributed PV-BES, the standalone distributed PV-BES generator replaces the FC stack corresponding to the grid-connected distributed FC generator, where the output voltage and currents become control objectives. The design and implementation of controllers play a crucial role in achieving a balanced output voltage and power in the DGs [92].

The dynamics of VSCs are becoming more attractive to researchers, where converters have been brought many issues to the integration of DGs into the DC-bus or utility grid [93]. The switching function, time-varying DC voltage and current provide nonlinear dynamic behaviours of the VSCs, where stability is more sensitive than the linear system. The literature applies a linear controller to inject smooth power into the DC-bus or utility grid from the DGs. In [94], a digital proportional-integral (PI) controller has been proposed for the multilevel VSC of a grid-connected distributed PV generator to follow the AC signals, where the PI controller cannot keep to the reference AC signal except steady-state error. The hysteresis controller can overcome the steady-state error-associated

restriction of the PI controller and add to the low harmonic distortion, and unity power factor, which is proposed in [95], it may not be suitable for handling a varying switching frequency. The switching-frequency-associated issue can succeed in dealing with the design of a predictive controller [96, 97, 98], but the performance of this controller is degraded under the non-ideal model of the system. The major drawback of such controllers depends on a fixed set of operating points.

Nonlinear controller design techniques can overcome the operating point related limitations of linear control design approaches. A nonlinear sliding mode controller has been proposed in [99, 100, 101] for the DGs to an independent operating point, which provides robustness under parameter uncertainties. Still, the time-varying sliding surface selection of the sliding mode controller design is difficult because of the first changes in the atmospheric conditions in the RES-associated VSCs. A passive-based-control approach is proposed in [102] to control the DGs without considering the impact of the parametric uncertainty, which is one of the considerable weaknesses of designing a controller. A nonlinear backstepping approach is proposed in [103] to design an inner current control loop for a grid-connected DG, where the VSC control is the main issue. Such a type of approach works well when the nonlinear model is specific; however, it is unable to deal with parametric variations in the dynamic system. An adaptive backstepping approach has been offered in [104] to boost the accomplishment of a nonlinear backstepping controller in contrast to parametric variations. The key challenge with the adaptive backstepping controller is the selection of adaptation gains. The result of the controller reduces if these gains are not appropriately chosen. Feedback linearization (FBL) is another nonlinear control design approach that can transform into an exact or partial FBL model from a nonlinear system. In

power system control applications, the FBL control scheme has been widely accepted, such as excitation control of synchronous generators and switching input control of PEIs [105, 106]. In addition, the FBL control approach is highly sensitive to parameter variations [107], and parameter uncertainty is not considered in [108]. Moreover, the FBL control scheme does not take into account any parameter uncertainty in the system, where parameter dependency is the main drawback of this control technique.

Uncertainties related issues can be minimized by designing a robust controller, which is one of the significant innovations in the area of control systems and applications during the last few decades. The parametric uncertainties relevant problem has been addressed in [109], and further development of this theory can be seen in [110, 111]. A linear-quartic Gaussian control technique followed by loop transfer recovery has been proposed in [112] to guarantee robustness. The loop transfer recovery cannot deal with the plant input and output at the same time regarding performance and robust stability properties. In [113], a robust H_∞ control approach with variations in operating conditions, which are modeled as analytical uncertainties of the nominal plant. Further development is performed using this approach in [114, 115, 116], based on H_∞ optimization to improve the performance and robustness of the system. The H_∞ loop-shaping controller proposed in [117, 118] that can provide better performance and robustness over the H_∞ optimization-based controller. In [119, 120], a H_∞ loop-shaping controller has been proposed for the FBL model of the synchronous generator to enhance the transient stability and steady-state performance under parameter uncertainties, measurement noises and external disturbances.

The parameter uncertainties of DGs can be solved using a robust H_∞ loop-shaping control approach for the linearized part of the FBL control law, as

Table 3.1: Summary of controller design methods for distributed generators.

Control method	Strengths	Weaknesses
Linear	- Smooth power delivery [94] - Low harmonic distortion and unity power factor [95] - Minimum effect of switching frequency for ideal mode [96, 97, 98]	- Steady-state error - Time-varying switching frequency - Fixed set of operating points
Nonlinear	- Independent operating point [99, 100, 101], [102] and [103] - First transient [105, 106]	- Time-varying sliding surface selection - Parametric uncertainty - Adaptation gains selection
Robust	- Handle the parameter uncertainty [112] - Better performance and robustness [117,118]	- Cannot deal with the plant input and output at the same time - Steady-state error and slow response
Proposed	- Independent operating points - First transient with better performance and robustness and	- Parameter sensitivity

presented in [119, 120]. Whether the proposed controller design approach does not consider uncertainties against parameter variations and measurement noise, this chapter presents a robust FBL control scheme for the DGs. The performance of the proposed controller is explored under various possible worst scenarios.

The contributions of this chapter are as follows:

- Develop feedback linearization model of the standalone distributed photovoltaic generator including battery energy storage and designed robust controller for linearized model (Sections 3.2 and 3.3).

- Develop feedback linearization model of the grid-connected distributed fuel cell generator and designed robust controller for linearized model (Sections 3.4 and 3.5).

- Develop feedback linearization model of the two-stage distributed photovoltaic generator including battery energy storage and designed robust controller for linearized model (Sections 3.6 and 3.7).

- Performances are investigated of the designed robust nonlinear feedback linearized controllers corresponding to the three different distributed generators (Section 3.8).

3.2 Feedback Linearization of Standalone Distributed PV-BES Generator

Several control approaches have been applied in the literature to regulate the DC output voltage of DC-DC VSCs in DGs. Of these strategies, FBL along with linear control has newly been offered, which is highly encouraging. The generalized dynamic model of the DC-DC VSC in Figure 3.1 for the standalone distributed PV-BES generator discussed in Subsection 2.2.1 and is recalled below.

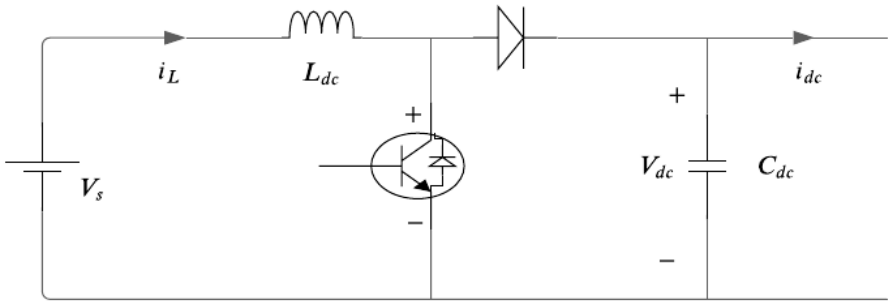

Figure 3.1: Circuit diagram of DC-link capacitor connected generalized distributed generator.

$$\begin{aligned} \frac{di_L}{dt} &= \frac{1}{L_{dc}}\left(V_s - mV_{dc}\right) \\ \frac{dV_{dc}}{dt} &= \frac{1}{C_{dc}}\left(mi_L - i_{dc}\right). \end{aligned} \tag{3.1}$$

The SISO characteristics model (3.1) can be expressed in the nonlinear form as follows:

$$\begin{aligned} \frac{dx}{dt} &= f(x) + g(x)u \\ y &= h(x) \end{aligned} \tag{3.2}$$

where $x = \begin{bmatrix} i_L \\ V_{dc} \end{bmatrix}$, $f(x) = \begin{bmatrix} \frac{V_s}{L_{dc}} \\ -\frac{i_{dc}}{C_{dc}} \end{bmatrix}$, and $g(x) = \begin{bmatrix} -\frac{V_{dc}}{L_{dc}} \\ \frac{i_L}{C_{dc}} \end{bmatrix}$, $u = m$ and $y = h(x) = V_{dc}$.

In equation (3.2), the state vector is x, the control input is u, the output function is y, and $n = 2$ is the generalized system order.

3.2.1 Determine relative degree

The Lie derivative of the vector field $f(x)$ regarding to the output function $h = V_{dc}$ is written as follows:

$$L_f h(x) = L_f V_{dc} = -\frac{i_{dc}}{C_{dc}}. \tag{3.3}$$

Besides, the Lie derivative of the vector field $g(x)$ respect to the output function $h = V_{dc}$ is determined as follows:

$$L_g L_f^{1-1} h(x) = L_g L_f^{1-1} V_{dc} = \frac{i_L}{C_{dc}}. \tag{3.4}$$

Because $L_g L_f^{1-1} V_{dc} \neq 0$, as indicated above, the relative degree $r = 1$ for the control objective V_{dc}. As a result, the relative degree is less than the original order

of the system, and system (3.1) is partially linearized with the control objective.

3.2.2 Nonlinear coordinate transformation

A new state can be achieved from the coordinate transformation, which is expressed as follows:

$$z_1 = L_f^{1-1} h = V_{dc}. \tag{3.5}$$

The dynamics of the anew achieved state from (3.5) become as follows:

$$\frac{dz_1}{dt} = v \tag{3.6}$$

where v is the linear control synthesis that can be obtained using a linear controller, designed in the next section.

3.2.3 Zero internal dynamic stability

From equation (3.1), one of the states of the dynamic model of the DC-DC VSC is not exactly linearized using the FBL approach. It is essential to ensure the stability of the left state that does not influence the system stability. At this point, requires to be chosen in a specified manner that fulfils:

$$\lim_{t \to \infty} h(x) \longrightarrow 0 \tag{3.7}$$

it is means that $h(x) = 0$ at steady state. For which,

$$\frac{dz_1}{dt} = 0 \tag{3.8}$$

Furthermore, z_2 is a nonlinear function that can represent the remaining state and must satisfy the following condition:

$$L_g z_2 = 0. \tag{3.9}$$

Condition (3.9) can be satisfied if,

$$z_2 = \frac{1}{2} L_{dc} i_L^2 + \frac{1}{2} C_{dc} V_{dc}^2. \tag{3.10}$$

The dynamics of equation (3.10) become as follows:

$$L_f z_2 = V_s i_L - V_{dc} i_{dc} = P_i - P_o \tag{3.11}$$

where the input power of the DC-DC VSC is $P_i = V_s i_L$ and the output power is $P_o = V_{dc} i_{dc}$. Owing to the ideal or lossless condition, $P_i = P_o$ for which equation (3.11) can be written as follows:

$$L_f z_2 = 0 \tag{3.12}$$

The inner dynamics did not affect the stability matter of the DC-DC VSC generalized model of the standalone distributed PV-BES generator. Therefore, a partial FBL control law can be developed as described in the following subsection.

3.2.4 Feedback linearized control law

The FBL control law can be obtained as follows:

$$u = \frac{v - L_f^r h(x)}{L_g L_f^{r-1} h(x)}. \tag{3.13}$$

The feedback linearized control law for the standalone distributed PV-BES generator is as follows:

$$m = \frac{C_{dc}v + i_{dc}}{i_L}. \tag{3.14}$$

In equation (3.14), each component is measurable or expressed considering the measured elements except the linear control synthesis v. A linear control approach is used to generate control input v.

3.2.5 Transfer function of linearized system

The Laplace transform of (3.6) is determined as follows:

$$V_{dc}(s) = \frac{1}{s}V(s). \tag{3.15}$$

After further simplification (3.15) can be written as follows:

$$\frac{V_{dc}(s)}{V(s)} = \frac{1}{s}. \tag{3.16}$$

The output voltage $V_{dc}(s)$ of the standalone distributed PV-BES generator is need to track the desired voltage $V_r(s)$, so the linear control input $V(s)$ can be obtained as follows:

$$V\,(s) = K(s)E(s) \tag{3.17}$$

where $K(s)$ is the linear controller in the Laplace domain and $E(s)$ is the Laplace transform of the steady-state error $e(t) = v_r(t) - v_{dc}(t)$. The FBL model of the standalone distributed PV-BES generator is $G(s) = \frac{1}{s}$. The Laplace domain func-

tions of sensitivity and complementary sensitivity with respect to the linearized plant $G(s)$ and controller $K(s)$ are expressed as follows:

$$\begin{aligned} S(s) &= \frac{1}{1+G(s)K(s)} \\ T(s) &= \frac{G(s)K(s)}{1+G(s)K(s)}. \end{aligned} \tag{3.18}$$

The control objective $V_{dc}(s)$ is proportional to the complementary sensitivity transfer function $T(s)$ and steady-state error $E(s)$ is proportional to the sensitivity transfer function $S(s)$. These can be obtained as follows:

$$\begin{aligned} V_{dc}(s) &= T(s)V_r(s) \\ E(s) &= S(s)V_r(s). \end{aligned} \tag{3.19}$$

To achieve the desired voltage V_r and minimize the steady-state error, a mixed-sensitivity based robust H_∞ loop-shaping controller is applied, which can generate an immeasurable variable V.

3.3 Robust Controller Design for Linearized Standalone Distributed PV-BES generator

This section presents the uncertainty model, noise decoupling capability and robust H_∞ controller for the standalone distributed PV-BES generator.

3.3.1 Uncertainty modeling

Parameter uncertainty is one of the familiar differences between the real and mathematical models of any system and it is important to address the design of

an effective controller. With parameter uncertainty, the dynamic model (3.1) of the nonlinear system is as follows:

$$\begin{aligned} \frac{dx}{dt} &= [f(x) + \Delta f(x)] + [g(x) + \Delta g(x)]u \\ y &= h(x). \end{aligned} \tag{3.20}$$

where the parameter mismatch is represented by Δ. The dynamic model of the standalone distributed PV-BES generator, including parameter uncertainties, is as follows:

$$\begin{aligned} \frac{di_L}{dt} &= \alpha_1 V_s - \alpha_1 m V_{dc} \\ \frac{dV_{dc}}{dt} &= \alpha_2 m i_L - \alpha_2 i_{dc} \end{aligned} \tag{3.21}$$

where $\alpha = \mu + \Delta\mu$. In the existence of uncertainties, parameters of the system are described in the Appendix A.1.1.

$$\begin{bmatrix} \frac{d\Delta i_L}{dt} \\ \\ \frac{d\Delta V_{dc}}{dt} \end{bmatrix} = \begin{bmatrix} \Delta\mu_1 V_s \\ \\ -\Delta\mu_2 i_{dc} \end{bmatrix} + \begin{bmatrix} -\Delta\mu_1 V_{dc} \\ \\ \Delta\mu_2 i_L \end{bmatrix} m. \tag{3.22}$$

To satisfy the robustness conditions corresponding to parameter uncertainties, the form of the uncertainties should satisfy the following requirement:

$$\Delta f(x) \quad and \quad \Delta g(x) \in \quad span\ g(x). \tag{3.23}$$

If this identical requirement holds, the following conditions will be accurate:

$$\bar{\omega} \ \geq r = \rho \tag{3.24}$$

where r, ρ and $\bar{\omega}$ are the relative degrees of the generalized system, $f(x)$ and

$g(x)$, respectively. To match the uncertainties of the system, ρ needs to be equal to the relative degree r as follows:

$$L_{\Delta f}h(x) = -\Delta\mu_2 i_{dc}. \tag{3.25}$$

The relative degree of $g(x)$ is $\bar{\omega} = 1$, with respect to the output function $h(x)$, which will occur if the $\Delta f(x)$ value is positive. The uncertainty of the vector field $\Delta g(x)$ matches if the following condition holds:

$$L_{\Delta g}h(x) = \Delta\mu_2 i_L \neq 0. \tag{3.26}$$

Owing to such situations, the uncertainty of the FBL system can be formed as follows:

$$\frac{dz}{dt} = [f(x) + \Delta f(x)] + [g(x) + \Delta g(x)]u. \tag{3.27}$$

The FBL model of the standalone distributed PV-BES generator includes the following uncertainties:

$$\frac{dV_{dc}}{dt} = v - \Delta\mu_2 i_{dc} + \Delta\mu_2 i_L m. \tag{3.28}$$

Substituting equation (3.14) into equation (3.28) can be simplified as follows:

$$\frac{dV_{dc}}{dt} = v\left(1 + \frac{\Delta\mu_2}{\mu_2}\right). \tag{3.29}$$

Assuming $\phi = \left(1 + \frac{\Delta\mu_2}{\mu_2}\right)$, and equation (3.29) is simplified as follows:

$$\frac{dV_{dc}}{dt} = v\phi. \tag{3.30}$$

Equation (3.30) become as follows Laplace transformation:

$$V_{dc}(s) = \frac{\phi}{s}V(s). \tag{3.31}$$

It is considered that the measurement noise influences the measurement output voltage of the DC-link. Thus, equation (3.31) can be expressed as follows:

$$V_{dc}(s) + N(s) = \frac{\phi}{s}V(s) \tag{3.32}$$

where $N(s)$ is the considered measurement noise.

3.3.2 Noise decoupling capability of designed control scheme

The FBL control scheme can be decoupled from the effects of noise. Considering exogenous noises, the nonlinear dynamic model (3.2) is as follows:

$$\begin{aligned} \frac{dx}{dt} &= f(x) + g(x)u + D(x)p \\ y &= h(x). \end{aligned} \tag{3.33}$$

where p is the vector of the measurement noise input and $D(x)$ is the vector field of the measurement noise.

To offer reliability to the FBL approach that has noise decoupling capability, the value of the nonlinear control input m from equation (3.14) is replaced into

equation (3.33). As a result, equation (3.33) is as follows:

$$\frac{dx}{dt} = f(x) + g(x)\frac{v - L_f^r h(x)}{L_g L_f^{r-1} h(x)} + D(x)p. \tag{3.34}$$

When $v = 0$, equation (3.34) can be written as follows:

$$\frac{dx}{dt} = f(x) - g(x)c(x) + D(x)p \tag{3.35}$$

where $c(x) = \frac{L_f^r h(x)}{L_g L_f^{r-1} h(x)}$. In the normal operation mode, the dynamics of the state become zero, $\frac{dx}{dt} = 0$. Thus, equation (3.35) become as follows:

$$D(x)p = g(x)c(x) - f(x). \tag{3.36}$$

After substituting the values of $c(x)$, $f(x)$ and $g(x)$ into equation (3.36). Equation (3.36) is formed as follows:

$$D(x)p = \begin{bmatrix} -\frac{V_{dc}}{L_{dc}} \\ \frac{i_L}{C_{dc}} \end{bmatrix} \left(-\frac{i_{dc}}{i_L} \right) - \begin{bmatrix} \frac{V_s}{L_{dc}} \\ -\frac{i_{dc}}{C_{dc}} \end{bmatrix}. \tag{3.37}$$

After simplifying (3.37) become as follows:

$$D(x)p = \begin{bmatrix} \frac{V_{dc}}{L_{dc}} \frac{i_{dc}}{i_L} - \frac{V_s}{L_{dc}} \\ 0 \end{bmatrix}. \tag{3.38}$$

From the above equation, the linearized portion is decoupled from the noise.

3.3.3 Robust H_∞ mixed-sensitivity loop-shaping controller design

The robust H_∞ loop-shaping controller design depends on the nature of the complementary sensitivity transfer function T(s) and the sensitivity transfer function S(s). The choice of weight functions respect to T(s) and S(s) performs an important role, which can be selected with fulfill the following requirements:

$$\begin{aligned} ||S(s)+T(s)||_\infty &\equiv 1,\ a \\ ||W_S(s)S(s)||_\infty &< 1,\ b \\ ||W_T(s)T(s)||_\infty &< 1,\ c \\ \left|\left|\frac{1}{W_S(s)}\right|\right|_\infty &> ||S(s)||_\infty,\ d \\ \left|\left|\frac{1}{W_T(s)}\right|\right|_\infty &> ||T(s)||_\infty,\ e. \end{aligned} \tag{3.39}$$

A traditional technique for selecting the weight function fulfills the expectations of low-pass and high-pass filters with respect to the complementary sensitivity function T(s) and sensitivity function S(s). Based on this traditional technique, both weight functions can be obtained as follows:

$$\begin{aligned} W_S(s) &= k\frac{s/M+\omega_0}{s+\omega_0 A} \\ W_T(s) &= g\frac{s+\omega_0/M}{As+\omega_0}. \end{aligned} \tag{3.40}$$

The FBL system with 10% parameter uncertainty is considered as G(s) = $\frac{\phi}{s} \approx \frac{0.91}{(s+0.001)}$, the weighting functions are as follows and details can find in

Appendix A.1.1:

$$W_S(s) = \frac{0.84615(s+6.5)}{(s+5\times10^{-4})}$$
$$W_T(s) = \frac{5900(s+3.846)}{(s+5\times10^{4})}. \tag{3.41}$$

The controller K(s) that applies can be simply computed using the MATLAB command $K(s) = mixsyn(G, W_S, [], W_T)$ as follows:

$$K_i(s) = \frac{4.078\times10^{7}s^2 + 2.039\times10^{12}s + 2.054\times10^{9}}{s^3 + 6.872\times10^{10}s^2 + 6.617\times10^{13}s + 3.266\times10^{10}}. \tag{3.42}$$

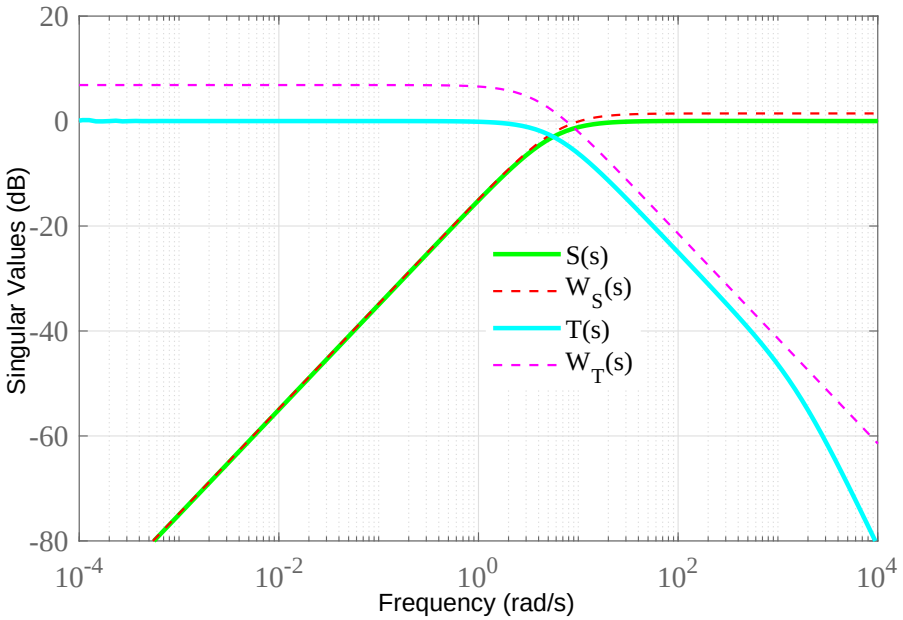

Figure 3.2: Weight and sensitivity functions in sigma plot.

The sigma plots of the sensitivity and weighting functions are displayed in Figure 3.2, like the lead-lag compensator. The gain value raises at a low frequency, which provides well disturbance rejection, whereas the loop gain of the sensitivity function S(s) is inversely related to the sensitivity weighting function.

The gain value of T(s) decreases at low frequencies, which can be offered with

Table 3.2: H_∞ norm value of weighting and sensitivity functions.

Conditions	H_∞ norm values
(3.39) a	$1 \cong 1.0410$
(3.39) b	$0.9787 < 1$
(3.39) c	$0.6636 < 1$
(3.39) d	$1.1818 > 1.0017$
(3.39) e	$2.2034 > 1.0180$

improved reference following ability. The loop gain of the complementary sensitivity functions T(s) is inversely proportional to the complementary sensitivity weighting function. The crossover frequency of T(s) is considerably bigger than that of S(s) and various weighting functions, and the resultant transfer function from $W_T(s)$ is appropriate. Table 3.2 presents the H_∞ norm values corresponding to equation (3.39), where all values fulfill the conditions.

3.4 Feedback Linearization of Grid-Connected Distributed FC Generator

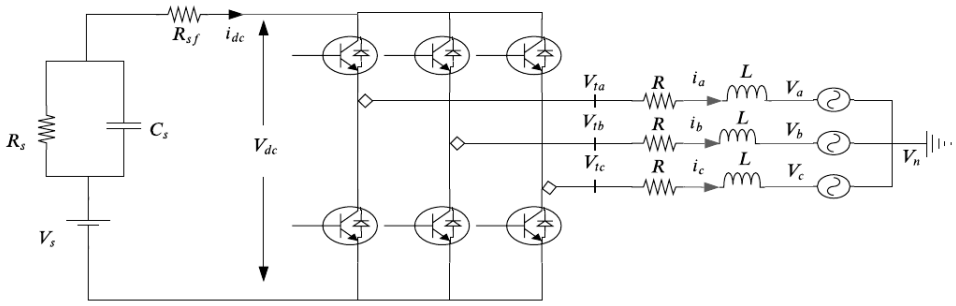

Figure 3.3: Circuit diagram of grid-connected distributed FC generator.

Different types of control approaches have been proposed in the literature to inject smooth power into the grid from a distributed FC generator. The FBL is the applied controller design procedure for DG, which is presented in this

section. Figure 3.3 shows the circuit diagram of the grid-connected distributed FC generator. The characteristic model of the distributed FC generator can be recalled from Chapter 2 (Subsection 2.2.2) and written as follows:

$$\begin{aligned} \frac{dV_c}{dt} &= \mu_1 V_{dc} - \mu_1 V_s + \frac{3\mu_{23} i_d}{4} m_d + \frac{3\mu_{23} i_q}{4} m_q \\ \frac{di_d}{dt} &= \frac{\mu_5 V_{dc}}{2} m_d + \omega i_q - \mu_5 V_d - \mu_4 i_d \\ \frac{di_q}{dt} &= \frac{\mu_5 V_{dc}}{2} m_q - \mu_4 i_q - \mu_5 V_q - \omega i_d. \end{aligned} \tag{3.43}$$

where $\mu_1 = \frac{1}{R_s C_s}$, $\mu_2 = \frac{1}{C_s}$, $\mu_3 = \frac{R_{sf}}{R_s C_s}$, $\mu_{23} = \mu_2 + \mu_3$, $\mu_4 = \frac{R}{L}$ and $\mu_5 = \frac{1}{L}$.

The mathematical model of the grid-connected distributed FC generator from equation (3.43) is written as the following nonlinear form:

$$\begin{aligned} \dot{x} &= f(x) + \sum_{i=1}^{N} g_i(x) u_i \\ y &= h_i(x) \end{aligned} \tag{3.44}$$

where $i = 1$ & 2 with $x = \begin{bmatrix} V_c \\ i_d \\ i_q \end{bmatrix}$, $f(x) = \begin{bmatrix} \mu_1 V_{dc} - \mu_1 V_s \\ -\mu_4 i_d - \mu_5 V_d + \omega i_q \\ -\mu_4 i_q - \mu_5 V_q - \omega i_d \end{bmatrix}$, $g_i(x) = \begin{bmatrix} \frac{3\mu_{23} i_d}{4} & \frac{3\mu_{23} i_q}{4} \\ \frac{\mu_5 V_{dc}}{2} & 0 \\ 0 & \frac{\mu_5 V_{dc}}{2} \end{bmatrix}$, $u_i = \begin{bmatrix} m_d \\ m_q \end{bmatrix}$ and $y = \begin{bmatrix} i_d \\ i_q \end{bmatrix}$.

In (3.44), x is the state variables, u_i is the multi-input vector, $y = h_i(x)$ is the multi-output vector, and $n = 3$ is the nonlinear system order.

3.4.1 Determine relative degree

The Lie derivative of the vector field $f(x)$ with respect to the control objective $h_1(x) = i_d$ and $h_2(x) = i_q$ can be obtained as follows:

$$\begin{aligned} L_f h_1(x) &= +\omega i_q - \mu_5 V_d - \mu_4 i_d \\ L_f h_2(x) &= -\mu_4 i_q - \mu_5 V_q - \omega i_d. \end{aligned} \tag{3.45}$$

The Lie derivative of the vector field $g_i(x)$ regarding to the control objective $h_1(x) = i_d$ and $h_2(x) = i_q$ can be obtained as follows:

$$\begin{aligned} L_{g_1} L_f^{1-1} h_1(x) &= \frac{\mu_5 V_{dc}}{2} \\ L_{g_2} L_f^{1-1} h_2(x) &= \frac{\mu_5 V_{dc}}{2}. \end{aligned} \tag{3.46}$$

In the case of a MIMO system, for each control objective $y = h_i(x)$, there is a corresponding relative degree r_i. Then, the relative degree of the grid-connected distributed FC generator forms a set as follows:

$$r = \{r_1,\ r_2\} \tag{3.47}$$

The total relative degree of the MIMO grid-connected distributed FC generator can be obtained as follows:

$$\sum_{i=1}^{2} r_i. \tag{3.48}$$

Therefore, the total relative degree of the linearized grid-connected distributed FC generator is two, which is less than the original order. As a result, it is partially linearized.

3.4.2 Nonlinear coordinate transformation

Two new coordinates can be obtained from the nonlinear coordinate transformation, where the relative degree of the linearized model is two. The new coordinates can be formed as follows:

$$\begin{aligned} z_1 &= L_f^{1-1} h_1 = i_d \\ z_2 &= L_f^{1-1} h_2 = i_q. \end{aligned} \tag{3.49}$$

Through the nonlinear coordinate transformation as represented using (3.49), the FBL model of the grid-connected distributed FC generator is expressed as follows:

$$\begin{aligned} \frac{dz_1}{dt} &= v_1 \\ \frac{dz_2}{dt} &= v_2 \end{aligned} \tag{3.50}$$

where v_1 and v_2 are the regulators of the output functions i_d and i_q.

3.4.3 Zero internal dynamic stability

The control law is needed to choose in such a way that fulfills the following situation owing to guarantee stability:

$$\lim_{x \to \infty} h_i(x) \longrightarrow 0 \tag{3.51}$$

which requires that $z_1 = z_2 = 0$ at steady-state for the grid-connected distributed FC generator. Therefore,

$$\begin{aligned} \frac{dz_1}{dt} &= 0 \\ \frac{dz_2}{dt} &= 0. \end{aligned} \tag{3.52}$$

Still, z_3 is a nonlinear function that can represent the remaining state and

satisfies the following conditions:

$$\begin{aligned} L_{g_1} z_3 &= 0 \\ L_{g_2} z_3 &= 0. \end{aligned} \tag{3.53}$$

Consequently, z_3 becomes as follows, which satisfies equation (3.53):

$$z_3 = \frac{1}{2}\frac{L}{V_{dc}} i_d^2 + \frac{1}{2}\frac{L}{V_{dc}} i_q^2 - \frac{1}{2\eta} V_c \tag{3.54}$$

where $\eta = \frac{3}{4}\mu_{23}$. Using $z_1 = i_d$ and $z_2 = i_q$, (3.54) is determined as follows:

$$V_c = -z_3 + \frac{\eta L}{V_{dc}} z_1^2 + \frac{\eta L}{V_{dc}} z_2^2 \tag{3.55}$$

Consequently, the remainder of the dynamics is obtained as follows:

$$L_f z_3 = -\frac{1}{2\eta} \frac{V_0 - V_c - i_{dc} R_{sf} - V_0}{\tau_1} \tag{3.56}$$

where $V_c \gg i_{dc} R_{sf}$, equation (3.56) become as follows:

$$L_f z_3 = \frac{1}{2\eta} \frac{V_c}{\tau_1}. \tag{3.57}$$

Substituting the value of V_c from (3.55) into (3.57), we can write it as follows:

$$L_f z_3 = \frac{1}{2\eta\tau_1} \left[- z_3 + \frac{\eta L}{V_{dc}} i_d^2 + \frac{\eta L}{V_{dc}} i_q^2 \right] \tag{3.58}$$

Again, considered $z_1 = z_2 = 0$, (3.58) can be simplified as:

$$L_f z_3 = -\frac{z_3}{2\eta\tau_1} \tag{3.59}$$

where η and τ_1 are positive variables. From (3.59), it is mathematically clear that the stability of the grid-connected distributed FC generator does not depend on the inner dynamics. The grid-connected distributed FC generator can be stabilized with a partial FBL control technique, which is designed in the following subsection.

3.4.4 Feedback linearized control law

The general form of FBL control law is written as follows:

$$u_i = \frac{v_i - a_i(x)}{b_i(x)} \tag{3.60}$$

where $a(x) = L_f h(x)$ and $b(x) = L_g L_f^{r-1} h(x)$. Then, the FBL control laws for grid-connected distributed FC generator are as follows:

$$\begin{aligned} m_d &= \frac{2}{\mu_5 V_{dc}} \left(v_1 + \mu_4 i_d + \mu_5 V_d - \omega i_q\right) \\ m_q &= \frac{2}{\mu_5 V_{dc}} \left(v_2 + \mu_4 i_q + \mu_5 V_q + \omega i_d\right) \end{aligned} \tag{3.61}$$

where the elements of equations (3.61) are either physically measurable or can be formed in terms of the measured variables, only the linear control inputs v_1 and v_2 must be obtained using a linear controller design approach for the FBL control laws.

3.4.5 Transfer function of linearized system

Using Laplace transformation, the linearized system (3.50) can be written as follows:

$$\begin{aligned} I_d(s) &= \frac{1}{s}V_1(s) \\ I_q(s) &= \frac{1}{s}V_2(s). \end{aligned} \tag{3.62}$$

The single-input single-output subsystems with transfer functions $\frac{I_d(s)}{V_1(s)} = \frac{1}{s}$ and $\frac{I_q(s)}{V_2(s)} = \frac{1}{s}$ are written in a compact form as $\frac{I_{dq}(s)}{V_{12}(s)} = \frac{1}{s} = G(s)$. The output current $I_{dq}(s)$ of the grid-connected distributed FC generator is normally needed to follow the reference current $I_{dqr}(s)$, the control input $V_{12}(s)$ can be obtained as follows:

$$V_{12}(s) = K_{dq}(s)E_{dq}(s) \tag{3.63}$$

where $K_{dq}(s)$ is the transfer function of the linear controller and $E_{dq}(s)$ is the Laplace transform of steady-state error $e_{dq}(t) = i_{dqr}(t) - i_{dq}(t)$. The linearized model of the grid-connected distributed FC generator is $G(s) = \frac{1}{s}$. The sensitivity and complementary sensitivity functions of the linearized closed-loop system are as follows:

$$\begin{aligned} S_{dq}(s) &= \frac{1}{1 + G(s)K_{dq}(s)} \\ T_{dq}(s) &= \frac{G(s)K_{dq}(s)}{1 + G(s)K_{dq}(s)}. \end{aligned} \tag{3.64}$$

The output current $I_{dq}(s)$ and steady-state error $E_{dq}(s)$ in the closed-loop system are associated to the reference current $I_{dqr}(s)$ as follows:

$$\begin{aligned} I_{dq}(s) &= T_{dq}(s)I_{\mathrm{dqr}}(s) \\ E_{dq}(s) &= S_{dq}(s)I_{\mathrm{dqr}}(s). \end{aligned} \tag{3.65}$$

The robust controller for the grid-connected distributed FC generator is designed using the FBL control technique and a linear controller design approach.

3.5 Robust Controller Design for Linearized Grid-Connected Distributed FC Generator

This section presents the uncertainty model, noise decoupling capability and robust H_∞ controller for the grid-connected distributed FC generator.

3.5.1 Uncertainty modeling

The dynamic model of the grid-connected distributed FC generator, including parameter uncertainties, (3.43) is as follows:

$$\begin{aligned} \frac{dV_c}{dt} &= \alpha_1 V_{dc} - \alpha_1 V_s + \frac{3\alpha_{23} i_d}{4} m_d + \frac{3\alpha_{23} i_q}{4} m_q \\ \frac{di_d}{dt} &= -\alpha_4 i_d + \omega i_q - \alpha_5 V_d + \frac{\alpha_5 V_{dc}}{2} m_d \\ \frac{di_q}{dt} &= -\omega i_d - \alpha_4 i_q - \alpha_5 V_q + \frac{\alpha_5 V_{dc}}{2} m_q \end{aligned} \tag{3.66}$$

where $\mu + \Delta\mu = \alpha$. It is crucial to deal with parameter deviation due to mathematical mismatches to any real system. In the existence of parameter uncertainty, the dynamic model of the nonlinear system becomes as follows for (3.45):

$$\begin{aligned} \frac{dx}{dt} &= [f(x) + \Delta f(x)] + [g_i(x) + \Delta g_i(x)] u_i \\ y &= h_i(x) \end{aligned} \tag{3.67}$$

where $\Delta f(x) = \begin{bmatrix} \Delta\mu_1 V_{dc} - \Delta\mu_1 V_s \\ -\Delta\mu_4 i_d - \Delta\mu_5 V_d \\ -\Delta\mu_4 i_q - \Delta\mu_5 V_q \end{bmatrix}$, $\Delta g_i(x) = \begin{bmatrix} \frac{3\Delta\mu_{23} i_d}{4} & \frac{3\Delta\mu_{23} i_d}{4} \\ \frac{\Delta\mu_5 V_{dc}}{2} & 0 \\ 0 & \frac{\Delta\mu_5 V_{dc}}{2} \end{bmatrix}$, Δ is denoted as the parameter variation and the detailed calculation of parameter uncertainty bounds can be expressed in the Appendix A.1.2.

The uncertainty structure should be fulfilled by following term for a robustness:

$$\Delta f(x) \quad \text{and} \quad \Delta g(x) \in \quad \text{span}\{g(x)\}. \tag{3.68}$$

If this term is fulfilled, the next mathematical argument will be true:

$$\varpi \geq r = \rho \tag{3.69}$$

where r, ρ and ϖ are the relative degrees of the system, and $\Delta f(x)$ and $\Delta g(x)$, respectively. To match the parameter variations of the system, ρ should be equal to r as follows:

$$\begin{aligned} L_{\Delta f} h_1(x) &= -\Delta\mu_4 i_d - \Delta\mu_5 V_d \\ L_{\Delta f} h_2(x) &= -\Delta\mu_4 i_q - \Delta\mu_5 V_q. \end{aligned} \tag{3.70}$$

The relative degree of the vector field $g_i(x)$ is ϖ, which is equal to the relative degree of the original system respect to the control objectives $h_1(x)$ and $h_2(x)$ if Δf_1 and Δf_2 are non-zero.

$$\begin{aligned} L_{\Delta g_1} h_1(x) &= \frac{\Delta\mu_5 V_{dc}}{2} \neq 0 \\ L_{\Delta g_2} h_2(x) &= \frac{\Delta\mu_5 V_{dc}}{2} \neq 0. \end{aligned} \tag{3.71}$$

The FBL model, with parameter uncertainties, is expressed as follows:

$$\frac{dz_i}{dt} = L_f h_i(x) + L_{\Delta f} h_i(x) + [L_{g_i} h_i(x) + L_{\Delta g_i} h_i(x)] u_i. \tag{3.72}$$

The dynamic model of the grid-connected distributed FC generator is as follows owing to the parametric uncertainty:

$$\begin{aligned} \frac{di_d}{dt} &= v_1 - \Delta\mu_4 i_d - \Delta\mu_5 V_d + \frac{\Delta\mu_5 V_{dc}}{2} m_d \\ \frac{di_q}{dt} &= v_2 - \Delta\mu_4 i_q - \Delta\mu_5 V_q + \frac{\Delta\mu_5 V_{dc}}{2} m_q. \end{aligned} \tag{3.73}$$

After substituting (3.61) into (3.73) can be simplified as follows:

$$\begin{aligned} \frac{di_d}{dt} &= \left(1 + \frac{\Delta\mu_5}{\mu_5}\right) v_1 - \left(\Delta\mu_4 - \frac{\mu_4 \Delta\mu_5}{\mu_5}\right) i_d - \frac{\omega \Delta\mu_5}{\mu_5} i_q \\ \frac{di_q}{dt} &= \left(1 + \frac{\Delta\mu_5}{\mu_5}\right) v_2 - \left(\Delta\mu_4 - \frac{\mu_4 \Delta\mu_5}{\mu_5}\right) i_q + \frac{\omega \Delta\mu_5}{\mu_5} i_d. \end{aligned} \tag{3.74}$$

Assuming $\phi_1 = 1 + \frac{\Delta\mu_5}{\mu_5}$, $\phi_2 = \Delta\mu_4 - \frac{\mu_4 \Delta\mu_5}{\Delta\mu_5}$ and $\phi_3 = \frac{\omega \Delta\mu_5}{\mu_5}$, and equation (3.74) can be simplified as follows:

$$\begin{aligned} \frac{di_d}{dt} &= v_1 \phi_1 - \phi_2 i_d - \phi_3 i_q \\ \frac{di_q}{dt} &= v_2 \phi_1 - \phi_2 i_q + \phi_3 i_d. \end{aligned} \tag{3.75}$$

After Laplace transformation (3.75) is as follows:

$$\begin{aligned} I_d(s) &= \frac{1}{s + \phi_2} [V_1(s)\phi_1 - \phi_3 I_q(s)] \\ I_q(s) &= \frac{1}{s + \phi_2} [V_2(s)\phi_1 + \phi_3 I_d(s)]. \end{aligned} \tag{3.76}$$

The measurement noise is considered as barrier to designing a robust con-

troller. Including the measurement noise equation (3.76) can be written as:

$$\begin{aligned} I_d(s) + N(s) &= \frac{1}{s+\phi_2}[V_1(s)\phi_1 - \phi_3 I_q(s)] \\ I_q(s) + N(s) &= \frac{1}{s+\phi_2}[V_2(s)\phi_1 + \phi_3 I_d(s)] \end{aligned} \tag{3.77}$$

where $N(s)$ is considered the measurement noise.

3.5.2 Noise decoupling capability of designed control scheme

Normally, a noise-decoupled system is not influenced by the output measurement in operation mode. This subsection analyses the noise decoupling ability of the proposed FBL control technique. With the effect of noise, the nonlinear dynamic system (3.44) can be written as follows:

$$\begin{aligned} \frac{dx}{dt} &= f(x) + g_i(x)u_i + D_i(x)p_i \\ y &= h_i(x) \end{aligned} \tag{3.78}$$

where $D_i(x)$ is the vector field of the input noise vector p_i. The control objective y is decoupled from input noise vector p_i. After substituting equation (3.60) into (3.78), it can be obtained as follows:

$$\frac{dx}{dt} = f(x) + g_i(x)\left(\frac{v_i - a_i(x)}{b_i(x)}\right) + D_i(x)p_i. \tag{3.79}$$

The control objective is decoupled from the disturbances at $v_i = 0$. Then, equation (3.79) is shortened as follows:

$$\frac{dx}{dt} = f(x) - g_i(x)c_i(x) + D_i(x)p_i \tag{3.80}$$

where $c_i(x) = \frac{a_i(x)}{b_i(x)}$. In the normal operation mode, the dynamics of the state variable $\frac{dx}{dt} = 0$; and thus, equation (3.80) becomes as follows:

$$D_i(x)p_i = g_i(x)c_i(x) - f(x). \tag{3.81}$$

Equation (3.81) can be used to determine, how many states are decoupled from the measurement noise. For the grid-connected distributed FC generator, (3.81) is written as follows:

$$D_i(x)p_i = \begin{bmatrix} \frac{3}{4}\alpha_5 \imath_d & \frac{3}{4}\alpha_6 \imath_q \\ \alpha_4 V_{dc} & 0 \\ 0 & \alpha_4 V_{dc} \end{bmatrix} \begin{bmatrix} \frac{f_2}{\alpha_4 V_d c} \\ \frac{f_3}{\alpha_4 V_d c} \end{bmatrix} - \begin{bmatrix} f_1 \\ f_2 \\ f_3 \end{bmatrix}. \tag{3.82}$$

Once matrix multiplication, (3.82) is shortened as follows:

$$D_i(x)p_p = \begin{bmatrix} \frac{3}{4}\alpha_5 \imath_d \frac{f_2}{\alpha_4 V_d c} + \frac{3}{4}\alpha_6 \imath_q \frac{f_3}{\alpha_4 V_d c} - f_1 \\ 0 \\ 0 \end{bmatrix}. \tag{3.83}$$

The FBL portion of the grid-connected distributed FC generator is decoupled from the effect of the measurement noise. The designed FBL control law can reduce noise from the linearized two states.

3.5.3 Robust H_∞ mixed-sensitivity loop-shaping controller design

The loop shape of the sensitivity and complementary sensitivity functions is essential for designing a robust H_∞ controller. This subsection presents the robust H_∞ controller designed approach for the linearized portion of the FBL control laws.

To obtain robust performance from the mixed-sensitivity based robust H_∞ loop-shaping controller, it is crucial to keep the following requirements:

$$\begin{aligned} ||S(s)+T(s)||_\infty &\equiv 1,\ a \\ ||W_S(s)S(s)||_\infty &< 1,\ b \\ ||W_T(s)T(s)||_\infty &< 1,\ c \\ \left|\left|\frac{1}{W_p(s)}\right|\right|_\infty &> ||S(s)||_\infty,\ d \\ \left|\left|\frac{1}{W_T(s)}\right|\right|_\infty &> ||T(s)||_\infty,\ e \end{aligned} \tag{3.84}$$

where $W_S(s)$ and $W_T(s)$ are the weighting functions of the sensitivity function S(s) and complementary sensitivity function T(s), respectively. By accurate selection of the weighting function parameters, these conditions can be fulfilled. The weight functions are as follows:

$$\begin{aligned} W_S &= k\frac{s/M+\omega_0}{s+\omega_0 A} \\ W_T &= g\frac{s+\omega_0/M}{As+\omega_0} \end{aligned} \tag{3.85}$$

where M is the highest amplitude in the sigma plot of sensitivity function, which can maintain a robustness. The minimum value of the fixed offset is A, ω_0 is the connected frequency of the $S(s)$ and $T(s)$, and k and g are regulation gain values that regulate the sigma plots of sensitivity and complementary sensitivity weight

functions, respectively.

For the developed partially FBL plant $G(s) = \frac{0.77}{(s+2.31)}$ corresponding to 30% parameter variation with weighting functions are $W_S(s)$ and $W_T(s)$, the controller K(s), which applies can be simply computed by the MATLAB command $K(s) = \text{mixsyn}(G, W_S, [], W_T)$, and the controller as follows:

$$K(s) = \frac{3.359\times10^6 s^2 + 5.047\times10^9 s + 1.164\times10^{10}}{s^3 + 6.431\times10^5 s^2 + 2.534\times10^9 s + 2.181\times10^6}. \tag{3.86}$$

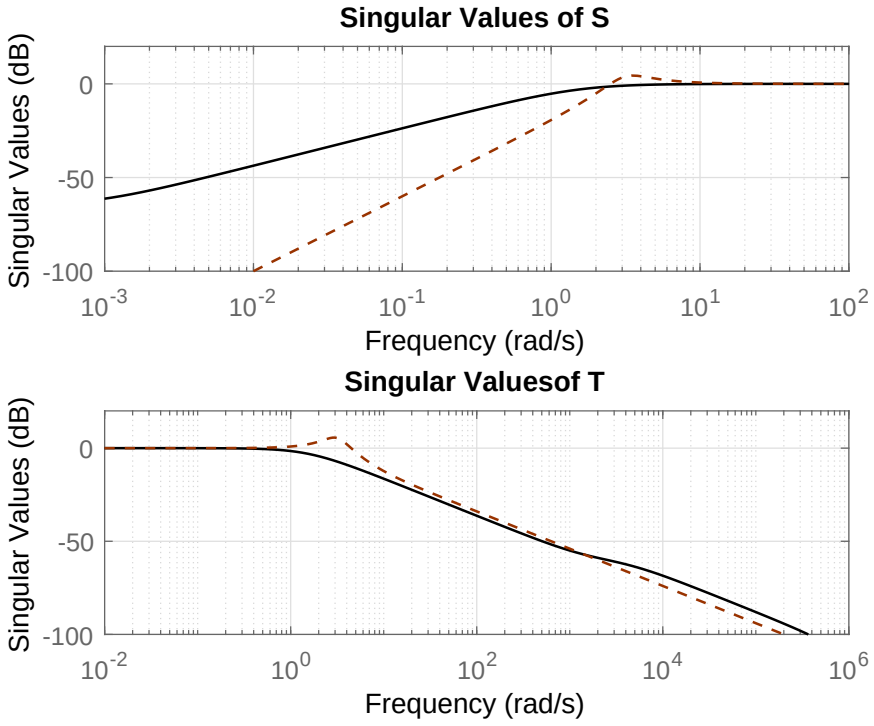

Figure 3.4: Weight and sensitivity functions in sigma plot.

The frequency response of the $\frac{1}{W_S(s)}$ and $\frac{1}{W_T(s)}$ are applied to design the controller (3.86) and the frequency responses of the functions S(s) and T(s) are presented in Figure 3.4. As shown in the plots, the weighting functions $W_S(s)$ and $W_T(s)$ are sensible for the good nature of functions S(s) and T(s), respectively.

Table 3.3: H_∞ norm value of weighting and sensitivity functions

Conditions	H_∞ norm values
(3.84) a	$1 \equiv 1$
(3.84) b	$0.9297 < 1$
(3.84) c	$0.8466 < 1$
(3.84) d	$1.2632 > 1.0000$
(3.84) e	$1.4458 > 0.9994$

Table 3.3 is satisfied all conditions of equation (3.84).

3.6 Feedback Linearization of Two-Stage Distributed PV-BES Generator

This section presents the FBL control scheme for the integrated configuration of the previously considered standalone distributed PV-BES and grid-connected distributed FC generators. The standalone distributed PV-BES generator replaces the FC stack in this integrated configuration, so this structure becomes a grid-connected (two-stage) distributed PV-BES generator. The detailed configuration and mathematical modeling of the hybrid system are presented in Section 2.2. Figure 3.5 presents the circuit diagram of the two-stage distributed PV-BES generator. The FBL control laws are developed in this section for the nonlinear dynamic model of the two-stage distributed PV-BES generator. The nonlinear characteristic model of the two-stage distributed PV-BES generator can be recalled as follows, from Subsection 2.2.3.

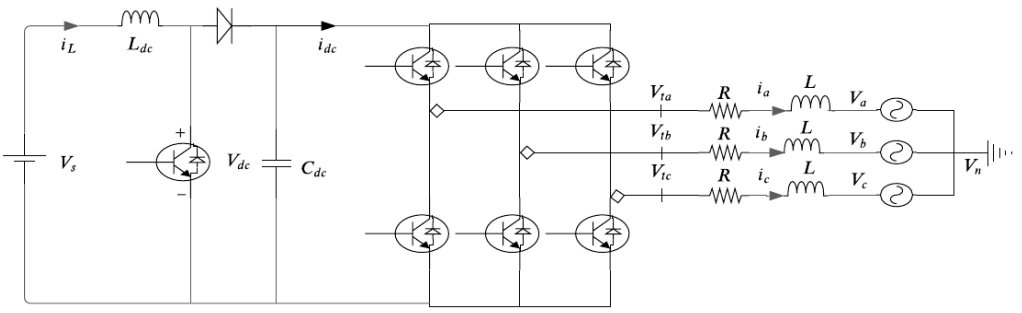

Figure 3.5: Circuit diagram of two-stage distributed PV-BES generator.

$$\begin{aligned}
\frac{di_L}{dt} &= \frac{1}{L_{dc}}\left(V_s - mV_{dc}\right) \\
\frac{dV_{dc}}{dt} &= \frac{1}{C_{dc}}\left(mi_L - i_{dc}\right) \\
\frac{di_d}{dt} &= \frac{1}{L}\left(\frac{V_{dc}}{2}m_d - Ri_d - V_d\right) + \omega i_q \\
\frac{di_q}{dt} &= \frac{1}{L}\left(\frac{V_{dc}}{2}m_q - Ri_q - V_q\right) - \omega i_d.
\end{aligned} \tag{3.87}$$

The nonlinear dynamic model of the two-stage distributed PV-BES generator can be represented as follows:

$$\begin{aligned}
\dot{x} &= f\left(x\right) + \sum_{i=1}^{N} g_i(x)u_i \\
y &= h_i(x)
\end{aligned} \tag{3.88}$$

where x is the state vector, and $f(x)$ and $g_i(x)$ are the vector fields of state variables with n dimensions. The controls input and control objective of the system are u_i and y, respectively. The two-stage distributed PV-BES generator

is represented as follows:

$$\begin{bmatrix} \frac{di_L}{dt} \\ \frac{dV_{dc}}{dt} \\ \frac{di_d}{dt} \\ \frac{di_q}{dt} \end{bmatrix} = \begin{bmatrix} \frac{V_s}{L_{dc}} \\ -\frac{i_{dc}}{C_{dc}} \\ \frac{1}{L}\left(-Ri_d - V_d\right) + \omega i_q \\ \frac{1}{L}\left(-Ri_q - V_q\right) - \omega i_d \end{bmatrix} + \begin{bmatrix} -\frac{V_s}{L_{dc}} & 0 & 0 \\ \frac{i_L}{C_{dc}} & 0 & 0 \\ 0 & \frac{V_{dc}}{2L} & 0 \\ 0 & 0 & \frac{V_{dc}}{2L} \end{bmatrix} \begin{bmatrix} m \\ m_d \\ m_q \end{bmatrix} \tag{3.89}$$

$$y = \begin{bmatrix} h_1(x) \\ h_2(x) \\ h_3(x) \end{bmatrix} = \begin{bmatrix} V_{dc} \\ i_d \\ i_q \end{bmatrix}.$$

3.6.1 Determine relative degree

The Lie derivative $L_f h(x)$ for three different control objectives V_{dc}, i_d and i_q can be computed as follows:

$$\begin{aligned} L_f h_1(x) &= \frac{\partial V_{dc}}{\partial x} f(x) = -\frac{i_{dc}}{C_{dc}} \\ L_f h_2(x) &= \frac{\partial i_d}{\partial x} f(x) = \frac{1}{L}\left(-Ri_d - V_d\right) + \omega i_q \\ L_f h_3(x) &= \frac{\partial i_q}{\partial x} f(x) = \frac{1}{L}\left(-Ri_q - V_q\right) - \omega i_d. \end{aligned} \tag{3.90}$$

The Lie derivative $L_{g_i} h_i(x)$ for three different control objectives V_{dc}, i_d and i_q can be computed as follows:

$$\begin{aligned} L_{g_1} h_1(x) &= \frac{\partial V_{dc}}{\partial x} g_1(x) = \frac{i_L}{C_{dc}} \\ L_{g_2} h_2(x) &= \frac{\partial i_d}{\partial x} g_2(x) = \frac{V_{dc}}{2L} \\ L_{g_3} h_3(x) &= \frac{\partial i_q}{\partial x} g_3(x) = \frac{V_{dc}}{2L}. \end{aligned} \tag{3.91}$$

In the situation of a MIMO system, there is a corresponding relative degree r_i for output $h_i(x)$. As a result, the relative degree of the MIMO system forms a

set as:

$$r = \{r_1,\ r_2, \cdots, r_i, \cdots, r_N\} \tag{3.92}$$

and the overall relative degree of the system is written as follows:

$$\sum_{i=1}^{N} r_i. \tag{3.93}$$

Therefore, the linearized system's overall relative degree is three, which is smaller than the original order of the two-stage distributed PV–BES generator. Thus, it is partially linearized.

3.6.2 Nonlinear coordinate transformation

Three new coordinates can be obtained from the coordinate transformation, where the relative degree of the linearized model is three. The three new coordinates can be determined as follows:

$$\begin{aligned} z_1(x) &= L_f^{1-1} h_1(x) = V_{dc} \\ z_2(x) &= L_f^{1-1} h_2(x) = i_d \\ z_3(x) &= L_f^{1-1} h_3(x) = i_q. \end{aligned} \tag{3.94}$$

Through the coordinate transformation as represented by (3.94), the FBL model of the two-stage distributed PV-BES generator is written as follows:

$$\begin{aligned} \frac{dz_1}{dt} &= v_1 \\ \frac{dz_2}{dt} &= v_2 \\ \frac{dz_3}{dt} &= v_3 \end{aligned} \tag{3.95}$$

where v_1, v_2 and v_3 are linear control inputs that can be obtained by any linear control approach.

3.6.3 Zero internal dynamic stability

The control law is needed to choose in such a way that fulfills the following term owing to guarantee stability:

$$\lim_{x\to\infty} h_i(x) \longrightarrow 0 \tag{3.96}$$

which represents that $z_1 = z_2 = z_3 = 0$ at the steady-state for the two-stage PV-BES generator. Therefore,

$$\begin{aligned} \frac{dz_1}{dt} &= 0 \\ \frac{dz_2}{dt} &= 0 \\ \frac{dz_3}{dt} &= 0. \end{aligned} \tag{3.97}$$

Still, z_4 is a nonlinear function that can represent the remaining state and satisfies the following conditions:

$$\begin{aligned} L_{g_1} z_4(x) &= 0 \\ L_{g_2} z_4(x) &= 0 \\ L_{g_3} z_4(x) &= 0. \end{aligned} \tag{3.98}$$

Consequently, z_4 becomes, which satisfies the equations (3.98),

$$z_4 = \frac{1}{2} L_i i_i^2 + \frac{1}{2} C_{dc} V_{dc}^2. \tag{3.99}$$

Therefore, the remainder of the dynamics can be obtained as follows:

$$L_f z_4 = V_{in} i_i - V_{dc} i_{dc} \tag{3.100}$$

where the input power of the DC-DC VSC is $V_s i_L$ and the output power is $V_{dc} i_{dc}$. Owing to the ideal or lossless condition, $V_s i_L = V_{dc} i_{dc}$ for which equation (3.11) is written as follows:

$$L_f z_4 = 0. \tag{3.101}$$

The inner dynamics did not affect the stability of the two-stage distributed PV-BES system. Therefore, a partial FBL control law can be designed as described in the following subsection.

3.6.4 Feedback linearized control law

The generalized FBL control law can be form as follows:

$$u_i = \frac{v_i - a_i(x)}{b_i(x)} \tag{3.102}$$

where $a_i(x)$ and $b_i(x)$ are the non-zero Lie derivatives $L_f^r(x)$ and $L_g L_f^{r-1}(x)$, respectively. The feedback linearized control law for the control objectives V_{dc}, i_d and i_q are obtained as follows:

$$\begin{aligned} m &= \frac{C_{dc} v_1 + i_{dc}}{i_L} \\ m_d &= \frac{2L}{V_{dc}} \left(v_2 + \frac{R}{L} i_d + \frac{V_d}{L} - \omega i_q \right) \\ m_q &= \frac{2L}{V_{dc}} \left(v_3 + \frac{R}{L} i_q + \frac{V_q}{L} + \omega i_d \right) \end{aligned} \tag{3.103}$$

All the components of (3.103) are measurable or can be formed in terms of the measured variables. However, the linear control inputs v_1, v_2 and v_3 need to be obtained using a linear control design approach.

3.6.5 Transfer function of linearized system

Using the Laplace transformation, the linearized subsystem (3.95) can be written as:

$$\begin{aligned} V_{dc}(s) &= \frac{1}{s}V_1(s) \\ I_d(s) &= \frac{1}{s}V_2(s) \\ I_q(s) &= \frac{1}{s}V_3(s). \end{aligned} \tag{3.104}$$

The decoupled SISO systems with the same transfer function $\frac{V_{dc}(s)}{V_1(s)} = \frac{I_{dq}(s)}{V_{23}(s)} = \frac{1}{s}$, can be stabilized by a linear controller. Typically, $V_{dc}(s)$, $I_d(s)$ and $I_q(s)$ are required to track their references V_r, $I_{dr}(s)$ and $I_{qr}(s)$, so the control inputs $V_1(s)$, $V_2(s)$ and $V_3(s)$ can be generated by

$$V_i(s) = K_i(s)E_i(s), \qquad i = 1, 2, 3 \tag{3.105}$$

where $K_1(s)$, $K_2(s)$ and $K_3(s)$ are the transfer functions of the controller, and $E_1(s)$, $E_2(s)$ and $E_3(s)$ are the Laplace transforms of $e_1(t) = V_{dcr}(t) - V_{dc}(t)$, $e_2(t) = i_{dr}(t) - i_d(t)$, and $e_3(t) = i_{qr}(t) - i_q(t)$, respectively. Plant $G(s) = \frac{1}{s}$ is the transfer function of the FBL subsystem. The sensitivity and complementary sensitivity functions of the closed-loop system are obtained as follows:

$$\begin{aligned} S_i(s) &= \frac{1}{1 + G(s)K_i(s)} \\ T_i(s) &= \frac{G(s)K_i(s)}{1 + G(s)K_i(s)}. \end{aligned} \tag{3.106}$$

The control objective $Y_i(s)$ and error $E_i(s)$ are related to the command reference $Y_{ir}(s)$ by

$$\begin{aligned} Y_i(s) &= T_i(s)Y_r(s) \\ E_i(s) &= S_i(s)Y_r(s). \end{aligned} \tag{3.107}$$

A nonlinear controller is proposed, where a linear controller is used to stabilize the two-stage distributed PV-BES generator.

3.7 Robust Controller Design for Linearized Two-Stage Distributed PV-BES Generator

This section presents the uncertainty model, noise decoupling capability and robust H_∞ controller for the two-stage distributed PV-BES generator.

3.7.1 Uncertainty modeling

The FBL model with parametric uncertainty of two-stage distributed PV-BES generator can be written from Subsections 3.3.1 and 3.5.1 as follows:

$$\begin{aligned} V_{dc}(s) + N(s) &= \frac{\phi}{s}V_1(s) \\ I_d + N(s) &= \frac{1}{s+\phi_2}[V_2(s)\phi_1 - \phi_3 I_q(s)] \\ I_q + N(s) &= \frac{1}{s+\phi_2}[V_3(s)\phi_1 + \phi_3 I_d(s)]. \end{aligned} \tag{3.108}$$

3.7.2 Noise decoupling capability of designed control scheme

Similarly, the noise decoupling capability of the FBL system of the two-stage distributed PV-BES generator can be computed using the following formula from

Subsections 3.3.2 and 3.5.2:

$$D(x)p_i = g_i(x)c_i(x) - f(x) \tag{3.109}$$

where $c_i(x) = \frac{a_i(x)}{b_i(x)}$. The values of the vector fields $f(x)$, $g_i(x)$ and $c_i(x)$ are substituting into equation (3.109) can be represented as follows:

$$D(x)p_i = \begin{bmatrix} -\frac{V_s}{L_{dc}} & 0 & 0 \\ \frac{i_L}{C_{dc}} & 0 & 0 \\ 0 & \frac{V_{dc}}{2L} & 0 \\ 0 & 0 & \frac{V_{dc}}{2L} \end{bmatrix} \begin{bmatrix} \frac{i_{dc}}{i_L} \\ \frac{2L}{V_{dc}}\left(\frac{R}{L}i_d + \frac{V_d}{L} - \omega i_q\right) \\ \frac{2L}{V_{dc}}\left(\frac{R}{L}i_q + \frac{V_q}{L} + \omega i_d\right) \end{bmatrix} - \begin{bmatrix} \frac{V_s}{L_{dc}} \\ -\frac{i_{dc}}{C_{dc}} \\ \frac{1}{L}\left(-Ri_d - V_d\right) + \omega i_q \\ \frac{1}{L}\left(-Ri_q - V_q\right) - \omega i_d \end{bmatrix}. \tag{3.110}$$

The simplified equation (3.110) become as follows:

$$D(x)p_i = \begin{bmatrix} -\frac{V_{dc}i_{dc}}{L_{dc}i_L} - \frac{V_s}{L_{dc}} \\ 0 \\ 0 \\ 0 \end{bmatrix}. \tag{3.111}$$

The FBL portion of the two-stage distributed PV-BES generator is decoupled from the effect of the measurement noise. The designed FBL controller can reduce the noise from the linearized three states.

3.7.3 Robust H_∞ mixed-sensitivity loop-shaping controller design

The mixed-sensitivity based H_∞ loop-shaping controller for the two-stage distributed PV-BES generator from subsections 3.3.3 and 3.5.3 as follows:

$$\begin{aligned} K_1(s) &= \frac{4.078 \times 10^7 s^2 + 2.039 \times 10^{12} s + 2.054 \times 10^9}{s^3 + 6.872 \times 10^{10} s^2 + 6.617 \times 10^{13} s + 3.266 \times 10^{10}} \\ K_{23}(s) &= \frac{3.359{\times}10^6 s^2 + 5.047{\times}10^9 s + 1.164{\times}10^{10}}{s^3 + 6.431{\times}10^5 s^2 + 2.534{\times}10^9 s + 2.181{\times}10^6}. \end{aligned} \tag{3.112}$$

3.8 Performance Evaluation of Design Controllers

The details transient stability analysis has been investigated for designed controller. This section presents compression between the designed and existing FBL controller performance for three different distributed generators.

3.8.1 Stability analysis of distributed generators

The primary purpose of designing a controller is to provide system stability. It is necessary to analyse the closed-loop operation instead of the implementation of the designed controller. This section presents an analysis of stability enhancement using the proposed H_∞ controller over the existing conventional PI controller for the FBL control scheme of the standalone distributed PV-BES and grid-connected distributed FC generators, which also presents the stability analyses of the two-stage distributed PV-BES generator.

Figures 3.6 and 3.7 are presented the responses of the sensitivity and complementary sensitivity functions in step response, sigma plot and Nyquist plot. These are the well-recognized tools for stability testing of the linear system in the time- and frequency-domain platforms. The step responses of the sensitivity

and complementary sensitivity function are shown in Figures 3.6 and 3.7, where the responses for H_∞ controllers becomes steady-state considerably faster over the responses for PI controllers without transient overshoot. The green-blue and red-purple colours are the closed-loop system response with the designed robust H_∞ controller and the existing conventional PI controller, respectively. Besides, those figures are shown the frequency-domain responses of the sensitivity and complementary sensitivity functions.

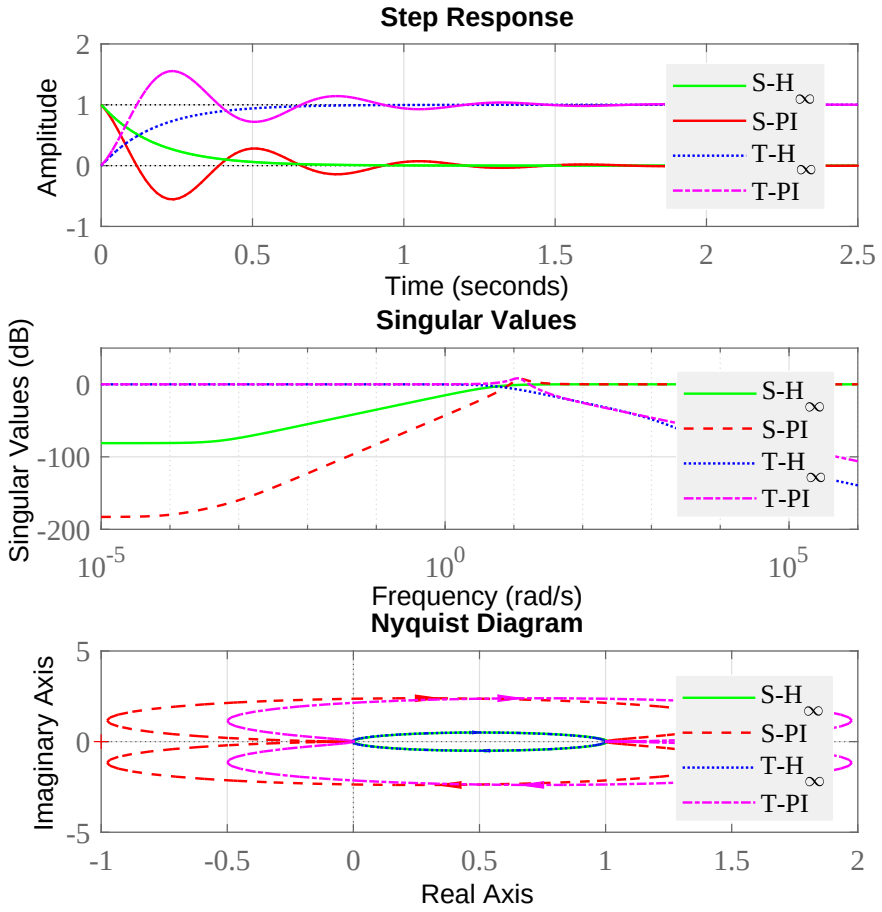

Figure 3.6: Sensitivity functions responses with proposed H_∞ and existing PI controller for standalone distributed PV-BES generator.

Traditional power systems face low-frequency disturbances from the begin-

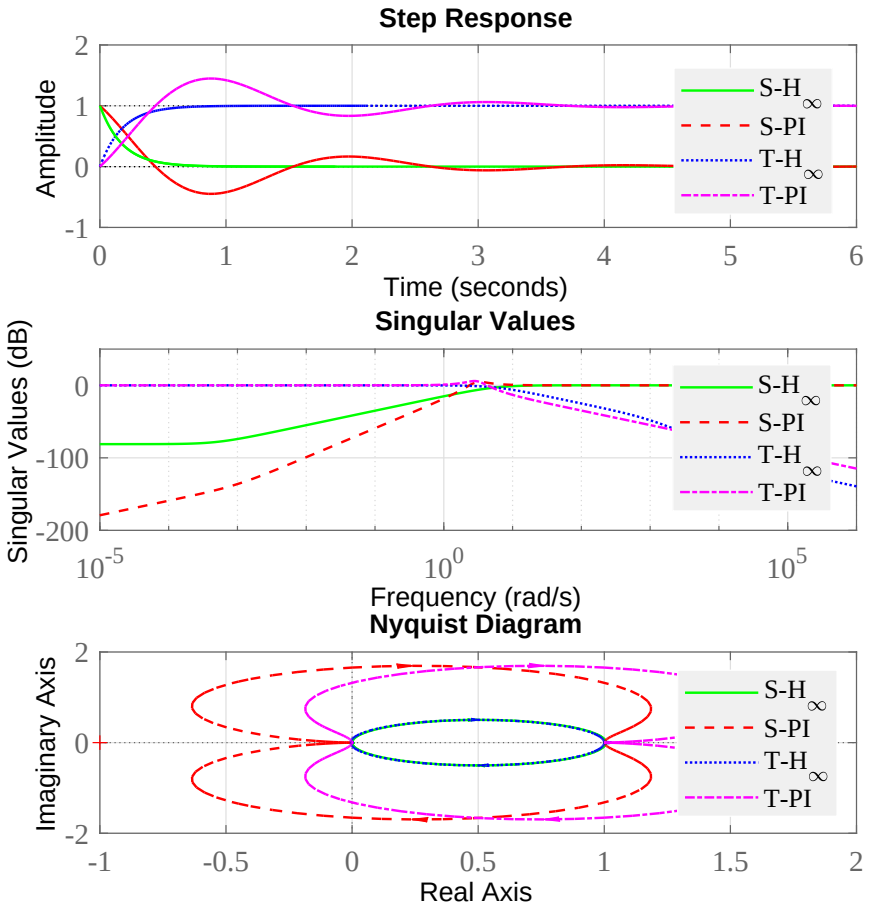

Figure 3.7: Sensitivity functions responses with proposed H_∞ and existing PI controller for grid-connected distributed FC generator.

ning. Similar disturbances can influence the performance of DGs. Such an effect can be measured using the sensitivity function response, which is offered an understanding of the disturbance cancellation ability of the linear controller. The H_∞ norm value of the sensitivity function S(s) is given with the highest amplification ability of the steady-state error from the reference signal. This disturbance can be reduced by a controller whose sensitivity crossover frequency is larger than the disturbances. The sigma plot of the S(s) functions is shown in Figures 3.6 and 3.7 for the designed robust H_∞ controller and the existing

conventional PI controller of the FBL system.

Figures 3.6 and 3.7 are shown the sensitivity function response for existing conventional PI controller in sigma plot, where the crossover frequency is $2.5001\,\mathrm{rad\,s^{-1}}$, and maximum sensitivity is 1.6656 dB. Whether the crossover frequency is $4.4814\,\mathrm{rad\,s^{-1}}$ and maximum sensitivity is 1.0000 dB for the designed robust H_∞ controller. The existing conventional PI controller for the FBL control law can reject disturbances with frequencies less than $2.5001\,\mathrm{rad\,s^{-1}}$. The contrary designed controller can be minimized disturbance with frequencies less than $4.4814\,\mathrm{rad\,s^{-1}}$ with maximum amplification of disturbance at higher frequencies of 1.0000 dB. The designed robust H_∞ controller can be cut disturbances over a greater frequency range than the existing conventional PI controller, which is confirmed improved disturbance rejection capacity.

The complementary sensitivity function T(s) is directly associated to the robust stability margin of the DGs. The inverse H_∞ norm value of the complementary sensitivity function T(s) provides the lowest stability margin. The robust stability margin can be obtained from the sigma plot of T(s), as displayed in Figures 3.6 and 3.7 of the existing conventional PI and designed robust H_∞ controllers. Figures 3.6 and 3.7 show that the H_∞ norm value in dB for existing PI controller is $||\mathrm{T(s)}||_\infty = 1.9224$ and the designed robust H_∞ controller is 0.9994. For the existing controller, the robust stability margin is $||\mathrm{T(s)}||_\infty^{-1} = 0.5202$ and the designed controller is 1.0006. The designed controller operates with bigger variations over the existing controller, thus confirming better robustness with worst-situations, which is well-defined from the Nyquist plot in both figures.

3.8.2 Performance evaluation of standalone distributed PV-BES generator

To implement a nonlinear FBL control scheme for the generalized DC-DC VSC requires the measurement signals of the DC-link voltage and input and output current of the VSC. The implementation block diagram of the designed control technique is shown in Figure 3.8, where the nonlinear controller inputs are the output of the linear controller, and the input and output current of the DC-DC VSC. The difference between the measured and commended output voltages is used to the designed robust H_∞ controller to obtain immeasurable V(s). This immeasurable V(s) is combined with the developed nonlinear FBL control law to obtain the wanted switching input of DC-DC VSCs of the standalone distributed PV-BES generator. The designed controller is based on the local signals of the individual components in the standalone distributed PV-BES generator.

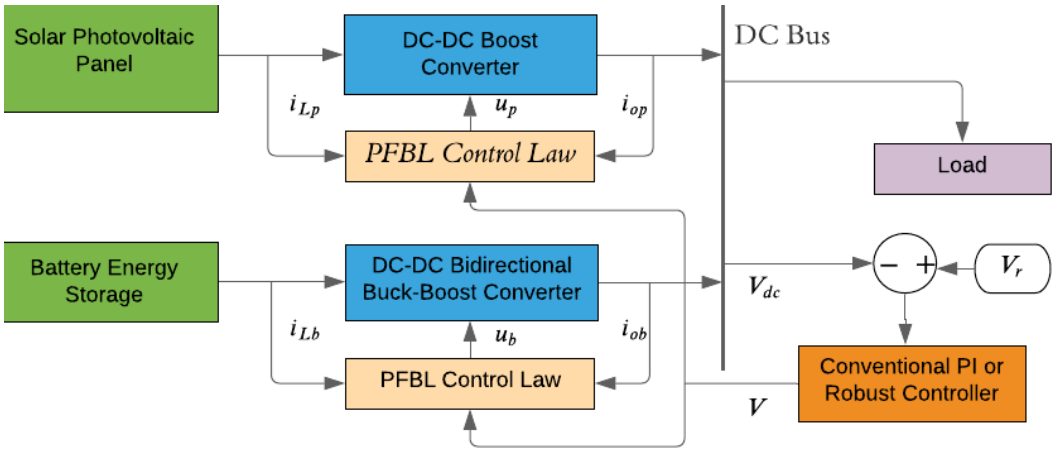

Figure 3.8: Implementation block diagram of proposed controller for standalone distributed PV-BES generator.

The performance of the designed robust H_∞ controller for the FBL control scheme is illustrated using the test standalone distributed PV-BES generator. The test standalone distributed PV-BES generator has a solar PV unit with an

output power of 26 kW and 280 nominal DC voltage. Twelve strings are connected in parallel in the distributed PV generator, and eight cells are connected in series modules per string. The current and voltage at the maximum power point are 35 V and 7.72 A, respectively. A DC-DC boost converter (with L_{dcp} =8 mH) is applied among the output voltage 280 V of the solar PV panel and the desired output DC-link voltage 500 V. The value of the DC-link capacitor is 5 mF. The BES system is linked to the same DC-link capacitor by a DC-DC buck-boost VSC (L_{dcb} =10 mH). It is a nickel-cadmium battery with a operational output voltage of 320 V, the rated capability is 20 A h, the initial state-of-charge is 85%, and the battery response time is 30 s. A fixed resistive load is connected at the DC-link, a power rating of 6.25 kW.

The robustness of the proposed $\text{FBL}_{\text{H}_\infty}$ controller is compared with the existing FBL_{PI} controller. The performance of the designed robust H_∞ controller for the FBL control scheme is illustrated over a significant change in operating points to validate the argument of the operating point independence of the designed robust FBL controller. The stability improvement ability of the designed robust H_∞ controller over the existing conventional PI controller is investigated, and these operating point variations are classified into the following subsections.

Performance evaluation under generation change

A constant resistive load is connected at the DC-link that illustrates the achievement of the designed robust FBL controller under generation variation. At the beginning of such a condition, a distributed PV generator generates a rated power of 26 kW. On the other hand, the resistive load is connected to a DC-link with a rating of 6.25 kW. Therefore, a surplus 19.75 kW generated power from the distributed PV generator entering the battery as storage power during 0 s to

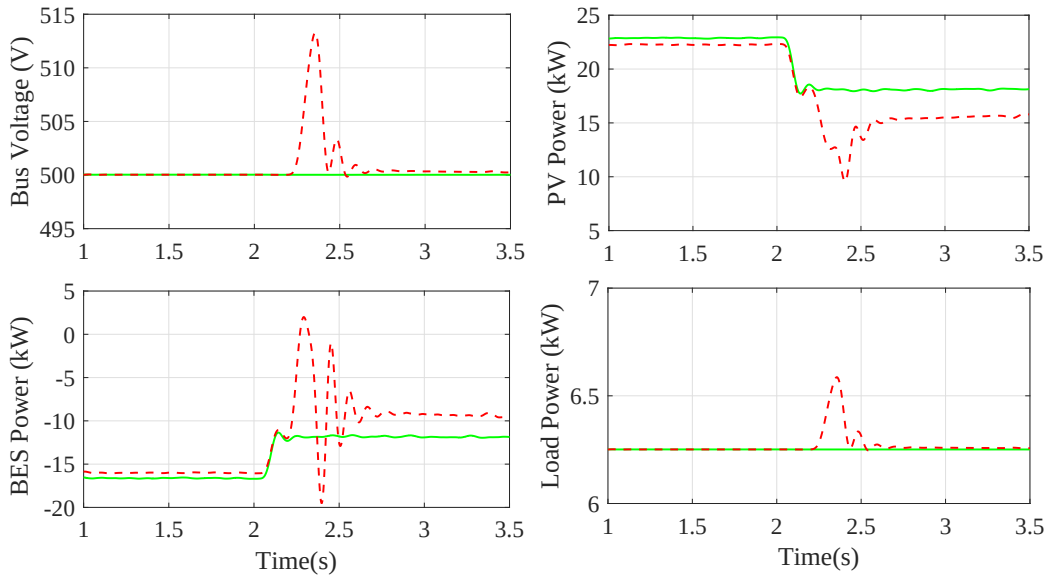

Figure 3.9: Bus voltage and different power responses under generation change (FBL_{H_∞}-solid line and FBL_{PI}-desh line).

2 s. At 2 s, the power production from the distributed PV generator is suddenly reduced to 18 kW from 26 kW owing to the solar irradiation changes. Accordingly, the rate of energy storage in the battery is reduced to 11.75 kW from 19.75 kW.

Figure 3.9 shows that the BES system's storage power has been affected at 2 s owing to the unexpected variation in generation from the distributed PV generator. The transient effect on the BES and the DC-link voltage is comparatively less with the designed FBL_{H_∞} controller over the existing FBL_{PI} controller. The settling time and overshoot of measured responses are larger for the existing controller. The considerable settling time and significant overshoot of any system may be responsible for pausing into instability reasons.

Performance evaluation under load variation

In this case, the study reflected that the distributed PV generator is produced constant power, and the demand power at the DC-link is varied. At the beginning

of such a condition, the distributed PV generator produced a rated power of 26 kW. On the other hand, the demand power is connected to a DC-link with a rating of 6.25 kW. Therefore, a surplus 19.75 kW produced power from the distributed PV generator entering the battery as storage power during 0 s to 2 s. At 2 s, the demand power of the common DC-link rapidly rises from 6.25 kW to 12.5 kW owing to the equal demand connected in the DC-link. Subsequently, the rate of energy storage in the battery is reduced from 19.75 kW to 7.25 kW.

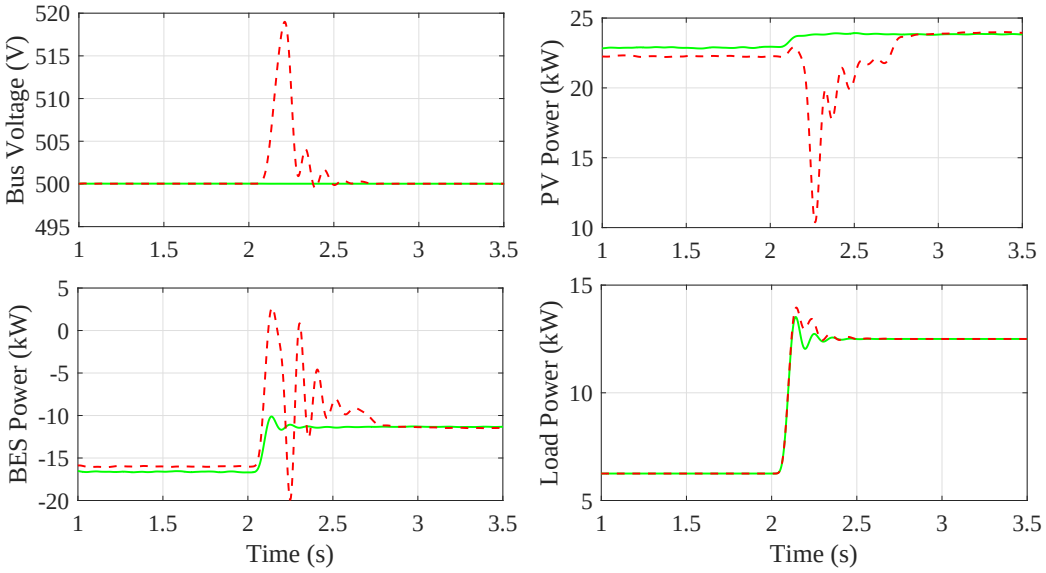

Figure 3.10: Bus voltage and different power responses under load variation (FBL_{H_∞}-solid line and FBL_{PI}-desh line).

Figure 3.10 is shows, the distributed PV generator and BES powers have been affected at 2 s owing to the unexpected demand changes in the DC-link. The transient effect on the BES, distributed PV generator production powers and the DC-link voltage are more affected with the existing FBL_{PI} controller over the designed FBL_{H_∞} controller. The settling time and overshoot of measured responses are larger for the existing FBL_{PI} controller. The more settling time and high overshoot of any system may be responsible for pausing into instability

reason.

Performance evaluation under parameter variation

Parameter uncertainty is a common issue in control system studies, which can occur owing to the mismatch between the actual and mathematical models. In addition, it can occur with respect to an extensive time duration. This case study presents a pictorial view of Subsection 3.3.1. In this case study, the standalone distributed PV-BES generator worked with a nominal parameter from 0 s to 2 s. At 2 s, it is considered that the DC-link capacitor has been changed by 10%.

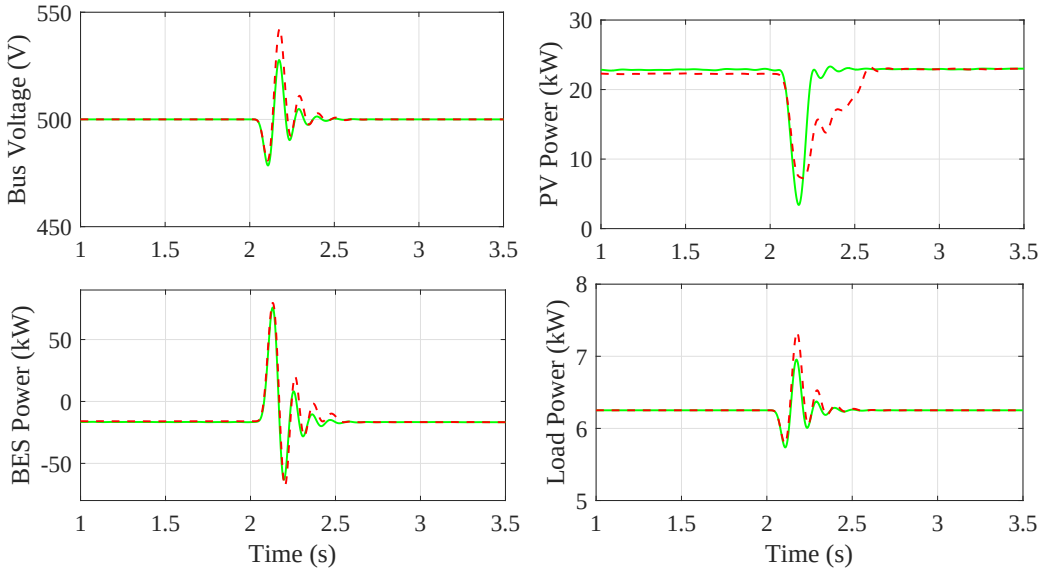

Figure 3.11: Bus voltage and different power responses under parameter variation (FBL_{H_∞}-solid line and FBL_{PI}-desh line).

Therefore, the generated and stored powers from the distributed PV generator and the BES system are heavily affected. In this situation, the designed FBL_{H_∞} controller is provided with a good voltage and power profile than the existing $PFBL_{PI}$ controller, which is cleared from Figure 3.11.

Performance evaluation under measurement noise

The measured information can be corrupted by the measuring noise of implemented controller in the feedback or a closed-loop system. The noisy measurement signals are highly responsible for reducing the performance of any feedback system. The white Gaussian noise has been injected into the output DC-link voltage with 0.01 amplitude to observe the robustness of the designed $\text{FBL}_{\text{H}_\infty}$ controller under measurement noise, white Gaussian noise.

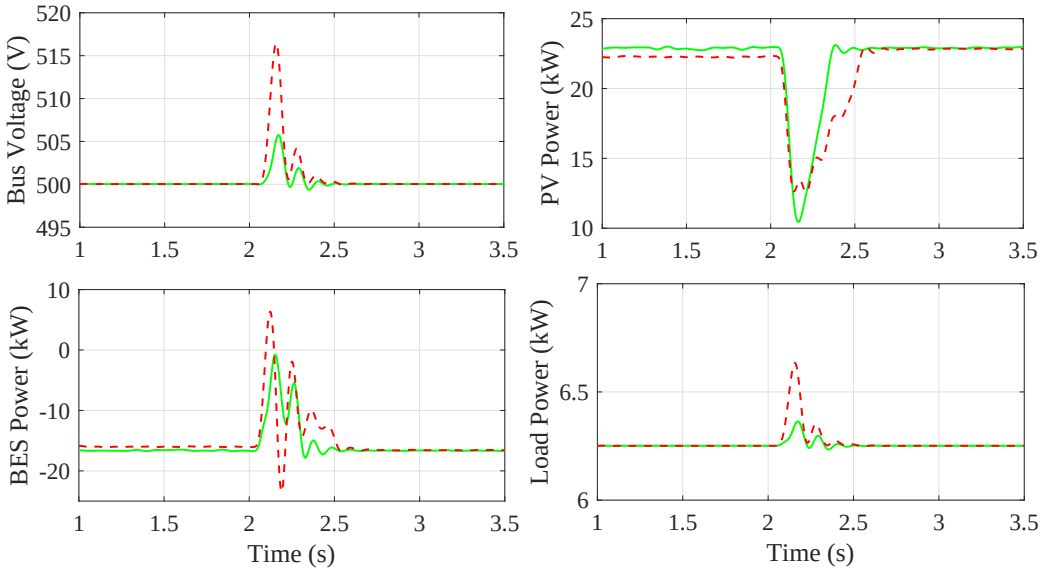

Figure 3.12: Bus voltage and different power responses under measurement noise ($\text{FBL}_{\text{H}_\infty}$-solid line and FBL_{PI}-desh line).

The measured output DC voltage is affected at 2 s by the measurement noise. Therefore, the distributed PV generator's output power and battery storage power are significantly affected, as shown in Figure 3.12, those responses are illustrated. The designed control technique offers quicker steady-state responses and a reduced overshoot than the existing controller.

3.8.3 Performance evaluation of grid-connected distributed FC generator

Based on the design process and implementation block diagram in Figure 3.13, the performance of the proposed controller is investigated by considering different operating scenarios in a real-time simulation platform. The following situations are chosen in this section to demonstrate the designed robust H_∞ controller for the FBL control law of the grid-connected distributed FC generator.

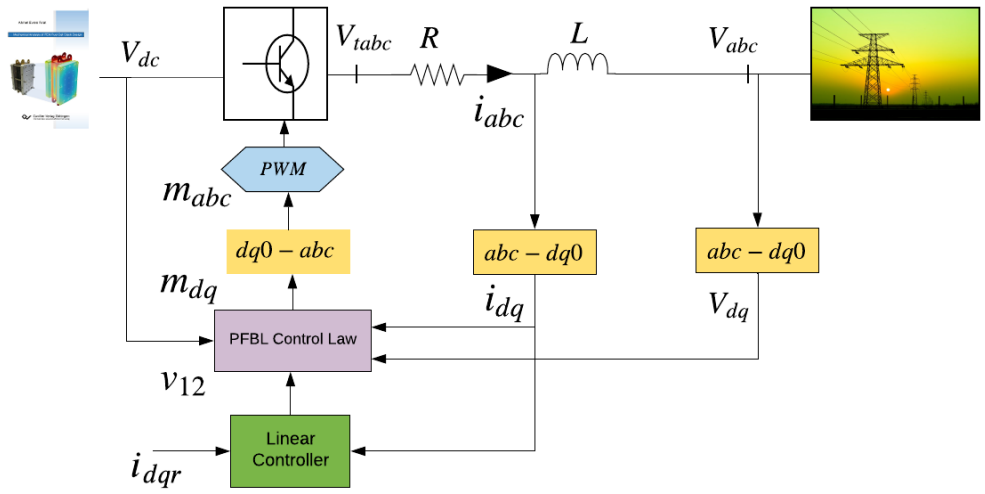

Figure 3.13: Implementation block diagram of the proposed controller for grid-connected distributed FC generator.

Performance evaluation under sudden power factor change

The power factor specified that the operational step changed from its nominal value (0.8) in this case study. The change is considered to be 0.8 to 0.9 at time 5 s.

Figure 3.14 the responses of the dq-axis output currents and powers are affected with power factor changes. The weakness is that an existing FBL_{PI}

controller's performance is reduced to the current and power responses, where the designed $\mathrm{FBL}_{\mathrm{H}_\infty}$ controller offers much better than the existing $\mathrm{FBL}_{\mathrm{PI}}$ controller.

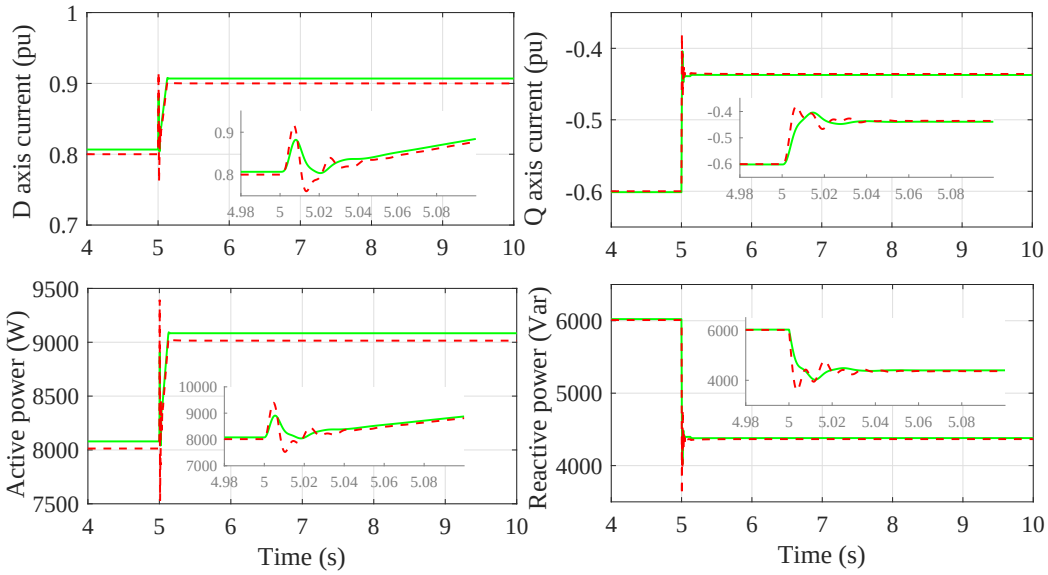

Figure 3.14: In dq frame output current and power under power factor change ($\mathrm{FBL}_{\mathrm{H}_\infty}$-solid line and $\mathrm{FBL}_{\mathrm{PI}}$-desh line).

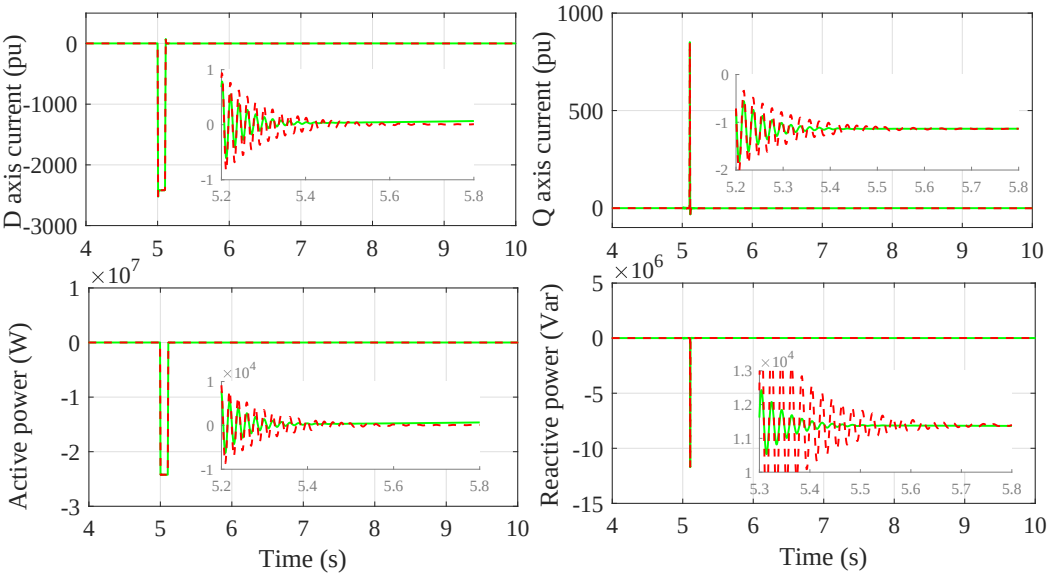

Figure 3.15: In dq frame output current and power under three-phase short-circuit fault ($\mathrm{FBL}_{\mathrm{H}_\infty}$-solid line and $\mathrm{FBL}_{\mathrm{PI}}$-desh line).

Controller performance evaluation under three-phase short-circuit fault

A short-circuit fault is the common disturbance in the power system, and a three-phase short-circuit fault is one of the most severe problems. This type of fault is occurred at $t = 5\,\mathrm{s}$ and the fault is cleared at $t = 5.1\,\mathrm{s}$ at the AC side terminal of the grid-connected distributed FC generator. In a power system, a fault is defined as a serious fault if the time interval between the fault happens and the clearance is greater than $t_f > 0.06\,\mathrm{s}$ for a 50 Hz power system. Under such a serious disturbance, the current response in the dq frame takes more time to reach a steady-state with a higher overshoot which is responsible for the riskiness of the system where the existing $\mathrm{FBL_{PI}}$ controller is presented. Additionally, the grid's active and reactive power injection from the grid-connected distributed FC generator directly depends on the d- and q-axis currents, respectively. Therefore, the response of the active and reactive powers of the grid-connected distributed FC generator requires more settling time with a significant overshoot, which is shown in Figure 3.15.

The proposed $\mathrm{FBL_{H_\infty}}$ controller provides much better performance under the same disturbance corresponding to settling time and overshoot. Figure 3.15 is displayed that the current and power responses with the designed $\mathrm{FBL_{H_\infty}}$ controller (solid line) is more efficient to keep the stability of the system over the existing $\mathrm{FBL_{PI}}$ controller (dash line).

Performance evaluation under change of parameters

Parameter uncertainties are a long-standing concern in studies on control systems. A parametric uncertain model of the considered grid-connected distributed FC generator is presented in Section 3.5.1. In this scenario, parameter changes are indicated as uncertainties. Figure 3.16 demonstrates measured outputs responses

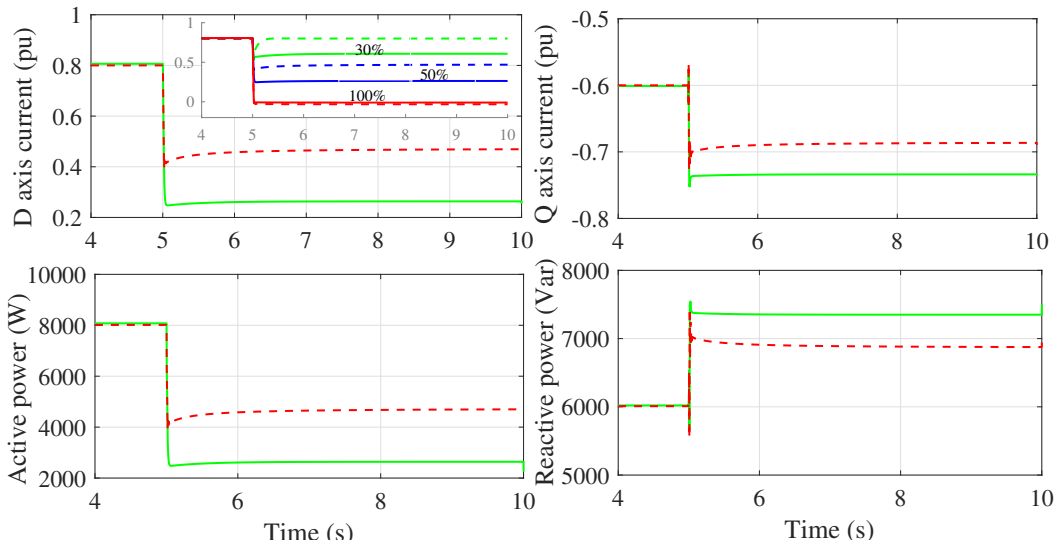

Figure 3.16: In dq frame output current and power under parameter variation (FBL_{H_∞}-solid line and FBL_{PI}-desh line).

for the 30 % changes in the passive filtering elements R and L. These changes show that the system varies slightly from its nominal point.

The existing FBL_{PI} controller cannot properly control the unexpected transient of the system, where the parameters vary with time. The existing controller cannot sense the parameter deviation properly. The designed FBL_{H_∞} controller provides better performance than the existing controller under the parameter changes to stabilize the nonlinear FBL control scheme. Figure 3.16 illustrates the performance comparison between the existing FBL_{PI} and designed FBL_{H_∞} controllers with different parameter value for the grid-connected distributed FC generator (d-axis current). Figure 3.16 represents that the existing conventional PI controller cannot accurately follow the parameter change, where the current drop for 30 % and 50 % is higher for the designed robust H_∞ controller it has become vice versa for 100 % parameter change.

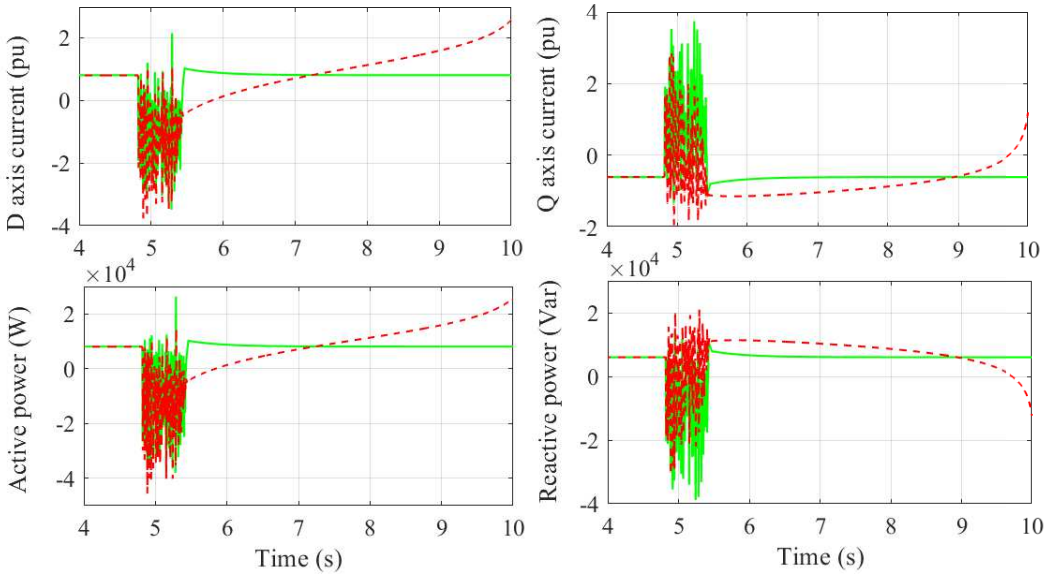

Figure 3.17: In dq frame output current and power under measurement noise (FBL_{H_∞}-solid line and FBL_{PI}-desh line).

Performance evaluation under measurement noise

Measurement noise is a familiar problem in feedback systems. The designed nonlinear FBL controller is a closed-loop control technique, in which different measured outputs are combined with the control scheme. A high-frequency signal can affect these measured outputs, which is typically considered white Gaussian noise. The measurement noises are considered with the output functions i_d and i_q (output currents), where the considered noise is white Gaussian noise with variances of 0.01.

Figure 3.17 shows active and reactive powers responses with measurement noise with d- and q-axis currents. The existing FBL_{PI} controller took more time and offered a large overshoot to settle down on steady-state after affecting the output currents. On the other hand, the designed FBL_{H_∞} controller is provided better performance with respect to settling time and overshoot. The settling time for the measured outputs is too large with the existing FBL_{PI} controller.

3.8.4 Performance evaluation of two-stage PV-BES generator

This section investigates the performance of the designed controller through electromagnetic transient simulations in MATLAB/Simulink. Different case studies are considered by considering the effect of generation change, power factor change and measurement noise on the performance of the designed robust FBL controller ($\mathrm{FBL}_{\mathrm{H}_\infty}$), and compared with the existing FBL controller that uses a PI controller for the linear control input ($\mathrm{PFBL}_{\mathrm{PI}}$).

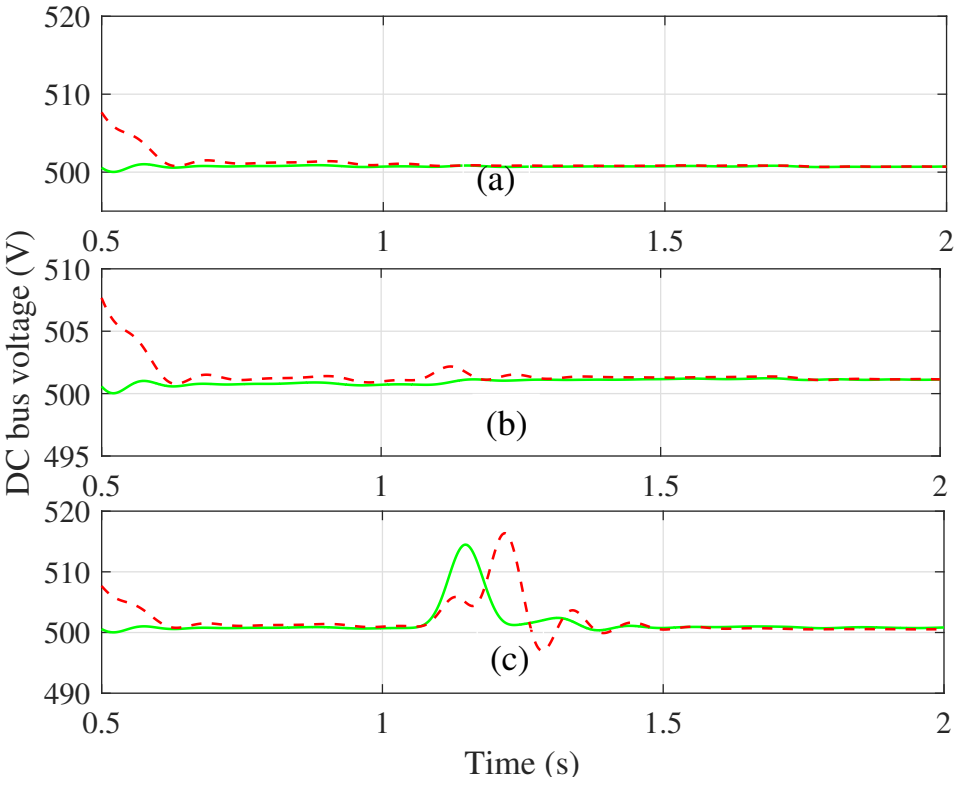

Figure 3.18: DC-bus voltage under (a) generation change, (b) power factor change and (c) measurement noise ($\mathrm{FBL}_{\mathrm{H}_\infty}$-solid line and $\mathrm{FBL}_{\mathrm{PI}}$-desh line).

Performance evaluation corresponding to DC-bus voltage

The distributed PV generator works as the primary source, which varies on the environmental conditions. If the output power from the distributed PV generator is more than sufficient to meet the load power, the extra energy is stored in the BES. However, if the distributed PV generator fails to meet the demand, the battery will supply power to the load. In addition, three different case studies are investigated in Subsection 3.8.2. Figure 3.18 demonstrates the DC-link voltage under a change in distributed PV generator, change in power factor and measurement noise, where the distributed PV generator is directly, and other scenarios are indirectly related to the DC-link voltage control scheme. The illustrated results show that changes in the DC or AC sides can affect the DC-link voltage. The proposed controller provides better performance than the existing controller to regulate the DC-link voltage.

Performance investigation corresponding to AC output current

The AC output power of the two-stage PV-BES is injected into the grid through a DC-AC VSC. The output powers are proportional to the d- and q-axis currents, as discussed in Section 3.6. Different scenarios are investigated to illustrate the FBL control scheme with the designed robust H_∞ and the existing conventional PI controllers. Figure 3.19 shows the designed(FBL_{H_∞}) controller is more effective than the existing (FBL_{PI}) controller. The control objective of the DC-AC converter is significantly affected by changes in the AC side. At time 1 s, the generation and power factors are changed, and the measurement noise also influences the measured values of the output functions. The proposed control scheme is much faster than the existing controller because it becomes a steady-state after considering issues.

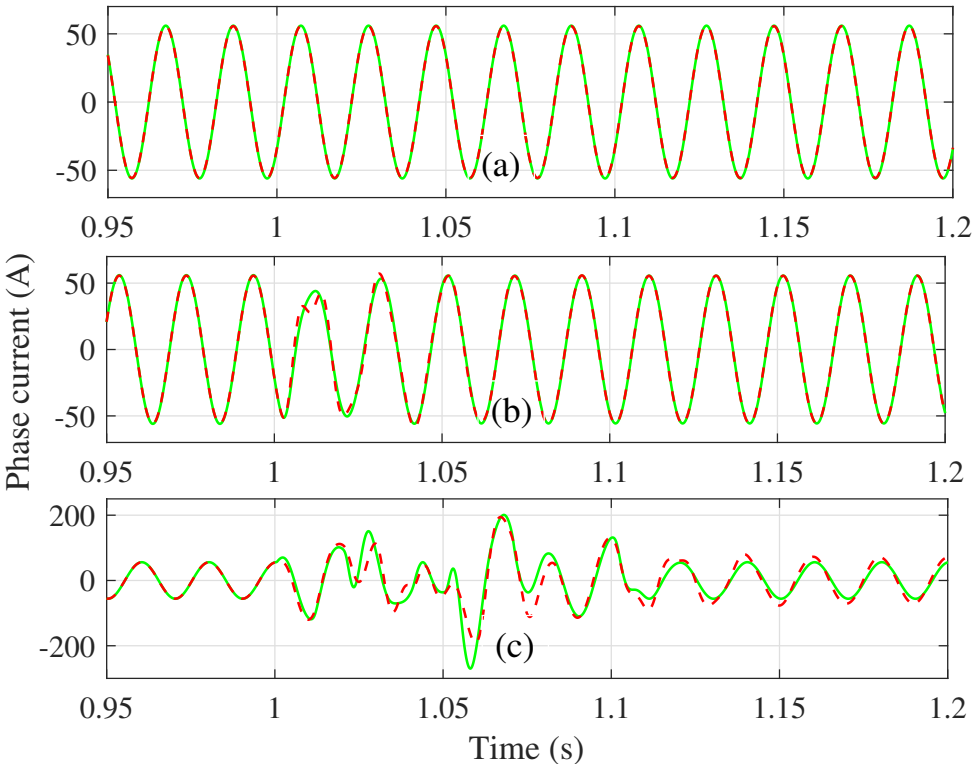

Figure 3.19: AC output current under (a) generation change, (b) power factor change and (c) measurement noise ($\mathrm{FBL}_{\mathrm{H}_\infty}$-solid line and $\mathrm{FBL}_{\mathrm{PI}}$-desh line).

3.9 Chapter Summary

This chapter presents a nonlinear partial FBL control technique with a robust H_∞ controller as an alternative for the existing PI controller with the same control technique. A parametric uncertainty model is established for the FBL control scheme of DGs. The designed robust H_∞ controller has been able to provide more disturbance rejection capability and stability margin, which are investigated by well-established controller performance analysis tools. In addition, the performance of the designed $\mathrm{FBL}_{\mathrm{H}_\infty}$ is demonstrated under different familiar worst cases, where the controller works much better than the compared $\mathrm{FBL}_{\mathrm{PI}}$ controller.

Chapter 4

Nonlinear Controller Design for Islanded Microgrids

The work presented in this chapter has been published in the following articles:

- **Mahmud, M. R.**, and Pota, H.. " Nonlinear controller design to enhance voltage restoration and current sharing accuracy of islanded dc microgrids," *IEEE Systems Journal*, 2021 (Accepted).
- **Mahmud, M. R.**, and Pota, H.. " Nonlinear feedback linearized controller design for islanded ac microgrids," *IEEE Transactions on Power Systems*, 2021 (Under revision).
- **Mahmud, M. R.**, and Pota, H.. " Transient stability analysis of partial feedback linearized islanded hybrid dc/ac microgrids," *IEEE Transactions on Smart Grid*, 2021 (Submitted).

- **Mahmud, M. R.**, and Pota, H.. " Robust feedback linearizing controller design for dc microgrid connected dc-dc converter," in *Proceedings of IEEE Texas Power and Energy Conference (TPEC)*, Texas, USA, 2021.
- **Mahmud, M. R.**, Hossain, M. A., and Pota, H.. " Nonlinear output feedback droop control for parallel inverters in standalone microgrids," in *Proceedings of 9th International Conference on Power and Energy Systems (ICPES)*, Perth, Australia, 2019.
- **Mahmud, M. R.**, and Pota, H.. " Nonlinear partial feedback linearized controller design for islanded ac microgrid connected distributed generations," in *Proceedings of 21st International Conference on Environment and Electrical Engineering (EEEIC 2021)* , Bari, Italy, 2019.

Abstract

This chapter develops feedback linearized control scheme for the single-input two-output control problem of islanded microgrids. This control design approach aims to reduce the voltage deviation and improve current-sharing accuracy in the islanded microgrid; thus, the output voltages and currents are considered to control objectives. However, there is only one switching control input for each pair between the output current and voltage. Subsequently, the main concern is to control two objectives using a single control input of each converter; therefore, this issue is considered a single-input two-output control problem.

4.1 Introduction

Currently, DGs are receiving increasing attention owing to their high penetration into the existing electrical network to meet the rapidly increasing electricity

demand [121]. The concept of a microgrid is a popular solution for integrating different types of DGs. Usually, microgrids are small-size power systems, where DGs, energy storage devices and community loads are connected. It can work in grid-connected or islanded modes. The grid-connected microgrid is not economically serviceable in terms of supplying electric power to a remote area. Often, this can be overcome by installing an islanded microgrid, where the DGs are interconnected for power-sharing [122, 123].

Based on their common bus voltage, the islanded microgrids can be DC, AC, or hybrid DC/AC. The DC type microgrid is becoming more attractive as DGs primarily generate DC power [124]. Solar photovoltaics, fuel cells, wind turbines, and battery energy storage units are the traditional elements in microgrids that generate and store DC power, except for wind turbines. Even with a wind turbine, permanent magnet synchronous generators have their output power converted to DC, as they do not produce electricity at 50 Hz or a constant frequency, as it depends on the wind speed. To achieve the feeding quality level of DG generated power for loads, VSCs are essential interfaces between generators and loads [125, 126], due to DC-DC, DC-AC or AC-DC voltage conversion. The DC-DC and DC-AC VSCs are taken in a central place, and as a result, the microgrids are receiving more attention [126, 127].

Different forms of droop-control approaches have been described in the literature. In [128], an adaptive droop-control has been proposed based on three different operation modes, where an energy storage unit plays a significant role. The operation of this droop controller varies on the storage power level of the energy storage system in islanded microgrids. However, without an energy storage system, such a control scheme cannot operate. An adaptive droop controller is proposed in [129, 130] to reduce voltage deviation, improve current-sharing

accuracy, and maintain a steady circulating current. On the other hand, a droop controller has been developed to reduce the generation cost in the microgrids and enhance the accuracy of the load current-sharing [131, 132]. A variable droop gain is presented in [133] to improve the load current by sharing better. A similar technique is reported in [134], which is primarily dependent on the energy storage system. Additionally, a control scheme has been proposed to improve the output current and voltage responses using the virtual capacitance concept in [135]. However, the main drawback of droop-control approaches is the inverse relationship between the voltage deviation and droop gain.

The droop-control scheme is a conventional procedure to achieve power-sharing accuracy in an interconnected electrical network, applied in an islanded microgrid to enhance the current-sharing accuracy. However, it is responsible for producing a voltage deviation in the microgrids. A centralized secondary controller is proposed in [126], which can minimize the voltage deviation in the microgrid to overcome such a conflicting situation. Still, there has been a performance-related problem owing to the current-sharing accuracy. A controller is proposed based on the average output current of the DGs in the microgrid [127], and this control scheme provides good voltage restoration performance unless current-sharing accuracy is achieved. The leading cause of this controller is low current-sharing accuracy; the average output current of the VSCs is considered the control objective rather than the individual output current of the VSCs in the islanded microgrid.

One of the underlying drawbacks of linear controller design approaches for nonlinear systems is the operating point dependency. The operating point independent performance can be obtained using a nonlinear controller for the microgrids. The commonly used nonlinear controllers are the sliding mode control

scheme, backstepping controller, and FBL controller [136]. A sliding mode control approach is proposed to regulate the bus voltage, where bidirectional power flow is considered [137]. Such a controller can provide robust performance under parameter variations and external disturbances. However, selecting a changeable sliding surface is difficult, and the effect of unpredictable renewable power generation is neglected. A nonlinear backstepping and FBL controller has been proposed [138, 139] for power-sharing to bus connected loads, and further improvement of the controller is achieved by applying an adaptive control technique [140]. It is difficult to control the circulating current in the islanded microgrids without including the transmission line dynamics in the control design [130, 141].

The FBL control scheme is a well-established approach in the field of electric power systems to improve the transient stability of the system, which is used in different sites of the power system, for example, excitation control of synchronous generators [142, 143, 144] and grid-connected VSC systems [145, 146, 147]. In [148], a decentralized robust nonlinear controller is proposed for a partially FBL model of an islanded microgrid, where the central control objective is the bus voltage. A secondary distributed cooperative control scheme is developed in [149] based on an FBL model to improve the system reliability.

The output feedback linearized controllers are designed in [145, 146, 147] for grid-connected DGs to control single-input single-output control problems. However, the primary control problem in islanded microgrids is a single-input two-output control problem. This chapter describes developing a nonlinear single-input two-output feedback linearized control scheme to design a primary controller for the islanded microgrids. The proposed control scheme improves the power-sharing capability and reduces voltage deviation. Overall, this control approach provides independent operating points of the islanded microgrids. The

performance of the designed feedback linearized control approach for the single-input two-output control problem is illustrated under the worst-case scenarios.

Table 4.1: Summary of controller design methods for islanded microgrids.

Control method	Strengths	Weaknesses
Droop control	Adaptive droop controller [129, 130] - Reduce voltage deviation - Improve current-sharing accuracy - Maintain a steady circulating current	- Inverse relationship between the voltage deviation and droop gain
Existing SISO-FBL control	Feedback linearized controller [138, 139] - Improve power-sharing - Reduce voltage deviation	- Line dynamics is not considered - Bus voltage is considered control objective
Proposed SITO-FBL control	- Improve power-sharing - Reduce voltage deviation - Individual output voltage and current both are considered control objective	- Developed control law complex over the existing SISO-FBL control

The contributions of this chapter are as follows:

- Develop feedback linearization model for single-input two-output control problem of the islanded DC microgrid (Section 4.2).
- Develop feedback linearization model for single-input two-output control problem of the islanded AC microgrid (Section 4.3).
- Develop feedback linearization model for single-input two-output control problem of the islanded hybrid DC/AC microgrid (Section 4.4).
- Develop conventional PI and PD controllers for the generalized linear part of the feedback linearized control laws (Section 4.5).
- Performances are investigated of the designed nonlinear single-input two-output feedback linearized controllers corresponding to the three different systems (Section 4.6).

4.2 Feedback Linearization of Islanded DC Microgrid

The characteristic model of the islanded DC microgrid is developed in Subsection 2.3.1 from Figure 4.1 to design an FBL controller in which the dynamic model is rewritten as follows:

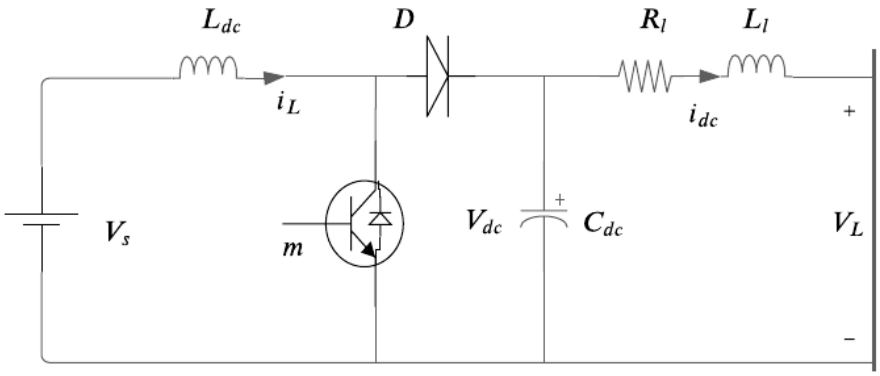

Figure 4.1: Circuit diagram of DC microgrid connected DC-DC boost converter.

$$\begin{aligned} \frac{di_L}{dt} &= \frac{1}{L_{dc}}\left(V_s - mV_{dc}\right) \\ \frac{dV_{dc}}{dt} &= \frac{1}{C_{dc}}\left(mi_L - i_{dc}\right) \\ \frac{di_{dc}}{dt} &= \frac{1}{L_l}\left(V_{dc} - R_l i_{dc} - V_L\right). \end{aligned} \tag{4.1}$$

The nonlinear dynamic system (4.1) can be written as follows state-space form:

$$\begin{aligned} \frac{dx}{dt} &= f(x) + g(x)u \\ y &= h(x) \end{aligned} \tag{4.2}$$

where $x = \begin{bmatrix} i_L \\ V_{dc} \\ i_{dc} \end{bmatrix}$, $f(x) = \begin{bmatrix} \frac{1}{L_{dc}} V_s \\ -\frac{1}{C_{dc}} i_{dc} \\ \frac{1}{L_l}\left(V_{dc} - R_l i_{dc} - V_L\right) \end{bmatrix}$, $g(x) = \begin{bmatrix} -\frac{1}{L_s} V_{dc} \\ \frac{1}{C_{dc}} i_L \\ 0 \end{bmatrix}$, $u = m$ and $y = \begin{bmatrix} h_1 \\ h_2 \end{bmatrix} = \begin{bmatrix} V_{dc} \\ i_{dc} \end{bmatrix}$.

There are two control objectives V_{dc} and i_{dc} with one control input, the switching rate (or whatever is the name given to $u = m$). Such a system can be defined as a SITO control problem. There are two control outputs, that is, tracking the output voltage V_{dc} and current i_{dc}, which can be tracked by control law.

4.2.1 Lie derivative and relative degree

The Lie derivative of the vector field $f(x)$ with respect to the output function $h_1(x) = V_{dc}$ is obtained as follows:

$$L_f h_1(x) = \frac{\partial V_{dc}}{\partial x} f(x) = -\frac{1}{C_{dc}} i_{dc} \tag{4.3}$$

The Lie derivative of the vector field $g(x)$ for the output function $L_f^{1-1} h_1(x) = V_{dc}$ is obtained as follows:

$$L_g L_f^{1-1} h_1(x) = \frac{\partial V_{dc}}{\partial x} g(x) = \frac{1}{C_{dc}} i_L \neq 0 \tag{4.4}$$

where the relative degree is 1 for control objective V_{dc}.

The Lie derivative of the vector field $f(x)$ for the output function $h_2(x) = i_{dc}$

is obtained as follows:

$$L_f h_2(x) = \frac{\partial i_{dc}}{\partial x} f(x) = \frac{1}{L_l}(V_{dc} - R_l i_{dc} - V_L). \tag{4.5}$$

We need to calculate $L_g L_f^{1-1} h_2(x)$ for the vector field $g(x)$ as follows:

$$L_g L_f^{1-1} h_2(x) = \frac{\partial i_{dc}}{\partial x} g(x) = 0 \tag{4.6}$$

As $L_g L_f^{1-1} h_2(x) = 0$, $L_f^2 h_2(x)$ must be calculated as follows:

$$L_f^2 h_2(x) = \frac{\partial (L_f h_2(x))}{\partial x} f = \frac{1}{L_l} f_2 - \frac{R_l}{L_l} f_3. \tag{4.7}$$

For the function $L_f h_2(x)$, the Lie derivative $L_g L_f^{2-1} h_2(x)$ is obtained as follows:

$$L_g L_f^{2-1} h_2(x) = \frac{\partial (L_f h_2(x))}{\partial x} g(x) = \frac{1}{L_l C_{dc}} i_L \neq 0 \tag{4.8}$$

where the relative degree is 2 for the control objective i_{dc}.

The relative degrees are 1 and 2 for control objectives V_{dc} and i_{dc}, respectively. Both are less than the order of the microgrid. Therefore, the islanded DC microgrid is only partially linearized.

4.2.2 Nonlinear coordinate transformation

In the SITO control problem, the maximum relative degree for any control objective is the relative degree of the linearized system. As a result, the relative degree of the islanded DC microgrid is two. Two new coordinate transformations are achieved from the coordinate transformation corresponding to the control

objectives V_{dc} and i_{dc}, which are expressed as follows:

$$\begin{aligned} z_v &= L_f^{1-1} h_1(x) = V_{dc} \\ z_i &= L_f^{1-1} h_2(x) = i_{dc}. \end{aligned} \tag{4.9}$$

Using the coordinate transformation as represented by equations (4.9), the FBL system can be obtained as follows:

$$\begin{aligned} \frac{dz_v}{dt} &= v_v \\ \frac{d^2 z_i}{dt^2} &= v_i \end{aligned} \tag{4.10}$$

where v_v and v_i are immeasurable variables, which can be obtained by linear control approach, as shown in Section 4.5.

4.2.3 Stability of internal dynamics

The earlier step shows that the r number of equations is converted into linear subsystems. Estimating the remaining $n - r$ number of equations through an appropriate transformation to ensure stability. At this point, must be chosen in such a way that it satisfies:

$$\lim_{t \to \infty} h(x) \longrightarrow 0 \tag{4.11}$$

which means that $z_v = z_i = 0$ at steady-state for the islanded microgrid. The remaining state z_3 satisfies the following conditions:

$$L_g z_3(x) = 0. \tag{4.12}$$

Equation (4.12) will be satisfied if

$$z_3 = \frac{1}{2}L_{dc}^2 + \frac{1}{2}CV_{dc}^2 + \frac{1}{2}L_l i_{dc}^2. \tag{4.13}$$

The dynamics of (4.13) can be simplified as follows:

$$L_f z_3 = V_s i_L - R_l i_{dc} - V_{dc} i_{dc} = P_i - P_l - P_o \tag{4.14}$$

where $P_i = V_s i_L$, $P_o = V_{dc} i_{dc}$ and $P_l = R_l i_{dc}$ are the input, output, and transmission line loss powers of the DC microgrid connected VSCs, respectively. Therefore, equation (4.14) is shortened as follows:

$$L_f z_3 = 0. \tag{4.15}$$

Subsequently, the islanded DC microgrid-connected VSC can be controlled using a partial FBL control scheme formulated in the following subsection.

4.2.4 Feedback linearized control law

The control laws corresponding to V_{dc} and i_{dc} are as follows:

$$\begin{aligned} u_v &= \frac{v_v - L_f h_1(x)}{L_g h_1(x)} \\ u_i &= \frac{v_i - L_f^2 h_2(x)}{L_g L_f h_2(x)}. \end{aligned} \tag{4.16}$$

Every DC-DC converter in the DC microgrid is controlled by a SITO control law. The control law for the output voltage (V_{dc}) of the DC-DC boost VSC is as

follows:

$$m_v = \frac{C_{dc}v_v + i_{dc}}{i_L}. \tag{4.17}$$

Correspondingly, the control law for the injected current (i_{dc}) into the DC-bus from the DC-DC boost VSC is as follows:

$$m_i = \frac{C_{dc}(v_i L_l - f_2 + R_l f_3)}{i_L} \tag{4.18}$$

where v_v and v_i are linear controllers. The control laws m_v and m_i should be able to adjust the DC-bus voltage and let $m_v = m_i = m$. After summing equations (4.17) and (4.17), the final control law is obtained as follows from Section 2.6:

$$m = \alpha_1 \frac{C_{dc}v_v + i_{dc}}{2i_L} + \alpha_2 \frac{C_{dc}(v_i L_l - f_2 + R_l f_3)}{2i_L}. \tag{4.19}$$

All the components of (4.19) are measurable or can be obtained in functions of the measured signals. The linear control inputs v_v and v_i must be obtained by a linear controller for the FBL law.

4.3 Feedback Linearization of Islanded AC Microgrid

This section presents the FBL control scheme for an islanded AC microgrid. The output currents and voltages are considered as the control objectives, and the switching inputs are the control inputs for each VSC. As a result, the N-inputs and 2N-outputs associated AC microgrid control issue is a single-input two-output control problem. The mathematical model of the islanded AC microgrid is

developed in Subsection 2.3.2 from Figure 4.2 to design an FBL controller, in which the dynamic model is rewritten as follows:

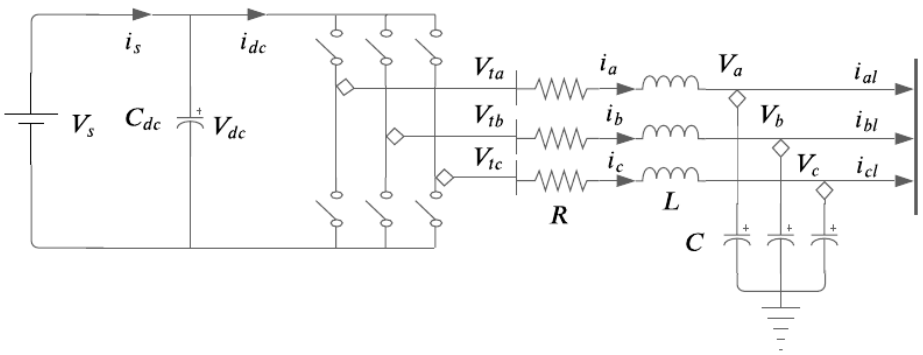

Figure 4.2: Circuit diagram of AC microgrid connected DC-AC converter.

$$\begin{aligned}
\frac{dV_{dc}}{dt} &= \frac{1}{C_{dc}}\left(i_s - i_d m_d - i_q m_q\right) \\
\frac{di_d}{dt} &= \frac{1}{L}\left(\frac{V_{dc}}{2}m_d - Ri_d - V_d\right) + \omega i_q \\
\frac{di_q}{dt} &= \frac{1}{L}\left(\frac{V_{dc}}{2}m_q - Ri_q - V_q\right) - \omega i_d \\
\frac{dV_d}{dt} &= \frac{1}{C}(i_d - i_{dl}) + \omega V_q \\
\frac{dV_q}{dt} &= \frac{1}{C}\left(i_q - i_{ql}\right) - \omega V_d.
\end{aligned} \tag{4.20}$$

It is important to present the nonlinear dynamic in the general form to design the feedback linearized controller of a MIMO system as follows:

$$\begin{aligned}
\dot{x} &= f(x) + \sum_{i=1}^{N} g_i(x)u_i \\
y &= h_i(x)
\end{aligned} \tag{4.21}$$

where

$$f(x) = \begin{bmatrix} \frac{1}{C_{dc}} i_s \\ \frac{1}{L}\left(-Ri_d - V_d\right) + \omega i_q \\ \frac{1}{L}\left(-Ri_q - V_q\right) - \omega i_d \\ \frac{1}{C}(i_d - i_{dl}) + \omega V_q \\ \frac{1}{C}\left(i_q - i_{ql}\right) - \omega V_d \end{bmatrix},$$

$$g_i(x) = \begin{bmatrix} -\frac{1}{C_{dc}} i_d & -\frac{1}{C_{dc}} i_q \\ \frac{V_{dc}}{2L} & 0 \\ 0 & \frac{V_{dc}}{2L} \\ 0 & 0 \\ 0 & 0 \end{bmatrix}, \quad x = \begin{bmatrix} V_{dc} \\ i_d \\ i_q \\ V_d \\ V_q \end{bmatrix},$$

$$u_i = \begin{bmatrix} u_1 \\ u_2 \end{bmatrix} = \begin{bmatrix} m_d \\ m_q \end{bmatrix} \quad \& \quad y = \begin{bmatrix} h_1(x) \\ h_2(x) \\ h_3(x) \\ h_4(x) \end{bmatrix} = \begin{bmatrix} i_d \\ i_q \\ V_d \\ V_q \end{bmatrix}.$$

4.3.1 Lie derivative and relative degree

The Lie derivative of the vector field $f(x)$ for the output function $h_1(x) = i_d$ is obtained as follows:

$$L_f h_1(x) = \frac{\partial i_d}{\partial x} f(x) = \frac{1}{L}\left(-Ri_d - V_d\right) + \omega i_q. \tag{4.22}$$

The Lie derivative of the vector field $g_1(x)$ for the output function $L_f^{1-1}h_1(x) = i_d$ is obtained as follows:

$$L_{g_1} L_f^{1-1} h_1(x) = \frac{\partial i_d}{\partial x} g_1(x) = \frac{V_{dc}}{2L} \neq 0 \tag{4.23}$$

where the relative degree is 1 for control objective i_d.

Similarly, the Lie derivatives of the vector fields $f(x)$ and $g_2(x)$ corresponding to $h_2(x) = i_q$ and $L_f^{1-1}h_2(x) = i_q$ are as follows:

$$\begin{aligned} L_f h_2(x) &= \frac{\partial i_q}{\partial x} f(x) = \frac{1}{L}\left(-Ri_q - V_q\right) - \omega i_d \\ L_{g_2} L_f^{1-1} h_2(x) &= \frac{\partial i_q}{\partial x} g_2(x) = \frac{V_{dc}}{2L} \neq 0 \end{aligned} \tag{4.24}$$

where also the relative degree is 1 for control objective i_q.

Moreover, the Lie derivative of the vector field $f(x)$ with respect to the output function $h_3(x) = V_d$ is obtained as follows:

$$L_f h_3(x) = \frac{\partial V_d}{\partial x} f(x) = \frac{1}{C}(i_d - i_{dl}) + \omega V_q. \tag{4.25}$$

The calculation of $L_{g_1} L_f^{1-1} h_2(x)$ for the vector field $g_1(x)$ is as follows:

$$L_{g_1} L_f^{1-1} h_3(x) = \frac{\partial V_d}{\partial x} g_1(x) = 0. \tag{4.26}$$

As $L_{g_1}L_f^{1-1}h_3(x) = 0$, it is required to determine $L_f^2h(x)$, which is obtained as follows:

$$L_f^2h_3(x) = \frac{\partial(L_fh_3(x))}{\partial x}f(x) = \frac{1}{C}f_1 + \omega f_4 - \frac{1}{C}f_5. \tag{4.27}$$

For the function $L_fh_3(x)$, the Lie derivative $L_gL_f^{2-1}h_3(x)$ is obtained as follows:

$$L_{g_1}L_f^{2-1}h_3(x) = \frac{\partial(L_fh_3(x))}{\partial x}g_1(x) = \frac{V_{dc}}{2LC} \neq 0 \tag{4.28}$$

where the relative degree is 2 for control objective V_d.

Similarly, the Lie derivatives of the vector field $f(x)$ and $g_2(x)$ corresponding to $h_4(x) = V_q$ are as follows:

$$\begin{aligned} L_fh_4(x) &= \frac{\partial V_d}{\partial x}f(x) = \frac{1}{C}\left(i_q - i_{ql}\right) - \omega V_d \\ L_{g_2}L_f^{1-1}h_4(x) &= \frac{\partial V_d}{\partial x}g_2(x) = 0 \\ L_f^2h_4(x) &= \frac{\partial(L_fh_4(x))}{\partial x}f(x) = \frac{1}{C}f_2 - \omega f_3 - \frac{1}{C_f}f_6 \\ L_{g_2}L_f^{2-1}h_4(x) &= \frac{\partial(L_fh_4(x))}{\partial x}g_2(x) = \frac{V_{dc}}{2LC} \end{aligned} \tag{4.29}$$

where the relative degree is 2 for the control objective V_q. The total relative degree of the islanded AC microgrid corresponding to V_d and V_q is $(2 + 2) = 4$. The details of the relative degree calculation procedure for the SITO control problem are presented in Section 2.5.

4.3.2 Nonlinear coordinate transformation

In the SITO control problem of the MIMO system, the summation of the maximum relative degree for each control output is the relative degree of the entire system. The relative degree of the islanded AC microgrid is four. Therefore, four new coordinate transformations are obtained from the nonlinear coordinate transformation for the control objectives i_d, i_q, V_d and V_q, which can be written as follows:

$$\begin{aligned} z_{di} &= L_f^{1-1} h_1(x) = i_d \\ z_{qi} &= L_f^{1-1} h_2(x) = i_q \\ z_{dv} &= L_f^{1-1} h_3(x) = V_d \\ z_{qv} &= L_f^{1-1} h_4(x) = V_q. \end{aligned} \tag{4.30}$$

Applying the nonlinear coordinate transformation, as presented by equations (4.30), the proposed FBL system can be obtained as follows:

$$\begin{aligned} \frac{dz_{di}}{dt} &= v_{di} \\ \frac{dz_{qi}}{dt} &= v_{qi} \\ \frac{d^2 z_{dv}}{dt^2} &= v_{dv} \\ \frac{d^2 z_{qv}}{dt^2} &= v_{qv} \end{aligned} \tag{4.31}$$

where v_{di}, v_{qi}, v_{dv} and v_{qv} are immeasurable functions that can be formed using a linear controller design approach.

4.3.3 Stability of internal dynamics

The control law is needed to choose in such a way that fulfills the following term owing to guarantee stability:

$$\lim_{t\to\infty} h(x) \longrightarrow 0 \tag{4.32}$$

which indicates that $z_{di} = z_{qi} = z_{dv} = z_{qv} = 0$ at the steady-state for the islanded AC microgrid. The remaining dynamics of state z_5 are as follows:

$$L_{g_1} z_5 (x) = 0 \tag{4.33}$$

$$L_{g_2} z_5 (x) = 0. \tag{4.34}$$

Previous condition (4.33) will be satisfied if

$$z_5 = \frac{1}{4} C_{dc} V_{dc}^2 + \frac{1}{2} L i_d^2 + \frac{1}{2} L i_q^2 + \frac{1}{2} C V_d^2 + \frac{1}{2} C V_q^2. \tag{4.35}$$

The dynamics of the coordinate transformation can be obtained as follows:

$$L_f z_5 = \frac{1}{2} V_{dc} i_s - R i_d^2 - R i_q^2 - V_d i_{dl} - V_d i_{ql} \tag{4.36}$$

where $V_{dc} i_s = \frac{1}{2} P_i$ and $(V_d i_{dl} + V_q i_{ql}) = \frac{2}{3} P_o$ is active power of AC side which is $\frac{1}{2} P_i$ for 0.75 power factor. The transmission line loss power is $P_l = R i_d^2 + R i_q^2$ of the AC bus-connected DC-AC VSC in the islanded AC microgrid. Then, equation (4.36) is written as follows:

$$L_f z_5 = -P_l. \tag{4.37}$$

Subsequently, islanded AC microgrid-connected VSIs can be stabilized with the nonlinear partial FBL control law, which is obtained in the next subsection.

4.3.4 Feedback linearized control law

The control laws corresponding to i_{dq} and V_{dq} are as follows:

$$\begin{aligned} m_{di} &= \frac{2L}{V_{dc}}\left(v_{di} + \frac{R}{L}i_d - \omega i_q + \frac{V_d}{L}\right) \\ m_{qi} &= \frac{2L}{V_{dc}}\left(v_{qi} + \frac{R}{L}i_q + \omega i_d + \frac{V_q}{L}\right) \\ m_{dv} &= \frac{2LC}{V_{dc}}\left(v_{dv} - \frac{1}{C}f_1 - \omega f_4\right) \\ m_{qv} &= \frac{2LC}{V_{dc}}\left(v_{qv} - \frac{1}{C}f_2 + \omega f_3\right) \end{aligned} \tag{4.38}$$

From equation (4.38) the SITO control laws can be written as follows:

$$\begin{aligned} m_d &= \alpha_1\frac{L}{V_{dc}}\left(v_{di} + \frac{R}{L}i_d - \omega i_q + \frac{V_d}{L}\right) + \alpha_2\frac{LC}{V_{dc}}\left(v_{dv} - \frac{1}{C}f_1 - \omega f_4\right) \\ m_q &= \alpha_1\frac{L}{V_{dc}}\left(v_{qi} + \frac{R}{L}i_q + \omega i_d + \frac{V_q}{L}\right) + \alpha_2\frac{LC}{V_{dc}}\left(v_{qv} - \frac{1}{C}f_2 + \omega f_3\right) \end{aligned} \tag{4.39}$$

where all variables in equations (4.39) are measurable except v_{di}, v_{qi}, v_{dv} and v_{qv}, which can be generated by the linear control technique.

4.4 Feedback Linearization Hybrid DC/AC Microgrid

This section develops the FBL controller for a hybrid DC/AC microgrid. For each VSC, the output currents and voltages are considered the objective functions and the switching input of the VSCs in the control input. As a result, there are N

SITO control problems.

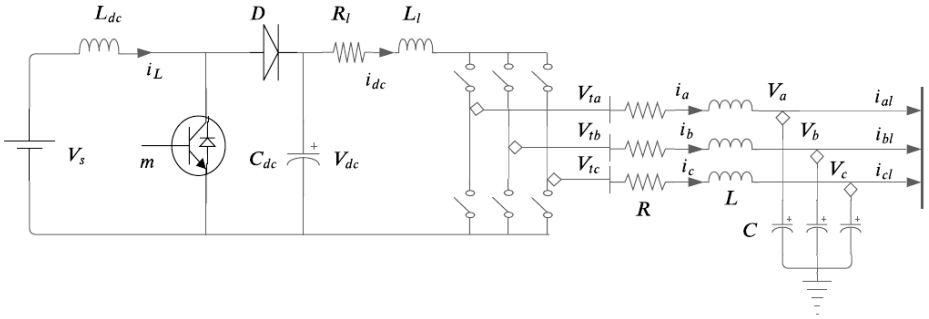

Figure 4.3: Circuit diagram of islanded hybrid DC/AC microgrid.

The complete characteristic model of the hybrid DC/AC microgrid from Subsection 2.3.3 corresponding to Figure 4.3 can be written as follows:

$$\begin{aligned}
\frac{di_L}{dt} &= \frac{1}{L_{dc}}\left(V_s - mV_{dc}\right) \\
\frac{dV_{dc}}{dt} &= \frac{1}{C_{dc}}\left(mi_L - i_{dc}\right) \\
\frac{di_{dc}}{dt} &= \frac{1}{L_l}\left(V_{dc} - R_l i_{dc} - V_L\right) \\
\frac{di_d}{dt} &= \frac{1}{L}\left(\frac{V_L}{2}m_d - Ri_d - V_d\right) + \omega i_q \\
\frac{di_q}{dt} &= \frac{1}{L}\left(\frac{V_L}{2}m_q - Ri_q - V_q\right) - \omega i_d \\
\frac{dV_d}{dt} &= \frac{1}{C}\left(i_d - i_{dl}\right) + \omega V_q \\
\frac{dV_q}{dt} &= \frac{1}{C}\left(i_q - i_{ql}\right) - \omega V_d.
\end{aligned} \tag{4.40}$$

It is necessary to present the nonlinear dynamic system in the conventional form for designing the feedback linearized controller of a MIMO system as follows:

$$\begin{aligned}
\dot{x} &= f(x) + \sum_{i=1}^{N} g_i(x)u_i \\
y &= h_i(x)
\end{aligned} \tag{4.41}$$

$$x = \begin{bmatrix} i_L & V_{dc} & i_{dc} & i_d & i_q & V_d & V_q \end{bmatrix}$$

$$f(x) = \begin{bmatrix} \frac{1}{L_{dc}} V_s \\ -\frac{1}{C_{dc}} i_{dc} \\ \frac{1}{L_l} \left(V_{dc} - R_l i_{dc} - V_L \right) \\ \frac{1}{L} \left(-R i_d - V_d \right) + \omega i_q \\ \frac{1}{L} \left(-R i_q - V_q \right) - \omega i_d \\ \frac{1}{C} \left(i_d - i_{ld} \right) + \omega V_q \\ \frac{1}{C} \left(i_q - i_{lq} \right) - \omega V_d \end{bmatrix}$$

$$g(x) = \begin{bmatrix} -\frac{V_{dc}}{L_{dc}} & 0 & 0 \\ \frac{i_L}{C_{dc}} & 0 & 0 \\ 0 & 0 & 0 \\ 0 & \frac{V_L}{2L} & 0 \\ 0 & 0 & \frac{V_L}{2L} \\ 0 & 0 & 0 \\ 0 & 0 & 0 \end{bmatrix}$$

$$u_i(x) = \begin{bmatrix} m \\ m_d \\ m_q \end{bmatrix}$$

$$y = \begin{bmatrix} V_{dc} & i_{dc} & i_d & i_q & V_d & V_q \end{bmatrix}.$$

4.4.1 Lie derivative and relative degree

The Lie derivatives for $h_1(x)$ and $h_2(x)$ as follows:

$$\begin{aligned} L_f h_1(x) &= -\frac{1}{C_{dc}} i_{dc} \\ L_{g_1} h_1(x) &= \frac{1}{C_{dc}} i_L \\ L_f^2 h_2(x) &= \frac{1}{L_l} f_2 - \frac{R_l}{L_l} f_3 \\ L_{g_1} L_f^{2-1} h_2(x) &= \frac{1}{L_l C dc} i_L \end{aligned} \tag{4.42}$$

where $r_1 = 1$ and $r_2 = 2$ are the relative degrees of $h_1(x) = V_{dc}$ and $h_2(x) = i_{dc}$, respectively.

The Lie derivatives are determined for the output current and voltage of the DC-AC VSCs in Subsection 4.3.1. The Lie derivatives for the d-axis outputs are as follows:

$$\begin{aligned} L_f h_3(x) &= -\frac{1}{L} \left(-R i_d - V_d\right) + \omega i_q \\ L_{g_2} h_3(x) &= \frac{V_L}{2L} \\ L_f^2 h_5(x) &= -\frac{1}{C} f_4 + \omega f_7 \\ L_{g_2} L_f^{2-1} h_5(x) &= \frac{V_L}{2LC} \end{aligned} \tag{4.43}$$

where $r_3 = 1$ and $r_5 = 2$ are the relative degrees for the control objectives $h_3(x) = i_d$ and $h_5(x) = V_d$, respectively.

Similarly, the Lie derivatives for the q-axis outputs are as follows:

$$\begin{aligned} L_f h_4(x) &= -\frac{1}{L}\left(-Ri_q - V_q\right) - \omega i_d \\ L_{g_3} h_4(x) &= \frac{V_L}{2L} \\ L_f^2 h_6(x) &= -\frac{1}{C} f_5 + \omega f_6 \\ L_{g_3} L_f^{2-1} h_6(x) &= \frac{V_L}{2LC} \end{aligned} \tag{4.44}$$

where $r_4 = 1$ and $r_6 = 2$ are the relative degrees for the control objectives $h_4(x) = i_q$ and $h_6(x) = V_q$, respectively.

The total relative degree of the interconnected MIMO system can be obtained as follows:

$$r = max(r_1, r_2) + max(r_3, r_5) + max(r_4, r_6). \tag{4.45}$$

The relative degree of the DC subsystem is 2, and the AC subsystem is 4. Thus, the DC subsystem (each DC-DC VSC) is partially linearized, and the AC subsystem (each DC-AC VSC) is fully linearized.

4.4.2 Nonlinear coordinate transformation

In the SITO control problem, the maximum relative degree for any control output is the relative degree of the entire system. The relative degrees of the DC-DC and DC-AC interfaces in the hybrid DC/AC microgrid is six. Six new coordinate transformations are obtained from the nonlinear coordinate transformation for

the control objectives V_{dc}, i_{dc}, i_d, i_q, V_d and V_q, which can be written as follows:

$$\begin{aligned} z_v &= L_f^{1-1} h_1(x) = V_{dc} \\ z_i &= L_f^{1-1} h_2(x) = i_{dc} \\ z_{di} &= L_f^{1-1} h_3(x) = i_d \\ z_{qi} &= L_f^{1-1} h_4(x) = i_q \\ z_{dv} &= L_f^{1-1} h_5(x) = V_d \\ z_{qv} &= L_f^{1-1} h_6(x) = V_q. \end{aligned} \tag{4.46}$$

Applying the nonlinear coordinate transformation, as presented by equations (4.46), the proposed FBL system can be obtained as follows:

$$\begin{aligned} \frac{dz_v}{dt} &= v_v \\ \frac{d^2 z_i}{dt^2} &= v_i \\ \frac{dz_{di}}{dt} &= v_{di} \\ \frac{dz_{qi}}{dt} &= v_{qi} \\ \frac{d^2 z_{dv}}{dt^2} &= v_{dv} \\ \frac{d^2 z_{qv}}{dt^2} &= v_{qv} \end{aligned} \tag{4.47}$$

where v_v, v_i, v_{di}, v_{qi}, v_{dv} and v_{qv} are immeasurable functions that can be designed by a linear control approach.

4.4.3 Stability of internal dynamics

The previous subsection shows that the two dynamic states of every DC-DC VSC are transformed into a linear system. It is important to define the rest of the

dynamic state of the DC-DC VSC through proper transformation. The transform requires to be preferred in such a way that it fulfills:

$$\lim_{t\to\infty} h(x) \longrightarrow 0 \tag{4.48}$$

which indicates that $z_v = z_i = 0$ at steady-state for the DC subsystem. The remaining state is z_7, and it should be satisfied the following condition:

$$L_{g_1} z_7 (x) = 0. \tag{4.49}$$

Condition (4.49) will be satisfied if

$$z_7 = \frac{1}{2} L i_L^2 + \frac{1}{2} C V_{dc}^2 + \frac{1}{2} L_l i_{dc}^2. \tag{4.50}$$

The dynamics with respect to this coordinate transformation can be obtained as follows:

$$L_f z_7 = V_s i_L - R_l i_{dc} - V_{dc} i_{dc} = P_i - P_l - P_o \tag{4.51}$$

where $P_i = V_s i_L$, $P_o = V_{dc} i_{dc}$ and $P_l = R_l i_{dc}$ are the input, output, and transmission line loss powers of the DC subsystem, respectively. Then, equation (4.51) is as follows:

$$L_f z_7 = 0. \tag{4.52}$$

Subsequently, the DC and AC subsystems can be controlled using a partial FBL control scheme formulated in the next subsection.

4.4.4 Feedback linearized control law

The SITO control law for DC subsystem can be obtained as follows:

$$m = \frac{C_{dc}\left(v_v + L_l v_i - f_2 + R_l f_3\right) + i_{dc}}{i_L} \tag{4.53}$$

The SITO control laws for AC subsystem are determined as follows:

$$\begin{aligned} m_d &= \frac{2L}{V_L}\left(v_{di} + C v_{dv} - 2f_4 - \omega f_7\right) \\ m_q &= \frac{2L}{V_L}\left(v_{qi} + C v_{qv} - 2f_5 + \omega f_6\right) \end{aligned} \tag{4.54}$$

where all variables in equations (4.53) and (4.54) are measurable except v_v, v_i, v_{di}, v_{qi}, v_{dv} and v_{qv}, which are generated through the conventional PI and PD linear controllers.

4.5 Linear Controller Design for Feedback Linearized Control Laws

Using the Laplace transformation, the FBL system from (4.10) and (4.31), or (4.47) can be written as:

$$\begin{aligned} V_{dc}(s) &= \frac{1}{s} V_v(s) \\ I_{dc}(s) &= \frac{1}{s^2} V_i(s) \\ I_d(s) &= \frac{1}{s} V_{di}(s) \\ I_q(s) &= \frac{1}{s} V_{qi}(s) \\ V_d(s) &= \frac{1}{s^2} V_{dv}(s) \\ V_q(s) &= \frac{1}{s^2} V_{qv}(s) \end{aligned} \tag{4.55}$$

where $\frac{1}{s}$ is the transfer function for the output functions V_{dc}, i_d and i_q. In contrast, $\frac{1}{s^2}$ is the transfer function for the output functions i_{dc}, V_d and V_q. Therefore, equation (4.56) is a simplified form of equation (4.55) to design linear controllers as follows:

$$\begin{aligned} \frac{V_{dc}(s)}{V_v(s)} = \frac{I_d(s)}{V_{di}(s)} = \frac{I_q(s)}{V_{qi}(s)} = \frac{Y_1(s)}{V_1(s)} = \frac{1}{s} \\ \frac{I_{dc}(s)}{V_i(s)} = \frac{V_d(s)}{V_{dv}(s)} = \frac{V_q(s)}{V_{qv}(s)} = \frac{Y_2(s)}{V_2(s)} = \frac{1}{s^2} \end{aligned} \tag{4.56}$$

where $Y_1 = \{V_{dc},\ I_d,\ I_q\}$, $V_1 = \{V_v,\ V_{di},\ V_{qi}\}$, $Y_2 = \{i_{dc},\ V_d,\ V_q\}$ and $V_2 = \{V_i,\ V_{dv},\ V_{qv}\}$. Two SISO subsystems, given by (4.56), can be stabilized by designing linear controllers. Normally, Y_1 and Y_2 are required to track the reference Y_{1r} and Y_{2r}; so, the control inputs V_1 and V_2 can be generated as follows:

$$\begin{aligned} V_1(s) = K_1(s)E_1(s) \\ V_2(s) = K_2(s)E_2(s) \end{aligned} \tag{4.57}$$

where $K_1(s)$ and $K_2(s)$ are the controllers, and $E_1(s)$ and $E_2(s)$ are the Laplace transforms of $e_1(t) = y_{1r}(t) - y_1(t)$ and $e_2(t) = y_{2r}(t) - y_2(t)$, respectively. The transfer functions of the feedback linearized subsystems are $G_1(s) = \frac{1}{s}$ and $G_2(s) = \frac{1}{s^2}$. The transfer functions are play a significant character in the design of the linear controllers. Among the different types of transfer functions are used to reduce the steady-state error and track the desired output. The sensitivity

and complementary sensitivity functions of the closed-loop system are as follows:

$$\begin{aligned} S_1(s) &= \frac{1}{1+G_1(s)K_1(s)} \\ T_1(s) &= \frac{G_1(s)K_1(s)}{1+G_1(s)K_1(s)} \\ S_2(s) &= \frac{1}{1+G_2(s)K_2(s)} \\ T_2(s) &= \frac{G_2(s)K_2(s)}{1+G_2(s)K_2(s)} \end{aligned} \tag{4.58}$$

The measured outputs Y_1 and Y_2, and the steady-state errors E_1 and E_2 are related to the command references Y_{1r} and Y_{2r}, respectively, as follows:

$$\begin{aligned} Y_1(s) &= T_1(s)Y_{1r}(s) \\ E_1(s) &= S_1(s)Y_{1r}(s) \\ Y_2(s) &= T_2(s)Y_{2r}(s) \\ E_2(s) &= S_2(s)Y_{2r}(s) \end{aligned} \tag{4.59}$$

To track the output Y_1 and Y_2, we also reduce the steady-state error E_1 and E_2, and a standard PI and PD controller are applied, respectively. The PI controller is used to obtain an immeasurable function V_1, and a PD controller is used to obtain an immeasurable function V_2. The transfer functions of the first-order FBL system and the standard PI controllers are obtained as follows:

$$\begin{aligned} G_1(s) &= \frac{1}{s} \\ K_1(s) &= \frac{K_{1P}s + K_{1I}}{s} \end{aligned} \tag{4.60}$$

Substituting (4.60) into (4.58), the sensitivity and complementary sensitivity

functions are obtained as follows:

$$\begin{aligned} S_1(s) &= \frac{s^2}{s^2 + K_{1P}s + K_{1I}} \\ T_1(s) &= \frac{K_{1P}s + K_{1I}}{s^2 + K_{1P}s + K_{1I}} \end{aligned} \tag{4.61}$$

The denominator of the functions $S_1(s)$ and $T_1(s)$ are the same and second-order polynomials. The standard form of the second-order polynomial is as follows:

$$s^2 + 2\xi\omega_n s + \omega_n^2 \tag{4.62}$$

where $K_{1P} = 2\xi\omega_n$, $K_{1I} = \omega_n^2$ and $K_{1I} = \left[\frac{K_{1P}}{2\xi}\right]^2$.

The transfer function of the second-order FBL system and standard PD controller can be determined as follows:

$$\begin{aligned} G_2(s) &= \frac{1}{s^2} \\ K_2(s) &= K_{2D}s + K_{2P} \end{aligned} \tag{4.63}$$

Substituting (4.63) into (4.58), the sensitivity and complementary sensitivity functions are obtained as follows:

$$\begin{aligned} S_2(s) &= \frac{s^2}{s^2 + K_{2D}s + K_{2P}} \\ T_2(s) &= \frac{K_{2D}s + K_{2P}}{s^2 + K_{2D}s + K_{2P}} \end{aligned} \tag{4.64}$$

Similar to the first-order FBL system, the denominator the functions $S_2(s)$ and $T_2(s)$ are the same and second-order polynomials. The standard form of the second-order polynomial is expressed as follows:

$$s^2 + 2\xi\omega_n s + \omega_n^2 \tag{4.65}$$

where $K_{2D} = 2\xi\omega_n$, $K_{2P} = \omega_n^2$ and $K_{2P} = \left[\frac{K_{2D}}{2\xi}\right]^2$.

The controllers corresponding to the first-order and second-order linearized systems are as follows:

$$\begin{aligned} K_1(s) &= \frac{15s + 115}{s} \\ K_2(s) &= 15s + 115 \end{aligned} \tag{4.66}$$

for $\xi = 0.7$.

4.6 Performance Evaluation of Designed Controllers

The details transient stability analysis is investigated for the conventional PID controller corresponding to the FBL model. This section also presents the designed FBL controller performance for different types of islanded microgrids.

4.6.1 Stability analysis of islanded microgrids

The main concern in designing a controller is to maintain the stability of the system. It is essential to analyse the closed-loop performance of the system before implementing the controller. The conventional PI and PD controllers are designed to adjust the output currents and voltages of the VSCs, respectively. The sensitivity functions of the voltage control and current control loops are the same as $\mathrm{S_1(s) = S_2(s) = S(s)}$, and the complementary sensitivity functions of the voltage control and current control loops are the same as $\mathrm{T_1(s) = T_2(s) = T(s)}$. As a result, a stability analysis illustrates for a common sensitivity function S(s) and complementary sensitivity function T(s). Figure 4.4 is illustrated the step response, sigma plot and Nyquist diagram for the time- and frequency-domain

functions S(s) and T(s). The solid green line is represented the responses of the sensitivity function S(s) and dash red line is represented the responses of the complementary sensitivity function T(s).

The step response, sigma plot and Nyquist diagram are well-established stability analysis tools for linear time-invariant systems. Figure 4.4 illustrates the step response of function S(s) and T(s). The time-domain step response of the sensitivity function S(s) becomes zero, which means that the linear controller can be provided as a minimum steady-state error. Similarly, the response of the complementary sensitivity functions T(s) becomes unity at the same time when the sensitivity function becomes zero, which means that the designed current and voltage regulators achieve the desired output.

The external disturbance is a long-term issue in conventional power systems and can decrease the performance of microgrids. Usually, the external disturbance in a power system is a low-frequency disturbance. The disturbance cancellation capability of the linear controller is addressed from the feedback system's sensitivity function response. The controller can be attenuated to the crossover frequency of the sensitivity function S(s). The crossover frequency of the sensitivity function S(s) is greater than $15\,\mathrm{rad\,s^{-1}}$, as illustrated in Figure 4.4. The contrary designed controller can be reduced with frequencies less than $15\,\mathrm{rad\,s^{-1}}$ with maximum amplification of a disturbance at higher frequencies of 1 dB.

The primary concern in designing a controller is to enhance the stability margin of the system. The stability margin is determined by the complementary sensitivity function response in the sigma plot. The inverse H_∞ norm value of the complementary sensitivity function, $||\mathrm{T(s)}||_\infty^{-1}$ can provide the minimum stability margin. For the designed controller $||\mathrm{T(s)}||_\infty = 0.7874$, as illustrated in Figure 4.4. The designed controller is operated with large uncertainty, which

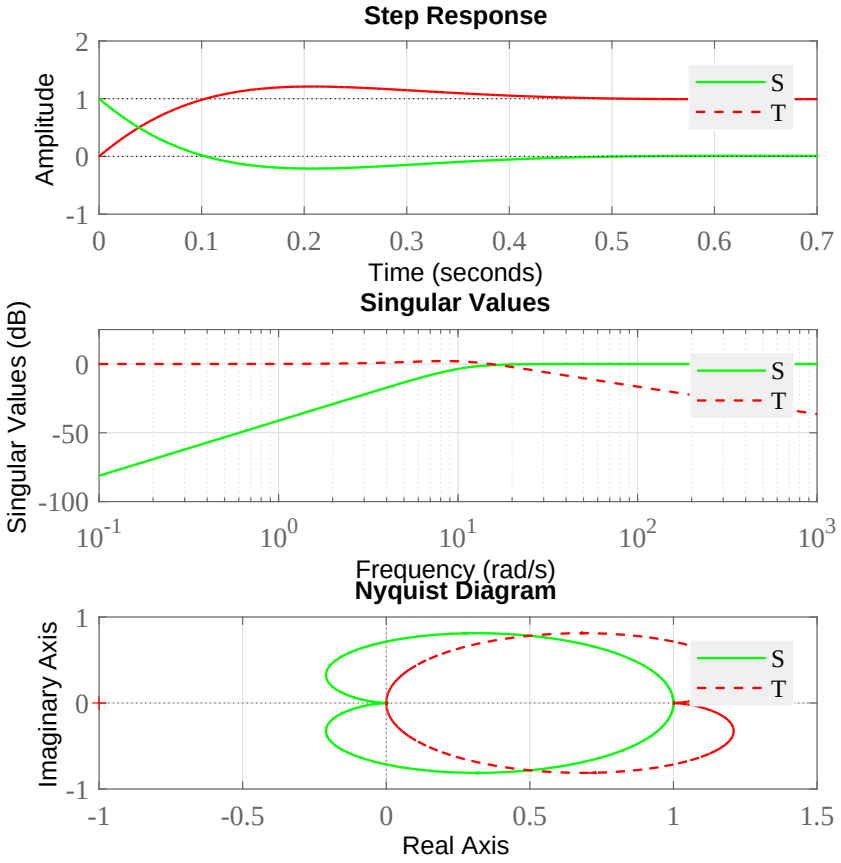

Figure 4.4: Responses of functions $S(s)$ and $T(s)$ with different stability analysing tools.

ensures greater robustness under the worst scenarios. The Nyquist diagram is shown in Figure 4.4 that the response of function T(s) is far away from -1, which means that the designed controller can be provided with a large stability margin.

4.6.2 Performance evaluation of islanded DC microgrid

Four different case studies are considered to assess the performance of the designed SITO-FBL control technique for an islanded DC microgrids. Figure 4.5

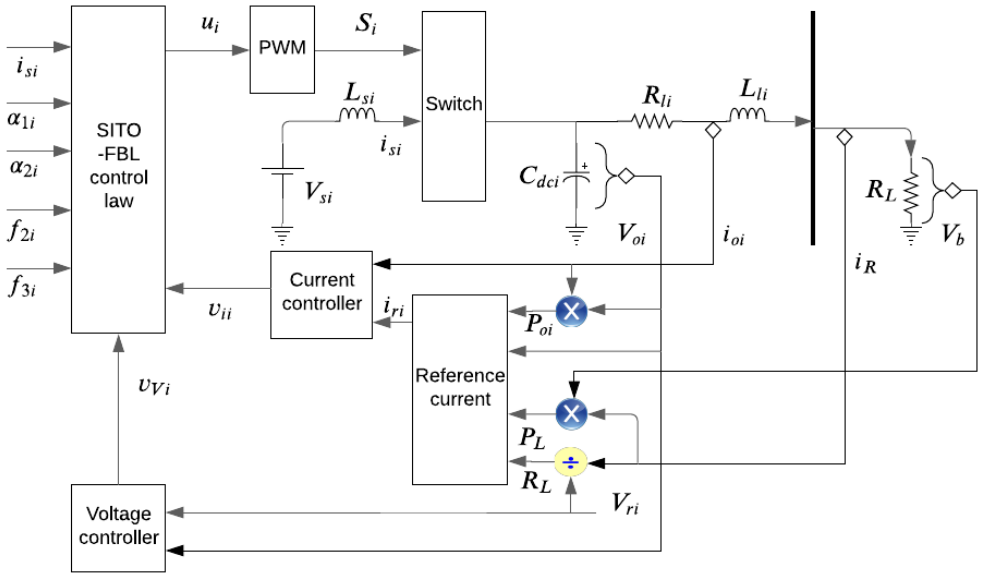

Figure 4.5: Proposed control implementation diagram for parallel connected DC-DC converters in DC microgrid.

represents the control implementation diagram of the designed controller. The proposed controller is a primary control scheme, where the conventional PI and PD controllers are applied to adjust the DC-bus voltage and output current of the individual VSC. The ratings of the DGs are considered 6 kW and 500 V output power and voltage, respectively. The impedance of the connection line between each DG and common DC-bus is selected as the only series impedance, where R_{l1} & L_{l1} and R_{l2} & L_{l2} represent the series impedance of the VSC $i = 1$ and $i = 2$, respectively. The demand power at the DC-bus is a purely resistive load. To investigate the performance of proposed controller in each case, the load is considered to be $R_L = 80\,\Omega$ until $t = 2\,\text{s}$, and after $t = 2\,\text{s}$ load becomes $R_L = 40\,\Omega$. Therefore, the output current and power varied from their nominal

rating. The reference currents can then be determined as follows:

$$i_{ri} = \frac{V_{oi} k_i}{R_L N} \tag{4.67}$$

where i_{ri} is the reference output current of i^{th} VSC, N is the total number of converters that are parallel-connected in the islanded DC microgrid and k_i is the current-sharing coefficient of the i^{th} converter. The current-sharing coefficient can be obtained as follows:

$$k_i = \frac{P_i}{P_L} N \tag{4.68}$$

where P_i and P_L are the generated power of the i^{th} VSC and the total demand power of the microgrid, respectively. Substituting the value of k_i from equation (4.68) into (4.67), it can be written as follows:

$$i_{ri} = \frac{V_{oi} P_i}{R_L P_L} \tag{4.69}$$

Three different case studies and one comparison are assessed to estimate the load-sharing accuracy of the designed control scheme, where the priority variable $\alpha_1 = \alpha_2$ is considered. Each of these situations is studied as follows.

Performance evaluation under equal rated power

The equal output power of the parallel-connected VSCs is considered to monitor the efficacy of the proposed SITO-FBL control scheme to stabilize the islanded DC microgrid. The DGs are almost equidistant from the microgrid, with only small line impedance differences between the two sources, $R_{l1} = 2\,\Omega$ and $R_{l1} = 2.1\,\Omega$. However, the change in demand power in any electrical system is a common

scenario, considering that the microgrid works, in which case the demand power is doubled from 3 kW for 2 s. As a result, the output current should be doubled, and there is no deviation in the output voltage.

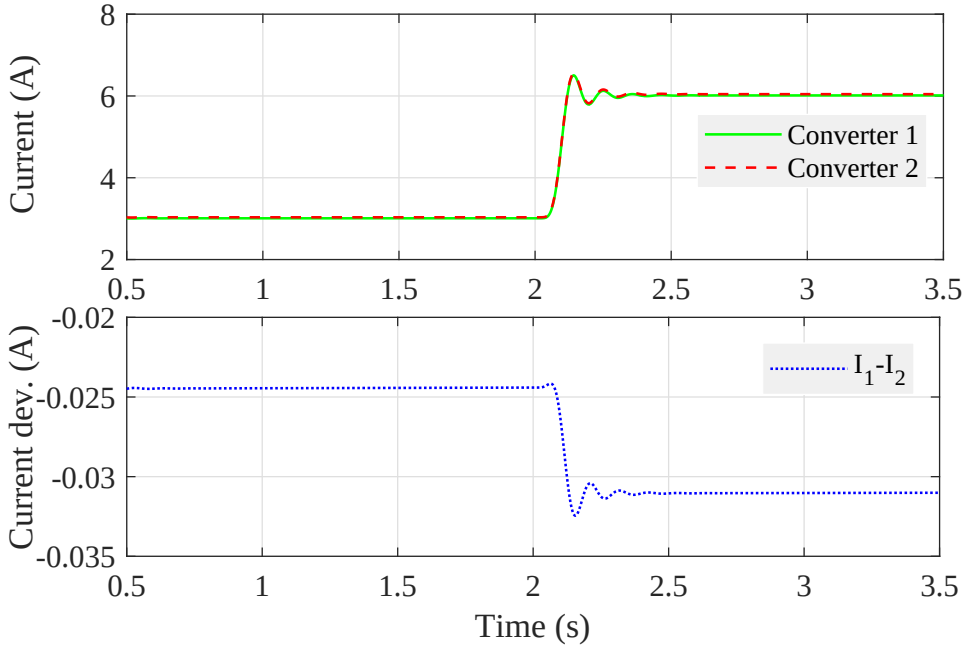

Figure 4.6: Output voltage under equal power generation.

Figures 4.6-4.8 illustrate the current, voltage and power responses of the VSCs connected to the microgrid. The resistance value of the resistive load is $R_L = 80\,\Omega$ until $t = 2\,\text{s}$, and the output voltages of the converters are 489.3 V and 489.3 V, which are equal. In this case, the output current and power of the converters are equal, but after 2 s, the demand power becomes doubles so that the output current and power are also doubled without a significant deviation. The change of output current, voltage and power before and after the variation of demand power for consideration conditions is detailed in Table 4.2. Above all, it can be concluded that the designed controller can carry out the appropriate operation subject to the many scenarios.

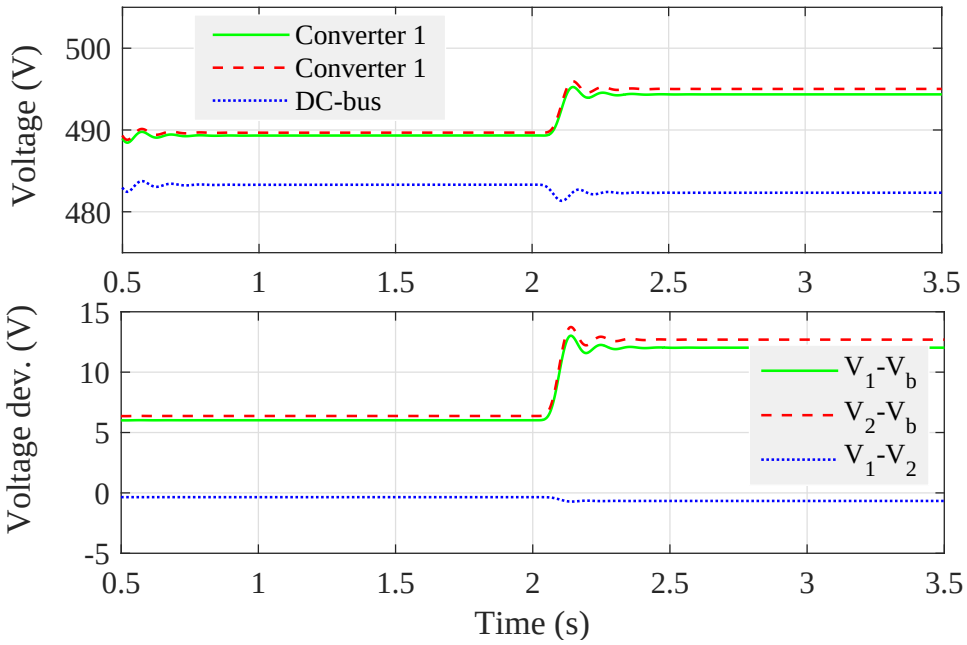

Figure 4.7: Output current under equal power generation.

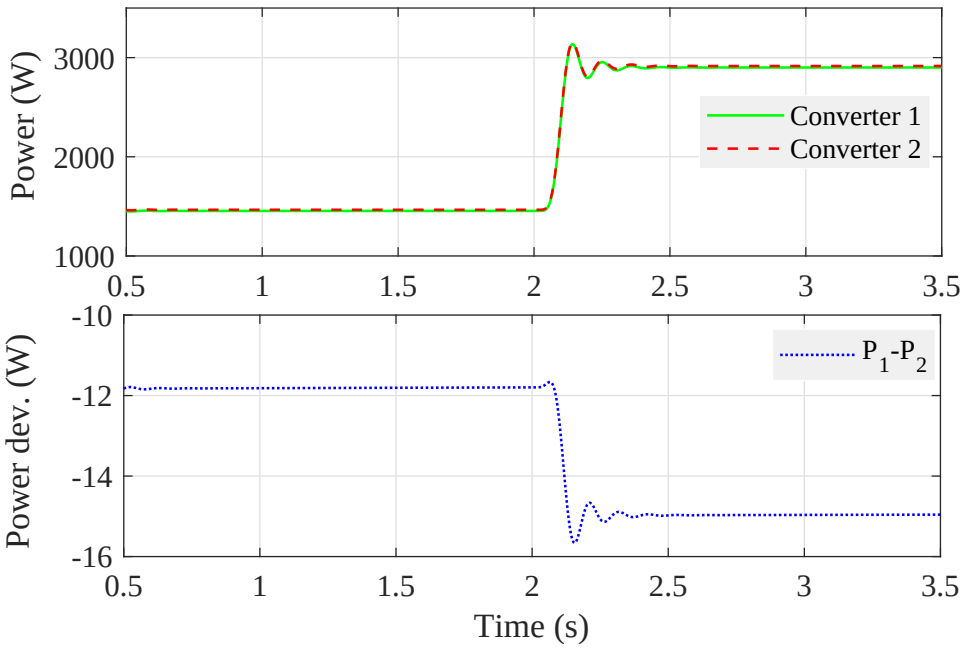

Figure 4.8: Output power under equal power generation.

Performance evaluation under unequal rated power

In this condition, parallel-connected VSCs are rated unequally. The output powers from Converter-1 and Converter-2 are $P_1 = 4\,\text{kW}$ and $P_2 = 2\,\text{kW}$,

respectively. The designed SITO-FBL controller can control such scenarios. The DC-bus voltage restoration and current-sharing accuracy are investigated with constant demand power and sudden change between operations. Figures 4.9-4.11 show the controller performance under-considered case study.

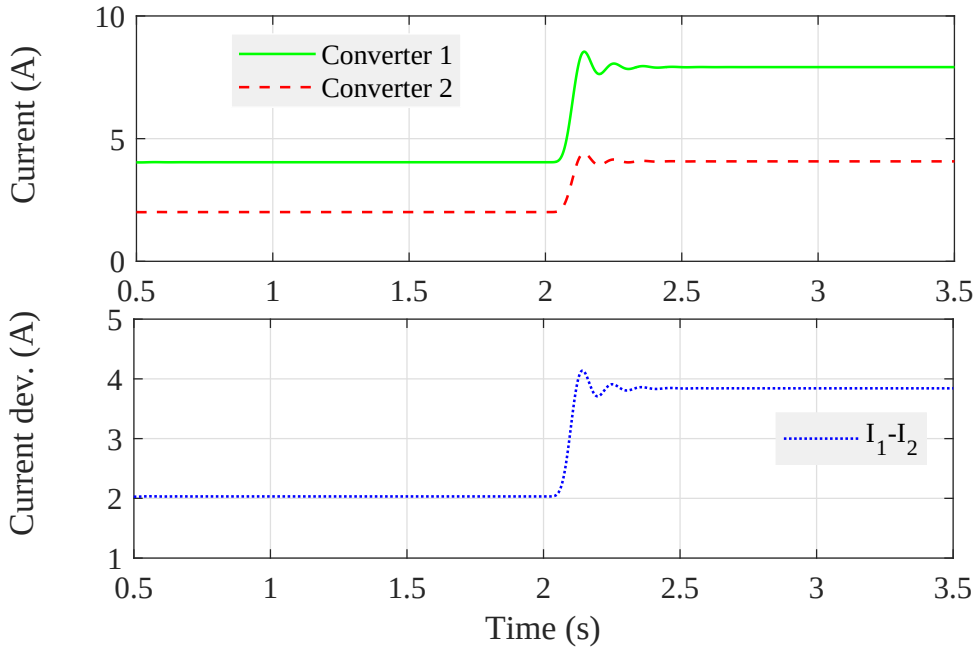

Figure 4.9: Output voltage under unequal power generation with $P_1 = 2P_2$.

Figure 4.9 displays the output voltage and their deviations from the two VSCs, where the output voltages of the converters are 491.8 V and 487.1 V, respectively. The output current and power of Converter-1 are double for Converter-2, and these are proportional to each other. The amplitude of output variables from Case-2, Table 4.2 shows that the output current and power of Converter-1 before the change in load are almost equal to the output current and power of Converter-2 after the change in load. Therefore, such a control system can stabilize the consider case study to operate correctly.

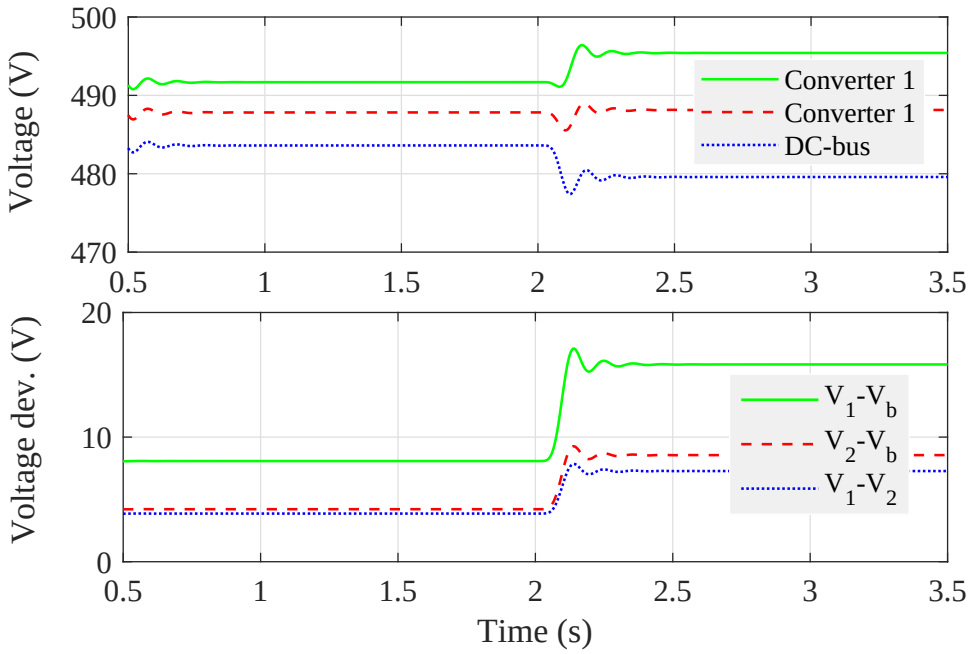

Figure 4.10: Output current under unequal power generation with $P_1 = 2P_2$.

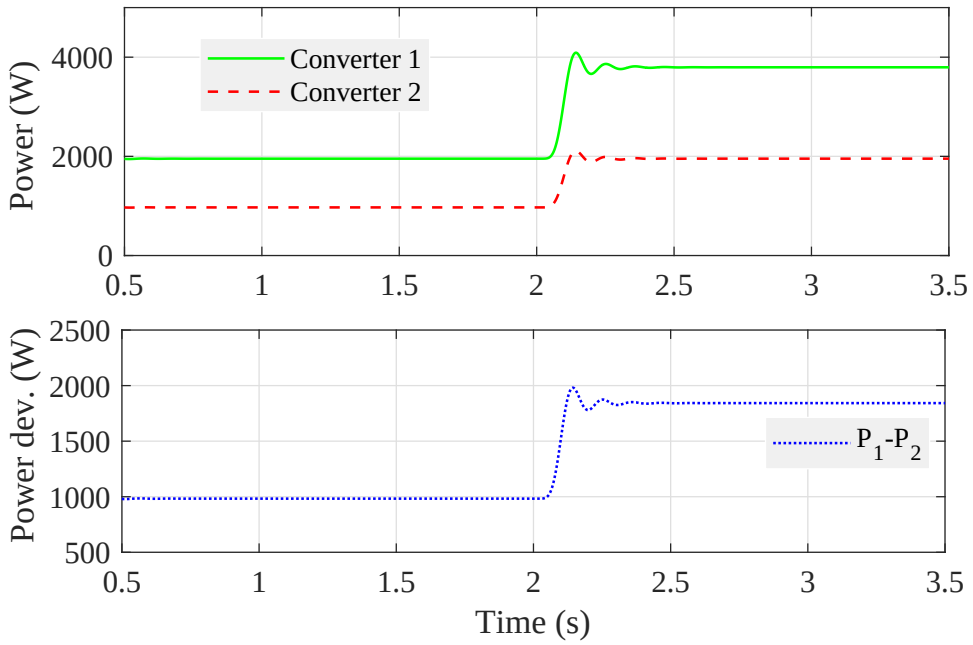

Figure 4.11: Output power under unequal power generation with $P_1 = 2P_2$.

Performance evaluation under different distance

A scenario that has been considered for performance investigation of the proposed controller, where DGs are generated with an equal amount of power. All the

system parameters are considered the same, considering only one thing differentiating between the two DGs. The first DG is considered five times farther from the second DG, so it is natural that differences in line resistance should occur. The performance of the proposed controller is monitored with line resistance $R_{l1} = 5\,\Omega$ of Converter-1 and line resistance $R_{l2} = 1\,\Omega$ of Converter-2.

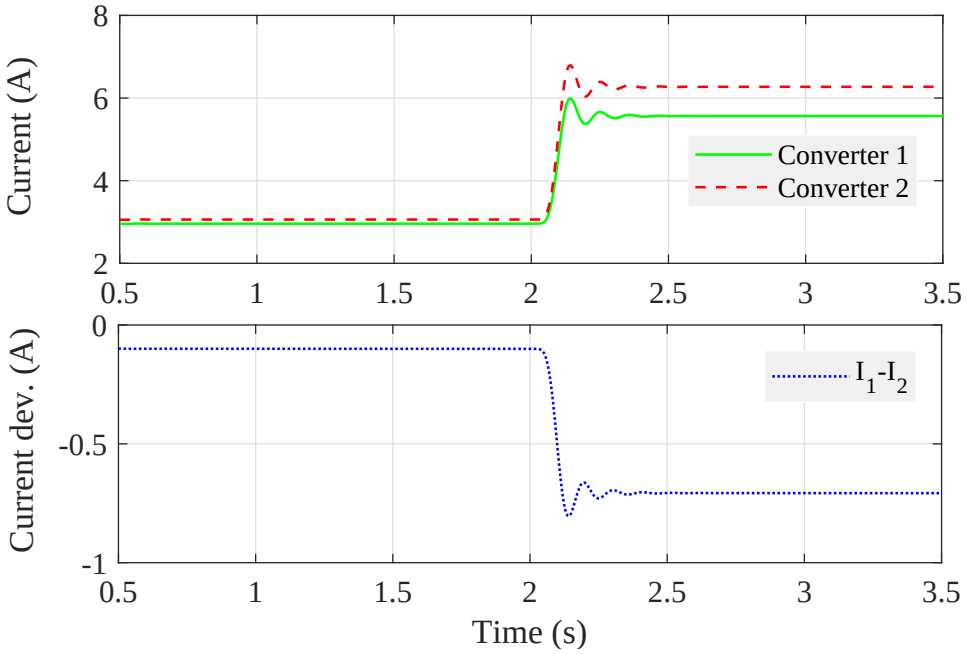

Figure 4.12: Output voltage under equal power generation with $R_{l1} = 5R_{l2}$.

Figures 4.12-4.14 attempt to represent the efficacy of the designed control method for the challenges considered in this case study. The output voltage of the Converter-1 and Converter-2 are 496.3 V and 484.6 V, respectively, but as the demand power doubles after a certain period, the output voltage changes to 501.3 V and 489.6 V, which is clear from Figure 4.13. In contrast, Figures 4.12 and 4.14 show that the shared current and power are identical. The supply from converter-1 is less than the converter-2 in current and power-sharing owing to high resistive impedance with line-1. In addition, the line current and power loss should be less for the low line resistance of the second DG, as shown in Figures 4.13 and 4.14.

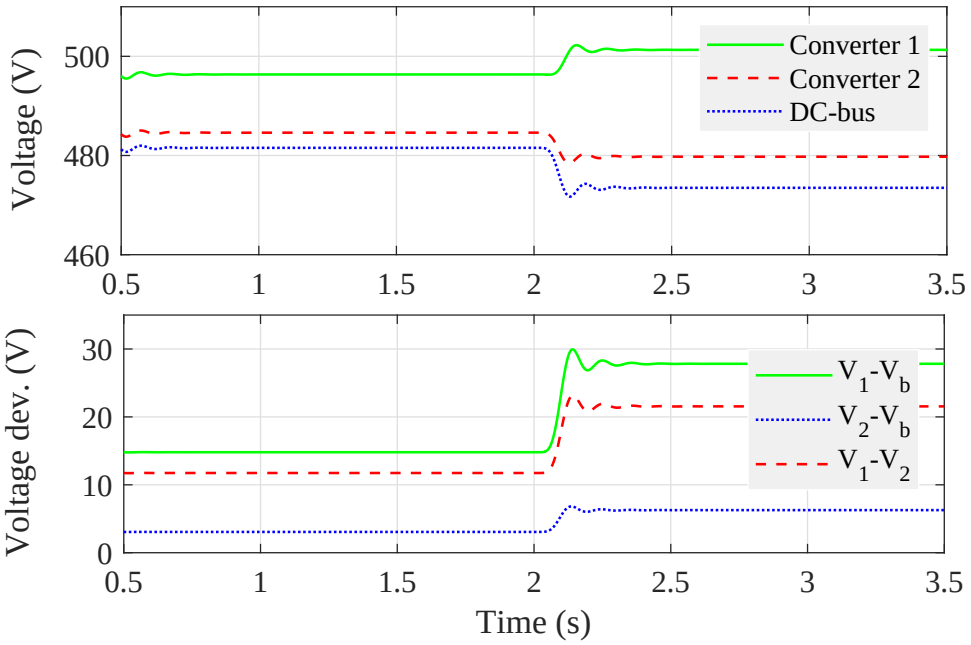

Figure 4.13: Output current under equal power generation with $R_{l1} = 5R_{l2}$.

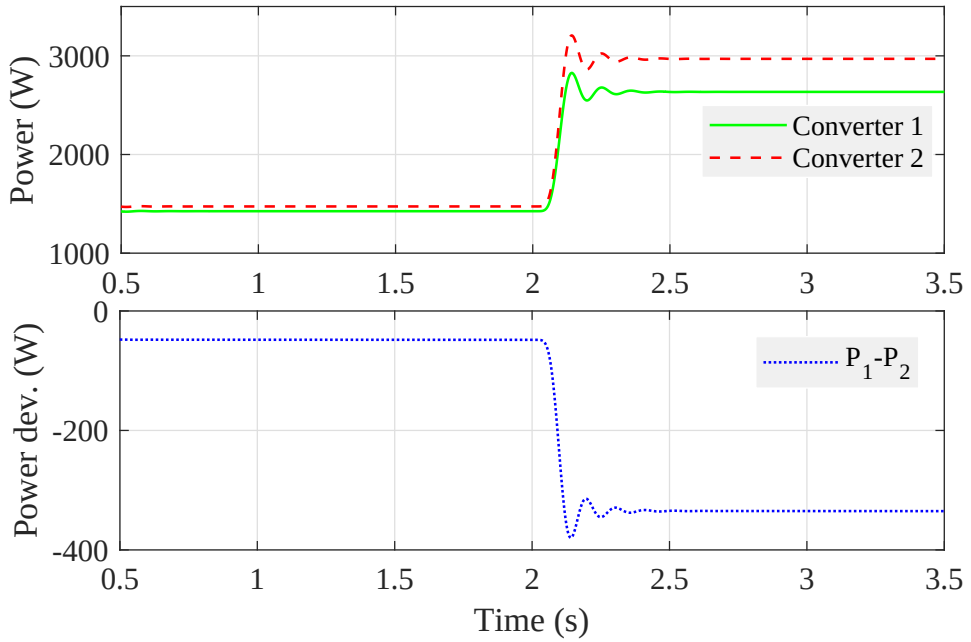

Figure 4.14: Output power under equal power generation with $R_{l1} = 5R_{l2}$.

Therefore, it can be said that the designed control method is reliable for solving such a real problem.

Table 4.2: Amplitude of output current, voltage and power under three different case studies for proposed control scheme.

Time	Cases	$V_1,\ V_2,\ V_A$ (V)	$I_1,\ I_2,\ I_A$ (A)	$P_1,\ P_2,\ P_A$ (W)
Before	1	489.3, 489.7, 489.5	3.009, 3.033, 3.021	1454, 1466, 1460
	2	491.7, 487.8, 489.8	4.039, 2.007, 3.023	1953, 970, 1462
	3	496.3, 484.6, 490.5	2.960, 3.060, 3.010	1425, 1473, 1449
After	1	494.4, 495.0, 494.7	6.013, 6.044, 6.023	2900, 2915, 2908
	2	495.4, 488.1, 491.8	7.915, 4.074, 5.995	3796, 1934, 2875
	3	501.3, 479.8, 490.6	5.564, 6.272, 5.918	2635, 2969, 2802

Table 4.3: Amplitude of output current, voltage and power under equal generation for three different droop-control.

Time	Methods	$V_1,\ V_2,\ V_A$ (V)	$I_1,\ I_2,\ I_A$ (A)	$P_1,\ P_2,\ P_A$ (W)
Before	CDC	103.5, 104.0, 103.8	11.79, 8.577, 10.18	1215, 888, 1052
	CSDC	104.0, 105.0, 104.5	10.29, 10.29, 10.29	1081, 1070, 1076
	PSDC	104.0, 105.0, 104.5	10.35, 10.25, 10.30	1076, 1076, 1076
After	DC	101.8, 102.1, 102.0	22.90, 16.66, 19.78	2900, 2915, 2908
	CSDC	103.2, 105.0, 104.1	20.19, 20.19, 20.19	2120, 2079, 2100
	PSDC	103.2, 105.0, 104.1	20.39, 20.01, 20.20	2101, 2101, 2101

Comparison between proposed control scheme and different droop-control technique under equal rated power

The above three subsections are investigated different practical problems that can be solved by the proposed control method, and in all these cases, the controller's efficiency is verified. The performance of the proposed SITO-FBL is compared in this study with the droop-control technique for parallel-connected VSCs in an islanded DC microgrid. In [131], a generalized droop-control scheme is proposed, and two approaches are developed based on the output current and power of the VSCs. On the other hand, the effectiveness of these two control methods has been compared with the conventional droop method. Consider a problem where DGs are produced with the same amount of power and are relatively equidistant from their position to the microgrid (as exact as in the first case study). An analytical comparison is developed among the proposed control scheme (PCS),

conventional droop-control (CDC), current-sharing droop-control (CSDC) and power-sharing droop-control (PSDC) to illustrate the effectiveness of PCS over other control schemes. The first case study in Table 4.2 and the consideration in Table 4.3 show the output voltage, current and power of the two converters before and after load change for the same problem.

Table 4.4: Deviation under equal power generation.

Cases	Before load change			After load change		
Deviation	ΔV %	ΔI %	ΔP %	ΔV %	ΔI %	ΔP %
PCS	2.01	0.79	0.82	1.06	0.51	0.52
CDC	3.80	31.5	31.0	2.00	31.5	30.5
CSDC	4.50	0.00	1.02	4.10	0.00	1.95
PSDC	4.50	0.97	0.00	4.10	1.88	0.00

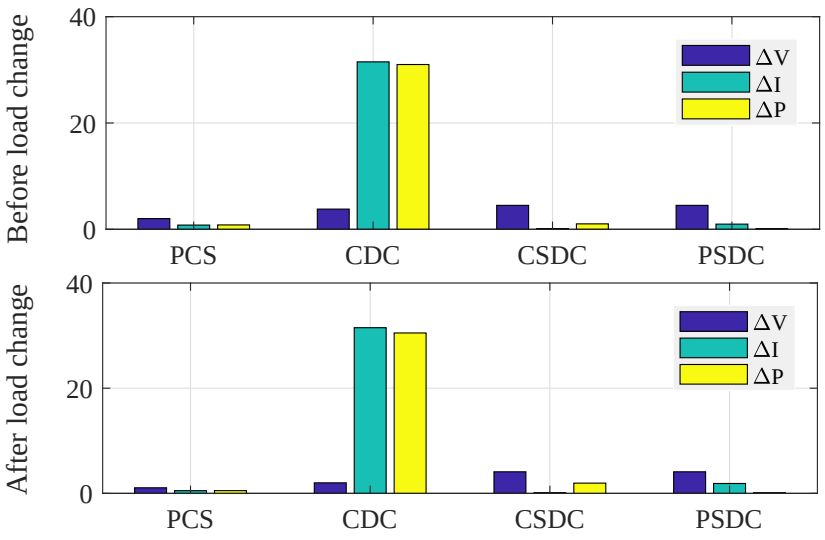

Figure 4.15: Output current, voltage and power deviation under equal generation.

On the other hand, the output voltage, current, and power deviations are given in Table 4.4 to consider the equivalence, and the other three droop-control methods for comparison are given subject to the proposed formula in Appendix B.1.1. Figure 4.15 illustrates Table 4.4, which gives an accurate idea of the functionality

of the controllers. Although the percentage of the output voltage deviation of the conventional droop-controller is satisfactory, current and power-sharing efficiencies are not expected. The CSDC and PSDC methods proposed in [131] are much better than the CDC method for current and power-sharing, respectively, but not as satisfactory in terms of voltage deviation. From this perspective, the PCS is superior to all other methods in reducing voltage deviation although it is slightly weaker than CSDC in terms of current deviation, it is better in terms of power-sharing. PSDC has shown somewhat better performance for power-sharing than PCS but lags in current-sharing. From the above discussion based on Table 4.4 and Figure 4.15, it is clear that the PCS can satisfactorily complete the operation over the existing droop-control methods in [131].

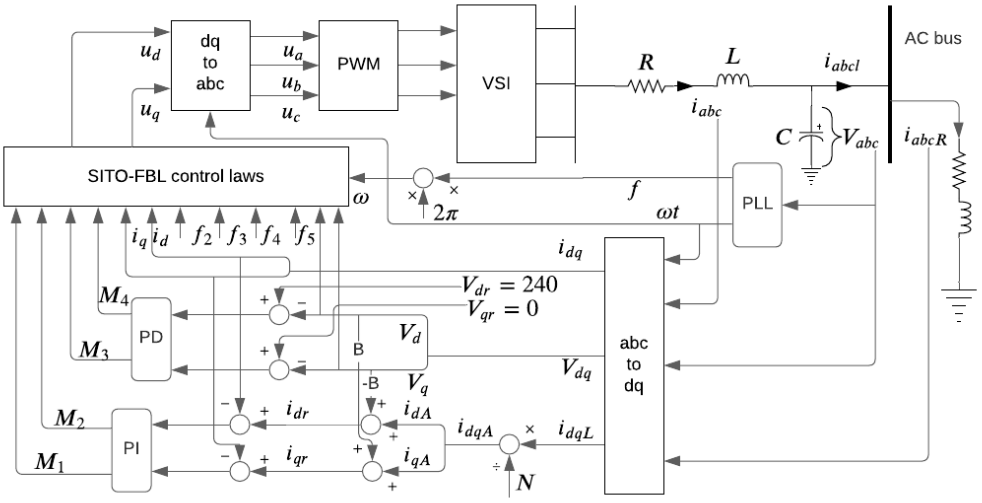

Figure 4.16: Proposed control implementation block diagram for parallel-connected VSCs in islanded AC microgrids.

4.6.3 Performance evaluation of islanded AC microgrid

Conventional PI and PD controllers are designed to adjust the DC-AC VSC output current i_{dq} and AC-bus voltage V_{dq}, respectively. The performance of the designed nonlinear SITO-FBL control scheme is investigated using different case studies. Figure 4.16 demonstrates the detailed control execution diagram of a parallel-connected DGs through DC-AC VSCs, which is known as voltage source inverters (VSIs) in the islanded AC microgrids. The AC-bus voltage is 240 V; thus, the reference voltages in the dq frame become $V_{dr} = 240\,\mathrm{V}$ and $V_{qr} = 0\,\mathrm{V}$. Besides, the control objectives of this control scheme are output currents of the VSIs, which are proportional to the output power of the VSIs. Therefore, a proper current-sharing approach can be obtained for desire power-sharing among parallel-connected VSIs in the islanded AC microgrid.

The reference current corresponding to the output currents i_d and i_q can be calculated to adjust the output currents of the VSIs using the following equations:

$$\begin{aligned} i_{dr} &= \frac{i_{dL}}{N} - \omega C V_q = i_{dA} - B V_q \\ i_{qr} &= \frac{i_{qL}}{N} + \omega C V_d = i_{qA} + B V_d \end{aligned} \tag{4.70}$$

where $\mathrm{i_{dqL}}$, $\mathrm{i_{dqA}}$ and N are the load current, average current, and number of VSIs in the microgrid.

PWM generation by proposed nonlinear control scheme

The two-level three-phase VSI operates based on alternate switching pairs for each phase. Each phase switch's turn-on or off commands are delivered across a pulse-width modulation (PWM) technique. The familiar PWM technique relates a high-frequency periodic triangular signal, the carrier signal, with a slow-shifting

signal define as the modulating signal. Figure 4.17 shows details of the generated modulating signals by the proposed SITO-FBL control scheme. The carrier signal is swigged between -1 and 1. The carrier's intersections and the modulating signals determine the switching instants of each pair of the three different arms. The PWM response for a single switch in phase a is illustrated in Figure 4.18.

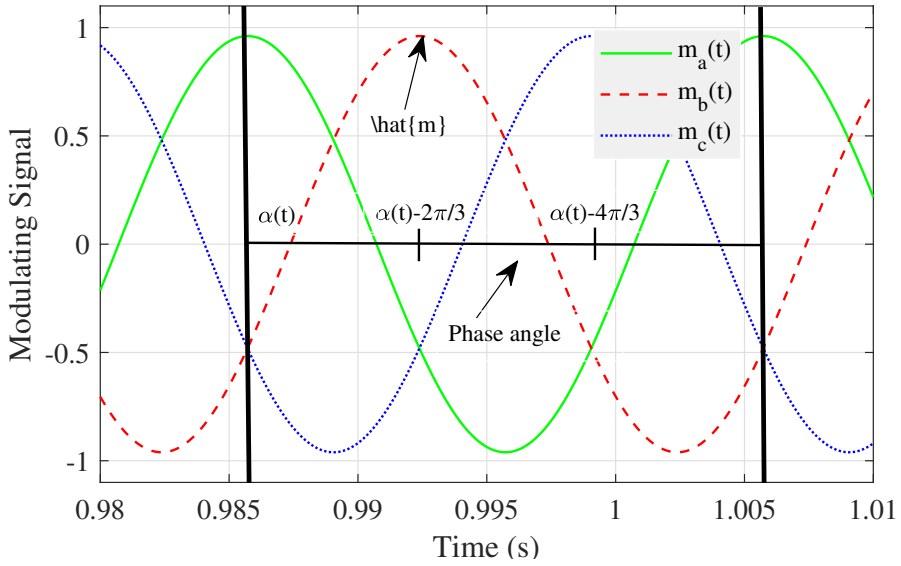

Figure 4.17: Generated modulating signals by proposed control scheme.

Thus, as Figure 4.18 demonstrates, once the modulating signal is greater than the carrier signal, a turn-on instruction is delivered for a switch of phase a, and the turn-on command of another switch of phase a is cancelled, and similar working principles are applicable for phase b and c. When the modulating signal is reduced than the carrier signal, the opposite is true. Figure 4.19 shows the operating PWM for each phase generated by the proposed control scheme for a single-input two-output control problem when the modulating signal is greater than the carrier signal. On the other hand, the operating PWM for each phase will be inverse with these PWM, as shown in Figure 4.19.

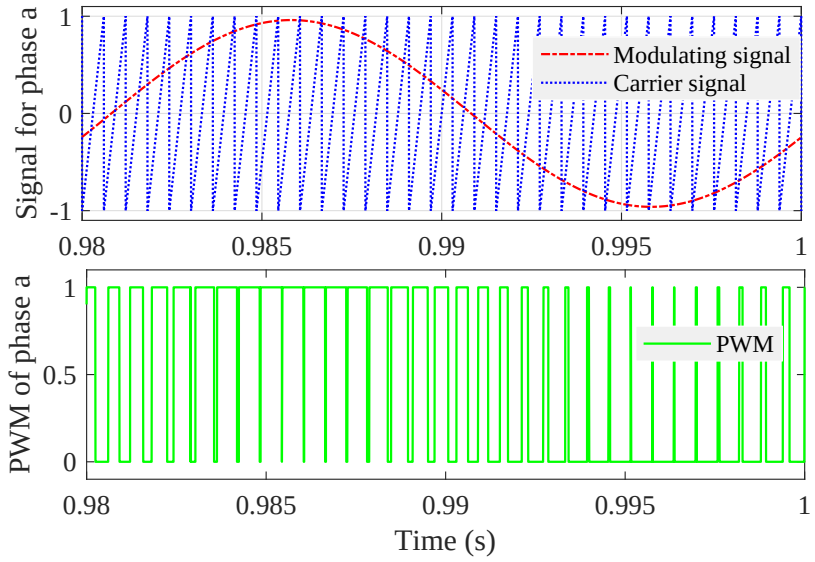

Figure 4.18: Signals based on PWM switching strategy.

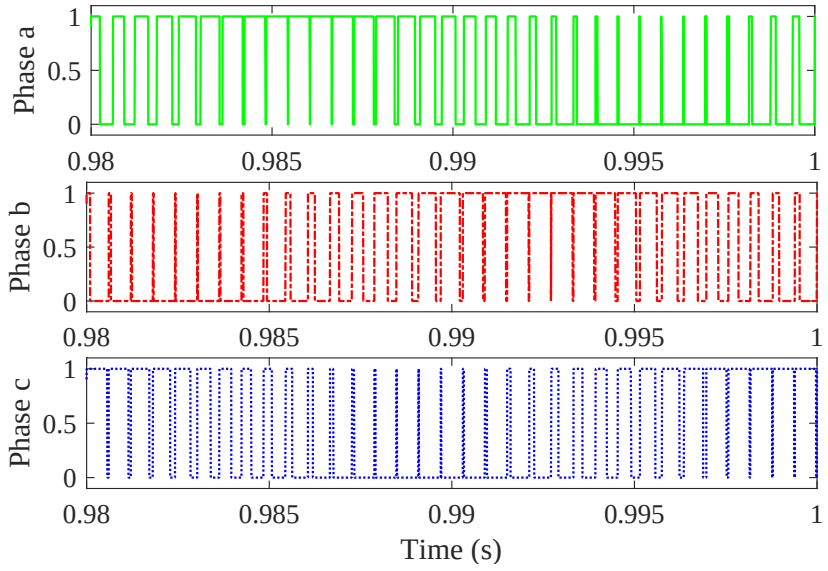

Figure 4.19: Pulse width modulation in abc frame.

Performance of proposed controller under demand power variation

In this case study, two DC-AC VSIs with a rated active power of 6 kW considered $P_1 = P_2$. The bus voltage restoration and current-sharing accuracy have been investigated with constant demand power and sudden changes in operations. The

results are shown in Figures 4.20-4.23. In constant load, Figure 4.21 shows that the demand current has equally shared between the VSIs. Figure 4.22 describes the output voltage has approached each other, and Figure 4.23 illustrates the power-sharing response between the VSIs equal to the deviated responses current, voltage, and power. The proposed SITO-PFBL control scheme can be implemented without a secondary controller.

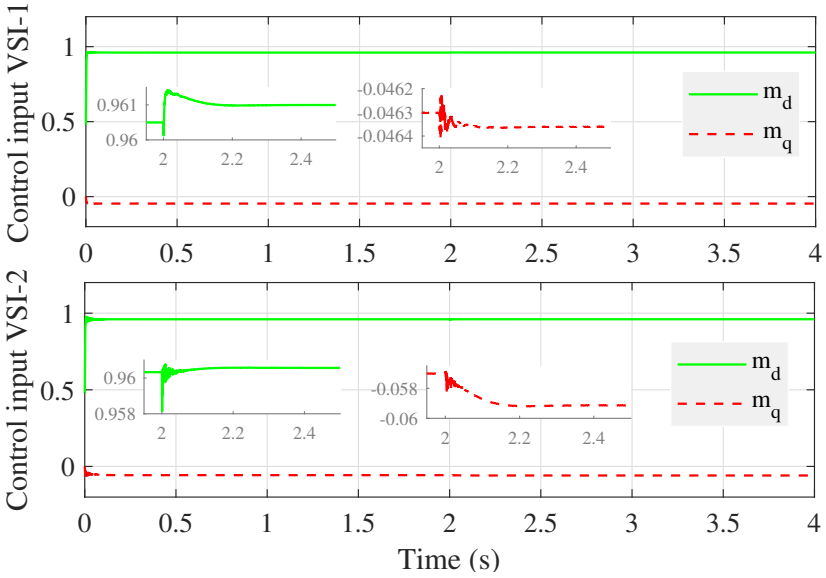

Figure 4.20: Control input in dq frame under demand power variation.

The demand power rating on the common bus of the islanded AC microgrid is 5 kW active power and 2 kVar reactive power up to 2 s. After 2 s, the demand power unexpectedly rises from 5 kW to 6 kW, and the action of the designed controller has been changed, which can adapt to the time. Figure 4.20 depict the design controller's response in the qd frame. Figures 4.21 and 4.22 show the output current and voltage of the DC-AC converters, respectively. Figure 4.21 illustrates that the change in output current in 2 s but does not show any change in the output voltage from Figure 4.22. The only reason for the change in the output current, as displayed in Figure 4.21 is the change in demand power, clear

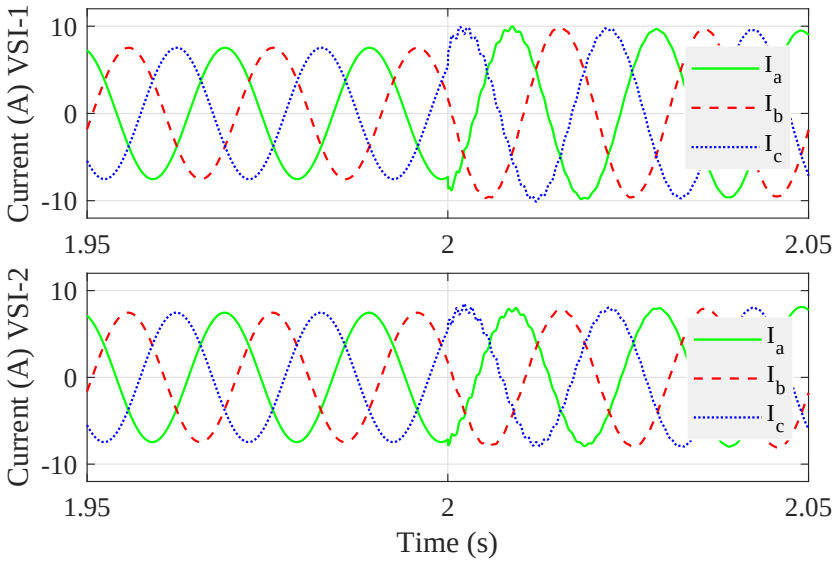

Figure 4.21: Output current of VSIs under demand power variation.

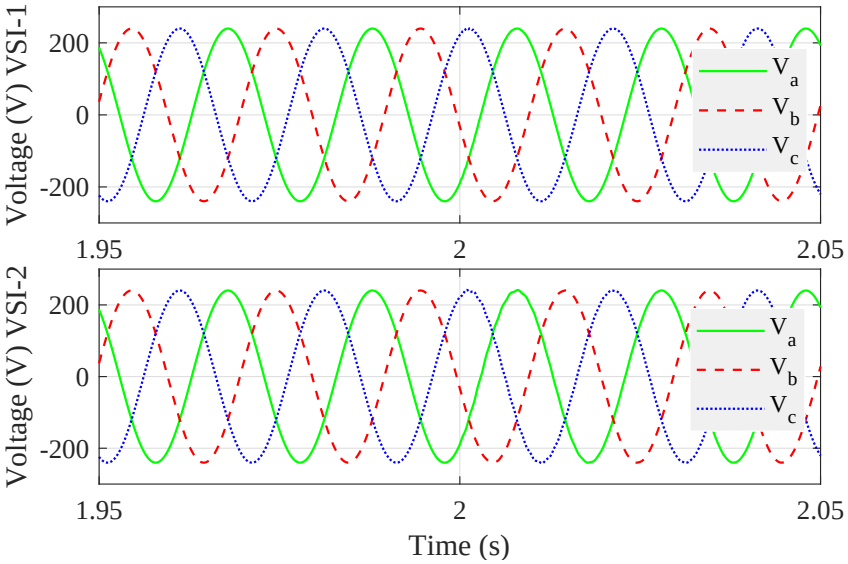

Figure 4.22: Output voltage of VSIs under demand power variation.

from Figure 4.23.

Performance of proposed controller under single-phase to ground fault

A short-circuit fault is a familiar disturbance in the power system, and the single-phase to ground short-circuit fault is one of the most severe problems.

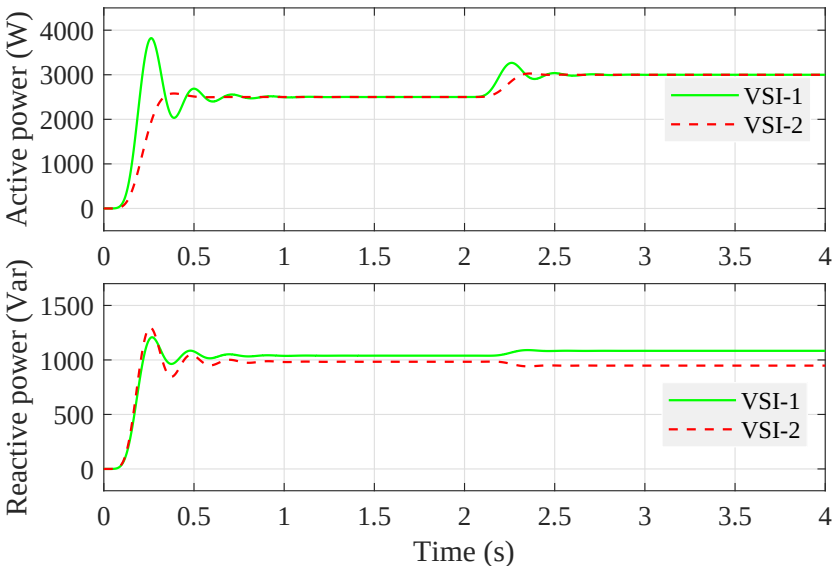

Figure 4.23: Total load of microgrid under demand power variation.

In this study, a single-phase terminal fault is considered at VSI-1. To examine the performance of the designed controller in a case study as follows:

- Fault happen at $t = 2\,\mathrm{s}$
- Fault cleared at $t = 2.1\,\mathrm{s}$

If a single-phase terminal fault occurs at VSI-1, VSI-1 will not properly deliver the demand power to load between 2 and 2.1 s. On the other hand, the islanded AC microgrid may become unstable during a large clearance time. This type of issue can be overcome by adding external damping to the islanded AC microgrid, for which a different type of linear controller is widely used. Nonlinear controllers can maintain transient stability, which is well-defined from the simulation outcomes, as shown in Figures 4.24-4.27.

Figures 4.24-4.27 show the control input, output current, voltage, and demand power responses of VSIs, which desired current-sharing is achieved during the post-fault steady-state operation. Also, the designed controller guarantees

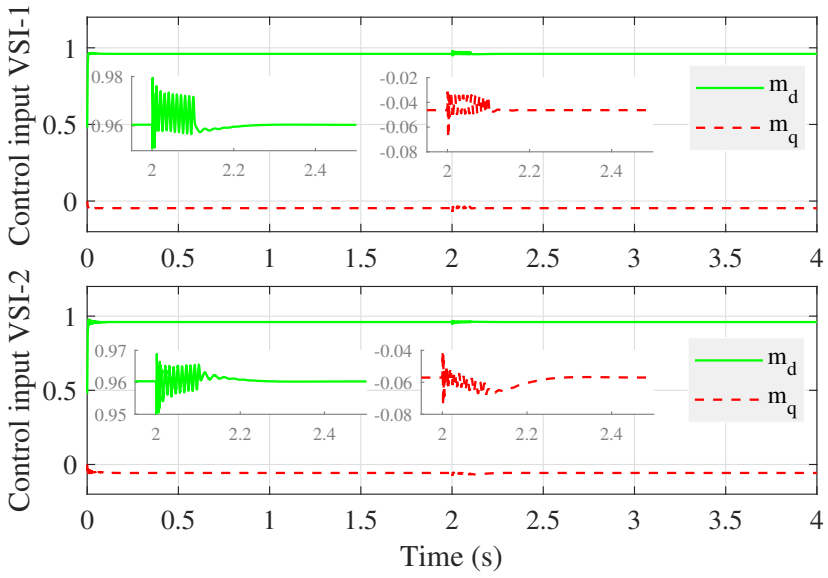

Figure 4.24: Control input in dq frame under terminal fault.

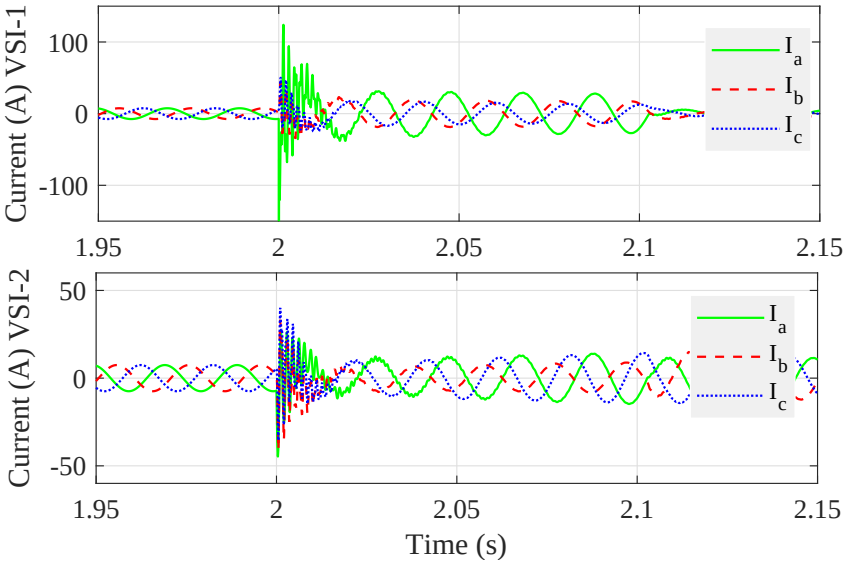

Figure 4.25: Output current of VSIs under terminal fault.

transient stability within the expected settling time.

Another essential factor is the frequency deviation in the transient stability analysis after post-fault and load demand in the islanded AC microgrids. Because the current and voltage dynamics provide the stability of the islanded AC microgrids, the frequency will be unaffected by external disturbances if stability

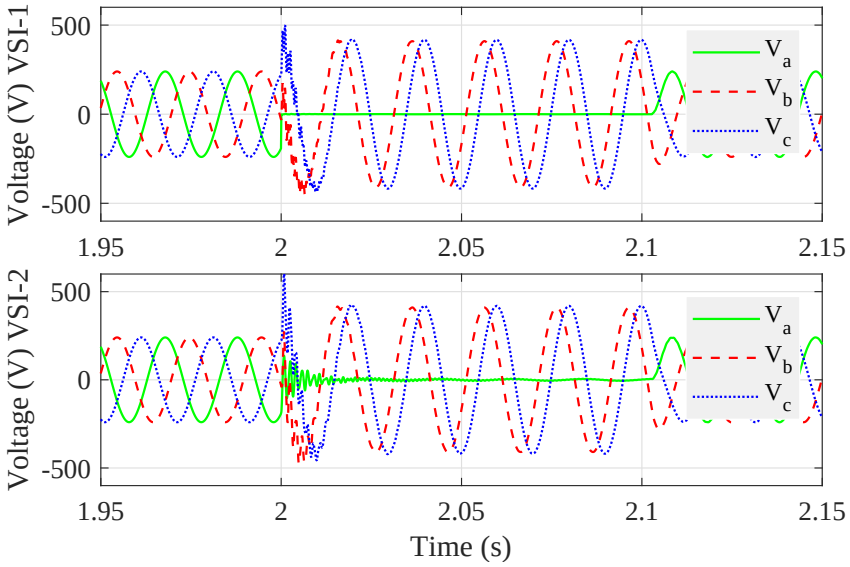

Figure 4.26: Output voltage of VSIs under terminal fault.

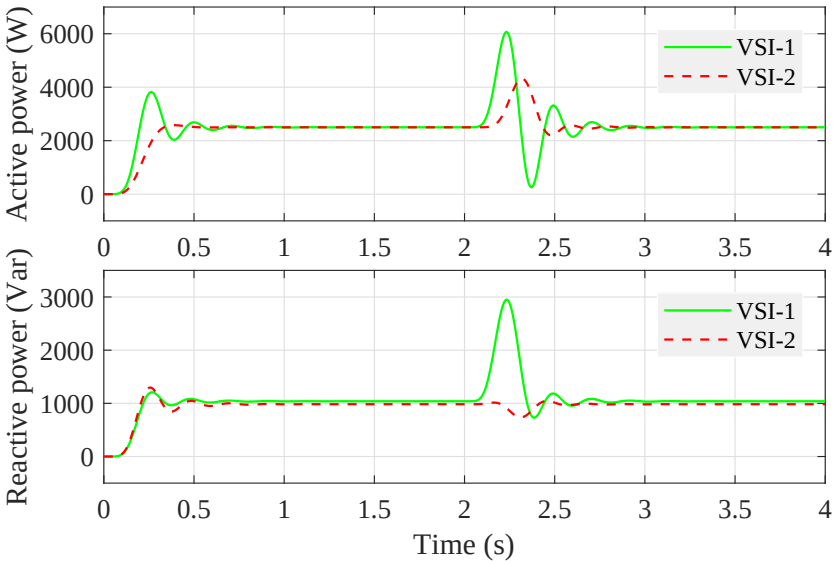

Figure 4.27: Total load of microgrid under terminal fault.

concerns associated with the current and voltage are ensured. As the designed controller provides the stable operation of the current and the voltage within the specified time frame, the islanded AC microgrid frequency is approximately 50 Hz for both case studies, as shown in Figure 4.28.

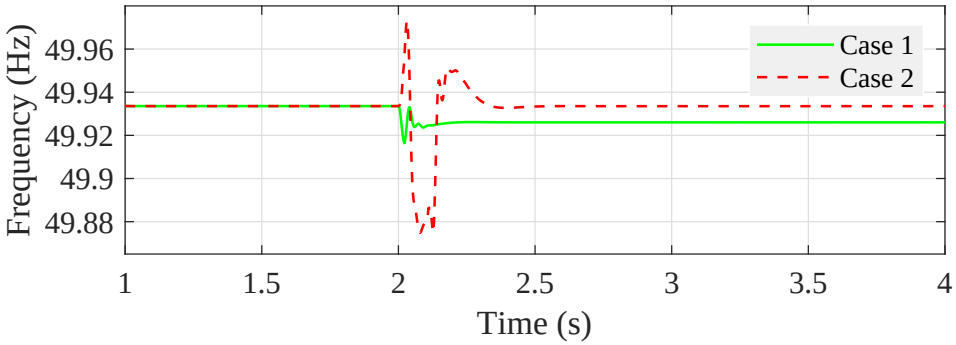

Figure 4.28: Frequency response of microgrid under different case studies.

4.6.4 Performance evaluation of hybrid DC/AC microgrid

The previous section clarifies that measured information are needed to implement the designed FBL controller for the SITO control problem in the islanded hybrid DC/AC microgrid. The measured signals are the output voltages and currents of the DC-DC VSCs and DC-bus voltage. On the other hand, line current and similar information are required to control the DC-AC VSC. Conventional PI and PD controllers are applied in the FBL control scheme to stabilize the SITO control problem of the hybrid DC/AC microgrid. A PI controller is applied to adjust the output voltages and currents of the DC-DC and DC-AC VSCs, respectively. The gain values of the PI controller are $K_P = 15$ & $K_I = 115$. In contrast, a PD controller is applied to stabilize the output currents and voltages of the DC-DC and DC-AC VSCs, respectively. The gain values of the PD controller are $K_P = 115$ & $K_D = 15$.

Proposed controller performance under demand power variation

Figure 2.11 is presented in Chapter 2 as a complete schematic diagram of the considered islanded hybrid DC/AC microgrid, where two DC sub-microgrids

and an AC sub-microgrid are connected. Two different load variations are used in simulations to evaluate the proposed controller performance. The first load variation happens in DC sub-bus number one at 4 s, and another one happens in AC sub-bus at 6 s. Figures 4.29-4.32 show the designed controller performance.

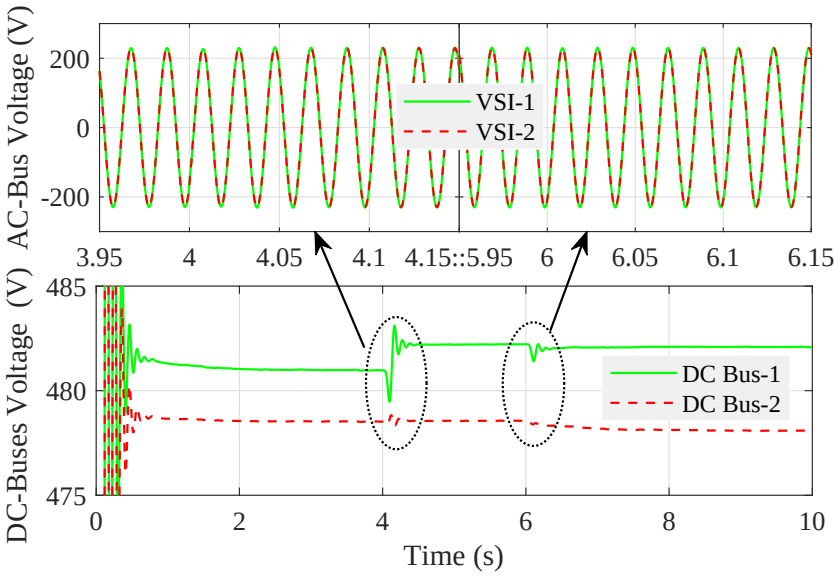

Figure 4.29: Output voltage of DC buses.

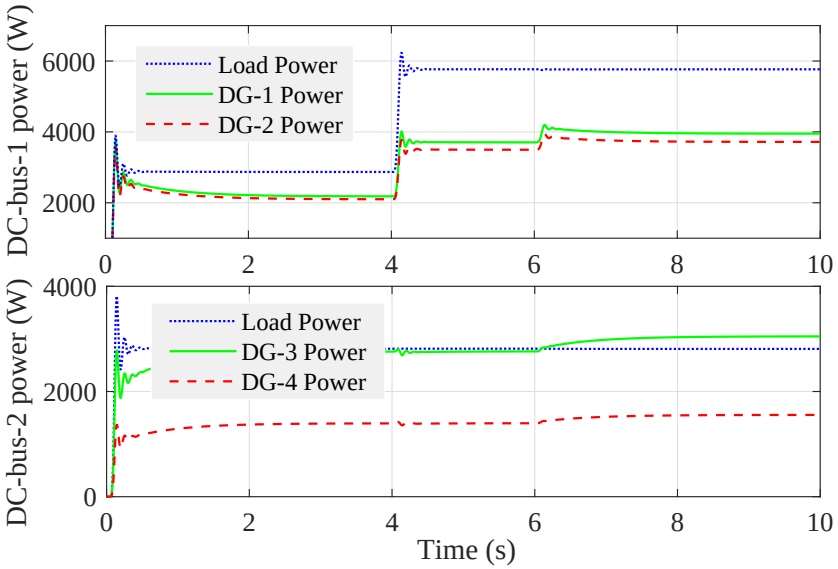

Figure 4.30: DC supply and demand power.

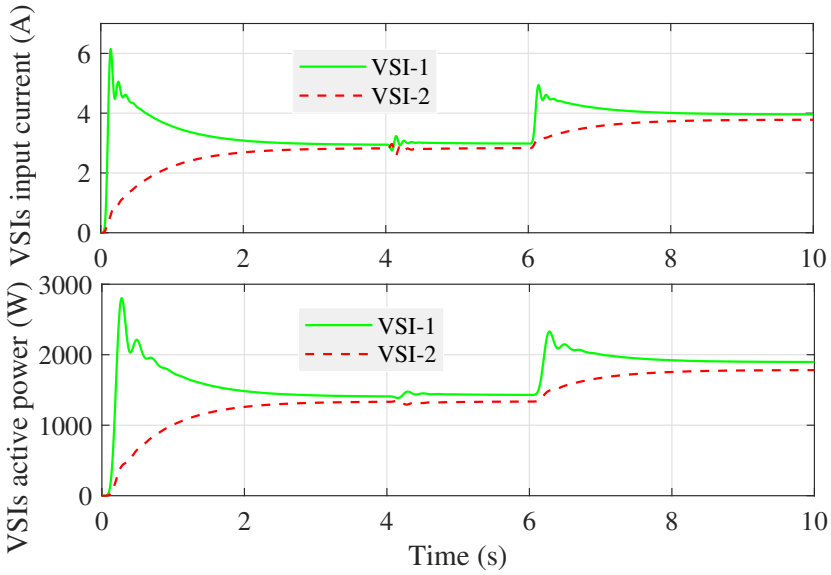

Figure 4.31: Input current and output active power of DC-AC VSCs.

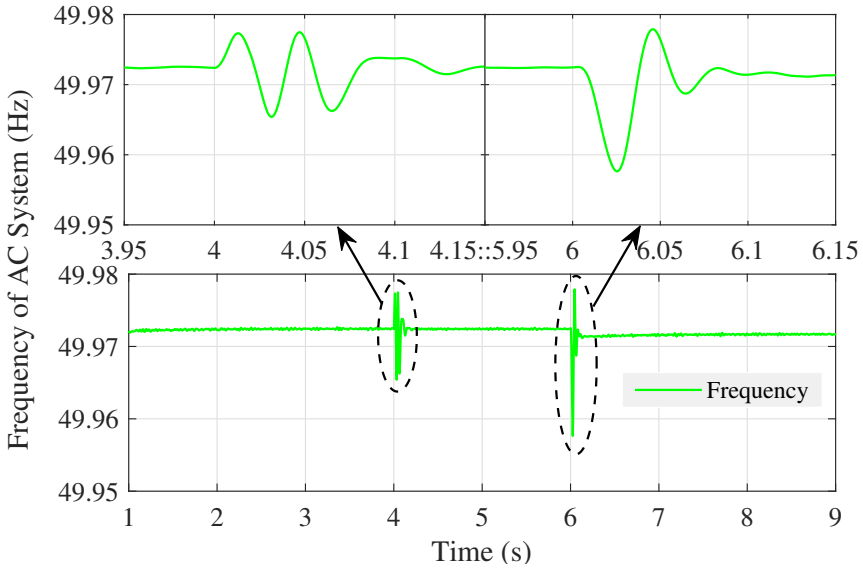

Figure 4.32: Frequency of AC sub-microgrid.

The input and output voltages of the DC-AC VSCs are displayed in Figure 4.29, where the DC-bus voltages are the input voltages of the DC-AC VSCs. The blue solid-line and red dashed-line represent the bus voltages of the DC sub-microgrids number one and two, respectively. At 4 s, the demand load becomes twice in DC sub-microgrid number one; thus, the DC-bus voltage in the

sub-microgrid is increased. The output DC-bus voltage is not affected when the demand power is changed in the AC sub-microgrid. On the other hand, the output voltages of the DC-AC VSCs are not affected at time 4 s, as shown in Figure 4.29. The output voltage should be the same for the synchronous operation of the parallel-connected AC electrical source (DC-AC VSCs). The output voltage amplitude and phase must be equal to each DC-AC VSC connected in the microgrid. Figure 4.29 clearly shows that there has not been any amplitude or phase difference between the VSC's output voltages.

The responses of the generated and demand power in DC sub-microgrids one and two are presented in Figure 4.30. From Figure 4.30, the supply power from DG-1 and DG-2 is almost equal, where the DC input voltage of the DC-DC VSCs are equally rated. At 4 s, the demand in the DC sub-microgrid one increases; thus, the supply power from the DGs is proportionally increased. However, the supply power at 4 s from DG-3 and DG-4 does not change. The supply power from DG-4 is half of the supply power from DG-3, where DG-3 is rated twice as much as DG-4. When the demand power is changed in the AC sub-microgrid, the generated power of all the DGs is altered.

After feeding the DC sub-microgrid connected load, the surplus currents from the DC sub-microgrids become input currents of the parallel-connected DC-AC VSCs, which is clearly illustrated in Figure 4.31. The shared active powers in the AC sub-microgrid load are precisely proportional to the input currents of the DC-AC VSCs. At 4 s, the input currents and the active supply powers responses do not change, but when the AC power demand is changed at 6 s, the input currents and supply active powers are changed proportionally.

Figure 4.32 represents the proposed controller performance corresponding to the frequency response. At 4 s and 6 s, the DC demand in DC sub-microgrid one

and AC demand in the AC sub-microgrid are changed, respectively. The hybrid DC/AC microgrid frequency is not changed owing to the variation of DC power demand, but the frequency is inversely changed, corresponding to AC demand variation.

Proposed controller performance under short-circuit fault

The unequal generation rating, variation in demand power and short-circuit fault are common issues in power systems. A test setup is considered to include such types of issues as follows:

- The generated power from DG-1 and DG-2 is equal to ($P_1 = P_2$), but the generated power from DG-3 and DG-4 is not equal to ($P_3 = 2P_4$).
- The demand power is fixed at DC-bus-1 and the AC bus, but the demand power at DC-bus-2 becomes twice at 4 s.
- A single-phase to ground fault is considered at 6 s (for 0.1 s time interval) at the terminal of VSI-1.

Figures 4.33-4.36 illustrate the effect of such consideration with respect to different output responses of the islanded hybrid DC/AC microgrid. Figure 4.33 shows the output currents of four different DGs and two different loads which are connected to DC-buses. The output currents at DC-bus-1 are equal, but the output currents at DC-bus-2 are not equal, and demand powers are equal until 4 s for both buses. When the demand power is changed at DC-bus-2, the outputs of DC-bus-1 are not affected. The active powers of VSIs are proportional to the surplus currents of DC-buses, which is cleared from Figure 4.34. The injected DC currents into VSIs are not much affected due to the demand power change

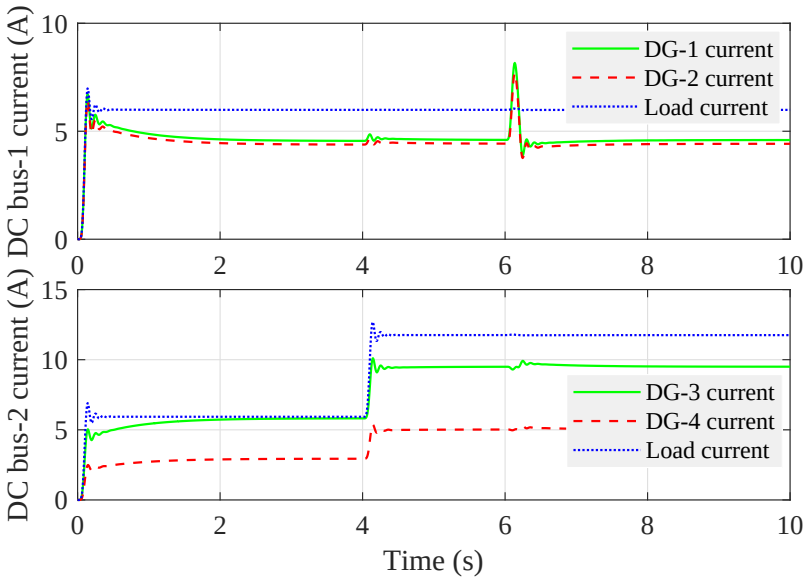

Figure 4.33: DC-buses currents.

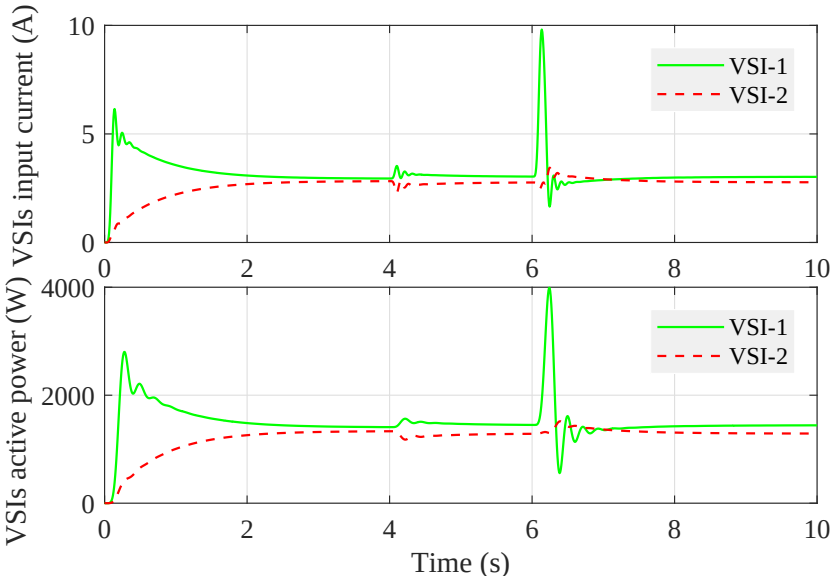

Figure 4.34: Input current and output active power of DC-AC VSCs.

in DC-bus-2 at 4 s. However, those currents are proportionally affected to active power at 6 s when the short-circuit fault has occurred at the VSI-1 terminal.

Figures 4.35 and 4.36 show the three-phase output currents and voltages of VSIs. The output of the AC side is not much affected owing to the change in the DC side. The output AC voltages and currents are heavily affected when the

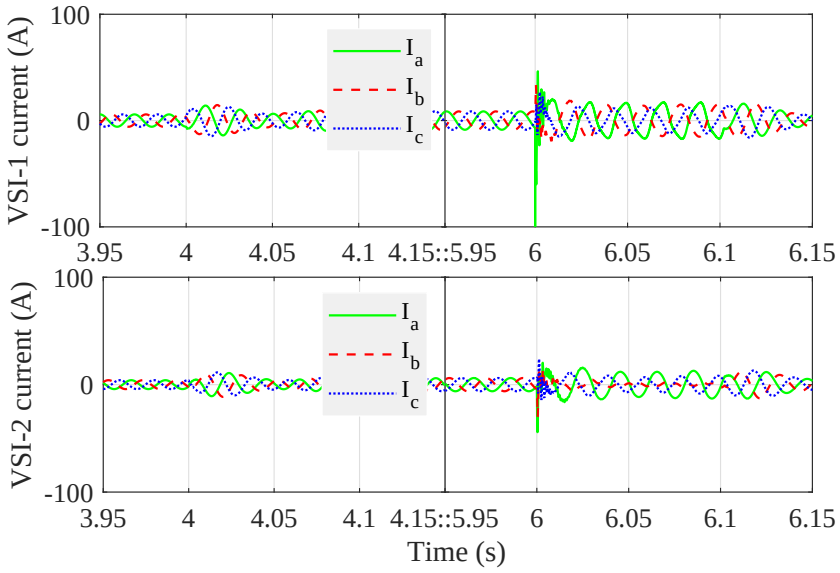

Figure 4.35: Output currents of DC-AC VSCs.

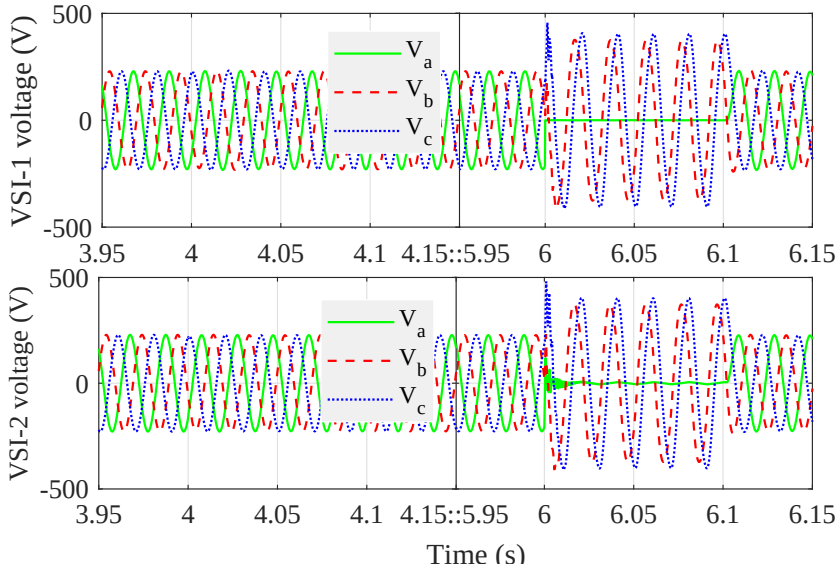

Figure 4.36: Output voltages of DC-AC VSCs.

short-circuit fault is happening on the AC side. As a result, the output currents become very high, and the output voltage of short-circuit phase becomes zero, and the same phase voltage for VSI-2 is about to zero. After fault clearance at 6.1 s, the output voltages come back to the reference voltages, and the output currents also achieved the previous value before short-circuit fault. From the discussion,

it is clear that the proposed SITO-FBL control scheme for the islanded hybrid DC/AC microgrid can provide stable operation under such a worst scenario.

4.7 Chapter Summary

This chapter develops a new nonlinear partial feedback linearized controller for a single-input two-output control problem to improve the transient stability of the islanded microgrids. The designed controllers are implemented on different types of the islanded microgrids. As can be seen, proportional-integral and proportional-derivative controllers have been applied with the SITO-FBL control scheme to control the output voltages and currents. To evaluate the load sharing and bus voltage restores the capability of the proposed controller, different case studies are investigated.

Chapter 5

Dynamic Phasor Modeling and Sensitivity Analysis

The work presented in this chapter has been published in the following articles:

- **Mahmud, M. R.**, Abdou, A. F., and Pota, H.. " Stability analysis of grid-connected photovoltaic systems with dynamic phasor model," *Electronics*, 2019 (https://doi.org/10.3390/electronics8070747).
- **Mahmud, M. R.**, and Pota, H.. " Multi-frequency averaging detail model of distributed photovoltaic generators," (Under preparation).

Abstract

The conventional structure of power systems is experiencing a significant change owing to the high penetration of distributed generators. The ongoing valuation of the power system requires more detailed and precise mathematical modeling techniques for distributed generators based on power electronic interfaces. Al-

though modeling approaches based on state-space averaging have conventionally been applied to mathematically present the dynamics of a power system, the performance of such a model-based system reduces under a high switching frequency. The multi-frequency averaging based higher-index dynamic phasor model has been developed in this chapter, which is new and may offer better approximations of dynamics. The switching frequency sensitivity analysis is demonstrated with a dynamic phasor model of the different structures of a distributed photovoltaic generator.

5.1 Introduction

Nowadays, DGs have gained more acceptance worldwide owing to their environmentally friendly operations and variable prices of fossil fuels. Solar PV generators are becoming one of the most popular DGs because of their sunlight-based power generation. In the literature, there are two modes of operation, standalone and grid-connected [150]. The load integrated into the solar PV generator relies heavily on VSCs; hence, there are more harmonics owing to the presence of such types of PEIs.

The ongoing interactions between power electronic converters (PECs) and DGs introduce new barriers to uncertain power generation associated to stability and control problems [151, 152, 153]. Small-and large-signal assessments are commonly used for the stability analysis of a dynamic system, which is a preliminary evaluation of its consistent operation. In addition, time-domain comprehensive switch simulation tools offer valuable insights into the out-of-turn small-signal behaviours of VSCs [154]. Such a type of analysis cannot provide proper transient behaviour estimation of VSCs. In addition, characterization of

converters to assess instability conditions would need massive simulations, which are time-consuming.

The electromagnetic transient program and quasi-steady-state approximations are well-established simulation tools for power systems, including developed and efficient VSCs [155]. Electromagnetic transient programs are widely accepted at the industry level for the dynamic simulation of systems and controllers [156, 157]; however, they are relatively complicated and time-consuming for larger networks [158]. Additionally, quasi-steady-state approximation models are normally helpful for electromechanical transient types of systems. However, this type of tool cannot work at electromagnetic transients, where PECs are high-frequency switching [159].

Most of the works on distributed PV generators is modeled based on the state-space averaging (SSA) approach to design a controller for the switching input of converters [160, 161, 162, 163]. In the different generation structures, the distributed PV generator, DC-DC, AC-DC, and/or DC-AC type PECs are operated as step-up/down or converted directly to alternative or vice versa to the required feeding load power. In this existing technique, the nonlinear switching function-based VSCs demand a convenient mathematical representation approach, including a higher index. The higher index nonlinearities of VSCs may not be possible to capture using SSA approaches, where only zero indexes of state variables have been addressed [164, 165].

The switching frequency sensitive multi-frequency averaging (MFA) based dynamic phasor (DP) technique is proposed as a straightforward mathematical representation technique for a dynamic system. DC, fundamental can address this approach, and other harmonic components of the state variable as a Fourier series form [165]. Moreover, this modeling technique can provide negligible

flexibility of the harmonic component, which has no considerable impact on the variable. It can be offered with a conventional SSA model when the involvement of fundamental and harmonic elements is not considered.

The dynamic characteristics of PECs with switched circuits may be modeled more accurately using the DP approach than the traditional SSA technique [164, 165, 166]. In [167, 168, 169] proposed a large-signal analysis of a transmission system based on DP for power flow control. The DP technique, which can be provided with a linearized time-invariant model of an unbalanced system, is used as the modeling approach [170, 171, 172]. The DP-based model of single-stage and two-stage grid-connected VSC systems are proposed in [173, 174], where the generation side is considered as an ideal DC supply. However, the grid-connected VSC associated with renewable energy sources is a more realistic challenge.

This chapter presents a detailed DP model with different distributed PV generators for DC and fundamental components. The other originality of this chapter includes all dynamic states owing to the passive energy storage elements. The eigenvalues and sensitivity study of the DP model are also studied, which is an essential evaluation for every dynamic system. The evaluation is performed for various switching frequencies to better understand the sensitivity of the switching frequency of the VSCs in the distributed PV generators.

The contributions of this chapter are as follows:

- Develop multi-frequency averaging based dynamic phasor model for the standalone distributed photovoltaic generator (Section 5.2).
- Develop multi-frequency averaging based dynamic phasor model for the grid-connected distributed photovoltaic generator (Section 5.3).
- Develop multi-frequency averaging based dynamic phasor model for the

Table 5.1: Summary of dynamic modeling methods for distributed PV generators.

Modeling method	Strengths	Weaknesses
Quasi steady state	- First response - Useful for electromechanical transient types of systems	- Cannot work at electromagnetic transients
State space averaging	- Simple and lees complex - Lower order linearized system - Can work at electromagnetic transients	- Cannot properly sense the switching frequency effect
Multi-frequency averaging	- Can work at electromagnetic transient - Can properly sense the switching frequency effect	- Complex - Provided higher order linearized system

two-stage grid-connected distributed photovoltaic generator (Section 5.4).

- Performances are investigated of the developed multi-frequency averaging based dynamic phasor models corresponding to the three different distributed PV generators (Section 5.5).

5.2 Dynamic Phasor Modeling of Standalone Distributed PV Generator

This section develops the MFA-based time-invariant dynamic model of a standalone distributed PV generator. A DC-DC boost VSC is an interface between the standalone distributed photovoltaic generator and the DC load. The detailed mathematical model of the standalone distributed photovoltaic generator is briefly introduced in Subsection 2.4.1 corresponding to Figure 5.1. The DP model of such a system is described in this section.

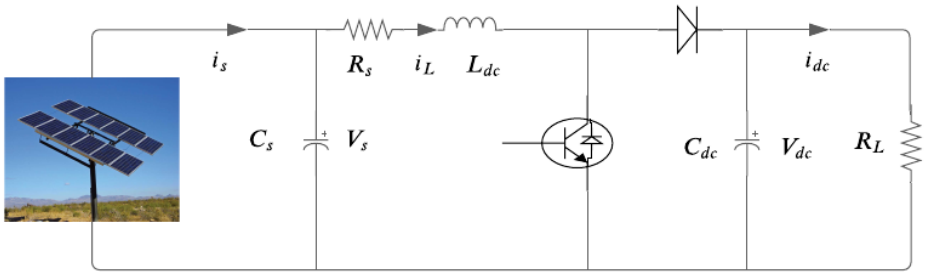

Figure 5.1: Circuit diagram of standalone distributed PV generator.

5.2.1 Conventional state space model

The conventional SSA model plays an essential role in developing the switching frequency-dependent DP model. In Subsection 2.4.1, the SAA model of a standalone distributed PV generator is obtained as follows:

$$\begin{aligned} \frac{dV_s}{dt} &= \frac{1}{C_s}(i_s - i_L) \\ \frac{di_L}{dt} &= \frac{1}{L_{dc}}(V_s - R_s i_L - mV_{dc}) \\ \frac{dV_{dc}}{dt} &= \frac{1}{C_{dc}}\left(mi_L - \frac{V_{dc}}{R_L}\right) \end{aligned} \tag{5.1}$$

The following Subsections 5.2.2 and 5.2.3 will develop the DP model for indexes $k = 0$ and $k = 1$, respectively.

5.2.2 Dynamic phasor model for index zero

The DP model of the DC power-generated standalone distributed solar PV generator corresponding to the index $k = 0$ can be written as follows:

$$\begin{aligned}
\frac{d\overline{V_s}_0}{dt} &= \frac{1}{C_s}\left(i_s - \overline{i_{L0}}\right) \\
\frac{d\overline{i_{L0}}}{dt} &= \frac{1}{L_{dc}}\left(\overline{V_s}_0 - R_s\overline{i_{L0}} - \overline{mV_{dc0}}\right) \\
\frac{d\overline{V_{dc0}}}{dt} &= \frac{1}{C_{dc}}\left(\overline{mi_{L0}} - \frac{1}{R_L}\overline{V_{dc0}}\right)
\end{aligned} \tag{5.2}$$

where $\overline{mV_{dc0}}$ and $\overline{mi_{L0}}$ are the products of the two time-dependent signals. Therefore, the products of the two signals are expressed as follows:

$$\begin{aligned}
\overline{mV_{dc0}} &= \overline{m}_0\overline{V_{dc0}} + 2\overline{m}_1^R\overline{V_{dc1}}^R + 2\overline{m}_1^I\overline{V_{dc1}}^I \\
\overline{mi_{L0}} &= \overline{m}_0\overline{i_{L0}} + 2\overline{m}_1^R\overline{i_{L1}}^R + 2\overline{m}_1^I\overline{i_{L1}}^I.
\end{aligned} \tag{5.3}$$

Finally, the DP model of the standalone distributed PV generator associated with DC-DC VSC owing to the index zero becomes as follows:

$$\begin{aligned}
\frac{d\overline{V_s}_0}{dt} &= \frac{1}{C_s}\left(i_s - \overline{i_{L0}}\right) \\
\frac{d\overline{i_{L0}}}{dt} &= \frac{1}{L_{dc}}\left(\overline{V_s}_0 - R_s\overline{i_{L0}} - \overline{m}_0\overline{V_{dc0}} - 2\overline{m}_1^R\overline{V_{dc1}}^R - 2\overline{m}_1^I\overline{V_{dc1}}^I\right) \\
\frac{d\overline{V_{dc0}}}{dt} &= \frac{1}{C_{dc}}\left(\overline{m}_0\overline{i_{L0}} + 2\overline{m}_1^R\overline{i_{L1}}^R + 2\overline{m}_1^I\overline{i_{L1}}^I - \frac{1}{R_L}\overline{V_{dc0}}\right).
\end{aligned} \tag{5.4}$$

Equation (5.4) represents the modified MFA averages of the standalone distributed PV generator for the index-0. The higher index of the Fourier coefficient might address details harmonic of the state variables, but due to the avoidance, the complexity of the higher-order linear system only index $k = 0$ & 1 are considered. Besides, without considering index $k = 1$, this equation can provide

a conventional SSA model of the standalone distributed PV generator.

5.2.3 Dynamic phasor model for index one

The DP model of the considered standalone distributed PV generator can be obtained corresponding to index one as follows:

$$\begin{aligned}
\frac{d\overline{V_{s1}}^R + jd\overline{V_{s1}}^I}{dt} &= -\frac{1}{C_s}\left(\overline{i_{L1}}^R + j\overline{i_{L1}}^I\right) - j\omega_s\left(\overline{V_{s1}}^R + j\overline{V_{s1}}^I\right) \\
\frac{d\overline{i_{L1}}^R + jd\overline{i_{L1}}^I}{dt} &= \frac{1}{L_{dc}}\left(\overline{V_{s1}}^R + j\overline{V_{s1}}^I\right) - \frac{R_s}{L_{dc}}\left(\overline{i_{L1}}^R + j\overline{i_{L1}}^I\right) \\
&-\frac{1}{L_{dc}}\left(\overline{mV_{dc1}}^R + j\overline{mV_{dc1}}^I\right) - j\omega_s\left(\overline{i_{L1}}^R + j\overline{i_{L1}}^I\right) \\
\frac{d\overline{V_{dc1}}^R + jd\overline{V_{dc1}}^I}{dt} &= \frac{1}{C_{dc}}\left(\overline{mi_{L1}}^R + j\overline{mi_{L1}}^I\right) \\
-\frac{1}{C_{dc}R_L}&\left(\overline{V_{dc1}}^R + j\overline{V_{dc1}}^I\right) - j\omega_s\left(\overline{V_{dc1}}^R + j\overline{V_{dc1}}^I\right)
\end{aligned} \tag{5.5}$$

Every index has two parts in DP modeling approach exact zero; so, the real and imaginary parts of the complex conjugate are differentiated from (5.5) as follows:

$$\begin{aligned}
\frac{d\overline{V_{s1}}^R}{dt} &= -\frac{1}{C_s}\overline{i_{L1}}^R + \omega_s\overline{V_{s1}}^I \\
\frac{d\overline{V_{s1}}^I}{dt} &= -\frac{1}{C_s}\overline{i_{L1}}^I - \omega_s\overline{V_{s1}}^R \\
\frac{d\overline{i_{L1}}^R}{dt} &= \frac{1}{L_{dc}}\left(\overline{V_{s1}}^R - R_s\overline{i_{L1}}^R - \overline{mV_{dc1}}^R\right) + \omega_s\overline{i_{L1}}^I \\
\frac{d\overline{i_{L1}}^I}{dt} &= \frac{1}{L_{dc}}\left(\overline{V_{s1}}^I - R_s\overline{i_{L1}}^I - \overline{mV_{dc1}}^I\right) - \omega_s\overline{i_{L1}}^R \\
\frac{d\overline{V_{dc1}}^R}{dt} &= \frac{1}{C_{dc}}\left(\overline{mi_{L1}}^R - \frac{1}{R_L}\overline{V_{dc1}}^R\right) + \omega_s\overline{V_{dc1}}^I \\
\frac{d\overline{V_{dc1}}^I}{dt} &= \frac{1}{C_{dc}}\left(\overline{mi_{L1}}^I - \frac{1}{R_L}\overline{V_{dc1}}^I\right) - \omega_s\overline{V_{dc1}}^R
\end{aligned} \tag{5.6}$$

where $\overline{mi_{L1}}^R$, $\overline{mi_{L1}}^I$, $\overline{mV_{dc1}}^R$ and $\overline{mV_{dc1}}^I$ are the products of two time-varying signals

that can be obtained as follows:

$$\begin{aligned}
\overline{mV_{dc1}}^R &= \overline{m}_0\overline{V_{dc1}}^R + \overline{m}_1^R\overline{V_{dc0}} \\
\overline{mV_{dc1}}^I &= \overline{m}_0\overline{V_{dc1}}^I + \overline{m}_1^I\overline{V_{dc0}} \\
\overline{mi_{L1}}^R &= \overline{m}_0\overline{i_{L1}}^R + \overline{m}_1^R\overline{i_{L0}} \\
\overline{mi_{L1}}^I &= \overline{m}_0\overline{i_{L1}}^I + \overline{m}_1^I\overline{i_{L0}}.
\end{aligned} \tag{5.7}$$

Substituting (5.7) into (5.6), the MFA model of the standalone distributed PV generator owing to the index $k = 1$ can be written as follows:

$$\begin{aligned}
\frac{d\overline{V_{s1}}^R}{dt} &= -\frac{1}{C_s}\overline{i_{L1}}^R + \omega_s\overline{V_{s1}}^I \\
\frac{d\overline{V_{s1}}^I}{dt} &= -\frac{1}{C_s}\overline{i_{L1}}^I - \omega_s\overline{V_{s1}}^R \\
\frac{d\overline{i_{L1}}^R}{dt} &= \frac{1}{L_{dc}}\left(\overline{V_{s1}}^R - R_s\overline{i_{L1}}^R - \overline{m}_0\overline{V_{dc1}}^R - \overline{m}_1^R\overline{V_{dc0}}\right) + \omega_s\overline{i_{L1}}^I \\
\frac{d\overline{i_{L1}}^I}{dt} &= \frac{1}{L_{dc}}\left(\overline{V_{s1}}^I - R_s\overline{i_{L1}}^I - \overline{m}_0\overline{V_{dc1}}^I - \overline{m}_1^I\overline{V_{dc0}}\right) - \omega_s\overline{i_{L1}}^R \\
\frac{d\overline{V_{dc1}}^R}{dt} &= \frac{1}{C_{dc}}\left(\overline{m}_0\overline{i_{L1}}^R + \overline{m}_1^R\overline{i_{L0}} - \frac{1}{R_L}\overline{V_{dc1}}^R\right) + \omega_s\overline{V_{dc1}}^I \\
\frac{d\overline{V_{dc1}}^I}{dt} &= \frac{1}{C_{dc}}\left(\overline{m}_0\overline{i_{L1}}^I + \overline{m}_1^I\overline{i_{L0}} - \frac{1}{R_L}\overline{V_{dc1}}^I\right) - \omega_s\overline{V_{dc1}}^R.
\end{aligned} \tag{5.8}$$

The characteristic equations (5.4) and (5.8) can provide the MFA model of the standalone distributed PV generator. The following subsection presents the state-space representation of the DP model.

5.2.4 State space representation of dynamic phasor model

The transfer function is a well-established design method for a linear system to obtain such a transfer function from a set of differential equations the state-space

representation plays a crucial role. Thus, the state-space presentation of a group of first-order dynamical equations obtained using the MFA can be represented as follows:

$$\begin{aligned} \frac{d}{dt}\begin{bmatrix}\alpha_0\\ \beta_1\end{bmatrix} &= \begin{bmatrix}A_{11} & A_{12}\\ A_{21} & A_{22}\end{bmatrix}\begin{bmatrix}\alpha_0\\ \beta_1\end{bmatrix} + \begin{bmatrix}B_1\\ 0\end{bmatrix} i_s \\ y &= \begin{bmatrix}C_1 & 0\end{bmatrix}\begin{bmatrix}\alpha_0\\ \beta_1\end{bmatrix} \end{aligned} \tag{5.9}$$

where α_0 and β_1 are the set of state vectors corresponding to index $k = 0$ and $k = 1$, which are written as follows:

$$\overline{\alpha}_0 = \begin{bmatrix}\overline{V_{s0}}\\ \overline{i_{L0}}\\ \overline{V_{dc0}}\end{bmatrix} \quad \& \quad \bar{\beta}_1 = \begin{bmatrix}\overline{V_{s1}}^R\\ \overline{V_{s1}}^I\\ \overline{i_{L1}}^R\\ \overline{i_{L1}}^I\\ \overline{V_{dc1}}^R\\ \overline{V_{dc1}}^I\end{bmatrix}$$

From equations (5.4) and (5.8) submatrices A_{11}, A_{12}, A_{21} and A_{22} of the identity matrix compared to (5.9) can be determined as follows:

$$A_{11} = \begin{bmatrix} 0 & -\frac{1}{C_s} & 0 \\ \frac{1}{L_{dc}} & -\frac{R_s}{L_{dc}} & \frac{\overline{m}_0}{L_{dc}} \\ 0 & \frac{\overline{m}_0}{C_{dc}} & -\frac{1}{R_L C_{dc}} \end{bmatrix}, \qquad A_{12} = \begin{bmatrix} 0 & 0 & 0 & 0 & 0 & 0 \\ 0 & 0 & 0 & 0 & \frac{2\overline{m}_1^R}{L_{dc}} & \frac{2\overline{m}_1^I}{L_{dc}} \\ 0 & 0 & -\frac{2\overline{m}_1^R}{C_{dc}} & -\frac{2\overline{m}_1^R}{C_{dc}} & 0 & 0 \end{bmatrix}$$

,

$$A_{21} = \begin{bmatrix} 0 & 0 & 0 \\ 0 & 0 & 0 \\ 0 & 0 & \frac{\overline{m}_1^R}{L_{dc}} \\ 0 & 0 & \frac{\overline{m}_1^I}{L_{dc}} \\ 0 & -\frac{\overline{m}_1^R}{C_{dc}} & 0 \\ 0 & -\frac{\overline{m}_1^R}{C_{dc}} & 0 \end{bmatrix}, \qquad A_{22} = \begin{bmatrix} 0 & \omega_s & -\frac{1}{C_s} & 0 & 0 & 0 \\ -\omega_s & 0 & 0 & -\frac{1}{C_s} & 0 & 0 \\ \frac{1}{L_{dc}} & 0 & -\frac{R_s}{L_{dc}} & \omega_s & -\frac{m_0}{L_{dc}} & 0 \\ 0 & \frac{1}{L_{dc}} & -\omega_s & -\frac{R_s}{L_{dc}} & 0 & -\frac{m_0}{L_{dc}} \\ 0 & \frac{m_0}{C_{dc}} & 0 & -\frac{1}{R_L C_{dc}} & 0 & \omega_s \\ 0 & 0 & 0 & \frac{u_0}{C_{dc}} & -\omega_s & -\frac{1}{R_L C_{dc}} \end{bmatrix}.$$

Finally, the input and output matrices can be determined as follows:

$$B_1 = \begin{bmatrix} \frac{1}{C_s} \\ 0 \\ 0 \end{bmatrix} \quad \& \quad C_1 = \begin{bmatrix} 0 & 0 & 1 \end{bmatrix}.$$

The submatrices A_{11}, A_{12}, A_{21} and A_{22} are the constitutional components of matrix A. This matrix form demonstrates wide analytical properties, and the switching frequency sensitivity analysis is analysed using both eigenvalue analysis and time- and frequency-domain simulation results.

5.3 Dynamic Phasor Modeling of Grid-Connected Distributed PV Generator

The grid-connected distributed PV generator is one of the most common configurations for large-scale power generation. This section describes the expansion of a detailed mathematical model based on the MFA-based DP model corresponding to Figure 5.2.

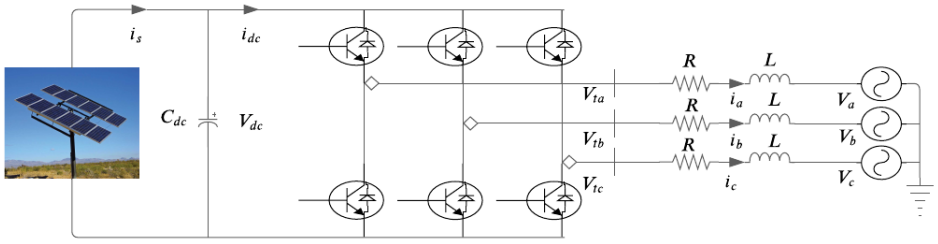

Figure 5.2: Circuit diagram of grid-connected distributed PV generator.

5.3.1 Conventional state space model

The conventional SSA characteristic model of the grid-connected distributed PV generator in the dq frame can be written as follows:

$$\begin{aligned}
\frac{dV_{dc}}{dt} &= \frac{1}{C_{dc}}\left(i_s - i_d m_d - i_q m_q\right) \\
\frac{di_d}{dt} &= \frac{V_{dc}}{2L}m_d - \frac{R}{L}i_d - \frac{V_d}{L} + \omega i_q \\
\frac{di_q}{dt} &= \frac{V_{dc}}{2L}m_q - \frac{R}{L}i_q - \frac{V_q}{L} - \omega i_d.
\end{aligned} \tag{5.10}$$

The details of equation (5.10) are provided in Section 2.4. The DP model is developed in the following subsections based on equation (5.10).

5.3.2 Dynamic phasor model for index zero

The DP model of the grid-connected distributed PV generator for zero index can be obtained as follows:

$$\begin{aligned}
\frac{d\overline{V_{dc0}}}{dt} &= \frac{1}{C_{dc}}\left(i_s - \overline{m_d i_{d0}} - \overline{m_q i_{q0}}\right) \\
\frac{d\overline{i_{d0}}}{dt} &= \frac{1}{2L}\overline{m_d V_{dc0}} - \frac{R}{L}\overline{i_{d0}} - \frac{V_d}{L} + \omega\overline{i_{q0}} \\
\frac{d\overline{i_{q0}}}{dt} &= \frac{1}{2L}\overline{m_q V_{dc_0}} - \frac{R}{L}\overline{i_{q0}} - \frac{V_q}{L} - \omega\overline{i_{d0}}
\end{aligned} \tag{5.11}$$

where $\overline{m_d i_{d0}}$, $\overline{m_q i_{q0}}$, $\overline{m_d V_{dc0}}$ and $\overline{m_q V_{dc0}}$ are the products of the two-time dependent function. Therefore, the products of the two signals are obtained as follows:

$$\begin{aligned}
\overline{m_d i_{d0}} &= \overline{m_{d0}}\,\overline{i_{d0}} + 2\overline{m_{d1}}^R\overline{i_{d1}}^R + 2\overline{m_{d1}}^I\overline{i_{d1}}^I \\
\overline{m_q i_{q0}} &= \overline{m_{q0}}\,\overline{i_{q0}} + 2\overline{m_{q1}}^R\overline{i_{q1}}^R + 2\overline{m_{q1}}^I\overline{i_{q1}}^I \\
\overline{m_d V_{dc0}} &= \overline{m_{d0}}\,\overline{V_{dc0}} + 2\overline{m_{d1}}^R\overline{V_{dc1}}^R + 2\overline{m_{d1}}^I\overline{V_{dc1}}^I \\
\overline{m_q V_{dc0}} &= \overline{m_{q0}}\,\overline{V_{dc0}} + 2\overline{m_{q1}}^R\overline{V_{dc1}}^R + 2\overline{m_{q1}}^I\overline{V_{dc1}}^I
\end{aligned} \tag{5.12}$$

Finally, the DP model of the grid-connected distributed PV generator corresponding to index zero is as follows:

$$\begin{aligned}
\frac{d\overline{V_{dc0}}}{dt} &= \frac{1}{C_{dc}}\left(i_s - \overline{m_{d0}}\,\overline{i_{d0}} - 2\overline{m_{d1}}^R\overline{i_{d1}}^R - 2\overline{m_{d1}}^I\overline{i_{d1}}^I - \overline{m_{q0}}\,\overline{i_{q0}} - 2\overline{m_{q1}}^R\overline{i_{q1}}^R - 2\overline{m_{q1}}^I\overline{i_{q1}}^I\right) \\
\frac{d\overline{i_{d0}}}{dt} &= \frac{1}{2L}\left(\overline{m_{d0}}\,\overline{V_{dc0}} + 2\overline{m_{d1}}^R\overline{V_{dc1}}^R + 2\overline{m_{d1}}^I\overline{V_{dc1}}^I\right) - \frac{R}{L}\overline{i_{d0}} - \frac{V_d}{L} + \omega\overline{i_{q0}} \\
\frac{d\overline{i_{q0}}}{dt} &= \frac{1}{2L}\left(\overline{m_{q0}}\,\overline{V_{dc0}} + 2\overline{m_{q1}}^R\overline{V_{dc1}}^R + 2\overline{m_{q1}}^I\overline{V_{dc1}}^I\right) - \frac{R}{L}\overline{i_{q0}} - \frac{V_q}{L} - \omega\overline{i_{d0}}.
\end{aligned} \tag{5.13}$$

Equation (5.13) represents the simplified averages for index-0 of the grid-connected distributed PV generator. Without considering the presence of index-1 terms, equation (5.13) provide a standard SSA model of the system.

5.3.3 Dynamic phasor model for index one

A higher index of the Fourier coefficient might be able to describe the higher-order harmonics of the state variables. The DP model can be obtained corresponding

to index one of the grid-connected distributed PV generators as follows:

$$\begin{aligned}
\frac{d\overline{V_{dc1}}^R + jd\overline{V_{dc1}}^I}{dt} &= -\frac{1}{C_{dc}}\left(\overline{m_d i_{d1}}^R + j\overline{m_d i_{d1}}^I + \overline{m_q i_{q1}}^R + j\overline{m_q i_{q1}}^I\right) \\
&\quad -j\omega_s\left(\overline{V_{dc1}}^R + j\overline{V_{dc1}}^I\right) \\
\frac{d\overline{i_{d1}}^R + jd\overline{i_{d1}}^I}{dt} &= \frac{1}{2L}\left(\overline{m_d V_{dc1}}^R + j\overline{m_d V_{dc1}}^I\right) - \frac{R}{L}\left(\overline{i_{d1}}^R + j\overline{i_{d1}}^I\right) \\
&\quad +\omega\left(\overline{i_{q1}}^R + j\overline{i_{q1}}^I\right) - j\omega_s\left(\overline{i_{d1}}^R + j\overline{i_{d1}}^I\right) \\
\frac{d\overline{i_{q1}}^R + jd\overline{i_{q1}}^I}{dt} &= \frac{1}{2L}\left(\overline{m_q V_{dc1}}^R + j\overline{m_q V_{dc1}}^I\right) - \frac{R}{L}\left(\overline{i_{q1}}^R + j\overline{i_{q1}}^I\right) \\
&\quad -\omega\left(\overline{i_{d1}}^R + j\overline{i_{d1}}^I\right) - j\omega_s\left(\overline{i_{q1}}^R + j\overline{i_{q1}}^I\right)
\end{aligned} \tag{5.14}$$

where the real and imaginary parts of the complex conjugate are differentiated by following:

$$\begin{aligned}
\frac{d\overline{V_{dc1}}^R}{dt} &= -\frac{1}{C_{dc}}\left(\overline{m_d i_{d1}}^R + \overline{m_q i_{q1}}^R\right) + \omega_s\overline{V_{dc1}}^I \\
\frac{d\overline{V_{dc1}}^I}{dt} &= -\frac{1}{C_{dc}}\left(\overline{m_d i_{d1}}^I + \overline{m_q i_{q1}}^I\right) - \omega_s\overline{V_{dc1}}^R \\
\frac{d\overline{i_{d1}}^R}{dt} &= \frac{1}{2L}\overline{m_d V_{dc1}}^R - \frac{R}{L}\overline{i_{d1}}^R + \omega\overline{i_{q1}}^R + \omega_s\overline{i_{d1}}^I \\
\frac{d\overline{i_{d1}}^I}{dt} &= \frac{1}{2L}\overline{m_d V_{dc1}}^I - \frac{R}{L}\overline{i_{d1}}^I + \omega\overline{i_{q1}}^I - \omega_s\overline{i_{d1}}^R \\
\frac{d\overline{i_{q1}}^R}{dt} &= \frac{1}{2L}\overline{m_q V_{dc1}}^R - \frac{R}{L}\overline{i_{q1}}^R - \omega\overline{i_{d1}}^R + \omega_s\overline{i_{q1}}^I \\
\frac{d\overline{i_{q1}}^I}{dt} &= \frac{1}{2L}\overline{m_q V_{dc1}}^I - \frac{R}{L}\overline{i_{q1}}^I - \omega\overline{i_{d1}}^I - \omega_s\overline{i_{q1}}^R.
\end{aligned} \tag{5.15}$$

In equations (5.15), $\overline{m_d i_{d1}}^R$, $\overline{m_d i_{d1}}^I$, $\overline{m_q i_{q1}}^R$, $\overline{m_q i_{q1}}^I$, $\overline{m_d V_{dc1}}^R$, $\overline{m_d V_{dc1}}^I$, $\overline{m_q V_{dc_1}}^R$ and

$\overline{m_q V_{dc1}}^I$ are products of two time-varying signals, which can be obtained as follows:

$$\begin{aligned}
\overline{m_d i_{d1}}^R &= \overline{m_{d1}}^R \overline{i_{d0}} + \overline{m_{d0}}\,\overline{i_{d1}}^R \\
\overline{m_q i_{q1}}^R &= \overline{m_{q1}}^R \overline{i_{q0}} + \overline{m_{q0}}\,\overline{i_{q1}}^R \\
\overline{m_d i_{d1}}^I &= \overline{m_{d1}}^I \overline{i_{d0}} + \overline{m_{d0}}\,\overline{i_{d1}}^I \\
\overline{m_q i_{q1}}^I &= \overline{m_{q1}}^I \overline{i_{q0}} + \overline{m_{q0}}\,\overline{i_{q1}}^I \\
\overline{m_d V_{dc1}}^R &= \overline{m_{d1}}^R \overline{V_{dc0}} + \overline{m_{d0}}\,\overline{V_{dc1}}^R \\
\overline{m_d V_{dc1}}^I &= \overline{m_{d1}}^I \overline{V_{dc0}} + \overline{m_{d0}}\,\overline{V_{dc1}}^I \\
\overline{m_q V_{dc1}}^R &= \overline{m_{q1}}^R \overline{V_{dc0}} + \overline{m_{q0}}\,\overline{V_{dc1}}^R \\
\overline{m_q V_{dc1}}^I &= \overline{m_{q1}}^I \overline{V_{dc0}} + \overline{m_{q0}}\,\overline{V_{dc1}}^I.
\end{aligned} \tag{5.16}$$

Substituting (5.16) into (5.15), the MFA model of the grid-connected distributed PV generator owing to the index $k = 1$ can be written as follows:

$$\begin{aligned}
\frac{d\overline{V_{dc1}}^R}{dt} &= -\frac{1}{C_{dc}}\left(\overline{m_{d1}}^R \overline{i_{d0}} + \overline{m_{d0}}\,\overline{i_{d1}}^R + \overline{m_{q1}}^R \overline{i_{q0}} + \overline{m_{q0}}\,\overline{i_{q1}}^R\right) + \omega_s \overline{V_{dc1}}^I \\
\frac{d\overline{V_{dc1}}^I}{dt} &= -\frac{1}{C_{dc}}\left(\overline{m_{d1}}^I \overline{i_{d0}} + \overline{m_{d0}}\,\overline{i_{d1}}^I + \overline{m_{q1}}^I \overline{i_{q0}} + \overline{m_{q0}}\,\overline{i_{q1}}^I\right) - \omega_s \overline{V_{dc1}}^R \\
\frac{d\overline{i_{d1}}^R}{dt} &= \frac{1}{2L}\left(\overline{m_{d1}}^R \overline{V_{dc0}} + \overline{m_{d0}}\,\overline{V_{dc1}}^R\right) - \frac{R}{L}\overline{i_{d1}}^R + \omega \overline{i_{q1}}^R + \omega_s \overline{i_{d1}}^I \\
\frac{d\overline{i_{d1}}^I}{dt} &= \frac{1}{2L}\left(\overline{m_{d1}}^I \overline{V_{dc0}} + \overline{m_{d0}}\,\overline{V_{dc1}}^I\right) - \frac{R}{L}\overline{i_{d1}}^I + \omega \overline{i_{q1}}^I - \omega_s \overline{i_{d1}}^R \\
\frac{d\overline{i_{q1}}^R}{dt} &= \frac{1}{2L}\left(\overline{m_{q1}}^R \overline{V_{dc0}} + \overline{m_{q0}}\,\overline{V_{dc1}}^R\right) - \frac{R}{L}\overline{i_{q1}}^R - \omega \overline{i_{d1}}^R + \omega_s \overline{i_{q1}}^I \\
\frac{d\overline{i_{q1}}^I}{dt} &= \frac{1}{2L}\left(\overline{m_{q1}}^I \overline{V_{dc0}} + \overline{m_{q0}}\,\overline{V_{dc1}}^I\right) - \frac{R}{L}\overline{i_{q1}}^I - \omega \overline{i_{d1}}^I - \omega_s \overline{i_{q1}}^R.
\end{aligned} \tag{5.17}$$

Equations (5.13) and (5.17) represent a completed DP model of the grid-connected distributed PV generator corresponding to the indexes k = 0 & 1.

5.3.4 State space representation of dynamic phasor model

State space representation is a well-established design and analytical tool for linear systems. The developed DP model of the grid-connected distributed PV generator (5.13) and (5.17) can be formulated as follows:

$$\begin{aligned} \frac{d}{dt}\begin{bmatrix}\alpha_0\\ \beta_1\end{bmatrix} &= \begin{bmatrix}A_{11} & A_{12}\\ A_{21} & A_{22}\end{bmatrix}\begin{bmatrix}\alpha_0\\ \beta_1\end{bmatrix} + \begin{bmatrix}B_1\\ 0\end{bmatrix} i_s \\ y &= \begin{bmatrix}C_1 & 0\\ C_2 & 0\end{bmatrix}\begin{bmatrix}\alpha_0\\ \beta_1\end{bmatrix} \end{aligned} \tag{5.18}$$

where α_0 and β_1 are the set of state vectors corresponding to $k = 0$ and $k = 1$, which are written as follows:

$$\overline{\alpha}_0 = \begin{bmatrix}\overline{V_{dc0}}\\ \overline{i_{d0}}\\ \overline{i_{q0}}\end{bmatrix} \quad \& \quad \bar{\beta}_1 = \begin{bmatrix}\overline{V_{dc1}}^R\\ \overline{V_{dc1}}^I\\ \overline{i_{d1}}^R\\ \overline{i_{d1}}^I\\ \overline{i_{q1}}^R\\ \overline{i_{q1}}^I\end{bmatrix}.$$

These state variables have been separated into two different sets, $\overline{\alpha}_0$ defines the set of state variables for index-0 and $\overline{\beta}_1$ defines the set of state variables for index-1. Compared to the standard state-space form of (5.18) with the ninth-order differential equations in (5.13) and (5.17), the submatrices of A can

be obtained as follows:

$$A_{11} = \begin{bmatrix} 0 & -\frac{\overline{m_{d0}}}{C_{dc}} & -\frac{\overline{m_{q0}}}{C_{dc}} \\ \frac{\overline{m_{d0}}}{2L} & -\frac{R}{L} & \omega \\ \frac{\overline{m_{q0}}}{2L} & -\omega & -\frac{R}{L} \end{bmatrix}$$

$$A_{12} = \begin{bmatrix} 0 & 0 & -\frac{2\overline{m_{d1}}^R}{C_{dc}} & -\frac{2\overline{m_{d1}}^I}{C_{dc}} & -\frac{2\overline{m_{q1}}^R}{C_{dc}} & -\frac{2\overline{m_{q1}}^I}{C_{dc}} \\ \frac{\overline{m_{d1}}^R}{L} & \frac{\overline{m_{d1}}^I}{L} & 0 & 0 & 0 & 0 \\ \frac{\overline{m_{q1}}^R}{L} & \frac{\overline{m_{q1}}^I}{L} & 0 & 0 & 0 & 0 \end{bmatrix},$$

$$A_{21} = \begin{bmatrix} 0 & -\frac{\overline{m_{d1}}^R}{C_{dc}} & -\frac{\overline{m_{q1}}^R}{C_{dc}} \\ 0 & -\frac{\overline{m_{d1}}^I}{C_{dc}} & -\frac{\overline{m_{d1}}^I}{C_{dc}} \\ \frac{\overline{m_{d1}}^R}{2L} & 0 & 0 \\ \frac{\overline{m_{d1}}^I}{2L} & 0 & 0 \\ \frac{\overline{m_{q1}}^R}{2L} & 0 & 0 \\ \frac{\overline{m_{q1}}^I}{2L} & 0 & 0 \end{bmatrix}$$

$$A_{22} = \begin{bmatrix} 0 & \omega_s & -\frac{\overline{m_{d0}}}{C_{dc}} & 0 & -\frac{\overline{m_{q0}}}{C_{dc}} & 0 \\ -\omega_s & 0 & 0 & -\frac{\overline{m_{d0}}}{C_{dc}} & 0 & -\frac{\overline{m_{d0}}}{C_{dc}} \\ \frac{\overline{m_{d0}}}{2L} & 0 & -\frac{R}{L} & \omega_s & \omega & 0 \\ 0 & \frac{\overline{m_{d0}}}{2L} & -\omega_s & -\frac{R}{L} & 0 & \omega \\ \frac{\overline{m_{q0}}}{2L} & 0 & -\omega & 0 & -\frac{R}{L} & \omega_s \\ 0 & \frac{\overline{m_{q0}}}{2L} & 0 & -\omega & -\omega_s & -\frac{R}{L} \end{bmatrix}.$$

The input matrix is written as follows for the input variables $\overline{m_{d0}}$ and $\overline{m_{q0}}$:

$$B_1 = \begin{bmatrix} \frac{1}{C_{dc}} & 0 & 0 \end{bmatrix}^T.$$

Finally, the output matrices are written as follows for the two output variables

$\overline{i_{d0}}$ and $\overline{i_{q0}}$:

$$C_1 = \begin{bmatrix} 0 & 1 & 0 \end{bmatrix} \quad \& \quad C_2 = \begin{bmatrix} 0 & 0 & 1 \end{bmatrix}.$$

The submatrices A_{11}, A_{12}, A_{21} and A_{22} are the constitutional components of matrix A. This matrix form demonstrates wide analytical properties, and both eigenvalue analysis analyses the switching frequency sensitivity analyses of the grid-connected distributed PV generators, and time- and frequency-domain simulation results.

5.4 Dynamic Phasor Modeling of Two-Stage Distributed PV Generator

The two-stage distributed PV generator combines a standalone and a grid-connected distributed PV generators. This section describes the expansion of a detailed mathematical model based on the DP modeling approach corresponding to Figure 5.3.

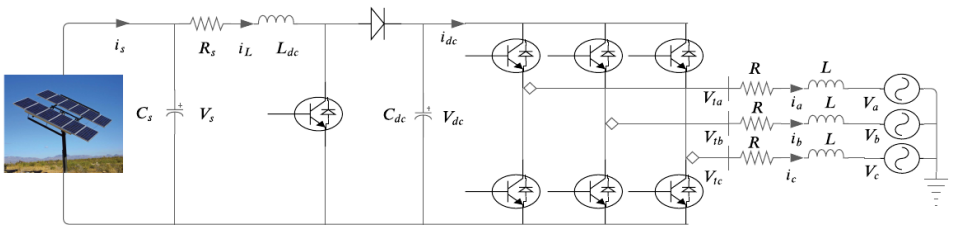

Figure 5.3: Circuit diagram of two-stage PV generator.

5.4.1 Conventional state space model

The conventional SSA model of the two-stage distributed PV generator with a dq frame can be written as follows:

$$\begin{aligned}
\frac{dV_s}{dt} &= \frac{1}{C_s}\left(i_s - i_L\right) \\
\frac{di_L}{dt} &= \frac{1}{L_{dc}}\left(V_s - mV_{dc}\right) \\
\frac{dV_{dc}}{dt} &= \frac{1}{C_{dc}}\left(mi_L - m_d i_d - m_q i_q\right) \\
\frac{di_d}{dt} &= \frac{V_{dc}}{2L}m_d - \frac{R}{L}i_d - \frac{V_d}{L} + \omega i_q \\
\frac{di_q}{dt} &= \frac{V_{dc}}{2L}m_q - \frac{R}{L}i_q - \frac{V_q}{L} - \omega i_d
\end{aligned} \tag{5.19}$$

The DP model of the two-stage distributed PV generator is developed in the following subsections corresponding to index k = 0 & 1.

5.4.2 Dynamic phasor model for index zero

The DP model of the two-stage distributed PV generator for the zero indexes is obtained as follows:

$$\begin{aligned}
\frac{d\overline{V_{s0}}}{dt} &= \frac{1}{C_s}\left(i_s - \overline{i_{L0}}\right) \\
\frac{d\overline{i_{L0}}}{dt} &= \frac{1}{L_{dc}}\left(\overline{V_{s0}} - \overline{mV_{dc0}}\right) \\
\frac{d\overline{V_{dc0}}}{dt} &= \frac{1}{C_{dc}}\left(\overline{mi_{L0}} - \overline{m_d i_{d0}} - \overline{m_q i_{q0}}\right) \\
\frac{d\overline{i_{d0}}}{dt} &= \frac{1}{2L}\overline{m_d V_{dc0}} - \frac{R}{L}\overline{i_{d0}} - \frac{V_d}{L} + \omega\overline{i_{q0}} \\
\frac{d\overline{i_{q0}}}{dt} &= \frac{1}{2L}\overline{m_q V_{dc_0}} - \frac{R}{L}\overline{i_{q0}} - \frac{V_q}{L} - \omega\overline{i_{d0}}
\end{aligned} \tag{5.20}$$

where $\overline{mV_{dc0}}$, $\overline{mi_{L0}}$, $\overline{m_d i_{d0}}$, $\overline{m_q i_{q0}}$, $\overline{m_d V_{dc0}}$ and $\overline{m_q V_{dc_0}}$ are the products of two the time-varying signals. Therefore, the products of the two signals are expressed as

follows:

$$\begin{aligned}
\overline{mV_{dc0}} &= \overline{m}_0\overline{V_{dc0}} + 2\overline{m}_1^R\overline{V_{dc1}}^R + 2\overline{m}_1^I\overline{V_{dc1}}^I \\
\overline{mi_{L0}} &= \overline{m}_0\overline{i_{L0}} + 2\overline{m}_1^R\overline{i_{L1}}^R + 2\overline{m}_1^I\overline{i_{L1}}^I \\
\overline{m_d i_{d0}} &= \overline{m_{d0}}\,\overline{i_{d0}} + 2\overline{m_{d1}}^R\overline{i_{d1}}^R + 2\overline{m_{d1}}^I\overline{i_{d1}}^I \\
\overline{m_q i_{q0}} &= \overline{m_{q0}}\,\overline{i_{q0}} + 2\overline{m_{q1}}^R\overline{i_{q1}}^R + 2\overline{m_{q1}}^I\overline{i_{q1}}^I \\
\overline{m_d V_{dc0}} &= \overline{m_{d0}}\,\overline{V_{dc0}} + 2\overline{m_{d1}}^R\overline{V_{dc1}}^R + \overline{m_{d1}}^I\overline{V_{dc1}}^I \\
\overline{m_q V_{dc0}} &= \overline{m_{q0}}\,\overline{V_{dc0}} + 2\overline{m_{q1}}^R\overline{V_{dc1}}^R + \overline{m_{q1}}^I\overline{V_{dc1}}^I
\end{aligned} \tag{5.21}$$

Finally, the DP model of the two-stage distributed PV generator is as follows because of the index zero:

$$\begin{aligned}
\frac{d\overline{V_{s0}}}{dt} &= \frac{1}{C_s}\left(i_s - \overline{i_{L0}}\right) \\
\frac{d\overline{i_{L0}}}{dt} &= \frac{1}{L_{dc}}\left(\overline{V_{s0}} - \overline{m}_0\overline{V_{dc0}} - 2\overline{m}_1^R\overline{V_{dc1}}^R - 2\overline{m}_1^I\overline{V_{dc1}}^I\right) \\
\frac{d\overline{V_{dc0}}}{dt} &= \frac{1}{C_{dc}}\left(\overline{m}_0\overline{i_{L0}} + 2\overline{m}_1^R\overline{i_{L1}}^R + 2\overline{m}_1^I\overline{i_{L1}}^I - \overline{m_{d0}}\,\overline{i_{d0}} - 2\overline{m_{d1}}^R\overline{i_{d1}}^R\right) \\
&\quad + \frac{1}{C_{dc}}\left(-2\overline{m_{d1}}^I\overline{i_{d1}}^I - \overline{m_{q0}}\,\overline{i_{q0}} - 2\overline{m_{q1}}^R\overline{i_{q1}}^R - 2\overline{m_{q1}}^I\overline{i_{q1}}^I\right) \\
\frac{d\overline{i_{d0}}}{dt} &= \frac{1}{2L}\left(\overline{m_{d0}}\,\overline{V_{dc0}} + 2\overline{m_{d1}}^R\overline{V_{dc1}}^R + \overline{m_{d1}}^I\overline{V_{dc1}}^I\right) - \frac{R}{L}\overline{i_{d0}} - \frac{V_d}{L} + \omega\overline{i_{q0}} \\
\frac{d\overline{i_{q0}}}{dt} &= \frac{1}{2L}\left(\overline{m_{q0}}\,\overline{V_{dc0}} + 2\overline{m_{q1}}^R\overline{V_{dc1}}^R + \overline{m_{q1}}^I\overline{V_{dc1}}^I\right) - \frac{R}{L}\overline{i_{q0}} - \frac{V_q}{L} - \omega\overline{i_{d0}}.
\end{aligned} \tag{5.22}$$

These equations characterize the modified averages for index-0 of the two-stage distributed PV generator. Without considering the presence of index-1 terms, these modified averages of index-0 provide a standard state-space averaged model of the two-stage distributed PV generator.

5.4.3 Dynamic phasor model for index one

The higher index of the Fourier coefficient for the two-stage distributed PV generator can address the higher-order harmonics of the state variables. The DP model of the two-stage distributed PV generator is obtained from index one as follows:

$$
\begin{aligned}
\frac{d\overline{V_{s1}}^R + jd\overline{V_{s1}}^I}{dt} &= -\frac{1}{C_s}\left(\overline{i_{L1}}^R + j\overline{i_{L1}}^I\right) - j\omega_s\left(\overline{V_{s1}}^R + j\overline{V_{s1}}^I\right) \\
\frac{d\overline{i_{L1}}^R + jd\overline{i_{L1}}^I}{dt} &= \frac{1}{L_{dc}}\left(\overline{V_{s1}}^R + j\overline{V_{s1}}^I\right) - \frac{1}{L_{dc}}\left(\overline{mV_{dc1}}^R + j\overline{mV_{dc1}}^I\right) \\
&\quad -j\omega_s\left(\overline{i_{L1}}^R + j\overline{i_{L1}}^I\right) \\
\frac{d\overline{V_{dc1}}^R + jd\overline{V_{dc1}}^I}{dt} &= \frac{1}{C_{dc}}\left(\overline{mi_{L1}}^R + j\overline{mi_{L1}}^I\right) - \frac{1}{C_{dc}}\left(\overline{m_d i_{d1}}^R + j\overline{m_d i_{d1}}^I\right) \\
&\quad -\frac{1}{C_{dc}}\left(\overline{m_q i_{q1}}^R + j\overline{m_q i_{q1}}^I\right) - j\omega_s\left(\overline{V_{dc1}}^R + j\overline{V_{dc1}}^I\right) \\
\frac{d\overline{i_{d1}}^R + jd\overline{i_{d1}}^I}{dt} &= \frac{1}{2L}\left(\overline{m_d V_{dc1}}^R + j\overline{m_d V_{dc1}}^I\right) - \frac{R}{L}\left(\overline{i_{d1}}^R + j\overline{i_{d1}}^I\right) \\
&\quad +\omega\left(\overline{i_{q1}}^R + j\overline{i_{q1}}^I\right) - j\omega_s\left(\overline{i_{d1}}^R + j\overline{i_{d1}}^I\right) \\
\frac{d\overline{i_{q1}}^R + jd\overline{i_{q1}}^I}{dt} &= \frac{1}{2L}\left(\overline{m_q V_{dc1}}^R + j\overline{m_q V_{dc1}}^I\right) - \frac{R}{L}\left(\overline{i_{q1}}^R + j\overline{i_{q1}}^I\right) \\
&\quad -\omega\left(\overline{i_{d1}}^R + j\overline{i_{d1}}^I\right) - j\omega_s\left(\overline{i_{q1}}^R + j\overline{i_{q1}}^I\right)
\end{aligned}
\tag{5.23}
$$

where the real and imaginary parts of the complex conjugate are separated as follows:

$$
\begin{aligned}
\frac{d\overline{V_{s1}}^R}{dt} &= -\frac{1}{C_s}\overline{i_{L1}}^R + \omega_s \overline{V_{s1}}^I \\
\frac{d\overline{V_{s1}}^I}{dt} &= -\frac{1}{C_s}\overline{i_{L1}}^I - \omega_s \overline{V_{s1}}^R \\
\frac{d\overline{i_{L1}}^R}{dt} &= \frac{1}{L_{dc}}\left(\overline{V_{s1}}^R - \overline{mV_{dc1}}^R\right) + \omega_s \overline{i_{L1}}^I \\
\frac{d\overline{i_{L1}}^I}{dt} &= \frac{1}{L_{dc}}\left(\overline{V_{s1}}^I - \overline{mV_{dc1}}^I\right) - \omega_s \overline{i_{L1}}^R \\
\frac{d\overline{V_{dc1}}^R}{dt} &= \frac{1}{C_{dc}}\left(\overline{mi_{L1}}^R - \overline{m_d i_{d1}}^R - \overline{m_q i_{q1}}^R\right) + \omega_s \overline{V_{dc1}}^I \\
\frac{d\overline{V_{dc1}}^I}{dt} &= \frac{1}{C_{dc}}\left(\overline{mi_{L1}}^I - \overline{m_d i_{d1}}^I - \overline{m_q i_{q1}}^I\right) - \omega_s \overline{V_{dc1}}^R \\
\frac{d\overline{i_{d1}}^R}{dt} &= \frac{1}{2L}\overline{m_d V_{dc1}}^R - \frac{R}{L}\overline{i_{d1}}^R + \omega \overline{i_{q1}}^R + \omega_s \overline{i_{d1}}^I \\
\frac{d\overline{i_{d1}}^I}{dt} &= \frac{1}{2L}\overline{m_d V_{dc1}}^I - \frac{R}{L}\overline{i_{d1}}^I + \omega \overline{i_{q1}}^R - \omega_s \overline{i_{d1}}^R \\
\frac{d\overline{i_{q1}}^R}{dt} &= \frac{1}{2L}\overline{m_q V_{dc1}}^R - \frac{R}{L}\overline{i_{q1}}^R - \omega \overline{i_{d1}}^R + \omega_s \overline{i_{q1}}^I \\
\frac{d\overline{i_{q1}}^I}{dt} &= \frac{1}{2L}\overline{m_q V_{dc1}}^I - \frac{R}{L}\overline{i_{q1}}^I - \omega \overline{i_{d1}}^I - \omega_s \overline{i_{q1}}^R
\end{aligned}
\tag{5.24}
$$

where $\overline{mV_{dc1}}^R$, $\overline{mV_{dc1}}^I$, $\overline{mi_{L1}}^R$, $\overline{mi_{L1}}^I$, $\overline{m_d i_{d1}}^R$, $\overline{m_d i_{d1}}^I$, $\overline{m_q i_{q1}}^R$, $\overline{m_q i_{q1}}^I$, $\overline{m_d V_{dc1}}^R$, $\overline{m_d V_{dc1}}^I$, $\overline{m_q V_{dc_1}}^R$ and $\overline{m_q V_{dc_1}}^I$ are product of two time-varying signals, those can be obtained as follows:

$$
\begin{aligned}
\overline{mV_{dc1}}^R &= \overline{m}_1^R \overline{V_{dc0}} + \overline{m}_0 \overline{V_{dc1}}^R \\
\overline{mV_{dc1}}^I &= \overline{m}_1^I \overline{V_{dc0}} + \overline{m}_0 \overline{V_{dc1}}^I \\
\overline{mi_{L1}}^R &= \overline{m}_1^R \overline{i_{L0}} + \overline{m}_0 \overline{i_{L1}}^R \\
\overline{mi_{L1}}^I &= \overline{m}_1^I \overline{i_{L0}} + \overline{m}_0 \overline{i_{L1}}^I \\
\overline{m_d i_{d1}}^R &= \overline{m_{d1}}^R \overline{i_{d0}} + \overline{m_{d0}} \overline{i_{d1}}^R \\
\overline{m_d i_{d1}}^I &= \overline{m_{d1}}^I \overline{i_{d0}} + \overline{m_{d0}} \overline{i_{d1}}^I
\end{aligned}
\tag{5.25}
$$

$$\overline{m_q i_{q1}}^R = \overline{m_{q1}}^R \overline{i_{q0}} + \overline{m_{q0}}\,\overline{i_{q1}}^R$$
$$\overline{m_q i_{q1}}^I = \overline{m_{q1}}^I \overline{i_{q0}} + \overline{m_{q0}}\,\overline{i_{q1}}^I$$
$$\overline{m_d V_{dc1}}^R = \overline{m_{d1}}^R \overline{V_{dc0}} + \overline{m_{d0}}\,\overline{V_{dc1}}^R$$
$$\overline{m_d V_{dc1}}^I = \overline{m_{d1}}^I \overline{V_{dc0}} + \overline{m_{d0}}\,\overline{V_{dc1}}^I$$
$$\overline{m_q V_{dc1}}^R = \overline{m_{q1}}^R \overline{V_{dc0}} + \overline{m_{q0}}\,\overline{V_{dc1}}^R$$
$$\overline{m_q V_{dc1}}^I = \overline{m_{q1}}^I \overline{V_{dc0}} + \overline{m_{q0}}\,\overline{V_{dc1}}^I$$

Substituting (5.25) into (5.24) the MFA-based model of the two-stage distributed PV generator can be written as follows:

$$\frac{d\overline{V_{s1}}^R}{dt} = -\frac{1}{C_s}\overline{i_{L1}}^R + \omega_s \overline{V_{s1}}^I$$
$$\frac{d\overline{V_{s1}}^I}{dt} = -\frac{1}{C_s}\overline{i_{L1}}^I - \omega_s \overline{V_{s1}}^R$$
$$\frac{d\overline{i_{L1}}^R}{dt} = \frac{1}{L_{dc}}\left(\overline{V_{s1}}^R - \overline{m_1}^R \overline{V_{dc0}} - \overline{m_0}\,\overline{V_{dc1}}^R\right) + \omega_s \overline{i_{L1}}^I$$
$$\frac{d\overline{i_{L1}}^I}{dt} = \frac{1}{L_{dc}}\left(\overline{V_{s1}}^I - \overline{m_1}^I \overline{V_{dc0}} - \overline{m_0}\,\overline{V_{dc1}}^I\right) - \omega_s \overline{i_{L1}}^R$$
$$\frac{d\overline{V_{dc1}}^R}{dt} = \frac{1}{C_{dc}}\left(\overline{m_1}^R \overline{i_{L0}} + \overline{m_0}\,\overline{i_{L1}}^R - \overline{m_{d1}}^R \overline{i_{d0}} - \overline{m_{d0}}\,\overline{i_{d1}}^R - \overline{m_{q1}}^R \overline{i_{q0}} - \overline{m_{q0}}\,\overline{i_{q1}}^R\right) + \omega_s \overline{V_{dc1}}^I$$
$$\frac{d\overline{V_{dc1}}^I}{dt} = \frac{1}{C_{dc}}\left(\overline{m_1}^I \overline{i_{L0}} + \overline{m_0}\,\overline{i_{L1}}^I - \overline{m_{d1}}^I \overline{i_{d0}} - \overline{m_{d0}}\,\overline{i_{d1}}^I - \overline{m_{q1}}^I \overline{i_{q0}} - \overline{m_{q0}}\,\overline{i_{q1}}^I\right) - \omega_s \overline{V_{dc1}}^R$$
$$\frac{d\overline{i_{d1}}^R}{dt} = \frac{1}{2L}\left(\overline{m_{d1}}^R \overline{V_{dc0}} + \overline{m_{d0}}\,\overline{V_{dc1}}^R\right) - \frac{R}{L}\overline{i_{d1}}^R + \omega \overline{i_{q1}}^R + \omega_s \overline{i_{d1}}^I$$
$$\frac{d\overline{i_{d1}}^I}{dt} = \frac{1}{2L}\left(\overline{m_{d1}}^I \overline{V_{dc0}} + \overline{m_{d0}}\,\overline{V_{dc1}}^I\right) - \frac{R}{L}\overline{i_{d1}}^I + \omega \overline{i_{q1}}^R - \omega_s \overline{i_{d1}}^R$$
$$\frac{d\overline{i_{q1}}^R}{dt} = \frac{1}{2L}\left(\overline{m_{q1}}^R \overline{V_{dc0}} + \overline{m_{q0}}\,\overline{V_{dc1}}^R\right) - \frac{R}{L}\overline{i_{q1}}^R - \omega \overline{i_{d1}}^R + \omega_s \overline{i_{q1}}^I$$
$$\frac{d\overline{i_{q1}}^I}{dt} = \frac{1}{2L}\left(\overline{m_{q1}}^I \overline{V_{dc0}} + \overline{m_{q0}}\,\overline{V_{dc1}}^I\right) - \frac{R}{L}\overline{i_{q1}}^I - \omega \overline{i_{d1}}^I - \omega_s \overline{i_{q1}}^R \tag{5.26}$$

Equations (5.22) and (5.26) are the DP models of the two-stage distributed

PV generator according to the index k = 0 & 1.

5.4.4 State space representation of dynamic phasor model

Similarly, the conventional state space form of the dynamic system can be represented as follows:

$$\begin{aligned} \frac{d}{dt}\begin{bmatrix}\alpha_0\\ \beta_1\end{bmatrix} &= \begin{bmatrix}A_{11} & A_{12}\\ A_{21} & A_{22}\end{bmatrix}\begin{bmatrix}\alpha_0\\ \beta_1\end{bmatrix} + \begin{bmatrix}B_1\\ 0\end{bmatrix} i_s \\ y &= \begin{bmatrix}C_1 & 0\\ C_2 & 0\\ C_3 & 0\end{bmatrix}\begin{bmatrix}\alpha_0\\ \beta_1\end{bmatrix} \end{aligned} \tag{5.27}$$

where α_0 and β_1 are set of the state vectors corresponding to $k = 0$ and $k = 1$ which are written as follows:

$$\overline{\alpha}_0 = \begin{bmatrix}\overline{V_{s0}} & \overline{i_{L0}} & \overline{V_{dc0}} & \overline{i_{d0}} & \overline{i_{q0}}\end{bmatrix}^T$$

$$\bar{\beta}_1 = \begin{bmatrix}\overline{V_{s1}}^R & \overline{V_{s1}}^I & \overline{i_{L1}}^R & \overline{i_{L1}}^I & \overline{V_{dc1}}^R & \overline{V_{dc1}}^I & \overline{i_{d1}}^R & \overline{i_{d1}}^I & \overline{i_{q1}}^R & \overline{i_{q1}}^I\end{bmatrix}^T$$

These state variables have been divided into two different sets, $\overline{\alpha}_0$ defines the set of state variables for index-0 and $\overline{\beta}_1$ defines the set of state variables for index-1. Compared to the standard state-space form of (5.18) with the fifteen-order differential equations in (5.13) and (5.17), the submatrices of A

can be obtained as follows:

$$A_{11} = \begin{bmatrix} 0 & -\frac{1}{C_s} & 0 & 0 & 0 \\ \frac{1}{L_{dc}} & 0 & -\frac{\overline{m}_0}{L_{dc}} & 0 & 0 \\ 0 & \frac{\overline{m}_0}{C_{dc}} & 0 & -\frac{\overline{m_{d0}}}{C_{dc}} & -\frac{\overline{m_{q0}}}{C_{dc}} \\ 0 & 0 & \frac{\overline{m_{d0}}}{2L} & -\frac{R}{L} & \omega \\ 0 & 0 & \frac{\overline{m_{q0}}}{2L} & -\omega & -\frac{R}{L} \end{bmatrix}$$

$$A_{12} = \begin{bmatrix} 0 & 0 & 0 & 0 & 0 & 0 & 0 & 0 & 0 & 0 \\ 0 & 0 & 0 & 0 & -\frac{2\overline{m}_1^R}{L_{dc}} & -\frac{2\overline{m}_1^I}{L_{dc}} & 0 & 0 & 0 & 0 \\ 0 & 0 & \frac{2\overline{m}_1^R}{C_{dc}} & \frac{2\overline{m}_1^I}{C_{dc}} & 0 & 0 & -\frac{2\overline{m_{d1}}^R}{C_{dc}} & -\frac{2\overline{m_{d1}}^I}{C_{dc}} & -\frac{2\overline{m_{q1}}^R}{C_{dc}} & -\frac{2\overline{m_{q1}}^I}{C_{dc}} \\ 0 & 0 & 0 & 0 & \frac{\overline{m_{d1}}^R}{L} & \frac{\overline{m_{d1}}^I}{L} & 0 & 0 & 0 & 0 \\ 0 & 0 & 0 & 0 & \frac{\overline{m_{q1}}^R}{L} & \frac{\overline{m_{q1}}^I}{L} & 0 & 0 & 0 & 0 \end{bmatrix}$$

$$A_{21} = \begin{bmatrix} 0 & 0 & 0 & 0 & 0 \\ 0 & 0 & 0 & 0 & 0 \\ 0 & 0 & -\frac{\overline{m}_1^R}{L_{dc}} & 0 & 0 \\ 0 & 0 & -\frac{\overline{m}_1^I}{L_{dc}} & 0 & 0 \\ 0 & \frac{\overline{m}_1^R}{C_{dc}} & 0 & -\frac{\overline{m_{d1}}^R}{C_{dc}} & -\frac{\overline{m_{q1}}^R}{C_{dc}} \\ 0 & \frac{\overline{m}_1^I}{C_{dc}} & 0 & -\frac{\overline{m_{d1}}^I}{C_{dc}} & -\frac{\overline{m_{q1}}^I}{C_{dc}} \\ 0 & 0 & \frac{\overline{m_{d1}}^R}{2L} & 0 & 0 \\ 0 & 0 & \frac{\overline{m_{d1}}^I}{2L} & 0 & 0 \\ 0 & 0 & \frac{\overline{m_{q1}}^R}{2L} & 0 & 0 \\ 0 & 0 & \frac{\overline{m_{q1}}^I}{2L} & 0 & 0 \end{bmatrix}$$

$$A_{22} = \begin{bmatrix} 0 & \omega_s & -\frac{1}{C_{dc}} & 0 & 0 & 0 & 0 & 0 & 0 & 0 \\ -\omega_s & 0 & 0 & -\frac{1}{C_{dc}} & 0 & 0 & 0 & 0 & 0 & 0 \\ \frac{1}{L_{dc}} & 0 & 0 & \omega_s & -\frac{\overline{m}_0}{L_{dc}} & 0 & 0 & 0 & 0 & 0 \\ 0 & \frac{1}{L_{dc}} & -\omega_s & 0 & 0 & -\frac{\overline{m}_0}{L_{dc}} & 0 & 0 & 0 & 0 \\ 0 & 0 & \frac{\overline{m}_0}{C_{dc}} & 0 & 0 & \omega_s & -\frac{\overline{m_{d0}}}{C_{dc}} & 0 & -\frac{\overline{m_{q0}}}{C_{dc}} & 0 \\ 0 & 0 & 0 & \frac{\overline{m}_0}{C_{dc}} & -\omega_s & 0 & 0 & -\frac{\overline{m_{d0}}}{C_{dc}} & 0 & -\frac{\overline{m_{q0}}}{C_{dc}} \\ 0 & 0 & 0 & 0 & \frac{\overline{m_{d0}}}{2L} & 0 & -\frac{R}{L} & \omega_s & \omega & 0 \\ 0 & 0 & 0 & 0 & 0 & \frac{\overline{m_{d0}}}{2L} & -\omega_s & -\frac{R}{L} & 0 & \omega \\ 0 & 0 & 0 & 0 & \frac{\overline{m_{q0}}}{2L} & 0 & -\omega & 0 & -\frac{R}{L} & \omega_s \\ 0 & 0 & 0 & 0 & 0 & \frac{\overline{m_{q0}}}{2L} & 0 & -\omega & -\omega_s & -\frac{R}{L} \end{bmatrix}$$

The input matrix is written as follows for the input variables $\overline{m}_0$, $\overline{m_{d0}}$ and $\overline{m_{q0}}$:

$$B_1 = \begin{bmatrix} \frac{1}{C_s} & 0 & 0 & 0 & 0 \end{bmatrix}^T$$

Finally, the output matrices are written as follows for the three output variables $\overline{V_{dc0}}$, $\overline{i_{d0}}$ and $\overline{i_{q0}}$:

$$C_1 = \begin{bmatrix} 0 & 0 & 1 & 0 & 0 \end{bmatrix}, \qquad C_2 = \begin{bmatrix} 0 & 0 & 0 & 1 & 0 \end{bmatrix} \quad \& \quad C_3 = \begin{bmatrix} 0 & 0 & 0 & 0 & 1 \end{bmatrix}$$

The submatrices A_{11}, A_{12}, A_{21} and A_{22} are the constitutional components of matrix A. This matrix form demonstrates wide analytical properties, and the dynamic stability of the two-stage distributed PV generator is analysed using both eigenvalue analysis and time- and frequency-domain simulation outcomes.

5.5 Switching Frequency Sensitivity Analysis of MFA Model

This section investigates the switching frequency sensitivity of the dynamic model of distributed PV generators with different configurations. The responses of the MFA-based DP model are investigated under switching frequencies f_s =1 kHz and f_s =10 kHz. On the other hand, the conventional SSA model responses are independent because of the change in switching frequency.

The performance of the MFA-based DP model of the standalone, grid-connected and two-stage distributed PV generators are analysed in the MATLAB platform. This section explains the necessity of the DP model for the proposed system. The change in the model depending on the switching frequency in the distributed PV generators is analysed. The developed DP and conventional state-space model behaviours are observed under eigenvalues, step responses as time-domain and sigma plot as frequency-domain analysis in the following subsections.

5.5.1 Performance analysis of standalone distributed PV generator

As mentioned in Section 5.2, the DP model is developed for the DC power generated standalone distributed PV generator. The parameter values of the system are presented in Appendix C.1. The operating time of the switch is defined as $m(t)$, and if it is considered as a fixed value d, the index-0 and index-1 averages of $m(t)$ are given as follows:

- $\overline{m}_0 = 1 - d$
- $\overline{m}_1^R = \frac{1}{2\pi}\sin(2\pi d)$

- $\overline{m}_1^I = \frac{1}{2\pi}(\cos(2\pi d) - 1)$

Therefore, $\overline{m}_0$, $\overline{m}_1^R$ and $\overline{m}_1^I$ are fixed values for the open-loop operation at a constant closing period of the switch.

Table 5.2: Eigenvalues of the standalone distributed PV generator under different switching frequencies.

k & f_s	1 k Hz	10 k Hz
0	$-160.700 \pm j4707.71$	$-147.711 \pm j4705.88$
	$-1484.00 \pm j0000.00$	$-1803.59 \pm j0000.00$
1	$-156.879 \pm j11038.1$	$-147.940 \pm j67545.4$
	$-291.490 \pm j1741.16$	$-148.099 \pm j58134.8$
	$-1798.72 \pm j6275.79$	$-1804.46 \pm j62831.6$

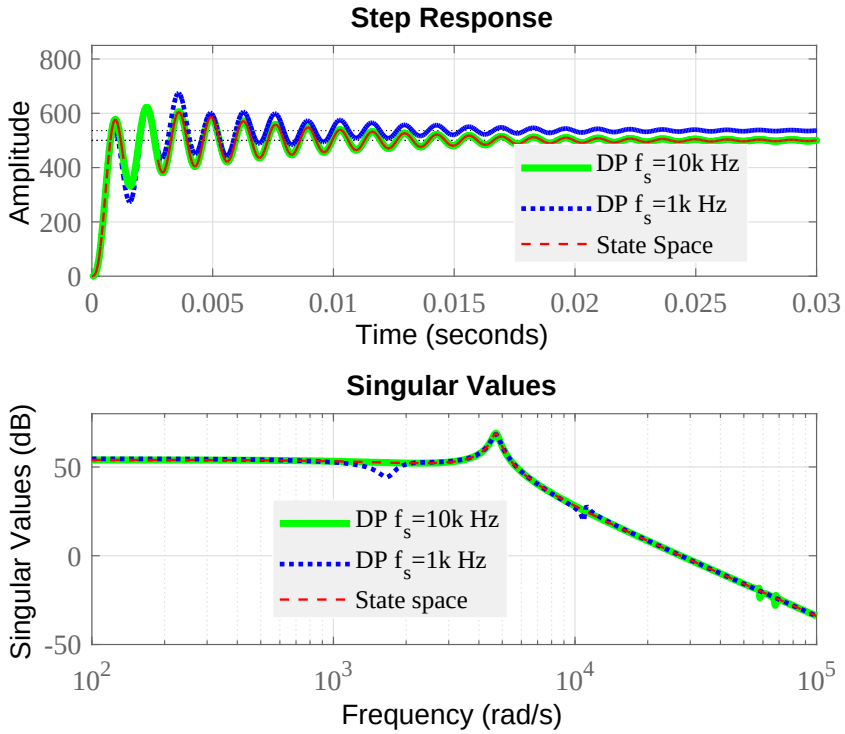

Figure 5.4: Output voltage of the standalone distributed PV generator.

The eigenvalues of A matrix are shown in Table 5.2, for the standalone distributed PV generator. The eigenvalues for the state-space averaging model are

$-147.748 \pm j4705.841$ and -1804.502; and thus, the eigenvalues of index-0 should be the same as the eigenvalues of state-space averaging with different switching frequencies. However, in f_s =1 kHz, the eigenvalues are far from the conventional SSA eigenvalues. In addition, the eigenvalues for f_s =10 kHz are almost equal to the eigenvalues of the SSA model. As a result, the switching frequency f_s =10 kHz can be provided with a better performance of the standalone distributed PV generator.

The time- and frequency-domain results of the existing state-space and the proposed DP averaging approach for the standalone distributed PV generator are illustrated in Figure 5.4 through the step response and sigma plot of the system. The responses for the standalone distributed PV generator change with variations in the switching frequency. Unfortunately, the conventional SSA approach cannot develop the characteristics of the dynamic model, including the switching frequency of the PEIs. As a result, the conventional averaging model cannot capture the switching frequency sensitivity, where the proposed MFA-based DP model may be able to capture the effect of switching frequency on the system, as shown in Figure 5.4.

5.5.2 Performance analysis of grid-connected distributed PV generator

As mentioned in Section 5.3, the DP model is developed using (5.13) and (5.17) based on the conventional SSA model (5.10) for a grid-connected distributed PV generator. The values of the system parameters are presented in the Appendix C.2. The operating time of the switch is defined as $m_{dq}(t)$, and if it is considered as a fixed value d, the index-0 and index-1 averages of $m_{dq}(t)$ are given

Table 5.3: Eigenvalues of grid-connected distributed PV generator at different switching frequencies.

k & f_s	1 k Hz	10 k Hz
0	$-9954.445 \pm j0000.000$	$-9979.014 \pm j0000.0000$
	$-72.77700 \pm j313.8380$	$-60.49200 \pm j314.28900$
1	$-9967.163 \pm j6291.011$	$-9979.446 \pm j62834.570$
	$-66.44300 \pm j6601.264$	$-60.31900 \pm j63147.517$
	$-66.39300 \pm j5972.931$	$-60.23400 \pm j62518.905$

as follows:

- $\overline{m_{dq0}} = 1 - d$
- $\overline{m_{dq1}}^R = \frac{1}{2\pi}\sin(2\pi d)$
- $\overline{m_{dq1}}^I = \frac{1}{2\pi}(\cos(2\pi d) - 1)$

Therefore, $\overline{m_{dq0}}$, $\overline{m_{dq1}}^R$ and $\overline{m_{dq1}}^I$ are fixed values for open-loop operation at constant closing period of the switch.

The eigenvalues of the A matrix are shown in Table 5.3 for the grid-connected distributed PV generator. The eigenvalues for the state-space averaging model are -9979.878 and $-60.06 \pm j314.316$; and thus, the eigenvalues of index-0 should be the same as the eigenvalues of state-space averaging with different switching frequencies. However, in f_s =1 kHz, the eigenvalues are far from the state-space value. In addition, the eigenvalues for f_s =10 kHz are almost equal to the eigenvalues of the state-space averaging model. As a result, the switching frequency f_s =10 kHz can be provided with a better performance of the grid-connected distributed PV generator.

The time- and frequency-domain responses of the developed multi-frequency averaging-based DP model and conventional state-space averaging model of the grid-connected distributed PV generator are shown in Figures 5.5 and 5.6. Figures 5.5 and 5.6 are shown the d- and q-axis AC output currents of the DC-AC

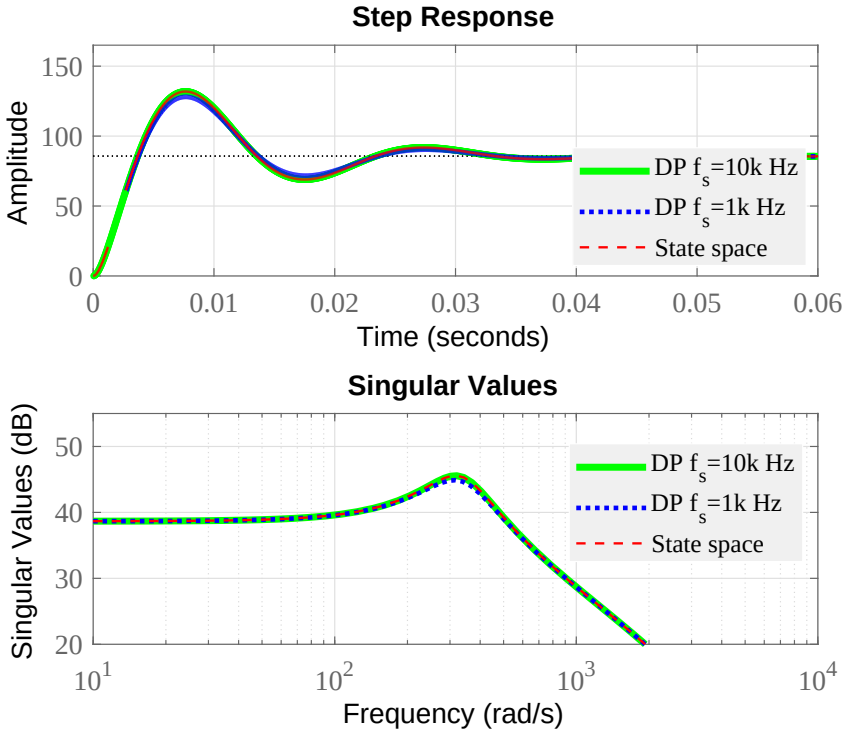

Figure 5.5: Output current of grid-connected distributed PV generator in d-axis.

voltage source converter, respectively. The responses for the grid-connected distributed PV generator vary with changes in the switching frequency. However, the conventional SSA averaging approach cannot sense the switching frequency variations of the power electronic interfaces. Therefore, such modeling approaches are limited to performing against switching issues; hence the proposed MFA-based DP modeling approach can be sensed by switching frequency.

5.5.3 Performance analysis of two-stage distributed PV generator

The two-stage PV generator combines a standalone and a grid-connected distributed PV generators. The DC-DC and DC-AC VSCs act as an interface

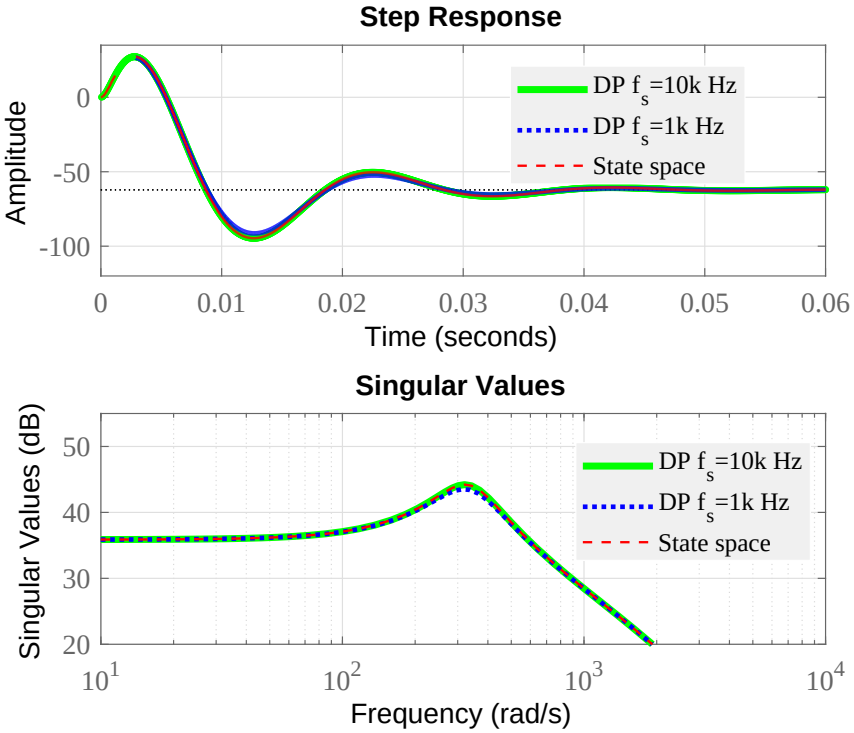

Figure 5.6: Output current of grid-connected distributed PV generator in q-axis.

between distributed PV generator and the utility grid. Such a system is relatively more challenging to handle than a single-stage associated system. This subsection presents an analytical discussion of the considered two-stage distributed PV generator owing to the developed switching-frequency-sensitive model.

As mentioned, in Section 5.4, the DP models are developed using (5.22) and (5.26) based on the conventional SSA model (5.18) for two-stage distributed PV generator. The values of the system parameters are similar to those of the standalone and grid-connected distributed PV generators, but only the DC load is absent.

The eigenvalues of the combined two-stage distributed PV generator is presented in Table 5.4. The eigenvalues for the state-space averaging model are $-615.979 \pm j4482.329$, -9747.909 and $-60.066 \pm 314.356i$, and thus, the eigen-

Table 5.4: Eigenvalues of two-stage distributed PV generator at different switching frequencies.

k & f_s	1 k Hz	10 k Hz
0	$-618.042 \pm j4479.58$	$-616.067 \pm j4482.29$
	$-9720.40 \pm j0.00000$	$-9746.87 \pm j0.00000$
	$-73.4180 \pm j314.357$	$-60.4980 \pm j314.335$
1	$-374.297 \pm j10960.3$	$-352.983 \pm j67530.0$
	$-515.272 \pm j1883.35$	$-482.540 \pm j58474.6$
	$-9574.54 \pm j5882.63$	$-9643.88 \pm j62490.4$
	$-67.0130 \pm j6601.31$	$-60.2790 \pm j63147.6$
	$-67.2150 \pm j5972.77$	$-60.3080 \pm j62518.9$

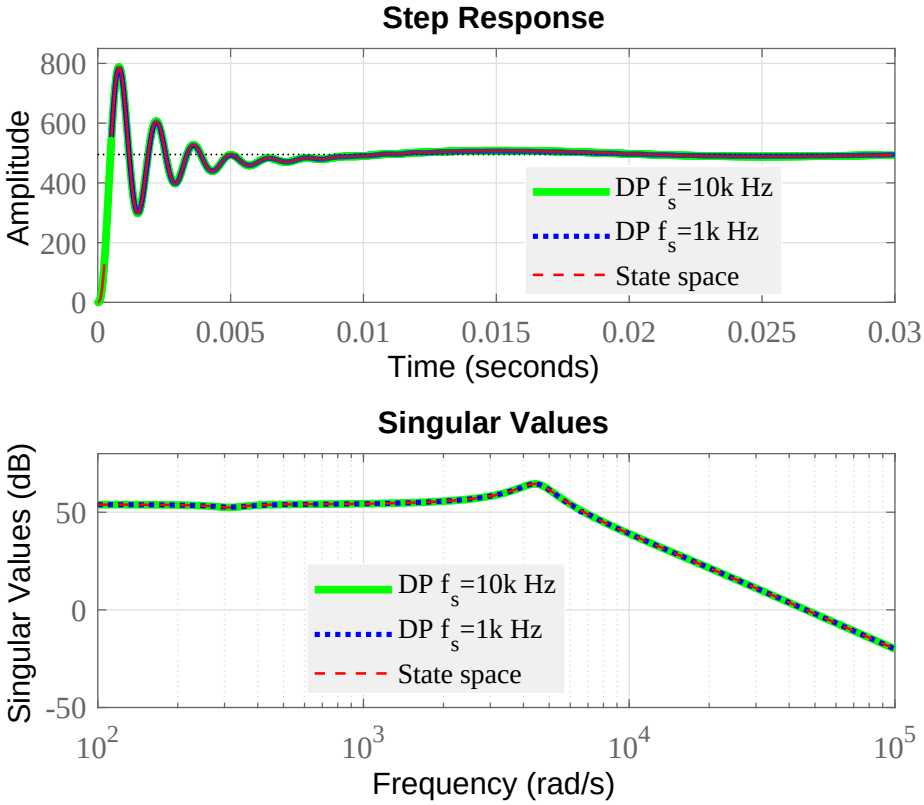

Figure 5.7: DC output voltage of two-stage distributed PV generator.

values of index-0 should be the same as the eigenvalues of the SSA with different switching frequencies. However, in f_s =1 kHz, the eigenvalues are far from the state-space value. In addition, the eigenvalues for f_s =10 kHz are almost equal

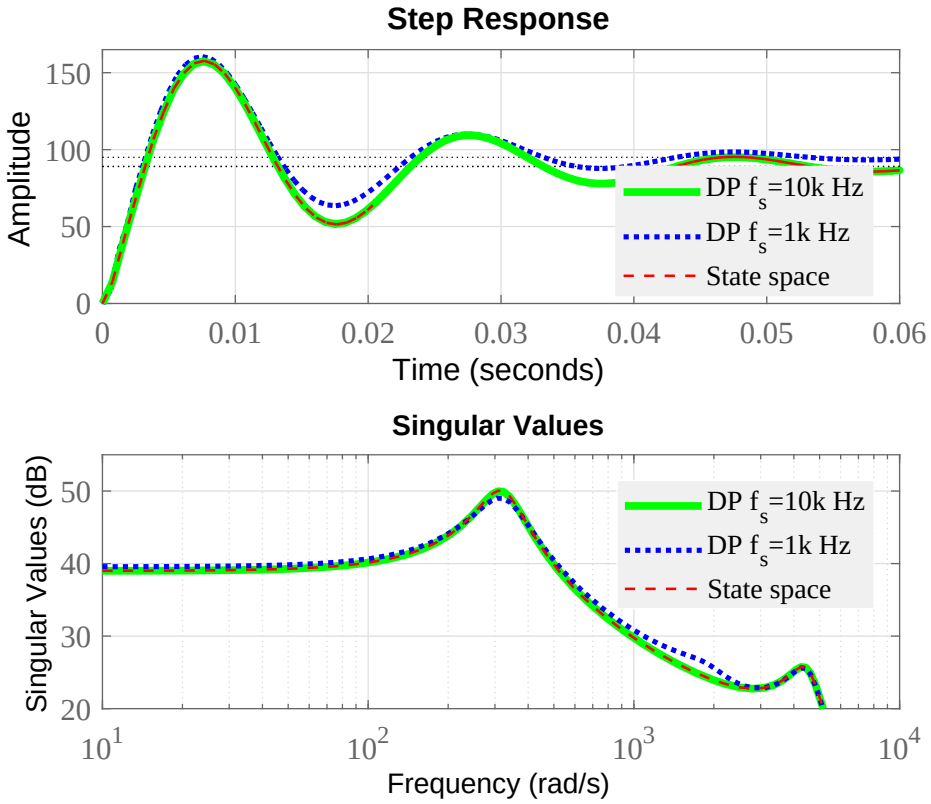

Figure 5.8: AC output current of two-stage distributed PV generator in d axis.

to the eigenvalues of the SSA model. The switching frequency f_s =10 kHz can be improved for a two-stage distributed PV generator.

An additional observation can be made by comparing the eigenvalues among standalone, grid-connected and two-stage distributed PV generators. The eigenvalues between standalone and two-stage distributed PV generators are not similar, but the eigenvalues between grid-connected and two-stage distributed PV generators are almost similar. Therefore, it is clear that the DC-load is responsible for the mismatch between the standalone and two-stage distributed PV generators.

Figure 5.7 represents the step responses and sigma plot of the output DC voltage of the DC-DC voltage source converters. Difference between responses corre-

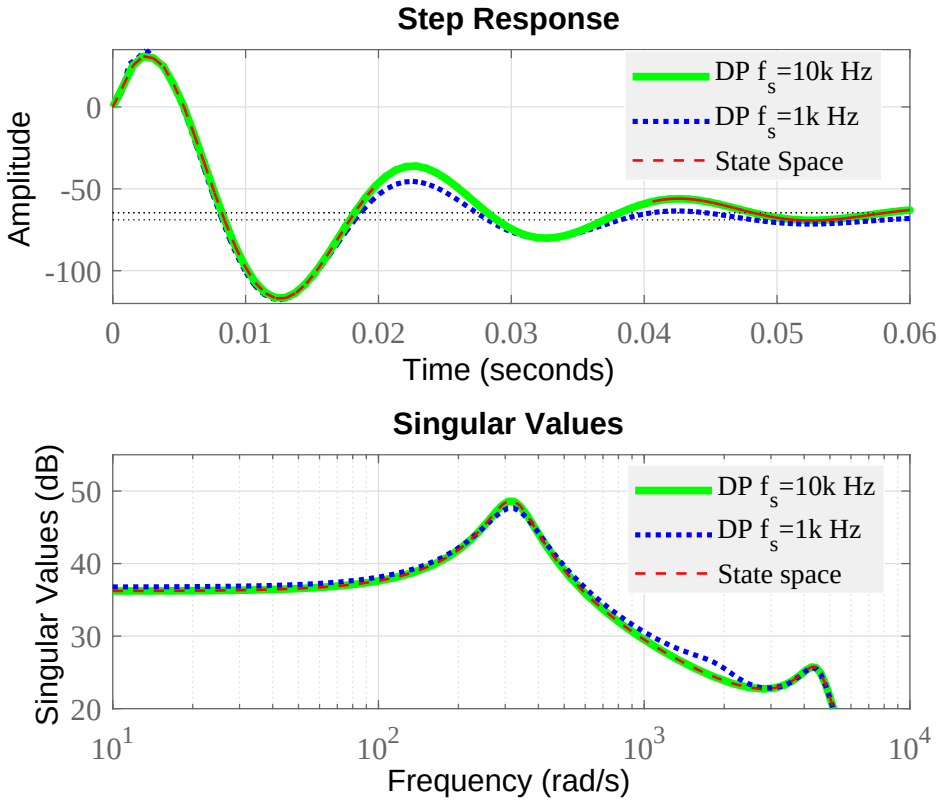

Figure 5.9: AC output current of two-stage distributed PV generator in q axis.

sponding to the f_s =1 kHz and f_s =10 kHz is not high as in Figure 5.7 for combination with DC-AC converters. In addition, the time- and frequency-domain responses of the output current of DC-AC are shown in Figures 5.8 and 5.9. The responses for a two-stage distributed PV generator is varied with a change in the switching frequency. On the other hand, the SSA-based model cannot sense the switching frequency variations of the power electronic converters. As a result, the existing averaging approach is limited to perform against the switching variations; hence the proposed DP modeling approach can be sensed by switching frequencies.

5.6 Chapter Summary

The MFA-based DP models of distributed PV generators have been developed in different configurations. The dynamic models are extended from the n-numbers to 3n-numbers differential equations. The DP modeling technique has switching frequency dependency properties, which may provide a better approximation of the power electronic interfaces in the distributed PV generators. A proper characteristic model is necessary to enhance the transient stability of the DGs, where the DP modeling approach will be provided with a convenient, dynamic model to design a controller for reliable operation. In future work, the proposed multi-frequency averaging based dynamic phasor model will be used to design a controller to enhance the transient stability of the distributed PV generators.

Chapter 6

Conclusions and Directions for Further Research

This thesis develops partial feedback linearized (feedback linearized) controllers and multi-frequency averaging DGs models. Dynamic models are presented to design a robust and SITO feedback linearized controller for distributed generators and islanded microgrids. In addition, a detailed characteristics model for the different generation structures of the distributed PV generators are introduced. In Chapter 2, a new SITO feedback linearization technique is developed for islanded microgrids based on the conventional feedback linearization approach for SITO control problems.

Parameter sensitivity is one of the most critical limitations of the feedback linearized system. Additionally, the performance of renewable energy-based DGs depends on the surrounding environment, which is responsible for creating a mismatch between the actual and mathematical models of the DGs. These types of mismatches are considered uncertain. Therefore, a robust H_∞ mixed-sensitivity loop-shaping controllers are designed to improve the transient stability of the

different DGs. As a result, the designed robust feedback linearized controllers work better than the existing feedback linearized controllers, investigated in Chapter 3.

The primary control issues of islanded microgrids are considered to be a SITO control problem. In Chapter 4, SITO feedback linearized controllers are designed for three different islanded microgrids as DC, AC, and hybrid DC/AC. Typically, the output voltages are considered the main control objectives in the islanded microgrids, but the output currents are also considered control objectives to enhance the performance. The proposed controller can provide the desired bus voltage and enhance the current-sharing accuracy among parallel-connected DGs in islanded microgrids.

In Chapter 5, the DC-DC and DC-AC VSCs are considered interfaces between distributed PV generators and loads to develop a MFA based dynamic phasor model. The dynamic phasor models are developed for three different layouts of the standalone, grid-connected and two-stage distributed PV generators. In addition, the switching frequency sensitivity of interfacing devices has been investigated for DC and fundamental components with switching frequencies of 1 kHz and 10 kHz.

From this thesis, the following conclusions can be addressed:

- Linear controllers may not be able to maintain stable operation against the operating point variations.
- Nonlinear controllers can provide operating point independence and enhanced transient stability under significant disturbances.
- The output feedback linearized control scheme is a well-established nonlinear control technique for power system dynamics.

- The proposed feedback linearized controller is simple as it provides a reduced-order linear subsystem.
- A linear controller can be applied to stabilize the linearized part of the nonlinear control law.
- Feedback linearized controllers are sensitive to parameter and measurement noise, where the exact parameter values and noise decoupling need to be implemented.
- The effect of parameter sensitivity and measurement noise can be minimized by designing a linear robust H_∞ mixed-sensitivity loop-shaping controller for the linearized part of the feedback linearized control law.
- The control problems of the islanded microgrids are single-input two-output control problems.
- A single-input two-output feedback linearized control scheme is developed based on the conventional single-input single-output feedback linearization approach.
- The developed single-input two-output linearized controllers are designed for the islanded DC, AC and hybrid DC/AC microgrids.
- The switching frequency is one of the parameters of power electronics interfaces that are not considered in the characteristics model in conventional state-space averaging techniques.
- A multi-frequency averaging-based dynamic phasor model has been developed for distributed PV generators to consider the switching frequency in dynamic models.

This thesis builds on three main objectives. First, robust nonlinear feedback linearized controllers are designed for the DGs. Second, single-input two-output feedback linearized controllers are designed for the islanded microgrids. Finally, this study develops the MFA-based dynamic phasor models for distributed PV generators. Moreover, three different test systems are considered to validate each objective, where the first two test systems are combined in the final test system for each objective.

6.1 Directions for Future Research

The designed controllers can improve the transient stability of the distributed generators and islanded microgrids. In addition, the MFA approach can be used to develop the switching-frequency-sensitive characteristic models of the distributed PV generators. However, the proposed methodologies can be extended to the following issues.

- The designed controllers are validated through a computer-aided simulation for the selected test system. As a result, the execution of the proposed controller in practical systems would provide more confidence.
- The designed control scheme could be implemented in a grid-connected distributed generator to detect the islanding operation mode.
- The designed controller could be extended to consider a distributed wind-generator to maintain the voltage stability.
- The robust controller could be designed for the single-input two-output feedback linearized model to enhance the transient stability of the islanded microgrids.

- The proposed control methodologies could be used to design secondary level controllers for microgrids.
- The multi-frequency averaging-based dynamic phasor modeling approach could be extended for different distributed generators.
- The developed dynamic phasor model could be extended to the designed controller to achieve better performance against harmonics.

6.2 Outcome and Benefit of Research

- Most of the distributed generators are renewable energy dependent, which are provided reduce carbon emission for future nation.
- Battery integrated distributed generators could be independent electric power suppler for those people who are not connected to the existing eclectic network.
- The battery installation cost is very high at a single time for some people, those could be connected together to buy or sell their require or surplus eclectic power. The microgrids could be reduced the battery installation cost.
- Higher harmonic can be destroy the performance of the power electronic interface associated distributed generators, where multi-frequency averaging model can provide a better idea about switching frequency.

References

[1] Stern, D.I., Burke, P.J., Bruns, S.B.: The impact of electricity on economic development: a macroeconomic perspective. (2019)

[2] Rahman, F.A., Aziz, M.M.A., Saidur, R., Bakar, W.A.W.A., Hainin, M., Putrajaya, R., Hassan, N.A.: Pollution to solution: Capture and sequestration of carbon dioxide (co2) and its utilization as a renewable energy source for a sustainable future. Renewable and Sustainable Energy Reviews **71** (2017) 112–126

[3] Gielen, D., Boshell, F., Saygin, D.: Climate and energy challenges for materials science. Nature materials **15**(2) (2016) 117–120

[4] Vidal-Amaro, J.J., Østergaard, P.A., Sheinbaum-Pardo, C.: Optimal energy mix for transitioning from fossil fuels to renewable energy sources–the case of the mexican electricity system. Applied Energy **150** (2015) 80–96

[5] Child, M., Kemfert, C., Bogdanov, D., Breyer, C.: Flexible electricity generation, grid exchange and storage for the transition to a 100% renewable energy system in europe. Renewable energy **139** (2019) 80–101

[6] Li, H.X., Edwards, D.J., Hosseini, M.R., Costin, G.P.: A review on renewable energy transition in australia: An updated depiction. Journal of cleaner production **242** (2020) 118475

[7] Liang, X.: Emerging power quality challenges due to integration of renewable energy sources. IEEE Transactions on Industry Applications **53**(2) (2016) 855–866

[8] Morvaj, B., Evins, R., Carmeliet, J.: Optimization framework for distributed energy systems with integrated electrical grid constraints. Applied Energy **171** (2016) 296–313

[9] Abdmouleh, Z., Gastli, A., Ben-Brahim, L., Haouari, M., Al-Emadi, N.A.: Review of optimization techniques applied for the integration of distributed generation from renewable energy sources. Renewable Energy **113** (2017) 266–280

[10] Parhizi, S., Lotfi, H., Khodaei, A., Bahramirad, S.: State of the art in research on microgrids: A review. Ieee Access **3** (2015) 890–925

[11] Hannan, M., Lipu, M.H., Ker, P.J., Begum, R., Agelidis, V.G., Blaabjerg, F.: Power electronics contribution to renewable energy conversion addressing emission reduction: Applications, issues, and recommendations. Applied energy **251** (2019) 113404

[12] Suntio, T., Messo, T., Puukko, J.: Power electronic converters: dynamics and control in conventional and renewable energy applications. John Wiley & Sons (2017)

[13] Hannan, M., Hussin, I., Ker, P.J., Hoque, M.M., Lipu, M.H., Hussain, A., Rahman, M.A., Faizal, C., Blaabjerg, F.: Advanced control strategies of vsc based hvdc transmission system: issues and potential recommendations. IEEE Access **6** (2018) 78352–78369

[14] Wang, S., Dehghanian, P., Alhazmi, M., Nazemi, M.: Advanced control solutions for enhanced resilience of modern power-electronic-interfaced distribution systems. Journal of Modern Power Systems and Clean Energy **7**(4) (2019) 716–730

[15] Machowski, J., Lubosny, Z., Bialek, J.W., Bumby, J.R.: Power system dynamics: stability and control. John Wiley & Sons (2020)

[16] Demello, F.P., Concordia, C.: Concepts of synchronous machine stability as affected by excitation control. IEEE Transactions on power apparatus and systems **88**(4) (1969) 316–329

[17] Khodabakhshian, A., Hooshmand, R.: A new pid controller design for automatic generation control of hydro power systems. International Journal of Electrical Power & Energy Systems **32**(5) (2010) 375–382

[18] Yu, Y.N.: Electric power system dynamics. ACADEMIC PRESS, INC., 111 FIFTH AVE., NEW YORK, NY 10003, USA, 1983, 256 (1983)

[19] Kundur, P.: Power system stability. Power system stability and control (2007) 7–1

[20] Hasanovic, A., Feliachi, A., Bhatt, N., DeGroff, A.: Practical robust pss design through identification of low-order transfer functions. IEEE Transactions on Power systems **19**(3) (2004) 1492–1500

[21] Yue, M., Schlueter, R.: Robust control designs for multiple bifurcations. IEEE Transactions on Power Systems **20**(1) (2005) 301–311

[22] Pal, B., Chaudhuri, B.: Robust control in power systems. Springer Science & Business Media (2006)

[23] Mahmud, M.R.: Novel robust controller design to enhance transient stability of power systems. Ph. D. dissertation, Swinburne University of Technology (2017)

[24] Von Bremen, L.: Large-scale variability of weather dependent renewable energy sources. In: Management of weather and climate risk in the energy industry. Springer (2010) 189–206

[25] Bhandari, B., Poudel, S.R., Lee, K.T., Ahn, S.H.: Mathematical modeling of hybrid renewable energy system: A review on small hydro-solar-wind power generation. international journal of precision engineering and manufacturing-green technology **1**(2) (2014) 157–173

[26] Zhang, Y., Xie, L.: A transient stability assessment framework in power electronic-interfaced distribution systems. IEEE Transactions on Power Systems **31**(6) (2016) 5106–5114

[27] Mahmud, M.A., Pota, H., Hossain, M.: Full-order nonlinear observer-based excitation controller design for interconnected power systems via exact linearization approach. International Journal of Electrical Power & Energy Systems **41**(1) (2012) 54–62

[28] Mahmud, M., Hossain, M., Pota, H., Oo, A.: Robust nonlinear distributed controller design for active and reactive power sharing in islanded microgrids. IEEE Transactions on Energy Conversion **29**(4) (2014) 893–903

[29] Mahmud, M.A.: Robust nonlinear feedback linearizing control for power systems to enhance transient stability. PhD thesis, Master's thesis, The University of New South Wales (2012)

[30] Kaundinya, D.P., Balachandra, P., Ravindranath, N.H.: Grid-connected versus stand-alone energy systems for decentralized power—a review of literature. Renewable and Sustainable Energy Reviews **13**(8) (2009) 2041–2050

[31] Zhao, B., Wang, C., Zhang, X.: Grid-integrated and standalone photovoltaic distributed generation systems. Analysis, Design, and Control. Wiley (2017)

[32] Obi, M., Bass, R.: Trends and challenges of grid-connected photovoltaic systems–a review. Renewable and Sustainable Energy Reviews **58** (2016) 1082–1094

[33] Yasmeena, S., Das, G.T.: A review of technical issues for grid connected renewable energy sources. International Journal of Energy and Power Engineering **4**(5-1) (2015) 22–32

[34] Bajpai, P., Dash, V.: Hybrid renewable energy systems for power generation in stand-alone applications: A review. Renewable and Sustainable Energy Reviews **16**(5) (2012) 2926–2939

[35] Thopil, M., Bansal, R.C., Zhang, L., Sharma, G.: A review of grid connected distributed generation using renewable energy sources in south africa. Energy strategy reviews **21** (2018) 88–97

[36] Mirhosseini, M., Pou, J., Agelidis, V.G.: Single-and two-stage inverter-based grid-connected photovoltaic power plants with ride-through capability under grid faults. IEEE Transactions on sustainable energy **6**(3) (2014) 1150–1159

[37] Mahmud, M., Pota, H.: Robustness analysis of h_∞ controller for feedback linearized model of grid connected inverter. In: 2018 IEEE International Conference on Power Electronics, Drives and Energy Systems (PEDES), IEEE (2018) 1–6

[38] Mahmud, R., Hossain, M.A., Pota, H.: Robust nonlinear controller design for islanded photovoltaic system with battery energy storage. In: 2020 IEEE International Conference on Power Electronics, Smart Grid and Renewable Energy (PESGRE2020), IEEE (2020) 1–6

[39] Tan, K., So, P., Chu, Y., Kwan, K.: Modeling, control and simulation of a photovoltaic power system for grid-connected and stand-alone applications. In: 2010 Conference Proceedings IPEC, IEEE (2010) 608–613

[40] Salem, M., Atia, Y.: Control scheme towards enhancing power quality and operational efficiency of single-phase two-stage grid-connected photovoltaic systems. Journal of Electrical Systems and Information Technology **2**(3) (2015) 314–327

[41] Ahmed, K., Massoud, A., Adam, G., Zobaa, A.: A state of the art review of control techniques for power electronics converter based distributed generation systems in different modes of operation. In: 2013 International Conference on Renewable Energy Research and Applications (ICRERA), IEEE (2013) 1042–1047

[42] Papadimitriou, C., Kleftakis, V., Hatziargyriou, N.: Control strategy for seamless transition from islanded to interconnected operation mode of microgrids. Journal of Modern Power Systems and Clean Energy **5**(2) (2017) 169–176

[43] Olivares, D.E., Mehrizi-Sani, A., Etemadi, A.H., Cañizares, C.A., Iravani, R., Kazerani, M., Hajimiragha, A.H., Gomis-Bellmunt, O., Saeedifard, M., Palma-Behnke, R., et al.: Trends in microgrid control. IEEE Transactions on smart grid **5**(4) (2014) 1905–1919

[44] Sahoo, S.K., Sinha, A.K., Kishore, N.: Control techniques in ac, dc, and hybrid ac–dc microgrid: a review. IEEE Journal of Emerging and Selected Topics in Power Electronics **6**(2) (2017) 738–759

[45] Dragičević, T., Lu, X., Vasquez, J.C., Guerrero, J.M.: Dc microgrids—part i: A review of control strategies and stabilization techniques. IEEE Transactions on power electronics **31**(7) (2015) 4876–4891

[46] Pogaku, N., Prodanovic, M., Green, T.C.: Modeling, analysis and testing of autonomous operation of an inverter-based microgrid. IEEE Transactions on power electronics **22**(2) (2007) 613–625

[47] Liu, X., Wang, P., Loh, P.C.: A hybrid ac/dc microgrid and its coordination control. IEEE Transactions on smart grid **2**(2) (2011) 278–286

[48] Kannan, N., Vakeesan, D.: Solar energy for future world:-a review. Renewable and Sustainable Energy Reviews **62** (2016) 1092–1105

[49] Devabhaktuni, V., Alam, M., Depuru, S.S.S.R., Green II, R.C., Nims, D., Near, C.: Solar energy: Trends and enabling technologies. Renewable and Sustainable Energy Reviews **19** (2013) 555–564

[50] Kaundinya, D.P., Balachandra, P., Ravindranath, N.H.: Grid-connected versus stand-alone energy systems for decentralized power—a review of literature. Renewable and Sustainable Energy Reviews **13**(8) (2009) 2041–2050

[51] Krithiga, S., Gounden, N.G.A.: Power electronic configuration for the operation of pv system in combined grid-connected and stand-alone modes. IET Power Electronics **7**(3) (2013) 640–647

[52] Shair, J., Li, H., Hu, J., Xie, X.: Power system stability issues, classifications and research prospects in the context of high-penetration of renewables and power electronics. Renewable and Sustainable Energy Reviews **145** (2021) 111111

[53] Laux, S.E.: Techniques for small-signal analysis of semiconductor devices. IEEE Transactions on Electron Devices **32**(10) (1985) 2028–2037

[54] Guinjoan, F., Calvente, J., Poveda, A., Martinez, L.: Large-signal modeling and simulation of switching dc-dc converters. IEEE Transactions on Power Electronics **12**(3) (1997) 485–494

[55] Safaee, A., Karimi-Ghartemani, M., Jain, P.K., Bakhshai, A.: Time-domain analysis of a phase-shift-modulated series resonant converter with an adaptive passive auxiliary circuit. IEEE Transactions on Power Electronics **31**(11) (2016) 7714–7734

[56] Orillaza, J.R.C., Wood, A.R.: Harmonic state-space model of a controlled tcr. IEEE Transactions on Power Delivery **28**(1) (2012) 197–205

[57] Maksimovic, D., Stankovic, A.M., Thottuvelil, V.J., Verghese, G.C.: Modeling and simulation of power electronic converters. Proceedings of the IEEE **89**(6) (2001) 898–912

[58] Sanders, S.R., Noworolski, J.M., Liu, X.Z., Verghese, G.C.: Generalized averaging method for power conversion circuits. IEEE Transactions on power Electronics **6**(2) (1991) 251–259

[59] Kimbark, E.W.: Power system stability. Volume 1. John Wiley & Sons (1995)

[60] Mahmud, A.: Large scale renewable power generation. (2014)

[61] Yang, Z., Wang, C., Che, Y.: A small-scale microgrid system with flexible modes of operation. Automation of Electric Power Systems **33**(14) (2009) 89–92

[62] Bouzid, A.M., Guerrero, J.M., Cheriti, A., Bouhamida, M., Sicard, P., Benghanem, M.: A survey on control of electric power distributed generation systems for microgrid applications. Renewable and Sustainable Energy Reviews **44** (2015) 751–766

[63] Rocabert, J., Luna, A., Blaabjerg, F., Rodriguez, P.: Control of power converters in ac microgrids. IEEE transactions on power electronics **27**(11) (2012) 4734–4749

[64] Mattavelli, P., Stankovic, A.M., Verghese, G.C.: Ssr analysis with dynamic phasor model of thyristor-controlled series capacitor. IEEE Transactions on Power Systems **14**(1) (1999) 200–208

[65] Bonkile, M.P., Ramadesigan, V.: Power management control strategy using physics-based battery models in standalone pv-battery hybrid systems. Journal of Energy Storage **23** (2019) 258–268

[66] Mahmud, M.R., Pota, H.: Robust partial feedback linearized controller design for standalone hybrid pv-bes system. Electronics **10**(7) (2021) 772

[67] Mahmud, M.R., Pota, H.: Robust nonlinear controller design for dc-ac converter in grid connected fuel cell system. IEEE Journal of Emerging and Selected Topics in Industrial Electronics (2021)

[68] Bortolini, M., Gamberi, M., Graziani, A.: Technical and economic design of photovoltaic and battery energy storage system. Energy Conversion and Management **86** (2014) 81–92

[69] Naqvi, S.B.Q., Singh, B.: Grid connected two stage pv-battery system with pv intermittency mitigation and improved power quality. In: 2020 International Conference on Electrical and Electronics Engineering (ICE3), IEEE (2020) 761–766

[70] Mahmud, M.A., Roy, T.K., Islam, S.N., Saha, S., Haque, M.E.: Nonlinear decentralized feedback linearizing controller design for islanded dc microgrids. Electric Power Components and Systems **45**(16) (2017) 1747–1761

[71] Ceraolo, M.: New dynamical models of lead-acid batteries. IEEE transactions on Power Systems **15**(4) (2000) 1184–1190

[72] Vasebi, A., Partovibakhsh, M., Bathaee, S.M.T.: A novel combined battery model for state-of-charge estimation in lead-acid batteries based on extended kalman filter for hybrid electric vehicle applications. Journal of Power Sources **174**(1) (2007) 30–40

[73] Yazdani, A., Iravani, R.: Voltage-sourced converters in power systems. Volume 39. Wiley Online Library (2010)

[74] Mohiuddin, S., Mahmud, M.A., Haruni, A., Pota, H.: Design and implementation of partial feedback linearizing controller for grid-connected fuel cell systems. International Journal of Electrical Power & Energy Systems **93** (2017) 414–425

[75] Baimel, D., Belikov, J., Guerrero, J.M., Levron, Y.: Dynamic modeling of networks, microgrids, and renewable sources in the dq0 reference frame: A survey. Ieee Access **5** (2017) 21323–21335

[76] Sarkar, I.: Power electronics interfaces in microgrid applications. Microgrid Technologies (2021) 121–144

[77] Andersson, G.: Power electronics solutions for sustainability. In: IEEE Power Engineering Society General Meeting, 2004., IEEE (2004) 2304–2308

[78] Hossain, E., Kabalci, E., Bayindir, R., Perez, R.: Microgrid testbeds around the world: State of art. Energy Conversion and Management **86** (2014) 132–153

[79] Justo, J.J., Mwasilu, F., Lee, J., Jung, J.W.: Ac-microgrids versus dc-microgrids with distributed energy resources: A review. Renewable and sustainable energy reviews **24** (2013) 387–405

[80] Nian, H., Song, Y., Zhou, P., He, Y.: Improved direct power control of a wind turbine driven doubly fed induction generator during transient grid voltage unbalance. IEEE Transactions on Energy Conversion **26**(3) (2011) 976–986

[81] Mahmud, M.R., Pota, H.: Robust feedback linearizing controller design for dc microgrid connected dc-dc converter. In: 2021 IEEE Texas Power and Energy Conference (TPEC), IEEE (2021) 1–6

[82] Zhang, H., Baeyens, J., Degrève, J., Cacères, G.: Concentrated solar power plants: Review and design methodology. Renewable and sustainable energy reviews **22** (2013) 466–481

[83] Khan, J., Arsalan, M.H.: Solar power technologies for sustainable electricity generation–a review. Renewable and Sustainable Energy Reviews **55** (2016) 414–425

[84] Isidori, A., Sontag, E., Thoma, M.: Nonlinear control systems. Volume 3. Springer (1995)

[85] Demiray, T.: Simulation of power system dynamics using dynamic phasor models. PhD thesis, ETH Zurich (2008)

[86] Infield, D., Freris, L.: Renewable energy in power systems. John Wiley & Sons (2020)

[87] Safwat Kabel, T., Bassim, M.: Reasons for shifting and barriers to renewable energy: A literature review. International Journal of Energy Economics and Policy **10**(2) (2020) 89–94

[88] Xiang, Y., Cai, H., Gu, C., Shen, X.: Cost-benefit analysis of integrated energy system planning considering demand response. Energy **192** (2020) 116632

[89] Mahmud, M.A., Hossain, M.J., Pota, H.R.: Selection of output function in nonlinear feedback linearizing excitation control for power systems. In: 2011 Australian Control Conference, IEEE (2011) 458–463

[90] Karlsson, P., Svensson, J.: Dc bus voltage control for a distributed power system. IEEE transactions on Power Electronics **18**(6) (2003) 1405–1412

[91] Mohiuddin, S., Mahmud, M.A., Haruni, A., Pota, H.: Design and implementation of partial feedback linearizing controller for grid-connected fuel cell systems. International Journal of Electrical Power & Energy Systems **93** (2017) 414–425

[92] Parthasarathy, C., Hafezi, H., Laaksonen, H., Kauhaniemi, K.: Modelling and simulation of hybrid pv & bes systems as flexible resources in smartgrids–sundom smart grid case. In: 2019 IEEE Milan PowerTech, IEEE (2019) 1–6

[93] Harnefors, L., Wang, X., Yepes, A.G., Blaabjerg, F.: Passivity-based stability assessment of grid-connected vscs—an overview. IEEE Journal of emerging and selected topics in Power Electronics **4**(1) (2016) 116–125

[94] Sun, L., Jin, Y., Pan, L., Shen, J., Lee, K.Y.: Efficiency analysis and control of a grid-connected pem fuel cell in distributed generation. Energy Conversion and Management **195** (2019) 587–596

[95] Weyers, C., Bocklisch, T.: Simulation-based investigation of energy management concepts for fuel cell–battery–hybrid energy storage systems in mobile applications. Energy Procedia **155** (2018) 295–308

[96] Shen, D., Lim, C.C., Shi, P.: Robust fuzzy model predictive control for energy management systems in fuel cell vehicles. Control Engineering Practice **98** (2020) 104364

[97] Chen, X., Cao, W., Zhang, Q., Hu, S., Zhang, J.: Artificial intelligence-aided model predictive control for a grid-tied wind-hydrogen-fuel cell system. IEEE Access **8** (2020) 92418–92430

[98] Cao, B., Chang, L., Shao, R.: Predictive current controller for single-phase grid-connected vsis with compensation for time-delay effect and system uncertainty. IEEE Journal of Emerging and Selected Topics in Power Electronics **6**(4) (2018) 1761–1768

[99] Sekhar, P., Mishra, S.: Sliding mode based feedback linearizing controller for grid connected multiple fuel cells scenario. International Journal of Electrical Power & Energy Systems **60** (2014) 190–202

[100] Baghaee, H.R., Mirsalim, M., Gharehpetian, G.B., Talebi, H.A.: A decentralized power management and sliding mode control strategy for hybrid ac/dc microgrids including renewable energy resources. IEEE transactions on industrial informatics (2017)

[101] Raeispour, M., Atrianfar, H., Baghaee, H.R., Gharehpetian, G.B.: Robust sliding mode and mixed $h_2\backslash h_\infty$ output feedback primary control of ac microgrids. IEEE Systems Journal (2020)

[102] Tan, K., So, P., Chu, Y., Chen, M.: Coordinated control and energy management of distributed generation inverters in a microgrid. IEEE Transactions on Power Delivery **28**(2) (2013) 704–713

[103] Mehrasa, M., Adabi, M.E., Pouresmaeil, E., Adabi, J.: Passivity-based control technique for integration of dg resources into the power grid. International Journal of Electrical Power & Energy Systems **58** (2014) 281–290

[104] Roy, T.K., Mahmud, M.A.: Active power control of three-phase grid-connected solar pv systems using a robust nonlinear adaptive backstepping approach. Solar Energy **153** (2017) 64–76

[105] Mahmud, M.A., Pota, H., Hossain, M.: Dynamic stability of three-phase grid-connected photovoltaic system using zero dynamic design approach. IEEE Journal of Photovoltaics **2**(4) (2012) 564–571

[106] Mahmud, M.R.: Novel robust controller design to enhance transient stability of power systems. Masters dissertation, Swinburne University of Technology (2017)

[107] Mahmud, M., Hossain, M., Pota, H., Oo, A.M.: Robust partial feedback linearizing excitation controller design for multimachine power systems. IEEE Transactions on Power Systems **32**(1) (2016) 3–16

[108] Mohiuddin, S., Mahmud, M.A., Haruni, A., Pota, H.: Design and implementation of partial feedback linearizing controller for grid-connected fuel cell systems. International Journal of Electrical Power & Energy Systems **93** (2017) 414–425

[109] Kharitonov, V.: Asymptotic stability of an equilibrium position of a family of systems of differential equations. Differential equations **14** (1978) 1483

[110] Petersen, I.R.: A new extension to kharitonov's theorem. In: 26th IEEE Conference on Decision and Control. Volume 26., IEEE (1987) 2070–2075

[111] Dasgupta, S.: Kharitonov's theorem revisited. Systems & Control Letters **11**(5) (1988) 381–384

[112] Anderson, B.D., Moore, J.B.: Optimal control: linear quadratic methods. Courier Corporation (2007)

[113] Chow, J., Harris, L., Kale, M., Othman, H., Sanchez-Gasca, J., Terwilliger, G.: Robust control design of power system stabilizers using multivariable frequency domain techniques. In: 29th IEEE Conference on Decision and Control, IEEE (1990) 2067–2073

[114] Ohtsuka, K., Taniguchi, T., Sato, T., Yokokawa, S., Ueki, Y.: h_∞ optimal theory-based generator control system. IEEE transactions on energy conversion **7**(1) (1992) 108–115

[115] Asgharian, R.: A robust h_∞ power system stabilizer with no adverse effect on shaft torsional modes. IEEE transactions on energy conversion **9**(3) (1994) 475–481

[116] Chen, S., Malik, O.: Power system stabilizer design using h_∞ μ synthesis. IEEE Transactions on Energy Conversion **10**(1) (1995) 175–181

[117] Zhu, C., Khammash, M., Vittal, V., Qiu, W.: Robust power system stabilizer design using h_∞ loop shaping approach. IEEE Transactions on Power Systems **18**(2) (2003) 810–818

[118] Modi, N., Saha, T., Mithulananthan, N.: Decentralized power system damping controller design using h_∞ loop-shaping technique. In: 2010 Conference Proceedings IPEC, IEEE (2010) 481–486

[119] Mahmud, R., Hossain, M.A., Pota, H.: Nonlinear output feedback droop control for parallel inverters in standalone microgrids. In: 2019 9th International Conference on Power and Energy Systems (ICPES), IEEE (2019) 1–6

[120] Mahmud, R., Hossain, M.A., Pota, H.R.: Robust nonlinear controller design for islanded photovoltaic system with battery energy storage. In: 2020 IEEE International Conference on Power Electronics, Smart Grid and Renewable Energy (PESGRE2020), IEEE (2020) 1–6

[121] Roy, N., Pota, H.R.: Current status and issues of concern for the integration of distributed generation into electricity networks. IEEE Systems Journal **9**(3) (2014) 933–944

[122] Chowdhury, S., Chowdhury, S., Crossley, P.: Islanding protection of active distribution networks with renewable distributed generators: A comprehensive survey. Electric Power Systems Research **79**(6) (2009) 984–992

[123] Olivares, D.E., Mehrizi-Sani, A., Etemadi, A.H., Cañizares, C.A., Iravani, R., Kazerani, M., Hajimiragha, A.H., Gomis-Bellmunt, O., Saeedifard, M., Palma-Behnke, R., et al.: Trends in microgrid control. IEEE Transactions on Smart Grid **5**(4) (2014) 1905–1919

[124] Dragičević, T., Lu, X., Vasquez, J.C., Guerrero, J.M.: Dc microgrids—part i: A review of control strategies and stabilization techniques. IEEE Transactions on Power Electronics **31**(7) (2015) 4876–4891

[125] Vechiu, I., Curea, O., Llaria, A., Camblong, H.: Control of power converters for microgrids. COMPEL-The International Journal for Computation and Mathematics in Electrical and Electronic Engineering **30**(1) (2011) 300–309

[126] Biczel, P.: Power electronic converters in dc microgrid. In: 2007 Compatibility in Power Electronics, IEEE (2007) 1–6

[127] Benadero, L., Cristiano, R., Pagano, D.J., Ponce, E.: Nonlinear analysis of interconnected power converters: A case study. IEEE Journal on Emerging and Selected Topics in Circuits and Systems **5**(3) (2015) 326–335

[128] Gu, Y., Xiang, X., Li, W., He, X.: Mode-adaptive decentralized control for renewable dc microgrid with enhanced reliability and flexibility. IEEE Transactions on Power Electronics **29**(9) (2013) 5072–5080

[129] Augustine, S., Mishra, M.K., Lakshminarasamma, N.: Adaptive droop control strategy for load sharing and circulating current minimization in low-voltage standalone dc microgrid. IEEE Transactions on Sustainable Energy **6**(1) (2014) 132–141

[130] Niyitegeka, G., Choi, J., Ok, Y.: Improved droop control for effective load sharing and voltage regulation in dc microgrids. In: 2016 Electric Power Quality and Supply Reliability (PQ), IEEE (2016) 125–132

[131] Golshannavaz, S., Mortezapour, V.: A generalized droop control approach for islanded dc microgrids hosting parallel-connected ders. Sustainable Cities and Society **36** (2018) 237–245

[132] Moayedi, S., Davoudi, A.: Unifying distributed dynamic optimization and control of islanded dc microgrids. IEEE Transactions on Power Electronics **32**(3) (2016) 2329–2346

[133] Lu, X., Sun, K., Huang, L., Guerrero, J.M., Vasquez, J.C., Xing, Y.: Virtual impedance based stability improvement for dc microgrids with constant power loads. In: 2014 IEEE Energy Conversion Congress and Exposition (ECCE), IEEE (2014) 2670–2675

[134] Tahim, A.P.N., Pagano, D.J., Lenz, E., Stramosk, V.: Modeling and stability analysis of islanded dc microgrids under droop control. IEEE Transactions on Power Electronics **30**(8) (2014) 4597–4607

[135] Xu, Q., Hu, X., Wang, P., Xiao, J., Tu, P., Wen, C., Lee, M.Y.: A decentralized dynamic power sharing strategy for hybrid energy storage system in autonomous dc microgrid. IEEE Transactions on Industrial Electronics **64**(7) (2016) 5930–5941

[136] Khalil, H.K., Grizzle, J.W.: Nonlinear systems. Volume 3. Prentice hall Upper Saddle River, NJ (2002)

[137] Tahim, A.P., Pagano, D.J., Ponce, E.: Nonlinear control of dc-dc bidirectional converters in stand-alone dc microgrids. In: 2012 IEEE 51st IEEE Conference on Decision and Control (CDC), IEEE (2012) 3068–3073

[138] Mahmud, M.A., Roy, T.K., Islam, S.N., Saha, S., Haque, M.E.: Nonlinear decentralized feedback linearizing controller design for islanded dc microgrids. Electric Power Components and Systems **45**(16) (2017) 1747–1761

[139] Roy, T.K., Mahmud, M.A., Oo, A.M.T., Haque, M.E., Muttaqi, K.M., Mendis, N.: Nonlinear adaptive backstepping controller design for islanded dc microgrids. IEEE Transactions on Industry Applications **54**(3) (2018) 2857–2873

[140] Mahmud, M.A., Roy, T.K., Saha, S., Haque, M.E., Pota, H.R.: Robust nonlinear adaptive feedback linearizing decentralized controller design for islanded dc microgrids. IEEE Transactions on Industry Applications **55**(5) (2019) 5343–5352

[141] Ghanbari, N., Bhattacharya, S.: Adaptive droop control method for suppressing circulating currents in dc microgrids. IEEE Open Access Journal of Power and Energy **7** (2020) 100–110

[142] Mahmud, M., Pota, H., Aldeen, M., Hossain, M.: Partial feedback linearizing excitation controller for multimachine power systems to improve transient stability. IEEE Transactions on Power systems **29**(2) (2013) 561–571

[143] Mahmud, M.A., Pota, H., Hossain, M.: Full-order nonlinear observer-based excitation controller design for interconnected power systems via exact linearization approach. International Journal of Electrical Power & Energy Systems **41**(1) (2012) 54–62

[144] Mahmud, M.R.: Novel robust controller design to enhance transient stability of power systems. (2017)

[145] Mahmud, M.A., Pota, H., Hossain, M.: Dynamic stability of three-phase grid-connected photovoltaic system using zero dynamic design approach. IEEE Journal of Photovoltaics **2**(4) (2012) 564–571

[146] Mahmud, M., Pota, H., Hossain, M.: Nonlinear current control scheme for a single-phase grid-connected photovoltaic system. IEEE Transactions on Sustainable Energy **5**(1) (2013) 218–227

[147] Mahmud, M., Pota, H.: Robustness analysis of h_∞ controller for feedback linearized model of grid connected inverter. In: 2018 IEEE International Conference on Power Electronics, Drives and Energy Systems (PEDES), IEEE (2018) 1–6

[148] Mahmud, M.A., Roy, T.K., Saha, S., Haque, M.E., Pota, H.R.: Robust nonlinear adaptive feedback linearizing decentralized controller design for islanded dc microgrids. IEEE transactions on industry applications **55**(5) (2019) 5343–5352

[149] Bidram, A., Davoudi, A., Lewis, F.L., Guerrero, J.M.: Distributed cooperative secondary control of microgrids using feedback linearization. IEEE Transactions on Power Systems **28**(3) (2013) 3462–3470

[150] Eftekharnejad, S., Vittal, V., Heydt, G.T., Keel, B., Loehr, J.: Impact of increased penetration of photovoltaic generation on power systems. IEEE Trans. Power Syst **28**(2) (2013) 893–901

[151] Shah, D.G., Crow, M.: Stability design criteria for distribution systems with solid-state transformers. IEEE Transactions on Power Delivery **29**(6) (2014) 0–0

[152] Emadi, A., Khaligh, A., Rivetta, C.H., Williamson, G.A.: Constant power loads and negative impedance instability in automotive systems: definition, modeling, stability, and control of power electronic converters and motor drives. IEEE Transactions on vehicular technology **55**(4) (2006) 1112–1125

[153] Riccobono, A., Cupelli, M., Monti, A., Santi, E., Roinila, T., Abdollahi, H., Arrua, S., Dougal, R.A.: Stability of shipboard dc power distribution: Online impedance-based systems methods. IEEE Electrification Magazine **5**(3) (2017) 55–67

[154] Chiniforoosh, S., Jatskevich, J., Yazdani, A., Sood, V., Dinavahi, V., Martinez, J., Ramirez, A.: Definitions and applications of dynamic average models for analysis of power systems. IEEE Transactions on Power Delivery **25**(4) (2010) 2655–2669

[155] Bui, L., Casoria, S., Morin, G., Reeve, J.: Emtp tacs-fortran interface development for digital controls modeling. IEEE transactions on power systems **7**(1) (1992) 314–319

[156] Dommel, H.W.: Digital computer solution of electromagnetic transients in single-and multiphase networks. IEEE transactions on power apparatus and systems (4) (1969) 388–399

[157] Dommel, H.W.: Electromagnetic Transients Program: Reference Manual:(EMTP theory book). Bonneville Power Administration (1986)

[158] Hannan, M., Chan, K.: Modern power systems transients studies using dynamic phasor models. In: Power System Technology, 2004. PowerCon 2004. 2004 International Conference on. Volume 2., IEEE (2004) 1469–1473

[159] Tadmor, G.: On approximate phasor models in dissipative bilinear systems. IEEE Transactions on Circuits and Systems I: Fundamental Theory and Applications **49**(8) (2002) 1167–1179

[160] Mohan, N., Undeland, T.M.: Power electronics: converters, applications, and design. John wiley & sons (2007)

[161] Mahmud, M., Pota, H., Hossain, M.: Nonlinear current control scheme for a single-phase grid-connected photovoltaic system. IEEE Transactions on Sustainable Energy **5**(1) (2014) 218–227

[162] Mahmud, M.A., Pota, H., Hossain, M.: Dynamic stability of three-phase grid-connected photovoltaic system using zero dynamic design approach. IEEE Journal of Photovoltaics **2**(4) (2012) 564–571

[163] Mahmud, M., Pota, H.: Robustness analysis of h_∞ controller for feedback linearized model of grid connected inverter. In: 2018 IEEE International Conference on Power Electronics, Drives and Energy Systems (PEDES), IEEE (2018) 1–6

[164] Sanders, S.R., Noworolski, J.M., Liu, X.Z., Verghese, G.C.: Generalized averaging method for power conversion circuits. IEEE Transactions on Power Electronics **6**(2) (1991) 251–259

[165] Caliskan, V.A., Verghese, O., Stankovic, A.M.: Multifrequency averaging of dc/dc converters. IEEE Transactions on Power Electronics **14**(1) (1999) 124–133

[166] Emadi, A.: Modeling of power electronic loads in ac distribution systems using the generalized state-space averaging method. IEEE Transactions on Industrial Electronics **51**(5) (2004) 992–1000

[167] Stefanov, P.C., Stankovic, A.M.: Modeling of upfc operation under unbalanced conditions with dynamic phasors. IEEE Transactions on Power Systems **17**(2) (2002) 395–403

[168] Qi, Q., Yu, C., Wai, C.K., Ni, Y.: Modeling and simulation of a statcom system based on 3-level npc inverter using dynamic phasors. In: Power Engineering Society General Meeting, 2004. IEEE, IEEE (2004) 1559–1564

[169] Yao, W., Wen, J., He, H., Cheng, S.: Modeling and simulation of vsc-hvdc with dynamic phasors. In: Electric Utility Deregulation and Restructuring and Power Technologies, 2008. DRPT 2008. Third International Conference on, IEEE (2008) 1416–1421

[170] Stankovic, A.M., Sanders, S.R., Aydin, T.: Dynamic phasors in modeling and analysis of unbalanced polyphase ac machines. IEEE Transactions on Energy Conversion **17**(1) (2002) 107–113

[171] Chudasama, M.C., Kulkarni, A.M.: Dynamic phasor analysis of ssr mitigation schemes based on passive phase imbalance. IEEE Transactions on Power Systems **26**(3) (2011) 1668–1676

[172] Patel, D.C., Chandorkar, M.: Small-signal transient analysis of induction machines with stator inter-turn faults using dynamic phasors. In: Energy Conversion Congress and Exposition (ECCE), 2012 IEEE, IEEE (2012) 3008–3015

[173] Nagarajan, A., Ayyanar, R.: Dynamic phasor model of single-phase inverters for analysis and simulation of large power distribution systems. In: 2013 4th IEEE International Symposium on Power Electronics for Distributed Generation Systems (PEDG), IEEE (2013) 1–6

[174] Coronado-Mendoza, A., Pérez-Cisneros, M.A., Domínguez-Navarro, J.A., Osuna-Enciso, V., Zúñiga-Grajeda, V., Gurubel-Tun, K.J.: Dynamic phasors modeling for a single phase two stage inverter. Electric Power Systems Research **140** (2016) 854–865

Appendix A

Supplementary Material for Chapter 3

A.1 Standalone Distributed PV-BES Generator

A.1.1 Calculation of the uncertainties

The parameters of the standalone distributed PV-BES generator are considered as follows:

$$\mu_1 = \frac{1}{L_{dc}}$$
$$\mu_2 = \frac{1}{C_{dc}}$$

The system parameters become as follows after change in operation or within time:

$$\mu_1 + \Delta\mu_1 = \frac{1}{L_{dc} + \Delta L_{dc}}$$
$$\mu_2 + \Delta\mu_2 = \frac{1}{C_{dc} + \Delta C_{dc}}$$

Finally, the uncertainties portions of parameters of the standalone distributed

PV-BES generator can be determined as follows:

$$\Delta\mu_1 = \frac{1-(L_{dc}+\Delta L_{dc})}{L_{dc}(L_{dc}+\Delta L_{dc})}$$
$$\Delta\mu_2 = \frac{1-(C_{dc}+\Delta C_{dc})}{C_{dc}(C_{dc}+\Delta C_{dc})}$$

A.1.2 Parameters of design robust $\mathbf{H}_\infty$ controller

To design robust H_∞ mixed-sensitivity loop-shaping controller for standalone distributed PV-BES generator in Subsection 3.3.3 the following numerical values have been taken under consideration:

- Regulating values of $W_S(s)$, $k = 1.10$
- Regulating values of $W_T(s)$, $k = 0.59$
- Maximum acceptable fixed offset value, $A = 0.0001$
- The peak value of the sensitivity function, $M = 1.3$
- Cross over frequency of the sensitivity function ω =5 rad s^{-1}

A.1.3 Parameters of existing conventional PI controller

The gain values of conventional PI controller has been considered in existing work as follows:

- Proportional gain $k_P = 5$
- Integral gain $k_I = 140$

A.1.4 Physical parameters of standalone distributed PV-BES generator

The numerical value of the constant parameters in the standalone distributed PV-BES generator are considered in Subsection 3.8.2 to evaluates the proposed controller performances:

- Filtering inductor of boost VSC, $L_{dcp} = 8$ mH

- Filtering inductor of buck-boost VSC $L_{dcb} = 12\,\text{mH}$
- DC-link capacitor, $C_{dc} = 5\,\text{mF}$
- DC input voltage, $V_{dc} = 500\,\text{V}$
- Switching frequency of VSCs, $f_s = 20\,\text{kHz}$
- DC-link connected load, $R_L = 6.25$ or $12.5\,\text{kW}$

A.2 Grid-Connected Distributed FC Generator

A.2.1 Calculation of the uncertainties

The parameters of the grid-connected distributed FC generator are considered as follows:

$$\mu_1 = \frac{1}{R_s C_s}$$
$$\mu_2 = \frac{1}{C_s}$$
$$\mu_3 = \frac{R_{sf}}{R_s C_s}$$
$$\mu_4 = \frac{R}{L}$$
$$\mu_5 = \frac{1}{L}$$
$$\mu_{23} = \mu_2 + \mu_3$$

The system parameters with uncertainties can express as follows:

$$\frac{1}{(R_a + \Delta R_a)(C_a + \Delta C_a)} = \mu_1 + \Delta\mu_1$$
$$\frac{1}{C_a + \Delta C_a} = \mu_2 + \Delta\mu_2$$
$$\frac{R_r + \Delta R_r}{(R_a + \Delta R_a)(C_a + \Delta C_a)} = \mu_3 + \Delta\mu_3$$
$$\frac{R + \Delta R}{L + \Delta L} = \mu_4 + \Delta\mu_4$$
$$\frac{1}{L + \Delta L} = \mu_5 + \Delta\mu_5$$

where $\mu_1 = \frac{1}{R_a C_a} > 0$, $\mu_2 = \frac{1}{C_a} > 0$, $\mu_3 = \frac{R_r}{R_a C_a} > 0$, $\mu_4 = \frac{R}{L} > 0$ and $\mu_5 = \frac{1}{L} > 0$ are the nominal parameters of the grid-connected FC system, and

$$\Delta\mu_1 = \frac{1 - (R_a + \Delta R_a)(C_a + \Delta C_a)/R_a C_a}{(R_a + \Delta R_a)(C_a + \Delta C_a)}$$
$$\Delta\mu_2 = \frac{1 - (C_a + \Delta C_a)/C_a}{C_a + \Delta C_a}$$
$$\Delta\mu_3 = \frac{R_r + \Delta R_r - R_r(R_a + \Delta R_a)(C_a + \Delta C_a)/R_a C_a}{(R_a + \Delta R_a)(C_a + \Delta C_a)}$$
$$\Delta\mu_4 = \frac{R + \Delta R - R(L + \Delta L)/L}{L + \Delta L}$$
$$\Delta\mu_5 = \frac{1 - (L + \Delta L)/L}{L + \Delta L}$$

are the uncertainties of μ_1, μ_2, μ_3, μ_4, and μ_5.

A.2.2 Parameters of designed robust $\mathbf{H}_\infty$ controller

To design robust H_∞ mixed-sensitivity loop-shaping controller for grid-connected distributed FC generator in Subsection 3.5.3 the following numerical values have been taken under consideration:

- Regulating values of $W_S(s)$, $k = 0.95$
- Regulating values of $W_T(s)$, $g = 0.83$
- Maximum acceptable fixed offset value, $A = 0.001$
- The peak value of the sensitivity function, $M = 1.2$
- Cross over frequency of the sensitivity function ω =1.5 rad s^{-1}

A.2.3 Parameters of existing conventional PI controller

The gain values of conventional PI controller for grid-connected distributed FC generator has been considered in existing work as follows:

- Proportional gain, $k_P = 2$
- Integral gain, $k_I = 10$

A.2.4 Physical parameters of grid-connected distributed FC generator

The numerical value of the constant parameters in the grid-connected distributed FC generator are considered in Subsection 3.8.3 to evaluates the proposed controller performances:

- DC input voltage, $V_{dc} = 500\,\mathrm{V}$
- Filtering inductor, $L = 10\,\mathrm{mH}$
- The internal resistor of filtering inductor $R = 0.1\,\Omega$
- Switching frequency of VSCs, $f_s = 20\,\mathrm{kHz}$

A.3 Two-Stage Distributed PV-BES Generator

The all parameters of the standalone distributed PV-BES and grid-connected distributed FC generators are satisfied the two-stage distributed PV-BES generator in Subsection 3.8.4 except dc-link connected load.

Appendix B

Supplementary Material for Chapter 4

B.1 Islanded DC Microgrid

B.1.1 Physical parameters of islanded DC microgrid

The following physical parameters are considered in Subsection 4.6.2, to evaluate the designed controller performances of parallel connected distributed generators in islanded DC microgrid.

- Input voltage, $V_s = 250\,\mathrm{V}$
- Bus voltage, $V_{dc} = 500\,\mathrm{V}$
- Filtering inductor, $L = 12\,\mathrm{mH}$
- Filtering capacitor, $C_{dc} = 100\,\mu\mathrm{F}$
- Switching frequency, $f_s = 20\,\mathrm{kHz}$

B.1.2 Formulas for Table 4.4

To comparison between proposed SITO-FBL controller and existing droop control scheme the following formulas are introduced voltage, current and power deviations in percentage.

- Voltage deviation, $\Delta V = \mid \frac{V_r - V_A}{V_r} \times 100 \mid \%$

- Current deviation, $\Delta I = \mid \frac{I_1 - I_2}{I_A} \times 100 \mid \%$
- Power deviation, $\Delta P = \mid \frac{P_1 - P_2}{P_A} \times 100 \mid \%$

B.2 Islanded AC Microgrid

B.2.1 Physical parameters of islanded AC microgrid

The following physical parameters are considered in Subsection 4.6.3, to evaluate the proposed controller performances of parallel connected distributed generators in islanded AC microgrid.

- DC input voltage, $V_{dc} = 500\,\mathrm{V}$
- Bus voltage, $V_L = 240\,\mathrm{V}$
- Filtering resistor, $R = 0.1\,\Omega$
- Filtering inductor, $L = 0.135\,\mathrm{mH}$
- Filtering capacitor, $C = 50\,\mu\mathrm{F}$
- Frequency of AC microgrid, $f = 50\,\mathrm{Hz}$
- Switching frequency, $f_s = 20\,\mathrm{kHz}$

B.3 Islanded Hybrid DC/AC Microgrid

The all parameters of the islanded DC and islanded AC microgrids are satisfied the islanded hybrid DC/AC microgrid system in Subsection 4.6.4.

Appendix C

Supplementary Material for Chapter 5

C.1 Standalone Distributed PV Generator

To analysis the switching frequency sensitivity of the standalone distributed PV generator in Subsection 5.5.1 the following physical parameters are played an crucial role.

- PV output capacitance, C_s =50 µF
- Filtering inductance, L_{dc} =1 mH
- Filtering capacitance, C_{dc} =100 µF
- Output voltage, V_{dc} =500 V
- Output current, i_{dc} = 100 A
- Resistive load, R_L =5 Ω

C.2 Grid-Connected Distributed PV Generator

To analysis the switching frequency sensitivity of the grid-connected distributed PV generator in Subsection 5.5.2 the following physical parameters are played an crucial role.

- DC input voltage of DC-AC VSC, V_{dc} =500 V
- PV output capacitance, C_{dc} =100 µF
- Filtering inductance, L =2 mH
- Filtering resistance, R =0.1 Ω

C.3 Two-Stage Distributed PV Generator

The all parameters of the standalone and grid-connected distributed PV generators are satisfied the two-stage distributed PV generator in Subsection 5.5.3 except resistive load.